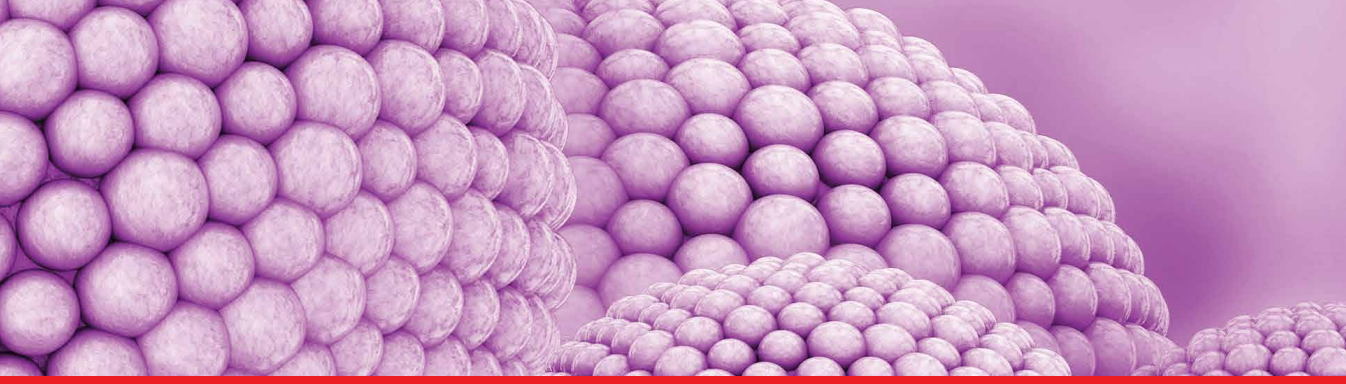

IntechOpen

IntechOpen Series
Nanotechnology and Nanomaterials, Volume 9

Zinc Oxide Nanoparticles

Fundamentals and Applications

Edited by Ana Rovisco and Ana Pimentel

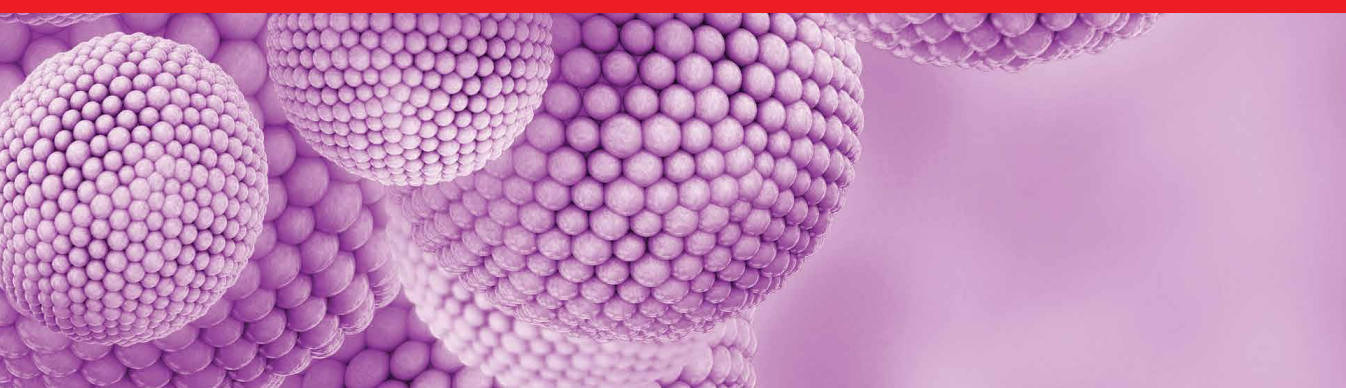

Zinc Oxide Nanoparticles - Fundamentals and Applications

Edited by Ana Rovisco and Ana Pimentel

Published in London, United Kingdom

Zinc Oxide Nanoparticles - Fundamentals and Applications
http://dx.doi.org/10.5772/intechopen.1001750
Edited by Ana Rovisco and Ana Pimentel

Contributors
Abhimanyu Kumar Singh, Abhishek Kumar Bhardwaj, Ajay Kumar Tiwari, Ana Rovisco, Andreea Costas, Bhagaban Kisan, Hadba Hussain, Irina Zgura, Jorge Martins, Jung-Hyuk Koh, Marcela Socol, Maria Morais, Mariana Cortinhal, Maryam Basit, Mohsin Saleem, Muhammad Aftab Akram, Nicoleta Preda, Norollah Kheyri, Pedro Barquinha, Rajat Kumar Das, Ram Raseele Awasthi, Rodrigo Martins, Saket Jha, Sharad Kumar Tripathi, Sofia Javed, Yahia Chergui

First published in London, United Kingdom, 2025 by IntechOpen
IntechOpen is the global imprint of INTECHOPEN LIMITED, registered in England and Wales, registration number: 11086078, 167-169 Great Portland Street, London, W1W 5PF, United Kingdom

For EU product safety concerns: IN TECH d.o.o., Prolaz Marije Krucifikse Kozulić 3, 51000 Rijeka, Croatia, info@intechopen.com or visit our website at intechopen.com.

British Library Cataloguing-in-Publication Data
A catalogue record for this book is available from the British Library

Zinc Oxide Nanoparticles - Fundamentals and Applications
Edited by Ana Rovisco and Ana Pimentel
p. cm.

This title is part of the Nanotechnology and Nanomaterials Book Series, Volume 9
Topic: Nanomaterials and Nanostructures
Series Editor: Jung Huang
Topic Editor: Alberto Jiménez-Suárez
Associate Topic Editor: Gonzalo Seisdedos

Print ISBN 978-0-85466-602-7
Online ISBN 978-0-85466-601-0
eBook (PDF) ISBN 978-0-85466-603-4
ISSN 3029-0538

IntechOpen Book Series

Nanotechnology and Nanomaterials

Volume 9

Aims and Scope of the Series

Humans face growing challenges in environmental sustainability. We need better materials, more effective devices, and higher computing power to conquer these challenges. Researchers have long explored the realm of science at the nanometer scale for developing novel problem-solving technologies. In the past decades, breakthroughs in multiscale computer simulation, novel hierarchical material and device structures, nanometrology, and new functionalities from interfacial and quantum size effects have enhanced our ability to utilize nanotechnology to solve real-world problems. This book series addresses important advancements in nanotechnology and nanomaterials. It showcases how nanotechnology is being continually developed and implemented in a variety of domains of science and technology. The two main topics this series covers are Nanotechnology and Nanodevices, and Nanomaterials and Nanostructures.

Meet the Series Editor

Jung Y. Huang, a university educator and researcher, has been working to unravel the structures and functional properties of materials and cellular events in living cells with varying optical methodologies. He has co-authored hundreds of journal papers and five book chapters. He also holds tens of patents in laser techniques and single-molecule/hyperspectral imaging and has developed architectural photonics based on hierarchically structured materials. Currently, his research focuses on the integration of artificial intelligence methodology with optics to automatically discover meaningful information from optical sensing/imaging data cubes. He has been an editorial board member and reviewer for several scientific journals. As a member of the global scientific community, he sincerely supports and endeavors to promote the spread of scientific knowledge.

Meet the Volume Editors

Ana Rovisco is an Assistant Researcher at CENIMAT|i3N and CEMOP/UNINOVA, NOVA School of Science and Technology (FCT-NOVA), Portugal. She holds a Ph.D. in Nanotechnologies and Nanosciences and an MSc in Physics Engineering from FCT-NOVA. Her expertise lies in electron microscopy, nanofabrication, and solution-based oxide nanostructures for multifunctional applications such as sensors, energy harvesters, and photocatalysis. She has authored numerous peer-reviewed articles and book chapters, with her work recognized and referenced within the scientific community. She has also taught nanofabrication, materials characterization, and advanced microscopy courses. An active mentor and collaborator, she contributes to international research projects and is a reviewer for leading journals, advancing knowledge in nanotechnology and sustainable materials.

Ana Pimentel completed her Ph.D. in Nanotechnologies and Nanoscience in 2011 from the NOVA School of Science and Technology. In 2012, she started a position as a Post-doctoral researcher at CENIMAT/I3N on the synthesis of metal oxide nanoparticles to be used in different areas of applications, like UV and biosensors, photocatalysis, and electrochromic devices. Between 2019 and 2023, she worked as an assistant researcher (CEEC 2017), focusing on the solution-based synthesis of metal and metal oxide nanostructures. Currently, she is a principal researcher at Cenimat/I3N, FCT-UNL, focusing on Scanning-transmission electron microscopy analyses. Her current research focuses are materials research using STEM and SEM; hydrothermal synthesis assisted by microwave radiation; spin-coating of thin films; metal oxides nanostructures grown on cellulosic and cork substrates; UV and biosensors; photocatalysis; antibacterial activity; and electrochromic applications.

Contents

Preface

This book presents the latest advancements and trends in ZnO nanostructures, encompassing their synthesis, applications, and theoretical insights. Key areas include environmental science, where ZnO nanoparticles offer significant potential for pollution control and sustainable development, and biomedical science, where their biocompatibility and multifunctionality pave the way for diagnostics, treatments, and drug delivery innovations.

Theoretical and computational studies provide a deeper understanding of ZnO's structural behavior under diverse conditions, expanding its technological applications. In addition, discussions on doped and structured ZnO nanomaterials highlight advancements in enhancing electrical, optical, and magnetic functionalities. Agricultural applications of ZnO nanoparticles demonstrate their role in improving crop yield and quality, addressing global food security challenges. Moreover, precise control of ZnO nanostructures continues to advance their use in sensors, electronics, and other technological devices.

The book also explores bioinspired approaches, showcasing how nature can inspire the design of nanomaterials with tailored properties, merging biology with cutting-edge nanotechnology.

By bridging diverse fields—environmental science, biomedicine, computational modelling, materials engineering, agriculture, and bioinspired nanotechnology—this book provides researchers, academics, and industry professionals with a comprehensive understanding of ZnO nanoparticles' critical role in addressing modern scientific and industrial challenges. It emphasizes their versatility and importance in shaping the future of science and technology.

Ana Rovisco and Ana Pimentel
CENIMAT/i3N, Department of Materials Science,
NOVA School of Science and Technology (NOVA-FCT) and CEMOP/UNINOVA,
NOVA University Lisbon,
Caparica, Portugal

Chapter 1

Review of Synthesis, Characteristics, and Applications of Doped Zinc Oxide Nanostructures

Hadba Hussain

Abstract

Zinc oxide (ZnO) is a unique material due to its physical and chemical properties, such as wide bandgap at room temperature (RT) (3.37 eV) and high binding energy (60 meV). This chapter contains the most important synthesis methods of doped ZnO nanostructure preparation. The most common methods for preparing nanoparticles (NPs) and thin films (TFs) are sol-gel, precipitation, and hydrothermal. The effects of doping appear in various forms and properties. Therefore, doped ZnO nanostructure characteristics are described to explain the structural properties, including the particle size measurement methods and the other features based on XRD data and others, and optical properties contain the approaches of bandgap energy calculations depending on UV-visible results, as well as electrical and magnetic properties. The doped ZnO nanostructures' properties change after doping with metals and non-metals. The last part of the chapter illustrates the most prevalent and crucial applications, starting with medicine, followed by photocatalysis, photovoltaic, UV absorbers and photodetectors, and sensors, and finishing with a light-emitting diode (LED). This review provides valuable information when dealing with works related to pure and doped ZnO nanostructures.

Keywords: ZnO, doped ZnO, nanostructures, nanoparticles, thin films, structure properties, optical properties, electrical properties, bandgap engineering, magnetic properties, synthesis, applications, drug delivery, photocatalysis, photovoltaic, sensor, UV absorber, light emitting diode (LED)

1. Introduction

Zinc oxide (ZnO) material is one of the most dominant materials due to its unique properties, such as bandgap energy at room temperature (RT) around 3.4 eV and its exciton binding energy ~ 60 meV [1]. In addition, it has the ability to grow one single crystal over the substrate, a favorite material with wet chemical processes such as etching, low threshold energy for optical applications, biocompatibility, and solidity of radiation.

ZnO has two structures, cubic shaped in zincblende and rocksalt (NaCl) structures; also hexagonal shaped in wurtzite structure; one single zinc (Zn) atom surrounded by four oxygen (O) atoms; and vice versa. The most known polar faces with an equal polarity with the same number of O and Zn atoms are the Zn face

(0001), which is the essential face, the O-face ($000\bar{1}$) (c-axis), and non-polar faces ($1\bar{1}20$) (a-axis) and ($1\bar{0}10$). The polarity of the structure faces contributes to determining the properties, where the O-terminated faces have various electronic structures; the (1010) face and polar surfaces are more stable, while the ($1\bar{1}20$) face is less stable and has a higher surface roughness [2, 3]. The a and c are the lattice parameters of the ZnO hexagonal unit cell, where a = 3.2495 Å and c = 5.2069 Å, while the density is 5.605 $g.cm^{-3}$ [4]. Thus, materials and elements are doping into ZnO structures for further improvements and enhancement. These dopants are rare earth, transmission metal, and other elements such as aluminum (Al), magnesium (Mg), nitrogen (N), and others, depending on specific applications.

Therefore, when an element is added to ZnO, the length of the lattice parameters changes as the added element atom replaces the Zn atom; this, in turn, affects the Full Width at Half Maximum (FWHM) of the XRD pattern of the structure, as well as the crystal's size, volume, interplanar space, strain, stress, and other properties. For instance, when ZnO is doped with a concentration starting from 0 to 1% of manganese (Mn), it increases linearly with the Mn content, meaning that Mn^{+2} ions substitute for Zn^{+2} ions [5], where doped ZnO by low concentration of Si enhanced the crystalline while it deteriorates with high Si content [6]. More details will appear in the later section.

ZnO nanostructures are naturally n-type and have high electron mobility and low resistivity; thus, they are good conductors [7]. Electron mobility is strongly affected by temperature, while resistivity depends on the thickness. In addition, the electron Hall mobility of ZnO at 300 K for low n-type conductivity is μ = 200 $cm^2/V.s$ and 5–50 $cm^2/V.s$ for low p-type conductivity [8].

The electronic band structure of ZnO is direct bandgap energy, and several investigations indicate that the valence band maxima and the lowest conduction band minima occur at the $\mathbf{\Gamma}$ point k = 0 [9–11]. Due to its optical features, ZnO has beneficial properties, including transparency and RT solid luminescence, which is directly influenced by band structure energy. Therefore, the photoluminescence (PL) spectra of ZnO assign many defect-related spectral features and a donor-acceptor pair (DAP) emission. The origin of its luminescence is a broad defect-related peak known as the green band. It has been attributed to various impurities and defects, as will become apparent below [12].

The electric currents and magnetic moments of pure ZnO elementary particles describe it as a diamagnetic material with a weak attraction to the magnet force [13]; however, in daily life, without any instrument to detect this tiny attraction, pure ZnO is classified as a non-magnetic material. Accordingly, numerous magnetic measurements indicate that pure ZnO is diamagnetic, and the doping process converts this feature to the opposite [14, 15].

This chapter will demonstrate the modification of properties of ZnO nanostructures after being doped by an element, and the preparation methods include physical and chemical methods for both nanoparticles (NPs) and thin films (TFs). In addition to their benefits and uses in industrial, aerospace, and medical applications.

2. Synthesis methods and characterization

2.1 Synthesis methods

Preparing doped ZnO nanostructures depends on the desired results. Therefore, multifactor enters to determine the shapes and the properties. To modify the

properties of the doped ZnO nanostructures, changing the preparation parameters leads to achieving this required feature. To illustrate, changing one factor while preparing copper (Cu)-doped ZnO will change the property; if the temperature [16], doped concentration [17], or pH [18] of the Cu-doped ZnO nanostructure were varied, the electrical and optical properties were enhanced, and improved.

On the other hand, to synthesize diverse morphologies of doped ZnO nanostructures, choosing the preparation method at the beginning tends to obtain the demand structures, so sol-gel [19–22], co-precipitation [23–26], and solvothermal [27, 28] and hydrothermal methods [29–33] are well-known processes for preparing doped ZnO NPs. While spin coating [34–37], chemical vapor deposition (CVD) [38–42], plasma-enhanced chemical vapor deposition (PECVD) [43–47], molecular organic chemical vapor deposition (MOCVD) [48–51], pulsed laser deposition (PLD) [52–55], atomic layer deposition (ALD) [56–59], and sputtering [60–63] methods are processes and techniques for growth and deposit doped ZnO TFs.

The rod particles are typically produced during the formation of Zn $(OH)_2$ with the precipitate agents. Additionally, the concentration and rate of the OH^- affected the morphology. Furthermore, when the OH^- and Zn^{2+} precursors mixed simultaneously, the chemical reaction became faster and produced nanosheets. Meanwhile, adding the precursor of OH^- slowly into the Zn^{2+} precursor tends to generate morphology in a hexagonal prism shape [64]. Moreover, the stabilizers are one of the parameters that affect the morphologies, such as sodium dodecyl sulfate (SDS) and polyvinylpyrrolidone (PVP), to form, for instance, sea urchin morphology [65] and nanorods [66].

Moreover, preparation methods can be classified based on wet chemical and combustion methods [67]. One of the challenges is to control the shapes and dimensions and determine the required structure during the preparation process, which plays a significant role in determining the uses of the structures. Therefore, the morphology and dimensions of the NPs can be controlled *via* surfactants such as sodium dodecyl sulfate or cetyltrimethylammonium bromide [68, 69].

Sol-gel and co-precipitation methods are the most well-known procedures for preparing doped ZnO NPs. Due to their low cost and equipment, high-quality produced materials with relatively good purity outcome, and versatility. Moreover, nontoxic solvents can shape the structure, low preparation temperatures, and resulting stoichiometry of the resulting material [67].

In the sol-gel, co-precipitation, and hydrothermal methods, a chemical bond formed between the zinc and OH atoms to form zinc hydroxide. Then, due to heat, zinc oxide nanostructures are formed [70–72] according to these equations [73]:

$$Zn^{2+} + 2OH^- \rightarrow Zn(OH)_2 \quad (1)$$

$$Zn(OH)_2 + 2OH^- \rightarrow Zn(OH)_4^{2-} \quad (2)$$

$$Zn(OH)_4^{2-} \rightarrow ZnO + H_2O + 2OH^- \quad (3)$$

Typically, this process depends on agents providing OH^- groups, such as sodium hydroxide (NaOH) [74, 75] and potassium hydroxide (KOH) [76, 77], to avoid precipitation of the zinc hydroperoxide ($ZnOH^-$) and facilitate ZnO formation.

The common zinc precursors used are zinc acetate [78], zinc chloride [79], and zinc nitrate [80], which are easily dissolved in well-known solvents such as water [81], ethanol [82], and methanol [40]. Sulfide is also one of the precursors used to form doped ZnO nanostructures [83]. Choosing corresponding dopant elements for

the dopant precursors is a good choice for forming doped ZnO nanostructures, acetates [84], chlorides [85], and nitrates [86]. Lamia Al-Farsi et al. prepared Al-doped ZnO nanorods by hydrothermal method using zinc nitrate hexahydrate (Zn $(NO_3)_2{\cdot}6H_2O$) and aluminum nitrate (Al $(NO_3)_3{\cdot}9H_2O$) [87].

2.2 Structure properties

ZnO nanostructures have hexagonal (wurtzite) structures, with lattice constants a = 3.253 Å and c = 5.206 Å [88]. Substitution and interstitial doped ZnO nanostructures by elements altered the nanostructure size, lattice constants, distance between layers, volume, strain, and dislocation density. Manipulating the doping amount and controlling the solvent amount during the doping process are ways to control the size of ZnO nanostructures. Jacek Wojnarowicz et al. [88] successfully controlled the crystalline size of 10% of Co-doped ZnO NPs precisely by controlling the water quantity in the precursor, as shown in **Figure 1** [88].

Nanostructure size is calculated using the Scherrer equation [89] by dividing the product of the Scherrer constant (K = 0.89) and the wavelength of the X-ray beam used (λ = 1.54,184 Å) by the product of the FWHM (β) of the peak and the Bragg angle θ Eq. (4) [90–92].

$$D = \frac{K\lambda}{\beta cos\theta} \tag{4}$$

Moreover, the scientists Williamson and Hall presented a method for clarifying the size broadening (β_D) and strain broadening (β_ε) as a function of diffraction angle (2θ), where the method is known as W-H equation. Thus, the observed line width is calculated by adding β_D and β_ε as $\beta = \beta_D + \beta_\varepsilon$. The W–H equation is represented in Eq. (5).

$$\beta cos\theta = \frac{K\lambda}{D_{WH}} + 4\varepsilon_{WH} \sin\theta \tag{5}$$

It corresponds to the uniform deformation model of the W–H method, where the strain is assumed to be uniform in all crystallographic directions. The plot shows the crystallite size estimated from the y-intercept, and the slope of the fit gives the strain, ε_{WH}. Furthermore, the third approach that can be used to measure the particle size

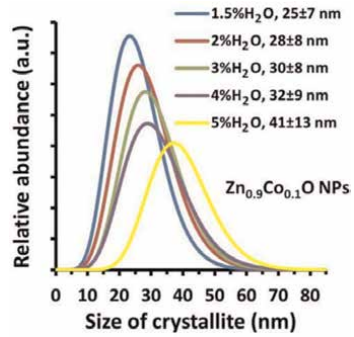

Figure 1.
Zn0.9Co0.1O NPs of crystallite size distributions. Reproduced with permission of Ref. [88].

and lattice strain from XRD data is the Halder-Wagner (H–W) method presented in Eq. (6).

$$\left(\frac{\beta}{tan\,\theta}\right)^2 = \frac{K\lambda}{D_{HW}} \bullet \frac{\beta}{sin\,\theta tan\theta} + 16\varepsilon_{HW}^2 \tag{6}$$

Where the plot is made $(\beta/\tan\theta)^2$ against $\beta/(\sin\theta\tan\theta)$. The slopes yield the Halder-Wagner crystallite size (D_{HW}), and the intercept gives the Halder-Wagner strain ε_{HW}. The abovementioned three methods of calculating the particle size from XRD data are presented in **Table 1**. Nusrat Jahan Tamanna et al. [93] calculated the particle size of the ZnO NPs using these three methods: Scherrer equation, Williamson and Hall (W-H), and Halder-Wagner (H–W) and found that the particle size is 1540.6, 69.675, and 72.463 nm, respectively.

In addition, scanning electron microscopy (SEM) and transmission electron microscopy (TEM) are methods to produce images and measure the nanostructures' size, as Khorsand Zak et al. [94] measured the ZnO NPs using these two methods.

For measuring the interplanar space d_{hkl} and lattice constants a and c of doped ZnO nanostructures using Eqs. (7)-(8), where hkl is the Miller indices. Calculating a and c can be done directly from Eqs. (9) and (10):

$$\frac{1}{{d_{hkl}}^2} = 4/3\left(\frac{h^2 + hk + k^2}{a^2}\right) + \frac{l^2}{c^2} \tag{7}$$

$$sin\,\theta^2 = \frac{\lambda^2}{4\,a^2}\left[\frac{4}{3}\left(h^2 + hk + k^2\right) + \left(\frac{a}{c}\right)^2 l^2\right] \tag{8}$$

$$a = \frac{\lambda}{\sqrt{3}}\,sin\,\theta \tag{9}$$

$$c = \frac{\lambda}{sin\,\theta} \tag{10}$$

In addition, volume (V) can be measured by Eq. (11). Strain (ε), stress (σ), and dislocation density (δ) are calculated *via* Eqs. (12)–(14) [95]. Where is the FWHM in radian, 'Y' is Young's Modulus of Elasticity.

$$V = \frac{\sqrt{3}\,a^2 c}{2} \tag{11}$$

$$\varepsilon = \frac{\beta\,cos\theta}{4\,sin\theta} \tag{12}$$

$$\sigma = Y\varepsilon \tag{13}$$

$$\delta = \frac{1}{D^2} \tag{14}$$

Anion-cation Zn–O bond length (L) and energy density (u), which is defined as strain energy per unit volume, are measured using Eqs. (15)–(16) [96]. Where "u" is the internal relaxation parameter for the wurtzite structure and is given by $u = \frac{a^2}{3c^2} + 0.25$. **Table 2** summarizes particle size calculation equations and all the hexagonal structure properties calculating formulas.

The method name	Formula
Scherrer equation	$D = \frac{K\lambda}{\beta cos\theta}$
Williamson and Hall (W-H)	$\beta \cos\theta = \frac{K\lambda}{D_{WH}} + 4\varepsilon_{WH} \sin\theta$
Halder-Wagner (H–W)	$\left(\frac{\beta}{\tan\theta}\right)^2 = \frac{K\lambda}{D_{HW}} \bullet \frac{\beta}{\sin\theta\tan\theta} + 16\varepsilon_{HW}^2$

Table 1.
Particle size calculation methods from XRD data.

Quantities	Symbols	Units	Formulas
Williamson and Hall (W-H) method of calculating particle size	D_{WH}	nm	$\beta \cos\theta = \frac{K\lambda}{D_{WH}} + 4\varepsilon_{WH} \sin\theta$
Halder-Wagner (H–W) method of calculating particle size	D_{HW}	nm	$\left(\frac{\beta}{\tan\theta}\right)^2 = \frac{K\lambda}{D_{HW}} \cdot \frac{\beta}{\sin\theta\tan\theta} + 16\varepsilon_{HW}^2$
Scherrer equation of calculating particle size	$D_{scherrer}$	nm	$D = \frac{K\lambda}{\beta cos\theta}$
			Where K is the Scherrer constant (K = 0.89), λ is the wavelength of the X-ray beam used (λ = 1.54,184 Å), β is the FWHM of the peak, and θ is the Bragg angle.
Interplanar spacing	d_{hkl}	nm	$\frac{1}{d_{hkl}^2} = 4/3\left(\frac{h^2+hk+k^2}{a^2}\right) + \frac{l^2}{c^2}$
			Where d_{hkl} is the interplanar spacing, hkl is the Miller indices, also a and c are lattice constants.
Lattice constants of hexagonal structure	a, b, and c	Å	$sin\,\theta^2 = \frac{\lambda^2}{4\,a^2}\left[\frac{4}{3}\left(h^2+hk+k^2\right) + \left(\frac{a}{c}\right)^2 l^2\right]$
			Where θ is the Bragg diffraction angle; the source of the X-ray wavelength is $\lambda(Cu)$ = 1.5406 Å; a and c are the lattice parameters; and h, k, and θ are Miller indices.
Lattice constants a	a	Å	$a = \frac{\lambda}{\sqrt{3}} \sin\theta$
			Where θ is for the Bragg diffraction angle that would calculate a for it.
Lattice constants c	c	Å	$c = \frac{\lambda}{\sin\theta}$
			Where θ is for the Bragg diffraction angle that would calculate c for it.
Volume	V	$Å^3$	$V = \frac{\sqrt{3}\,a^2 c}{2}$
			Where a and c are the lattice constants.
Strain	ε	—	$\varepsilon = \frac{\beta\, cos\theta}{4\, sin\theta}$
			Where is the FWHM in radian.
Stress	σ	Pa	$\sigma = Y\varepsilon$
			Where "Y" is Young's Modulus of Elasticity and ε is the strain.

Quantities	Symbols	Units	Formulas
Dislocation density	δ	1/ nm^2	$\delta = \frac{1}{D^2}$
			Where D is the particle size.
Bond length	L	Å	$L = \sqrt{\left(\frac{a^3}{3} + \left(\frac{1}{2} - u\right)^2 c^2\right)}$
			Where a and c are the lattice constants and "u" is internal relaxation parameter for wurtzite structure and is given by: $u = \frac{a^2}{3c^2} + 0.25$
Energy density	u	J/m^3	$u = \frac{\varepsilon^2 Y}{2}$
			Where ε is strain and Y Young's Modulus of Elasticity.

Table 2.
Summarizes particle size calculation equations and all the hexagonal structure properties calculating formulas.

$$L = \sqrt{\left(\frac{a^3}{3} + \left(\frac{1}{2} - u\right)^2 c^2\right)} \tag{15}$$

$$u = \frac{\varepsilon^2 Y}{2} \tag{16}$$

The difference between these three methods is that the Scherrer equation does not consider the strain, which is one of the parameters of broadening the FWHM, while the W-H does. Thus, in the Scherrer equation, calculating the crystal size relies only on the FWHM, and a large peak width will give a small crystallite size and vice versa.

There are some corrections to the Scherrer equation and W-H method. There are also other methods available to calculate the crystal size, where Marzieh Rabiei et al. [97] deeply measured hydroxyapatite's crystal size using all the methods depending XRD, TEM, and Brunauer-Emmett-Teller (BET), explain the difference between them and the accurate values which are close to the experiment results.

Doped ZnO nanostructures by Al decreased the particle size of the ZnO, from 30.21 to 25.48 nm using reduction method [98]; also, Pooja Nag Mishra et al. [99] investigated the structural properties of Al-doped ZnO (AZO) at constant temperature and found that with an increase in the amount of doping the crystallite size of AZO is seen to be decreased compared to the pure ZnO from 35.05 to 18.89 nm. At the same time, ZnO nanostructure size is increased with the increase in Mg content where the amount of Mg around x = 2% to x = 10% by 2% increment, and the crystallite size of Mg-doped ZnO was increased from 32.51 to 42.32 nm [96]. The decrease in the crystal size of Al-doped ZnO nanostructures is attributed to the substitution of Al^{+3} ions with Zn^{2+} ions, which have a smaller atomic radius r = 0.54 A° compared to the Zn^{+2} ion radius r = 0.74 A° [100], while the increasing with doped Mg is due to the ionic radius of Mg^{+2} r = 0.72 A° is very close to that of Zn^{+2} ions and with broader

bandgap energy (Eg) ∼ 7.8 eV of the MgO and ZnO gives rise to increase in bandgap energy [96].

Lithium (Li), sodium (Na), and potassium (K) elements of group 1 have ionic radii of 0.76, 1.0, and 1.38 Å, respectively, compared to Zn 0.74 Å. Li has the smallest radii, which allows it to be easily interstitial to the ZnO nanostructure. Although the Na and K have larger radii than the ZnO nanostructure, cations have smaller ionic radii than the origin element. However, the number of electrons in the outer shell plays a considerable role. The Na^{+1} ion has ten electrons in two energy levels, while the K^{+1} ion has 18 electrons in three energy levels, which leads to shrunk radii as the number of electrons has reduced, and this means the repulsive force between electrons is reduced, so Na and Li enter the ZnO crystal interstitial. Therefore, doped ZnO nanostructures by group one elements increase the particle size [101, 102]. On the other hand, doping ZnO nanostructures by manganese (Mn) and titanium (Ti) decrease the crystallite size [103–105].

2.3 Electrical properties

As known, doping ZnO by p-type is complex, so doped ZnO by Li is one of the approaches used to compensate n-type conductivity in the unintentionally doped ZnO aimed at obtaining a p-type ZnO. Li-doped ZnO has been successfully prepared using several methods to enhance its electrical features. Rajeev Gandhi et al. [106] reported Li-doped ZnO NPs and created supercapacitors with 401 F/g prepared by the co-precipitation method, also studied *via* the density functional theory (DFT) theoretical approach. In addition, Shawuti et al. [107] substituted zinc (Zn) atoms by 5 and 10% mol of Li atoms using the sol-gel process to enhance the electrical conductivity and measured complex analyzed of impedance at an intermediate temperature range from 100 to 400°C. Furthermore, increased excitation laser power raised carrier lifetime and PL response intensity.

Yttrium (Y) doping raises the electrical conductivity of ZnO into 19,336 $\times 10^{-5}$ $(\Omega\text{-cm})^{-1}$. At the same time, ZnO doped with Mg decreased the electrical conductivity to 0.1310 ($(x10^{-5})$ $(\Omega\text{-cm})^{-1}$) as compared with pure ZnO (1375 $\times 10^{-5}$ $(\Omega\text{-cm})^{-1}$) [108]. Where the resistivity of the ZnO TFs (1.03 $\times 10^{-1}$ Ω.cm) is decreased by doping 3% of Na (3.18 $\times 10^{-2}$ Ω.cm) and K (5.64 $\times 10^{-2}$ Ω.cm) prepared using spray pyrolysis method, due to the doping defect creation, and acts as scattering centers. In addition, the carrier concentrations increased from 5.17 $\times 10^{17}$ cm^{-3} pure ZnO to 1 $\times 10^{18}$ cm^{-3} K-Na doped ZnO TFs [109]. The electrical features of ZnO are controlled by doping. If the doping is metal elements such as copper (Cu) [110], silver (Ag) [111], iron (Fe) [112], and Al [113], the resistivity decreases; thus, the conductivity increases, and the charge carrier mobility increases. Furthermore, silicon (Si) and phosphor (P) enhanced the conductivity and carrier concentration, as Chaeseon Hong et al. [114] reported that Si-ZnO growth *via* ALD showed an increase in the electrical characteristics, the carrier concentration raised around 8.10 $\times 10^{20}$ cm^{-3}, and the resistivity reduced to 5.15 $\times 10^{-4}$ Ω·cm, [115, 116].

2.4 Optical properties

The optical properties of pure ZnO at RT are significantly great and show broad PL emission peaks in the visible region and near-band-edge emission caused by various intrinsic defects [117]. Therefore, doped ZnO nanostructures enhanced these features to another level, thus leading to improvement in the optoelectronic, optical, and

electronic devices' performances. The PL of doped ZnO nanostructures contains six contrasting defects: zinc and oxygen vacancies as void defects, zinc and oxygen as interstitial defects, and finally, acceptor and doner (dopants) as interstitial faults [118]. PL peaks of doped ZnO nanostructures are commonly located at 393–420 nm, which corresponds to band gap excitonic emission, and at 520–550 nm, due to the defects. The variation in the peak locations of the emission spectra corresponds to the changes in the defect densities on the surface of the doped ZnO nanostructures, and these changes originated during the synthesized process with various precursors and methods [119]. Andres Galdámez-Martinez et al. [120] investigated deeply the effect of a size reduction over the prominent bands of emission that originated several sub-peaks, which showed possible numerous, various energy levels, and produced a perfect summary of these bands' emissions. These bands shifted by dopants as Mohsin Khan et al. [121] investigated the PL of the ZnO TFs when it is doped by transition metals (Fe, Zr, and Co).

Li has an incredible impact on the optical properties of ZnO. The PL intensity significantly increased and reached almost 10^6 a.u. with various contents of Li (15, 31, 54, and 65%) in the ZnO crystals at wavelength started from 340 to 600 nm, as Patrik et al. [122] reported. The transmission spectra of the AZO films were above 80% in the visible wavelength, and a clear blue shift of the optical band edge with increasing Al concentration, as well as it appears in the PL spectra. Additionally, there was a substantial decrease in the PL intensity with an increase of the Al concentration from 0 to 3.2% in the as-prepared AZO films due to the introduction of the nonradiative recombination centers with increasing the concentration of the Al_2O_3 doping layers in AZO films [123]. Increasing temperatures increase the crystallinity of the doped ZnO structure and raise the PL intensity [124].

Ultraviolet–visible (UV-vis) spectroscopy measures the absorption, transmission, reflection, refractive index, absorption coefficient, and bandgap energy are measured depending on Beer Lambert's law; also the Tauc plot in Eq. (17) [125] and the Kubelka-Munk function relation in Eq. (18) [126] are methods to calculate the bandgap energy. The Tauc method is based on the energy-dependent absorption coefficient α. The measured reflectance spectra are transformed by the Kubelka-Munk function $F(R_\infty)$ to the corresponding absorption spectra. Where h is the Planck constant, ν is the photon's frequency, Eg is the band gap energy, and B is a constant. The n factor depends on the nature of the electron transition, whether direct or indirect transition bandgaps are equal to 1/2 or 2, respectively. In addition, bandgap energy depends on wavelength in Eq. (19), where c is the speed of light, and λ is the cutoff wavelength [127].

$$(\alpha.h\nu)^{1/n} = B\left(h\nu - E_g\right) \tag{17}$$

$$(F(R_\infty).h\nu)^{1/n} = B\left(h\nu - E_g\right) \tag{18}$$

$$E_g = \frac{hc}{\lambda} \tag{19}$$

Bhubesh Chander Joshi et al. [110] measured the bandgap energy of Cu-doped ZnO TFs with 3 and 6% doping concentrations using the Tauc plot approach, where the bandgap energy was 3.09 and 3.07 eV, respectively, as well as Refs. [128–130] reported. Kamlesh V. Chandekar et al. [131] measured the bandgap energy of Cu-doped ZnO NPs with 1, 2.5, and 5 wt.% using the Kubelka-Munk function found ∼ 3.150, 3.100, and 2.995 eV, respectively, as Abebe et al. [132] also reported.

Bandgap engineering of ZnO nanostructures is investigated widely to control energy and improve optical features. Mg and cadmium (Cd) are usually used to tunable the bandgap energy. Mg doping widens the band gap into a short wavelength (ultraviolet (UV) range) (3.37 eV to $\geq$ 4.0 eV), causing a blue shift in the absorption spectra, while Cd doping results in a red shift by narrowing the bandgap energy into a long wavelength (1.7–3.2 eV) [133]. Additionally, nickel (Ni) and silver (Ag) decrease the bandgap energy of ZnO nanostructures, where the bandgap energy of 1, 3, and 5 mol.% Ni decreased from 3.1 eV of ZnO into 3.05, 2.95, and 3 eV, respectively. Ag decreased the bandgap energy of ZnO further into 2.8, 2, and 1.8 eV for 1, 3, and 5 mol %, respectively. Ni enhanced ZnO UV absorption; in the visible region, 3 and 5% mol. % of Ag also improved it [134]. Increasing the AZO TFs thickness increased the absorption in the infrared region (800–5000 nm) as well as the extinction coefficient (k) raised significantly, and the metallic properties appeared beside the semiconductor features of these films where the bulk carrier concentration of AZO was near to $1.9 \times 10^{21}/cm^3$ [135]. Moreover, the transmittance of the films of Si-doped ZnO was above 80%, and the optical band gap increased from 3.29 to 3.47 eV with increasing the Si thickness [114].

2.5 Magnetic properties

The difference between diamagnetic and paramagnetic materials is that the former have paired electrons and are repelled by the magnetic field, while the latter have unpaired electrons and are attracted to it. Meanwhile, the material is called ferromagnetic when its electrons show high attraction to the magnetic field and become nearly magnetized [136].

A vibrating sample magnetometer (VSM) (also called M-H curve) is one approach to measuring magnetic properties; from the VSM, magnetization curve, hysteresis loop, demagnetization curve, saturation magnetization, and residual magnetization can be computed [137].

The VSM results revealed that the nature of pure ZnO is diamagnetic, with any particle size, and even in high fields. This feature completely converts when it is doping. Doping ZnO by Cu^{2+} ions changes to a ferromagnetic nature at RT due to free carriers induced by Cu^{2+} doped into ZnO nanoparticles. The reason behind the appearance of ferromagnetism is due to the oxygen vacancies and exchange interaction of Cu^{2+} with oxygen ions with the spin moment [138, 139]. Additionally, Co-doped ZnO NPs show superparamagnetic and ferromagnetic behavior co-existence at RT and 2 K [140]. In addition to the zirconium (Zr) element, doped ZnO by Zr converts the Zr-ZnO NPs into ferromagnetism at RT, and the results of Raman and X-ray photoelectron spectroscopy indicate that multiple oxygen vacancies in the Zr-ZnO NPs [141].

When the material's magnetization cannot be increased further when a magnetic field is applied, this state is called magnetic saturation. Hence, the hysteresis loop studies the relationship between the induced magnetic moment (m) and the applied magnetic field (H) at RT and can measure these magnetic properties: saturation magnetization (M_s), remnant magnetization (M_r), and coercive field (H_c). The actual unit for the m is erg per gauss or erg per oersted (Oe), but it is usually expressed as "emu," which is a unit for them. Therefore, "emu" indicates electromagnetic units [142].

The co-doping of Mn-Fe ions in the ZnO structure enhanced the magnetic properties, and the magnetic saturation M_s values of Mn and the Mn-Fe co-dopant into ZnO are greater than pure ZnO when the doping concentration of Mn is x = 0.05 and

maximal x = 0.09 [143]. Ti-doped ZnO NPs show ferromagnetic behavior and have M_s of 6.89 emu/g, M_r of 7.93 emu/g at RT, and a H_c of decomposition Ti-doped ZnO NPs of 1.500 Oe, and the squareness (remanence ratio: M_r/M_s) was 0.012 [144].

3. Applications

Numerous applications of doped ZnO are due to the ZnO properties and the improvement and enhancement of these features that are done by the doping process. Optoelectronics and transparent electronics are mainly used on doped ZnO because its bandgap is wide and direct, including favorable band-edge positions in an aqueous medium to generate oxygenated free radicals, high biocompatibility, high sensitivity to the light, broad UV and visible (solar) light absorption, large exciton binding energy (60 meV), high electron mobility, great flexibility in chemical functionalization, high transparency, and low-cost approach for large-scale synthesis with diverse morphologies [145]. Particularly in the medical field, doped ZnO nanostructures enter into multiple bio-applications, such as drug delivery and tissue engineering, as tools to promote the repair of damaged tissues and organs, *in vivo* imaging, and in antimicrobial agents. Doped ZnO is also used as therapeutics against cancer, as these bio-applications are still facing challenges and improving to live up to expectations and adapt to the constant updates of the present era and the current endless development and adapt to make life easier [67].

3.1 Drug delivery

Drug delivery systems (DDS) are technologies that help drugs, including pills and vaccines, be delivered into or throughout the body. These systems also explain how these drugs can be packaged to protect them from degradation and save them until they reach the needed part of the body [146]. The doping process enhances the ability of pure ZnO to deliver drugs. Where the pure ZnO nanostructure has a high drug loading of about 82%, this percentage increases to 89% when it is doped by graphene oxide (GO) [147].

Furthermore, doped ZnO quantum dots (QDs) by La enhance the fluorescent properties, especially with a doping concentration of x = 4%. The tumor cell activity after loading the drug was 15% at ZnO@DOX (Doxorubicin) and 12% at La-doped ZnO@DOX. The *in vitro* and *in vivo* experiments also revealed that La-doped ZnO QDs improved the antitumor effect [148]. Another study investigated the effect of Ag-doped ZnO nanostructures on enhanced drug delivery; the results revealed that $Zn_{0.97}Ag_{0.03}O$ hydrogels had high drug loading by 98.59 $\pm$ 2.11%, and the highest swelling ratio attributed to the $Zn_{0.91}Ag_{0.09}O$ (68 $\pm$ 3.40%) and, thus, the highest release (84 $\pm$ 2.18%) within 300 min [149].

Moreover, synthesizing Fe_3O_4@ZnO core-shell NPs to obtain mouse cancer immunotherapy by delivering carcinoembryonic antigen (CEA) drugs into dendritic cells (DCs) successfully achieved significant results. These NPs worked as nanocarriers to deliver antigens effectively and imaging agents for *in vitro* detection [150]. Furthermore, Licui Zhang et al. [151] used Al-doped ZnO NPs as a nanocarrier for Lenalidomide and around 71% drug loading capacity depending on pH and duration time, where the release profile showed a gradual release under physiological conditions (pH 7.4, 28%), whereas the pH 6.2 showed an accelerated release rate at (78%) in 48 h.

3.2 Photocatalysis

The photocatalysis process is a technique used to control the amount of biodegradation and limit pollution. This technique is primarily aimed at organic decomposition and degradation of other wastes [152]. The principle of this process depends on the materials' molecular photocatalysts when the molecules absorb the light and photogenerate electrons and holes to produce surface catalytic redox reactions. This mechanism is similar to that of semiconductors' VB and CB, where a molecular photocatalyst consists of the highest occupied molecular orbital (HOMO) and lowest unoccupied molecular orbital (LUMO) [153].

Doped ZnO has high efficiency for disinfecting water under visible light irradiation, where the doping reduces the chances of electron and hole pairs' recombination, consequently reducing their availability to degradation of water pollutants that are free-radical-based. Doped ZnO nanostructures by non-metal activate visible-light absorption and enhance its photocatalytic efficiency. Sulfur (S)-doped ZnO NPs with various concentrations where x = 0.5, 0.8, 1.1, 1.3, 2.1, 2.5, 3.2, 6.8, 7.8, 11.9, 12.3, and 17.4 wt.% were examined as photocatalysts to the degradation of the Rhodamine (B) contaminant. The sample with 0.10 g of ZnO doped with 0.5 wt.% of S degraded 100% of B at pH = 5 in 90 min, while 0.8 and 1.1 wt.% of S degraded 99 and 97% of B in 150 min, respectively [154].

Additionally, doped ZnO can decompose cationic and anionic harmful azo dyes with high photocatalytic activity as carbon (C)-doped ZnO TFs with 25 nm thickness can degrade the fluorescein dye in 240 min and B dye in 120 min under UV irradiation [155]. Doped ZnO nanostructures can degrade multiple pollutants totally or partially, such as methyl blue dye, malachite green, methylene blue, malachite green, methylene blue, Cibacron brilliant yellow 3G-B, and naphthol green B. Under visible light, La-doped ZnO degraded the methyl orange dye by 85.86%, as Loan et al. studied [156], Cu-doped ZnO decomposed direct blue 15 dye by around 70%, as Roya et al. investigated [157], and Nd-doped ZnO resolve Congo red by 93.7, as Zhang et al. examined [158].

The nature of ZnO nanostructures works as photosensitizers by generating electron–hole pairs in the presence of solar radiation. However, the high charge carrier recombination reduced the ZnO-efficient photocatalyst. Thus, doped ZnO NPs by noble metal Ag enhance the pure ZnO NPs photocatalyst. As a result, 96 and 94% of Congo red and methyl orange were removed using Ag-ZnO NPs compared to 38 and 35% by undoped ZnO under solar light in 80 min at pH 8. This superior performance of the Ag-doped ZnO NPs occurs *via* deposited metal ions that engorge electrons and decrease the recombination rate; thus, most of the electrons are utilized to generate superoxide radicals in the conduction band rather than recombined with holes [159].

Moreover, several studies investigated the photocatalysis properties such as La [156, 160–162], Ce [163–166], Pr [167–169], Er [170–173], and Yb [174] doped the ZnO nanostructures. Nonetheless, Fabrizio Sordello et al. [175] investigated the impact of doped ZnO by La, Pr, Er, Yb, and Ce; the results revealed that La and Pr have a limited role, Er enhanced the photocurrent, Yb showed significant accumulation of photoelectron, and Ce elevated the faster electron transfer.

A research group led by Md Elias [176] studied the photocatalytic performance of pure ZnO nanostructures, N-doped ZnO TFs, and N-doped ZnO/carbon nanotubes (CNTs). The results revealed excellent photocatalytic performance against cationic methylene blue (MB) dye degradation, with a 100% removal rate under UV light irradiation compared to N-doped ZnO (65%) and pure ZnO (47.36%); the photocatalytic mechanism is shown in **Figure 2**.

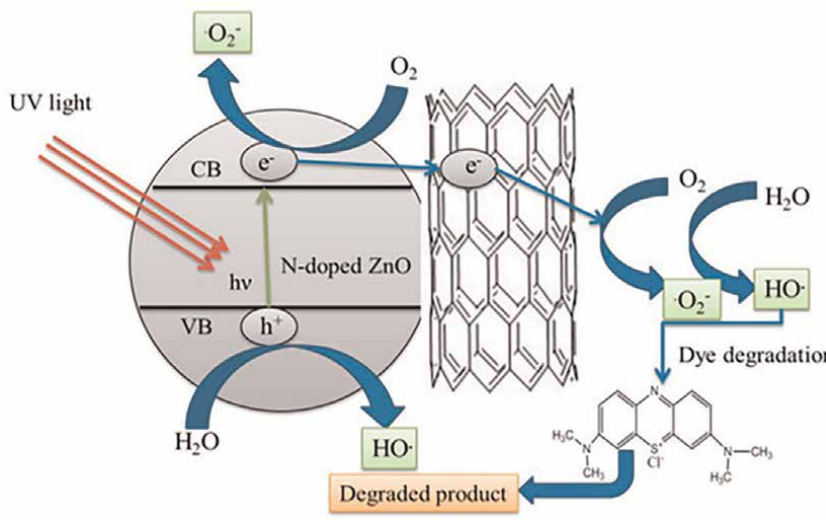

Figure 2.
The schematic of the photocatalytic mechanism of the N-doped ZnO/CNT TFs under UV light irradiation. Reproduced with permission of Ref. [176].

3.3 Photovoltaic

Solar cells are significantly fascinating to depend on renewable energy, where the solar cells convert sunlight energy into electrical energy, which requires a solar device such as a Si-based solar cell. Some nanomaterials can be active under solar light by catching and holding the energy into electricity. The photovoltaic cell mechanism absorbs the light and then obtains energy; the material transfers this energy to electrons. When the electrons move with energy more than the recombination energy, they flow through the material [177]. Dye-sensitized solar cells (DSSCs) are viable alternatives to Si-based solar cells due to their easier fabrication. DSSCs have four main parts: a photoanode, counter electrode, dye, and electrolyte. When light falls on the cell surface, photons enter the cell, and the holes move toward the HOMO. In contrast, electrons move toward the dye's LUMO [178].

ZnO nanostructures are one of the most suitable materials to be the alternative photoanode for DSSCs due to its possessing excellent electron diffusivity, which is higher than that of TiO_2, having diverse morphologies, a low-cost material, resistance to photocorrosion, and a high excitation binding energy (60 MeV), and has a surface that is easier to modify [179]. Nevertheless, pure ZnO nanostructures show low photovoltaic performance. Because of the narrow spectral range, the electron-hole recombination rate is rapid, and the nanostructure is unstable against acidic dye. That is why doped ZnO is vital for enhancing the features by replacing the Zn^{+2} ions and substituting the ZnO lattice [180].

Au-doped ZnO NPs with fixed concentrations of Sm (1 wt. %) indicate that cells fabricated with 1.5 wt % of Au-doped ZnO–Sm NPs film achieved a considerable efficiency of 4.35%, which is about 76% higher than that of 0.0 wt % of Au-doped ZnO–Sm-based cell (2.47%). This is because of the formation of a blocking layer at the ZnO–Sm/Au interface, which obstructs the recombination of electrons and is attributed to the addition of rare-earth ions in ZnO to enhance the non-absorbable wavelength region of light to convert near-infrared and ultraviolet radiations to visible

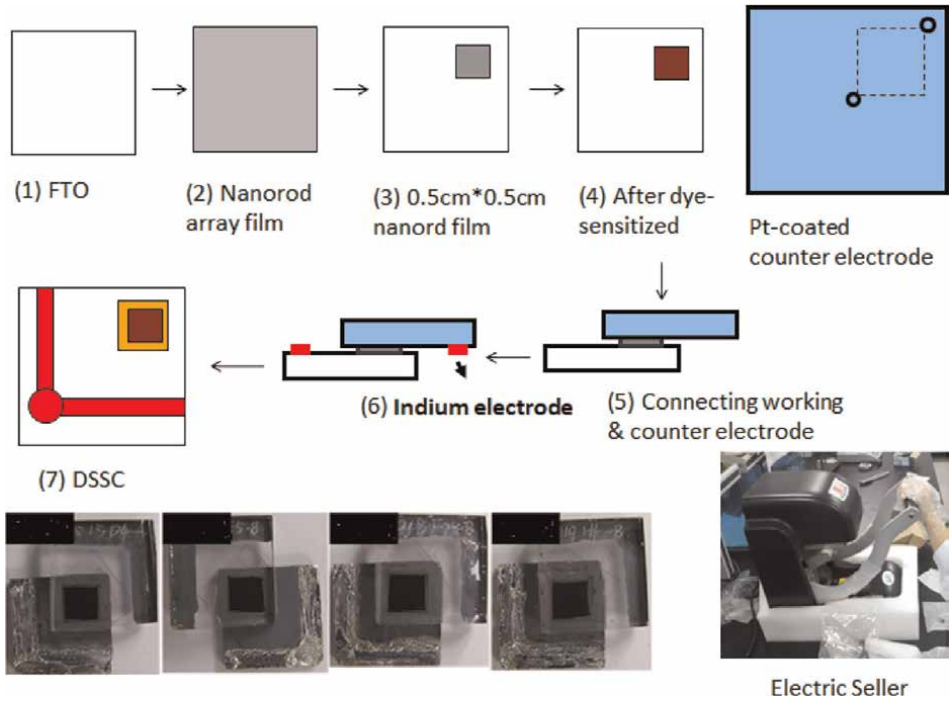

Figure 3.
Photovoltaic schematic illustration of Au-doped ZnO–Sm solar cells with various concentrations (0.0, 0.5, 1.0, and 1.5 wt %). Reproduced with permission of Ref. [181].

emission and decrease the electron recombination rate; the schematic diagram of Au-doped ZnO–Sm DSSC solar cells is shown in **Figure 3** [181].

The DSSCs fabricated with 1% Tungsten (W) and 1.4% S co-doped ZnO NPs exhibited the highest current density (J_{sc}) above 8.0 mA•cm^{-2}, open-circuit voltage (V_{oc}) higher than 0.6 V, Fill Factor (FF) higher the half, and efficiency (2.84%) [182], as well as other reports [183–186].

The pressure applied to the transparent conductive oxide (TCE) layer in Si-based solar cells, besides various temperatures on Ga-doped zinc oxide (GZO) TFs substrate, was studied to optimize the photovoltaic performance. The lowest resistivity was 2.0×10^{-3} Ω.cm when the pressure and temperature were 15 mTorr and 200°C, in the same condition, and the highest carrier concentration values were 1.6×10^{20} cm^{-3}. Hence, the conversion efficiency rose from 9.24 to 12.6%. This leads to the conclusion that increasing the deposition pressure over 15 mTorr and substrate temperature above 200°C enhances the crystallite size, widens the optical band gap, lowers the resistivity, and raises the carrier concentration [187].

3.4 UV absorbers and photodetectors

Doped ZnO nanostructures have an incredible ability to detect and absorb UV rays. Firstly, UV radiation covers the range from 100 to 400 nm of the electromagnetic spectrum and can be divided into three parts: near UV (UVA) 315–400 nm, which is available on the earth; medium UV (UVB) 280–315 nm, where it could be available. Also, the most dangerous one is deep UV (UVC) 100–280 nm. The objective

of UV absorbers is to protect materials by converting absorbed ultraviolet rays into low-impact heat and energy through chemical reactions and, subsequently, limiting the photodegradation in the materials by suppressing the generation of radicals that cause degradation. Hence, the UV absorber is a material that can absorb UV radiation, especially UVC. Photodetectors absorb and convert light's photon energy into electrical signals (not electricity, like photovoltaic). UV photodetectors are used in various aspects of life, such as biomedicine, light curing, environmental monitoring, military, and firefighting [188]. Pure ZnO nanostructures absorb only the near UV range due to their bandgap, whereas the doped ZnO nanostructures can catch deeper than UVA.

Co-doped ZnO nanostructures by fluorine (F) and Ag confirmed the UVC absorption realization. The undoped ZnO has an absorption edge at the UVA (376 nm) region. In comparison, all the co-doped ZnO samples have two absorption edges in UVA (370–375 nm) and UVC (244–249 nm), as significant evidence for absorption in this region. The existence of zinc interstitial resulting from Ag, F co-doping causes absorption in the UVC region. Thus, F, Ag co-doped ZnO nanostructures could be evaluated for a viable UVC photodetector. The absorption and extinction coefficients show significant suppression in the visible range [189].

Chongsri and Pecharapa [190] deposited AZO TFs on a fluorine tin oxide-coated glass substrate (FTO) using the spin coating so-gel method. The results revealed that the photodetector had a high UV response in the wavelength range of 250–380 nm, which could be tuned by raising the Al doping concentration. Sabah Ibrahim Abbas et al. [191] also synthesized AZO TFs using spray pyrolysis with 3 and 5 wt.%. The 3 wt.% AZO sample showed at a bias voltage V = 5 V the highest response current I_p = 47.6 μA and high photoconductive gain G = 10.57 when exposed to UV radiation $\lambda = 365$ nm. Mg transition metal also dramatically impacts the photodetectors based on ZnO. Several reports [192–195] revealed that the Mg-doped ZnO nanostructures had responsivity for the UV wavelength 365 nm around 0.118 A/W and reached 1.088 with 5% of Mg doping concentration.

Moreover, GZO nanorods are grown on a flexible substrate (poly (ethylene 2, 6-naphthalate)) at 80°C. Adding the Ga dopant improves the dark current and photocurrent, where the photocurrent-to-dark current ratios of pure ZnO and GZO are about 8.5 and 570.2 under a 1 V bias, respectively. Besides, GZO nanorods showed stable and reproducible transient response measurements; after multiple bending cycles, the results showed no change in the current-voltage characteristics [196]. The iron dopant also enhances ZnO nanostructures' photosensitivity. Fe-doped ZnO (FZO) TFs were grown on Corning glass substrates *via* radio frequency (RF) magnetron sputtering after 100 nm of pure ZnO films was grown as a seed layer to help the FZO TFs grow vertically. The FZO TFs exhibited a massive enhancement in the photosensitivity and rise/decay time, where the sensitivity of pure ZnO TFs at UV wavelength 380 nm was 43.1 and 471.1 for FZO TFs at 3 V bias. **Figure 4** shows the FZO NR PDs structure and the Schottky barrier formed between it and Ag electrodes [197].

The photodetectors based on doped ZnO nanostructures are also enhanced by other elements, such as chlorine [198], to improve the surface photo-charge and obtain dramatic photon detection speed achieved to a few ms, W element [199] with 2% doping content gives a higher responsivity of 3.84 A/W and photosensitivity value of 34 at UV wavelength of 365 nm, and 5% of Cd doping increased the ZnO nanostructures sensitivity into 762.40 and the rise/decay times were 2.5 and 4 s, respectively [200].

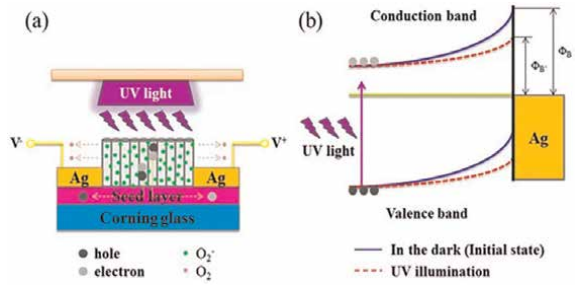

Figure 4.
(a) The illustration shows the schematic diagram FZO nanorods photodetectors (PDs) when exposed to UV light. (b) A Schottky barrier is established at the junction of the FZO nanorods and Ag electrodes, generating electron-hole pairs upon UV light exposure. Reproduced with permission of Ref. [197].

3.5 Sensors

Detecting harmful gases and the sensitive determination of these toxic gases are necessary. ZnO material is the typical metal oxide semiconductor (MOS) gas sensor used widely for various reasons: fast response, low detection limit, high selectivity, reliable performance, handy preparation, and low manufacturing cost [201]. ZnO belongs to surface-sensitive materials. Thus, when a gas-sensing element is prepared using ZnO, the gas-sensing mechanism can be summarized as adsorption-oxidation-desorption. One of the main factors in the sensing mechanism is the surface area, which differs from one structure to another and then changes the response strength of a gas-sensitive material. Thus, increasing the surface area leads to an increase in the amount of adsorbed gas, thereby improving sensitivity. Therefore, doped ZnO nanostructures are divided into four categories depending on their spatial dimension: 0D, 1D, 2D, and 3D nanomaterials.

The ability of doped ZnO nanostructures to determine and sense various gases is massive, such as nitrogen dioxide (NO_2)/1 ppm, carbon monoxide (CO)/80 ppm, methane (CH_4)/1%, ammonia (NH_3)/50 ppm, ethylene/29 ppm, ethanol/100 ppm, hydrogen sulfide (H_2S)/100 ppm, and triethylamine (TEA)/100 ppm [202]. Furthermore, pure ZnO nanostructures can sense and absorb multiple gases; once they are doped by other elements, the efficiency increases and improves the sensing performance [203]. Wei-Zhong Li et al. [204] studied gas sensors based on gallium (Ga)-doped ZnO epilayers grown by MOCVD. Findings that the Ga-doped ZnO epilayer has high performance for nitric oxide (NO) sensitivity when the flow rate of the Trimethylgallium (Known as TEGa) $Ga(C_2H_5)_3$) is lower compared to a higher flow rate. The sensitivity of Ga-doped ZnO epilayers for NO is 23.653 under a 2.5 ppm NO environment. Furthermore, the sensitivities are 5.321, 1.692, 3.320, 1.000, 1.066, and 1.163 for Ga-doped ZnO epilayers device with the atmosphere of NO (500 ppb), NO_2 (500 ppb), CO (100 ppm), CO_2 (1500 ppb), SO_2 (100 ppm), and NH_3 (100 ppm), respectively.

Additionally, when the ZnO doped by 4% La TFs, the results showed incredible CO_2 gas response with a flow rate of 200 standard cubic centimeters per minute (sccm) and exceptional performance of gas response with 114.22% [205–208]. In addition, Ramola et al. investigated the acetone and ethanol gases sensitivity *via* synthesized Ga-doped ZnO TFs with 5% doping content at various annealing temperatures: 400, 700, and 900°C using the spin coating sol-gel method. The gas sensitivity of the sample with 5% Ga-doped ZnO TFs annealed at 700 C was brilliant, showing at

750 sccm 41 for acetone and ethanol and at 1000 sccm 46 for acetone and 38 for ethanol [209–212]. Al, Mg [213], and In [214] are also elements doped with ZnO nanostructures to enhance the gas sensitivity.

3.6 Light emitting diode (LED)

Light-emitting diode (LED) has been widely investigated lately due to its massive potential in developing solid-state lighting technologies. LED is fabricated based on diverse materials, and the two most important ones are doped ZnO and gallium nitride (GaN). Doped ZnO nanostructures have several advantages over GaN, besides the wide bandgap and the large exciton binding energy (∼60 meV), a higher radiation hardness, simplified processing due to the capability to conventional chemical wet etching, and the availability of large area substrates with low costs [3, 215, 216].

However, Azizar Rahman et al. [217] studied the p-n homojunction of LED and prepared GZO for n-type onto p-type Li-doped ZnO (LZO); they found that the GZO nanorods are 16 times more efficient in electroluminescence (EL) compared to the equivalent LED made from ZnO nanorods. Furthermore, the optimized p-n homojunction based on 4% of GZO nanorods and 12 atoms % of LZO exhibits a low turn-on voltage of 3.2 V and a bright-yellow-orange EL band at 2.0 eV.

Islam Mohammad Shafiqul et al. [218] studied LED fabrication based on heterojunction ZnO. Using homojunction structure LED based on ZnO is not fully efficient because the carriers spread to each layer by diffusion, decreasing in the carrier density and reducing recombination probability. Therefore, to overcome this

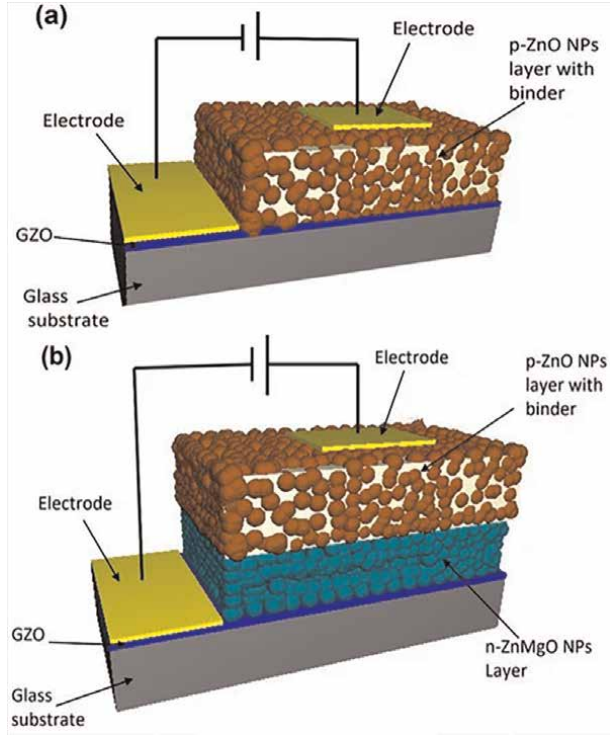

Figure 5.
The LEDs-based on ZnO NPs. (a) The LED structure of p-ZnO/GZO and (b) the LED structure of p-ZnO/n-ZnMgO/GZO. Reproduced with permission of Ref. [218].

issue, heterostructure LED based on ZnO nanostructures is one of the suggested solutions. For n-type ZnO, ZnMgO alloy is used and N-doped ZnO for p-type (p-ZnO/n-ZnMgO/GZO). Where the structure of homojunction UV LED uses n-type ZnO NPs and GZO NPs for p-type (p-ZnO/GZO), the two structures are illustrated in **Figure 5** [218].

Moreover, using the PLD method, Lichun Zhang and his team [219] fabricated n-ZnO/p-GaN heterojunction LEDs with zinc sulfide (ZnS) and aluminum nitride (AlN) as interfacial layers. The EL spectra of the n-ZnO/p-GaN LED display a broad blue-violet emission at 430 nm at RT, whereas the n-ZnO/ZnS/p-GaN and n-ZnO/AlN/p-GaN devices emit typical UVA emission peaks at around 381 nm.

Meanwhile, synthesizing LED-based ZnO doped with metals and transition metals is widely studied. Mg-doped ZnO nanostructures for organic LED (OLED) diodes showed prominent blue emission at 433, 460, and 490 nm at 6 V [220]. Moreover, AZO increased the luminous efficiency of the LED to 22.8%, which is higher than 10.8% of the LED based on pure ZnO TFs [221]. Besides, doped ZnO nanostructures are also used to produce high-efficiency transparent conductive layers [222] and electron transport layers [78].

4. Conclusions

Doped ZnO nanostructures have been studied widely and still need more investigation to cover all the needs in various fields in life. ZnO nanostructures can be doped by metal, non-metal, transition metal, and rare elements, resulting in diverse structures. The nanostructure particle size can be measured using one of these three approaches: Scherrer equation, Williamson and Hall (W-H), and Halder-Wagner (H–W) methods, depending on XRD data and other structure properties. In addition, the electrical features of ZnO after doping are massive, leading to an increase in carrier concentrations, charge carrier mobility, conductivity, and a decrease in resistivity, as well. Changing the particle size leads to modification of the bandgap energy, which is investigated by UV-vis and PL results, and the measurements rely on one of these methods: Kubelka-Munk function, Tauc relation, or energy law depending on wavelength. Furthermore, one of the incredible impacts of doping is converting ZnO from diamagnetic material into magnetized material. These improvements and enhancements in doped ZnO nanostructures appear in numerous applications in medicine and industry, such as drug delivery, photocatalysis, photocatalytic, UV absorbers and photodetectors, sensors, and LEDs.

Acknowledgements

The author would like to acknowledge King Abdulaziz City for Science and Technology (KACST) for its support during writing this chapter.

Author details

Hadba Hussain
Microelectronics and Semiconductors Institute, King Abdulaziz City for Science and Technology (KACST), Riyadh, Saudi Arabia

*Address all correspondence to: hadba.hussain.h@gmail.com; hhalqahtani@kacst.gov.sa

References

[1] Morkoç H, Özgür Ü. Zinc Oxide: Fundamentals, Materials and Device Technology. Wiley-VCH Verlag GmbH & Co. KGaA: John Wiley & Sons; 2008

[2] Coleman V, Jagadish C. Basic properties and applications of ZnO. In: Zinc Oxide Bulk, Thin Films and Nanostructures. Oxford: Elsevier Science Ltd.; 2006. pp. 1-120

[3] Borysiewicz MA. ZnO as a functional material, a review. Crystals. 2019;**9**(10): 505

[4] Vigué F, Vennéguès P, Deparis C, Vézian S, Laügt M, Faurie JP. Growth modes and microstructures of ZnO layers deposited by plasma-assisted molecular-beam epitaxy on (0001) sapphire. Journal of Applied Physics. 2001;**90**(10):5115-5119

[5] Luo J, Liang JK, Liu QL, Liu FS, Zhang Y, Sun BJ, et al. Structure and magnetic properties of Mn-doped ZnO nanoparticles. Journal of Applied Physics. 2005;**97**(8):086106

[6] Sorar I, Saygin-Hinczewski D, Hinczewski M, Tepehan FZ. Optical and structural properties of Si-doped ZnO thin films. Applied Surface Science. 2011;**257**(16):7343-7349

[7] Raimondi DL, Kay E. High resistivity transparent ZnO thin films. Journal of Vacuum Science and Technology. 1970; **7**(1):96-99

[8] Pearton SJ, Norton DP, Ip K, Heo YW, Steiner T. Retracted: Recent progress in processing and properties of ZnO. Progress in Materials Science. 2005;**50**(3):293-340

[9] Mang A, Reimann K, Rübenacke S. Band gaps, crystal-field splitting, spin-orbit coupling, and exciton binding energies in ZnO under hydrostatic pressure. Solid State Communications. 1995;**94**(4):251-254

[10] Jaffe JE, Snyder JA, Lin Z, Hess AC. LDA and GGA calculations for high-pressure phase transitions in ZnO and MgO. Physical Review B. 2000;**62**(3): 1660

[11] Chelikowsky JR. An oxygen pseudopotential: Application to the electronic structure of ZnO. Solid State Communications. 1977;**22**(6): 351-354

[12] Meyer BK, Alves H, Hofmann DM, Kriegseis W, Forster D, Bertram F, et al. Bound exciton and donor-acceptor pair recombinations in ZnO. Physica Status Solidi (b). 2004;**241**(2):231-260

[13] Garcia MA, Merino JM, Pinel EF, Quesada A, Jdl V, González MLR, et al. Magnetic properties of ZnO nanoparticles. Nano Letters. 2007;**7**(6): 1489-1494

[14] Sebayang K, Aryanto D, Simbolon S, Kurniawan C, Hulu SF, Sudiro T, et al. Effect of sintering temperature on the microstructure, electrical and magnetic properties of Zn0. 98 Mn0. 02O material. In: IOP Conference Series: Materials Science and Engineering. Sumatera Utara, Indonesia; Feb 2018. p. 012119

[15] Bomila R, Srinivasan S, Gunasekaran S, Manikandan A. Enhanced photocatalytic degradation of methylene blue dye, opto-magnetic and antibacterial behaviour of pure and La-doped ZnO nanoparticles. Journal of Superconductivity and Novel Magnetism. 2018;**31**:855-864

[16] Allabergenov B, Chung SH, Jeong SM, Kim S, Choi B. Enhanced blue photoluminescence realized by copper diffusion doping of ZnO thin films. Optical Materials Express. 2013;**3**(10): 1733-1741. DOI: 10.1364/OME.3.001733

[17] Ma Z, Ren F, Ming X, Long Y, Volinsky AA. Cu-doped ZnO electronic structure and optical properties studied by first-principles calculations and experiments. Materials (Basel). 2019; **12**(1):196

[18] Mittal M, Sharma M, Pandey OP. UV–visible light induced photocatalytic studies of Cu doped ZnO nanoparticles prepared by co-precipitation method. Solar Energy. 2014;**110**:386-397

[19] Vlăduț CM, Mocioiu OC, Soare EM. Coinage metals doped ZnO obtained by sol-gel method—A brief review. Gels. 2023;**9**(5):424

[20] Bokov D, Jalil AT, Chupradit S, Suksatan W, Ansari MJ, Shewael IH, et al. Nanomaterial by sol-gel method: Synthesis and application. Advances in Materials Science and Engineering. Dec 2021;**2021** (1):5102014

[21] Chehhat K, Mecif A, Mahdjoub AH, Nazir R, Pandit MA, Salhi F, et al. Sol-gel synthesis of porous cobalt-doped ZnO thin films leading to rapid and large scale Orange-II photocatalysis. Journal of Sol-Gel Science and Technology. 2023;**106**: 85-94

[22] Macías-Sánchez JJ, Hinojosa-Reyes L, Caballero-Quintero A, Wdl C, Ruiz-Ruiz E, Hernández-Ramírez A, et al. Synthesis of nitrogen-doped ZnO by sol–gel method: Characterization and its application on visible photocatalytic degradation of 2,4-D and picloram herbicides†. Photochemical & Photobiological Sciences. 2015;**14**: 536-542

[23] Naik EI, Naik HSB, Sarvajith MS, Pradeepa E. Co-precipitation synthesis of cobalt doped ZnO nanoparticles: Characterization and their applications for biosensing and antibacterial studies. Inorganic Chemistry Communications. 2021;**130**:108678

[24] Kanwal S, Khan MT, Mehboob N, Amami M, Zaman A. Room-temperature ferromagnetism in Cu/Co Co-doped ZnO nanoparticles prepared by the Co-precipitation method: For spintronics applications. ACS Omega. 2022;**7**(36): 32184-32193

[25] Kangathara N, Sabari V, Saravanan L, Elangovan S. Synthesis, characterization, and comparison of pure zinc oxide and magnesium-doped zinc oxide nanoparticles and their application on ethanol sensing activities. Journal of Nanomaterials. 2022;**2022**:1769278

[26] Parthasaradi V, Kavitha M, Sridevi A, Rubia JJ. Novel rare-earth Eu and La co-doped ZnO nanoparticles synthesized via co-precipitation method: Optical, electrical, and magnetic properties. Journal of Materials Science: Materials in Electronics. 2022;**33**: 25805-25819

[27] Cimitan S, Albonetti S, Forni L, Peri F, Lazzari D. Solvothermal synthesis and properties control of doped ZnO nanoparticles. Journal of Colloid and Interface Science. 2009; **329**(1):73-80

[28] Kalam A, Al-Sehemi AG, Ashrafuzzaman M, Allami SAS, Sharif AM, Yadav P, et al. Synthesis of gadolinium doped ZnO nanomaterials using the modified-solvothermal method and studied the effect of gadolinium on the structural, morphological, and optical properties. Journal of Inorganic and Organometallic Polymers and Materials. 2023;**33**:3076-3086

[29] Agarwal MB, Malaidurai M, Sharma A, Thangavel R. Effect of Al doping on hydrothermal growth and physical properties of doped ZnO nanoarrays for optoelectronic applications. Materials Today: Proceedings. 2020;**21**(4):1781-1786

[30] Shrisha BV, Bhat S, Kushavah D, Naik KG. Hydrothermal growth and characterization of Al-doped ZnO nanorods. Materials Today: Proceedings. 2016;**3**(6):1693-1701

[31] Luu TVH, Dao NN, Pham HAL, Nguyen QB, Nguyen VC, Dang PH. One-step hydrothermal preparation of Ta-doped ZnO nanorods for improving decolorization efficiency under visible light. RSC Advances. 2023;**13**(8): 5208-5218

[32] Young SJ, Chiou CL, Liu YH, Ji LW. Synthesis of Ga-doped ZnO nanorods by hydrothermal method and their application to ultraviolet photodetector. Inventions. 2016;**1**(1):3

[33] Gan YX, Jayatissa AH, Yu Z, Chen X, Li M. Hydrothermal synthesis of nanomaterials. Journal of Nanomaterials. 2020;**2020**:8917013

[34] Chaitra U, Ali AVM, Mahesha MG, Kompa A, Kekuda D, Rao KM. Property evaluation of spin coated Al doped ZnO thin films and Au/AZO/FTO Schottky diodes. Superlattices and Microstructures. 2021;**155**:106903

[35] Basyooni MA, Shaban M, Sayed AME. Enhanced gas sensing properties of spin-coated Na-doped ZnO nanostructured films. Scientific Reports. 2017;**7**:41716

[36] Salem M, Ghannam H, Almohammedi A, Salem J, Litaiem Y, Massoudi I, et al. Ag doped ZnO thin films deposited by spin coating for silicon surface passivation. Silicon. 2023; **15**(17):7321-7326

[37] Srinatha N, Raghu P, Mahesh H, Angadi B. Spin-coated Al-doped ZnO thin films for optical applications: Structural, micro-structural, optical and luminescence studies. Journal of Alloys and Compounds. 2017;**722**:888-895

[38] Zhao D, Sathasivam S, Li J, Carmalt CJ. Transparent and conductive molybdenum-doped ZnO thin films via chemical vapor deposition. ACS Applied Electronic Materials. 2020;**2**(1):120-125

[39] Ponja SD, Sathasivam S, Parkin IP, Carmalt CJ. Highly conductive and transparent gallium doped zinc oxide thin films via chemical vapor deposition. Scientific Reports. 2020;**10**:638

[40] Potter DB, Parkin IP, Carmalt CJ. The effect of solvent on Al-doped ZnO thin films deposited via aerosol assisted CVD. RSC Advances. 2018;**8**: 33164-33173

[41] Zhao D, Sathasivam S, Wang M, Carmalt CJ. Transparent and conducting boron doped ZnO thin films grown by aerosol assisted chemical vapor deposition. RSC Advances. 2022;**12**(51): 33049-33055

[42] Carlsson JO, Martin PM. Chapter 7 - Chemical Vapor Deposition. In: Handbook of Deposition Technologies for Films and Coatings. 3rd ed. Norwich, New Work, USA: William Andrew Publishing; 2010. pp. 314-363

[43] Hacini N, Ghamnia M, Dahamni MA, Boukhachem A, Pireaux JJ, Houssiau L. Compositional, structural, morphological, and optical properties of ZnO thin films prepared by PECVD technique. Coatings. 2021;**11** (2):202

[44] Olejníček J, Šmíd J, Čada M, Kment Š, Churpita O, Kšírová P, et al. ZnO thin films prepared by surfatron produced discharge. Catalysis Today. 2014;**230**: 119-124

[45] Arif B. Determination of optical constants of ZnO growth by PECVD method. Journal of Materials and Electronic Devices. 2015;**1**(1):24-28

[46] Zhao D, Mourey DA, Jackson TN. Low-temperature pulsed-PECVD ZnO thin-film transistors. Journal of Electronic Materials. 2010;**39**:554-558

[47] Jansen F. Plasma-enhanced chemical vapor deposition. In: Vacuum Science and Technology. San Diego: Academic Press; 1998. pp. 711-730

[48] Sbrockey NM, Ganesan S. ZnO thin films by MOCVD. III-Vs Review. 2004; **17**(7):23-25

[49] Lee CH, Kim DW. Preparation of Al doped ZnO thin films by MOCVD using ultrasonic atomization. Journal of Electroceramics. 2014;**33**:12-16

[50] Choi IH. Properties of boron-doped ZnO thin films grown by using MOCVD. Journal of the Korean Physical Society. 2013;**63**:1997-2001

[51] Ye Z, Wang J, Wu Y, Zhou X, Chen F, Xu W, et al. Growth of phosphorus-doped p-type ZnO thin films by MOCVD. Frontiers of Optoelectronics in China. 2008;**1**: 147-150

[52] Kaur G, Mitra A, Yadav KL. Pulsed laser deposited Al-doped ZnO thin films for optical applications. Progress in Natural Science: Materials International. 2015;**25**(1):12-21

[53] Venkatachalam S, Y. Iida YK. Preparation and characterization of Al doped ZnO thin films by PLD. Superlattices and Microstructures. 2008; **44**(1):127-135

[54] Pérez-Casero R, Gutiérrez-Llorente A, Pons-Y-Moll O, Seiler W, Defourneau RM, Defourneau D, et al. Er-doped ZnO thin films grown by pulsed-laser deposition. Journal of Applied Physics. 2005;**97**(5):054905

[55] Koo HS, Peng JC, Chen M, Chin HI, Chen JY, Wu MK. Optoelectronic characterization of Ta-doped ZnO thin films by pulsed laser deposition. Journal of Nanoscience and Nanotechnology. 2015;**15**(11):9222-9227

[56] Toan NV, Tuoi TTK, Inomata N, Toda M, Ono T. Aluminum doped zinc oxide deposited by atomic layer deposition and its applications to micro/ nano devices. Scientific Reports. 2021;**11**: 1204

[57] Petrova D, Napoleonov B, Minh CNH, Marinova V, Lan YP, Avramova I, et al. The effect of post deposition treatment on properties of ALD Al-doped ZnO films. Nanomaterials. 2023;**13**(5):800

[58] Yong Wu FC, Ji X. Optical and electrical properties of Al-doped ZnO thin films by atomic layer deposition. Journal of Materials Science: Materials in Electronics. 2020;**31**:17365-17374

[59] Gao Z, Banerjee P. Review article: Atomic layer deposition of doped ZnO films. Journal of Vacuum Science and Technology A. 2019;**37**(5):050802

[60] Badgujar AC, Yadav BS, Jha GK, Dhage SR. Room temperature sputtered aluminum-doped ZnO thin film transparent electrode for application in solar cells and for low-band-gap optoelectronic devices. ACS Omega. 2022;**7**(16):14203-14210

[61] Seawsakul K, Horprathum M, Eiamchai P, Pattantsetakul V, Limwichean S, Muthitamongkol P, et al. Effects of sputtering power toward the Al-doped ZnO thin film prepared by pulsed DC magnetron sputtering. Materials Today: Proceedings. 2017;**4**(5): 6466-6471

[62] Hopoğlu H, Aydınoğlu HS, Özer A, Tüzemen EŞ. Investigation of nitrogen doped ZnO thin films: Effects on their structural and optical properties. Optical Materials. 2021;**122**(Part A): 111685. DOI: 10.1016/j.optmat.2021.111685

[63] Simon AH. Chapter 7 - Sputter processing. In: Handbook of Thin Film Deposition. Oxford, United Kingdom: William Andrew Publishing; 2018. pp. 195-230

[64] Ong C, Ng L, Mohammad A. A review of ZnO nanoparticles as solar photocatalysts: Synthesis, mechanisms and applications. Renewable and Sustainable Energy Reviews. 2018;**81**: 536-551

[65] Hui A, Ma J, Liu J, Bao Y, Zhang J. Morphological evolution of Fe doped sea urchin-shaped ZnO nanoparticles with enhanced photocatalytic activity. Journal of Alloys and Compounds. 2017;**696**: 639-647

[66] Basnet P, Chatterjee S. Structure-directing property and growth mechanism induced by capping agents in nanostructured ZnO during hydrothermal synthesis—A systematic review. Nano-structures & Nano-objects. 2020;**22**:100426

[67] Carofiglio M, Barui S, Cauda V, Laurenti M. Doped zinc oxide nanoparticles: Synthesis, characterization and potential use in nanomedicine. Applied Sciences (Basel, Switzerland). 2020;**10**(15):5194

[68] Fageria P, Gangopadhyay S, Pande S. Synthesis of ZnO/Au and ZnO/Ag nanoparticles and their photocatalytic application using UV and visible light. RSC Advances. 2014;**4**(48):24962-24972

[69] Chen Y, Zeng D, Zhang K, Lu A, Wang L, Peng DL. Au–ZnO hybrid nanoflowers, nanomultipods and nanopyramids: One-pot reaction synthesis and photocatalytic properties. Nanoscale. 2014;**6**(2):874-881

[70] Byrappa K, Yoshimura M. Hydrothermal Technology. 2nd ed. William Andrew; 2012

[71] Hench LL, West JK. The sol-gel process. Chemical Reviews. 1990;**90**(1): 33-72

[72] Patnaik P, Dean J. Dean's Analytical Chemistry New York: McGraw-Hill; 2004

[73] Cauda V, Pugliese D, Garino N, Sacco A, Bianco S, Bella F, et al. Multi-functional energy conversion and storage electrodes using flower-like zinc oxide nanostructures. Energy. 2014;**65**: 639-646

[74] Chand P, Gaur A, Kumar A, Gaur UK. Effect of NaOH molar concentration on optical and ferroelectric properties of ZnO nanostructures. Applied Surface Science. 2015;**356**:438-446

[75] Munna N, Abdur R, Islam R, Bashar MS, Farhad SFU, Kamruzzaman M, et al. Influence of Sn doping on the optoelectronic properties of ZnO nanoparticles. Nanoscale Advances. 2023;**5**(18):4996-5004

[76] Gyawali S, Goni L, Chowdhury M, Laref A, Bajgai S, Chantrapromma S, et al. Effect of KOH concentration on the properties of ZnO nanoparticles.

Materials Research Express. 2022;**9**(5): 055004

[77] Khalid A, Ahmad P, Alharthi AI, Muhammad S, Khandaker MU, Faruque MRI, et al. Enhanced optical and antibacterial activity of hydrothermally synthesized cobalt-doped zinc oxide cylindrical microcrystals. Materials (Basel). 2021;**14**(12):3223

[78] Alexandrov A, Zvaigzne M, Lypenko D, Nabiev I, Samokhvalov P. Al-, Ga-, Mg-, or Li-doped zinc oxide nanoparticles as electron transport layers for quantum dot light-emitting diodes. Scientific Reports. 2020;**10**:7496

[79] Kerli S, Alver U, Tanrıverdi A, Avar B. Boron and fluorine doped ZnO films obtained from zinc chloride precursor via chemical spray pyrolysis. Protection of Metals and Physical Chemistry of Surfaces. 2014;**50**:797-802

[80] Din MI, Khalid R, Hussain Z, Gul S, Mujahid A. Synthesis and characterization of cobalt doped zinc oxide nanoparticles and their application for catalytic reduction of methylene blue dye. Desalination and Water Treatment. 2024;**317**:100002

[81] Safeen K, Safeen A, Arif D, Ali WHSA, Ali G, Hussain F, et al. Tuning the optical properties of ZnO by Co and Gd doping for water pollutant elimination. Water. 2023;**15**(8):1470

[82] Baig F, Ashraf MW, Asif A, Imran M. A comparative analysis for effects of solvents on optical properties of Mg doped ZnO thin films for optoelectronic applications. Optik. 2020; **208**:164534

[83] Gatou MA, Lagopati N, Vagena IA, Gazouli M, Pavlatou EA. ZnO nanoparticles from different precursors and their photocatalytic potential for biomedical use. Nanomaterials (Basel). 2023;**13**(1):122

[84] Kenanakis G, Katsarakis N, Koudoumas E. Influence of precursor type, deposition time and doping concentration on the morphological, electrical and optical properties of ZnO and ZnO:Al thin films grown by ultrasonic spray pyrolysis. Thin Solid Films. 2014;**555**:62-67

[85] Kaphle A, Reed T, Apblett A, Hari P. Doping efficiency in cobalt-doped ZnO nanostructured materials. Journal of Nanomaterials. 2019;**2019**:7034620

[86] Ghica D, Vlaicu ID, Stefan M, Maraloiu VA, Joita AC, Ghica C. Tailoring the dopant distribution in ZnO: Mn nanocrystals. Scientific Reports. 2019;**9**:6894

[87] Al-Farsi L, Souier TM, Al-Hinai M, Myint MTZ, Kyaw HH, Widatallah HM, et al. pH controlled nanostructure and optical properties of ZnO and Al-doped ZnO nanorod arrays grown by microwave-assisted hydrothermal method. Nanomaterials. 2022;**12**(21):3735

[88] Wojnarowicz J, Chudoba T, Gierlotka S, Sobczak K, Lojkowski W. Size control of cobalt-doped ZnO nanoparticles obtained in microwave solvothermal synthesis. Crystals. 2018; **8**(4):179

[89] Shiraishi M, Inagaki M. Chapter 10 - X-ray diffraction methods to study crystallite size and lattice constants of carbon materials. In: Carbon Alloys. Oxford: Elsevier Science; 2003. pp. 161-173. DOI: 10.1016/B978-008044163-4/ 50010-3

[90] Vinila VS, Isac J. Chapter 14 - Synthesis and structural studies of superconducting perovskite GdBa2Ca3Cu4O10.5+δ nanosystems.

In: Design, Fabrication, and Characterization of Multifunctional Nanomaterials. Amsterdam: Elsevier; 2022. pp. 319-341

[91] Talam S, Karumuri SR, Gunnam N. Synthesis, characterization, and spectroscopic properties of ZnO nanoparticles. International Scholarly Research Notices. 2012;2012

[92] Yokoyama T, Masuda H, Suzuki M, Ehara K, Nogi K, Fuji M, et al. Chapter 1 - Basic properties and measuring methods of nanoparticles. In: Nanoparticle Technology Handbook. Amsterdam: Elsevier; 2008. pp. 3-48

[93] Tamanna NJ, Hossain MS, Bahadur NM, Ahmed S. Green synthesis of Ag2O & facile synthesis of ZnO and characterization using FTIR, bandgap energy & XRD (Scherrer equation, Williamson-Hall, size-train plot, Monshi-Scherrer model). Results in Chemistry. 2024;**7**:101313

[94] Zak AK, Razali R, Majid WA, Darroudi M. Synthesis and characterization of a narrow size distribution of zinc oxide nanoparticles. International Journal of Nanomedicine. 2011;**6**:1399-1403

[95] Suryanarayana C, Norton M, Suryanarayana C, Norton M. Crystal structure determination. II: Hexagonal structures. In: Suryanarayana C, Norton MG, editors. X-Ray Diffraction a Practical Approach. New York: Springer New York, NY; 1998. pp. 125-152

[96] Sagheer R, Khalil M, Abbas V, Kayani ZN, Tariq U, Ashraf F. Effect of Mg doping on structural, morphological, optical and thermal properties of ZnO nanoparticles. Optik. 2020;**200**:163428

[97] Rabiei M, Palevicius A, Monshi A, Nasiri S, Vilkauskas A, Janusas G. Comparing methods for calculating nano crystal size of natural hydroxyapatite using X-ray diffraction. Nanomaterials (Basel). 2020;**10**(9):1627

[98] Akdağ A, Budak HF, Yılmaz M, Efe A, Büyükaydın M, Can M, et al. Structural and morphological properties of Al doped ZnO nanoparticles. Journal of Physics: Conference Series. 2016;**707**:012020

[99] Mishra PN, Mishra PK, Pathak D. The influence of Al doping on the optical characteristics of ZnO nanopowders obtained by the low-cost sol-gel method. Chemistry. 2022;**4**(4):1136-1146

[100] Urper O, Baydogan N. Effect of Al concentration on optical parameters of ZnO thin film derived by sol-gel dip coating technique. Materials Letters. 2020;**274**:128000

[101] Ahmad M, Ahmad MK, Mamat MH, Mohamed A, Suriani AB, Ismail NMAN, et al. Effects of group-I elements on output voltage generation of ZnO nanowires based nanogenerator; degradation of screening effects by oxidation of nanowires. Micromachines (Basel). 2022;**13**(9):1450

[102] Sellaiyan S, Uedono A, Devi LV, Sivaji K. Er3+ induced point defects in ZnO and impact of Li+/Na+/K+ on the vacancy defects in ZnO:Er studied by positron annihilation spectroscopy. Applied Physics A: Materials Science & Processing. 2019;**125**:497

[103] Suwanboon S, Amornpitoksuk P, Sukolrat A. Dependence of optical properties on doping metal, crystallite size and defect concentration of M-doped ZnO nanopowders (M = Al, Mg, Ti). Ceramics International. 2011;**37**(4): 1359-1365

[104] Straumal B, Baretzky B, Mazilkin A, Protasova S, Myatiev A,

Straumal P. Increase of Mn solubility with decreasing grain size in ZnO. Journal of the European Ceramic Society. 2009;**29**(10):1963-1970

[105] Shayesteh SF, Dizgah AA. Effect of doping and annealing on the physical properties of ZnO:Mg nanoparticles. Pramana. 2013;**81**:319-330

[106] Rajeevgandhi C, Bharanidharan S, Jayakumar T, Shailaja N, Anand P, Guganathan L, et al. Enhanced super capacitor applications of lithium doped zinc oxide nanoparticles with theoretical approach. Solid State Communications. 2023;**371**:115256

[107] Shawuti S, Sherwani AR, Can MM, Gülgün MA. Complex impedance analyses of Li doped ZnO electrolyte materials. Scientific Reports. 2022;**10**(1): 8228

[108] Majeed MH, Aycibin M, Imer AG. Study of the electronic, structure and electrical properties of Mg and Y single doped and Mg/Y co-doped ZnO: Experimental and theoretical studies. Optik. 2022;**258**:168949

[109] Cuadra JG, Porcar S, Fraga D, Stoyanova-Lyubenova T, Carda JB. Enhanced electrical properties of alkali-doped ZnO thin films with chemical process. Solar. 2021;**1**(1):30-40

[110] Joshi BC, Chaudhri AK. Sol-gel-derived Cu-doped ZnO thin films for optoelectronic applications. ACS Omega. 2022;**7**(25):21877-21881

[111] Ahmad I, Mazhar ME, Usmani MN, Khan K, Ahmad S, Ahmad J. Impact of silver dopant on electrical and dielectric properties of ZnO nanoparticles. Materials Research Express. 2019;**6**(3):035014

[112] Saadi H, Rhouma FIH, Benzarti Z, Bougrioua Z, Guermazi S, Khirouni K. Electrical conductivity improvement of Fe doped ZnO nanopowders. Materials Research Bulletin. 2020;**129**: 110884

[113] Jantrasee S, Moontragoon P, Pinitsoontorn S. Thermoelectric properties of Al-doped ZnO: Experiment and simulation. Journal of Semiconductors. 2016;**37**(9): 092002

[114] Hong C, Kang KM, Kim M, Wang Y, Kim T, Lee C, et al. Structural, electrical, and optical properties of Si-doped ZnO thin films prepared via supercycled atomic layer deposition. Materials Science and Engineering: B. 2021;**273**:115401

[115] Lim SH, Kim JW, Kang HS, Kim GH, Chang HW, Lee SY. Characterizations of phosphorus doped ZnO multi-layer thin films to control carrier concentration. Superlattices and Microstructures. 2005; **38**(4–6):377-384

[116] Rashidi N, Vai AT, Kuznetsov VL, Dilworth JR, Edwards PP. Origins of conductivity improvement in fluoride-enhanced silicon doping of ZnO films. Chemical Communications. 2015;**51**(45): 9280-9283

[117] Singh AK, Singh SK. Optical properties of ZnO. In: Awasthi K, editor. Nanostructured Zinc Oxide Synthesis, Properties and Applications. Amsterdam: Elsevier; 10 Aug 2021. pp. 189-208

[118] Deep R, Yoshida T, Fujita Y. Defects in nitrogen-doped ZnO nanoparticles and their effect on light-emitting diodes. Nanomaterials. 2024;**14**(11):977

[119] Jangir LK, Kumari Y, Kumar A, Kumar M, Awasthi K. Investigation of

luminescence and structural properties of ZnO nanoparticles, synthesized with different precursors. Materials Chemistry Frontiers. 2017;**1**(7): 1413-1421

[120] Galdámez-Martinez A, Santana G, Güell F, Martínez-Alanis PR, Dutt A. Photoluminescence of ZnO nanowires: A review. Nanomaterials (Basel). 2020; **10**(5):857

[121] Khan M, Nowsherwan GA, Ali R, Ahmed M, Anwar N, Riaz S, et al. Investigation of photoluminescence and optoelectronics properties of transition metal-doped ZnO thin films. Molecules. 2023;**28**(24):7963

[122] Ščajev P, Durena R, Onufrijevs P, Miasojedovas S, Malinauskas T, Stanionyte S, et al. Morphological and optical property study of Li doped ZnO produced by microwave-assisted solvothermal synthesis. Materials Science in Semiconductor Processing. 2021;**135**:106069

[123] Hou Q, Meng F, Sun J. Electrical and optical properties of Al-doped ZnO and ZnAl2O4 films prepared by atomic layer deposition. Nanoscale Research Letters. 2013;**8**(144):1-8

[124] Luka G, Krajewski T, Wachnicki L, Witkowski B, Lusakowska E, Paszkowicz W, et al. Transparent and conductive undoped zinc oxide thin films grown by atomic layer deposition. Physica Status Solidi (a). 2010;**207**(7): 1568-1571

[125] Mursyalaat V, Variani V, Arsyad W, Firihu M. The development of program for calculating the band gap energy of semiconductor material based on UV-vis spectrum using Delphi 7.0. Journal of Physics: Conference Series. 2023; **2498**(1):012042

[126] Makuła P, Pacia M, Macyk W. How to correctly determine the band gap energy of modified semiconductor Photocatalysts based on UV–vis spectra. Journal of Physical Chemistry Letters. 2018;**9**(23):6814-6817

[127] Reine MB. Semiconductor Materials — Mercury Cadmium Telluride. In Encyclopedia of Modern Optics. Amsterdam: Elsevier; 2005. pp. 392-402

[128] Das BK, Das T, Parashar K, Thirumurugan A, Parashar SKS. Structural, bandgap tuning and electrical properties of Cu doped ZnO nanoparticles synthesized by mechanical alloying. Journal of Materials Science: Materials in Electronics. 2017;**28**:15127-15134

[129] Prasad N, Saipavitra VMM, Swaminathan H, Thangaraj P, Viswanathan MR, Balasubramanian K. Microstress, strain, band gap tuning and photocatalytic properties of thermally annealed and Cu-doped ZnO nanoparticles. Applied Physics A: Materials Science & Processing. 2016; **122**:590

[130] Ag KW, Ef MT, Beyene TT. Effects of Sulfur doping and temperature on the energy bandgap of ZnO nanoparticles and their antibacterial activities. ACS Omega. 2022;**7**(12):10796-10803

[131] Chandekar KV, Shkir M, Al-Shehri BM, AlFaify S, Halor RG, Khan A, et al. Visible light sensitive Cu doped ZnO: Facile synthesis, characterization and high photocatalytic response. Materials Characterization. 2020;**165**:110387

[132] Abebe B, Tsegaye D, Sori C, Prasad RCR, Murthy HCA. Cu/CuO-doped ZnO nanocomposites via solution combustion synthesis for catalytic 4-Nitrophenol reduction. ACS Omega. 2023;**8**(10):9597-9606

[133] Woodley SB, Sokol AA, Catlow CRA, Al-Sunaidi AA, Woodley SM. Structural and optical properties of Mg and Cd doped ZnO nanoclusters. Journal of Physical Chemistry C. 2013;**117**(51): 27127-27145

[134] Al-Ariki S, Yahya NAA, Al-A'nsi SA, Jumali MHH, Jannah AN, Abd-Shukor R. Synthesis and comparative study on the structural and optical properties of ZnO doped with Ni and Ag nanopowders fabricated by sol gel technique. Scientific Reports. 7 Jun 2021; **11**(1):11948

[135] Zheng H, Zhang RJ, Li DH, Chen X, Wang SY, Zheng YX, et al. Optical properties of Al-doped ZnO films in the infrared region and their absorption applications. Nano Express. 12 May 2018;**13**(149):1-7

[136] Kaufman AA, Hansen RO, Kleinberg RLK. Chapter 6 paramagnetism, diamagnetism, and ferromagnetism. Methods in Geochemistry and Geophysics. 2008;**42**:207-254

[137] Asmatulu R, Khan WS. Chapter 13 - Characterization of electrospun nanofibers. In: Synthesis and Applications of Electrospun Nanofibers. Amsterdam: Elsevier; 2019. pp. 257-281

[138] Undre PG, Kharat PB, Kounsalye JS, Kathare RV, Jadhav KM. Structural, morphological and magnetic properties of Cu2+ doped ZnO nanoparticles. Journal of Physics: Conference Series. 2020;**1644**(1):012008

[139] Gora MK, Kumar A, Kumar S, Maheshwari PK, Patidar D, Dolia SN, et al. Electronic, optical and magnetic properties of Cu-doped ZnO, a possible system for eco-friendly and energy-efficient spintronic applications. Environmental Science and Pollution Research. 2023;**30**: 98632-98646

[140] Chanda A, Gupta S, Vasundhara M, Joshi SR, Mutta GR, Singh J. Study of structural, optical and magnetic properties of cobalt doped ZnO nanorods. RSC Advances. 2017;**7**(80): 50527-50536

[141] Zhang J, Gao D, Yang G, Zhang J, Shi Z, Zhang Z, et al. Synthesis and magnetic properties of Zr doped ZnO nanoparticles. Nanoscale Research Letters. 2011;**6**(1):587

[142] Goldfarb RB. Electromagnetic units, the Giorgi system, and the revised international system of units. IEEE Magnetics Letters. 2018;**9**:1-5

[143] Sebayang P, CandraKurniawan LRY, Priyadi I, N NM, Aryanto D. Investigation of microstructure and magnetic properties of Zn1-xMnxO and Zn0.98-x MnxFe0.02O (x = 0, 0.05, and 0.09) prepared by solid-state reaction method. Makara Journal of Science. 2020;**24**(2):5

[144] Etape EP, Foba-Tendo J, Ngolui LJ, Namondo BV, Yollande FC, Nguimezong MBN. Structural characterization and magnetic properties of undoped and Ti-doped ZnO nanoparticles prepared by modified oxalate route. Journal of Nanomaterials. 22 May 2018;**2018**(1): 9072325

[145] Kumar SG, Kavitha R, Sushma C. Chapter 9 - Doped zinc oxide nanomaterials: structure-electronic properties and photocatalytic applicationsa. In: Interface Science and Technology. Amsterdam: Elsevier; 2020. pp. 285-312

[146] Jain KK. Drug delivery systems - an overview. In: Drug Delivery Systems.

Methods in Molecular Biology. Totowa, NJ: Humana Press; 2008. pp. 1-50

[147] Afzal H, Ikram M, Ali S, Shahzadi A, Aqeel M, Haider A, et al. Enhanced drug efficiency of doped ZnO–GO (graphene oxide) nanocomposites, a new gateway in drug delivery systems (DDSs). Materials Research Express. 2020;**7**(1):015405

[148] Hao R, Luo S, Wang F, Pan X, Yao J, Wu J, et al. Enhancement of fluorescence and anti-tumor effect of ZnO QDs by La doping. Frontiers in Chemistry. 2022;**10**:1042038

[149] Khatir NM, Sabbagh F. Green facile synthesis of silver-doped zinc oxide nanoparticles and evaluation of their effect on drug release. Materials. 2022; **15**(16):5536

[150] Cho NH, Cheong TC, Min JH, Wu JH, Lee SJ, Kim D, et al. A multifunctional core–shell nanoparticle for dendritic cell-based cancer immunotherapy. Nature Nanotechnology. 2011;**6**:675-682

[151] Zhang L, Zhong C, Yang Q, Liu M. Al/ZnO nanoparticle as an effective nanocarrier in delivery of lenalidomide anti-multiple myeloma cancer drug. Materials Technology. 2024;**39**(1): 2335848

[152] Tahir MB, Riaz KN, Rafique M, Rafique MS, Yousaf N, Sagir M. Photocatalysis fundamentals. In: Nanotechnology and photocatalysis for environmental applications. Amsterdam: Elsevier; 2020. pp. 57-64

[153] Wang L, Yu J. Principles of photocatalysis. In: Interface Science and Technology. Amsterdam: Elsevier; 2023. pp. 1-52

[154] Mirzaeifard Z, Shariatinia Z, Jourshabani M, Darvishi SMR. ZnO photocatalyst revisited: Effective photocatalytic degradation of emerging contaminants using S-doped ZnO nanoparticles under visible light radiation. Industrial and Engineering Chemistry Research. 2020;**59**(36): 15894-15911

[155] Hosny NM, Gomaa I, Elmahgary MG, Ibrahim MA. ZnO doped C: Facile synthesis, characterization and photocatalytic degradation of dyes. Scientific Reports. 30 Aug 2023;**13**(1): 14173

[156] Nguyen LTT, Nguyen LTH, Duong ATT, Nguyen BD, Hai NQ, Chu VH, et al. Preparation, characterization and photocatalytic activity of La-doped zinc oxide nanoparticles. Materials. 2019;**12**(8):1195

[157] Ebrahimi R, Hossienzadeh K, Afshin Maleki RG, Rezaee R, Safari M, Shahmoradi B, et al. Effects of doping zinc oxide nanoparticles with transition metals (Ag, Cu, Mn) on photocatalytic degradation of direct blue 15 dye under UV and visible light irradiation. Journal of Environmental Health Science and Engineering. 2019;**17**:479-492

[158] Zhang J, Deng SJ, Liu SY, Chen JM, Han BQ, Wang Y, et al. Preparation and photocatalytic activity of Nd doped ZnO nanoparticles. Materials Technology. 2014;**29**(5):262-268

[159] Chauhan A, Verma R, Kumari S, Sharma A, Shandilya P, Li X, et al. Photocatalytic dye degradation and antimicrobial activities of pure and Ag-doped ZnO using Cannabis sativa leaf extract. Scientific Reports. 2020;**10**:7881

[160] Jian S, Tian Z, Hu J, Zhang K, Zhang L, Duan G, et al. Enhanced visible light photocatalytic efficiency of La-doped ZnO nanofibers via electrospinning-calcination technology.

Advanced Powder Materials. 2022;**1**(2): 100004

[161] Rani S, Sharma A, Tabasum S, Malik AQ, Chaudhary S, Kumar D, et al. Highly efficient photocatalytic properties of La-doped ZnO over pristine ZnO for degradation of 2-chlorophenol from aquatic agriculture waste. Chemistry Africa. 2023;**6**:1981-1990

[162] Atyaoui M, Hamouda F, Ezzaouia H. Growth of La-doped ZnO thin films on a porous silicon substrate for photocatalytic applications. Chemistry Select. 2023;**8**(10):e202300108

[163] Pathak TK, Coetsee-Hugo E, Swart HC, Swart CW, Kroon RE. Preparation and characterization of Ce doped ZnO nanomaterial for photocatalytic and biological applications. Materials Science and Engineering: B. 2020;**261**:114780

[164] Kumar R, Umar A, Kumar G, Akhtar MS, Wang Y, Kim SH. Ce-doped ZnO nanoparticles for efficient photocatalytic degradation of direct red-23 dye. Ceramics International. 2015;**41** (6):7773-7782

[165] Aisah N, Gustiono D, Fauzia V, Sugihartono I, Nuryadi R. Synthesis and enhanced photocatalytic activity of Ce-doped zinc oxide nanorods by hydrothermal method. In: Conf. Ser.: Mater. Sci. Eng. Purwokerto, Indonesia: IOP Publisher; 2017. p. 012037

[166] Hu B, Sun Q, Zuo C, Pei Y, Yang S, Zheng H, et al. A highly efficient porous rod-like Ce-doped ZnO photocatalyst for the degradation of dye contaminants in water. Beilstein Journal of Nanotechnology. 2019;**10**:1157-1165

[167] Ahmad I, Akhtar MS, Ahmed E, Ahmad M. Facile synthesis of Pr-doped ZnO photocatalyst using sol-gel method and its visible light photocatalytic activity. Journal of Materials Science: Materials in Electronics. 2020;**31**:1084-1093

[168] Chen JL, Neena Devi NL, Fu DJ, Ke XW. Synthesis of Pr-doped ZnO nanoparticles: Their structural, optical, and photocatalytic properties*. Chinese Physics B. 2018;**27**(8):086102

[169] Wang MH, Zhao ZY, Liu TT. Synthesis of Pr-doped ZnO nanoparticles by sol–gel method and varistor properties study. Journal of Alloys and Compounds. 2015;**621**:220-224

[170] Laokae D, Phuruangrat A, Wannapop S, Dumrongrojthanath P, Thongtem T, Thongtem S. Preparation, characterization and photocatalytic properties of Er-doped ZnO nanoparticles synthesized by combustion method. International Journal of Materials Research. 2022;**114** (1):34-42

[171] França R, Araujo FP, Castro-Lopes S, Neves L, Melo A, Jerônimo AG, et al. Effect of Cr cations addition on the structural, morphological, optical, and photocatalytic properties of Er-doped ZnO structures. Materials Today Communications. 2023;**37**:107419

[172] Choudhary S, Mohapatra S. Enhanced photocatalytic activity of Er doped ZnO nanospindles and nanorods for degradation of organic pollutants. Inorganic Chemistry Communications. 2024;**161**:111977

[173] Silva MCR, Castro-Lopes S, Jerônimo AG, Barbosa R, Lins A, Trigueiro P, et al. Green synthesis of Er-doped ZnO nanoparticles: An investigation on the methylene blue, eosin, and ibuprofen removal by photodegradation. Molecules. 2024;**29** (2):391

[174] Laokae D, Phuruangrat A, Thongtem T, Thongtem S. Preparation

of Yb-doped ZnO nanoparticles by combustion method combined with high temperature calcination for photodegradation of methylene blue under visible light irradiation. Materials Research Innovations. 2022;**26**(5): 303-315

[175] Sordello F, Berruti I, Gionco C, Paganini MC, Calza P, Minero C. Photocatalytic performances of rare earth element-doped zinc oxide toward pollutant abatement in water and wastewater. Applied Catalysis B: Environmental. 2019;**245**:159-166

[176] Elias M, Uddin MN, Saha JK, Hossain MA, Sarker DR, Akter S, et al. A highly efficient and stable photocatalyst; N-doped ZnO/CNT composite thin film synthesized via simple sol-gel drop coating method. Molecules. 2021;**26**(5): 1470

[177] Hussain CM. Engineered nanomaterials for energy applications. In: Hussain CM. Nanomaterials for Industrial Applications. Amsterdam: Elsevier; 2018. pp. 751-767

[178] Çakar S, Özacar M, Fındık F. MOFs-based dye-sensitized photovoltaics. In: Metal-Organic Framework-Based Nanomaterials for Energy Conversion and Storage. Amsterdam: Elsevier; 2022. pp. 487-506

[179] Esakki ES, Vivek P, Sundar SM. Influence on the efficiency of dye-sensitized solar cell using Cd doped ZnO via solvothermal method. Inorganic Chemistry Communications. 2023;**147**: 110213

[180] Amjad M, Khan MI, Alwadai N, Irfan M, Ikram-ul-Haq AH, et al. Photovoltaic properties of ZnO films Co-doped with Mn and La to enhance solar cell efficiency. Nanomaterials (Basel). 2022;**12**(7):1057

[181] Saleem M, Irshad K, Rehman SU, Javed MS, Hasan MA, Ali HM, et al. Characteristics and photovoltaic applications of Au-doped ZnO–Sm nanoparticle films. Nanomaterials. 11 Mar 2021;**11**(3):702

[182] Chundawat P, Vyas Y, Dharmendra D, Chaubis P, Ameta C. Improving the photovoltaic performance of dye-sensitized solar cells using a W and S Co-doped ZnO Photoanode. Journal of Electronic Materials. 2023;**52**:939-950

[183] Salah HY, Abdelfatah M, El-Shaer A, Oraby AH. Effect of Al doped ZnO on optical and photovoltaic properties of the p-Cu2O/n-AZO solar cells. Ceramics International. 2023;**49**(5):7746-7752

[184] Li L, Yang H, Yang P. Lutetium-doped ZnO to improve photovoltaic performance: A first-principles study. ACS Applied Electronic Materials. 2022; **4**(12):6253-6260

[185] Alfakes B, Villegas J, Apostoleris H, Devarapalli R, Tamalampudi S, Lu JY, et al. Optoelectronic tunability of Hf-doped ZnO for photovoltaic applications. Journal of Physical Chemistry C. 2019;**24** (123):15258-15266

[186] Orelusi AN, Owoeye VA, Dada JB, Salau AO, Boyo HO, Adewinbi SA. Investigation of microstructure and optical characteristics of Ti-doped ZnO thin films as an effective solar collector in photovoltaic solar cell applications using digitally controlled spray pyrolysis. Journal of Materials Research. Aug 2023; **38**:4192-4200

[187] Erkan S, Altuntepe A, Yazici D, Olgar MA, Zan R. Enhanced photovoltaic performance of silicon-based solar cell through optimization of Ga-doped ZnO layer. Physica Scripta. 2023;**98**(10):105928

[188] Banerjee D, Chattopadhyay KK. Hybrid inorganic organic perovskites: A low-cost-efficient optoelectronic material. In: Perovskite Photovoltaics. Oxford: Academic Press; 2018. pp. 123-162

[189] Muhammad A, Hassan Z, Mohammad SM, Rajamanickam S, Abed SM, Ashiq MGB. Realization of UV-C absorption in ZnO nanostructures using fluorine and silver co-doping. Colloid and Interface Science Communications. 2022;**47**:100588

[190] Chongsri K, Pecharapa W. UV photodetector based on Al-doped ZnO nanocrystalline sol-gel derived thin Fims☆. Energy Procedia. 2014;**56**: 554-559

[191] Abbas SI, Alattar AM, Al-Azawy AA. Enhanced ultraviolet photodetector based on Al-doped ZnO thin films prepared by spray pyrolysis method. Journal of Optics. 2024;**53**:396-403

[192] Sharma R, Saxena N, Pandey N, Dawar A, Ojha S, Chawla V, et al. Mg-doped tailoring of zinc oxide for UV-photodetection application. Optical Materials. 2022;**125**:112056

[193] Rana V, Rajput J, Pathak T, Purohit L. Multilayer MgZnO/ZnO thin films for UV photodetectors. Journal of Alloys and Compounds. 2018;**764**:724-729

[194] Alam M, Manzoor U, Mujahid M, Bhatti A. Highly responsive UV light sensors using Mg-doped ZnO nanoparticles. Journal of Sensors. 2016; **2016**:8296936

[195] Hameed H. Enhanced ultraviolet photodetector based on Mg-doped ZnO nanorods films. Al-Mustansiriyah Journal of Science. 2018;**29**(3):158-167

[196] Young SJ, Liu YH, Shiblee MDNI, Ahmed K, Lai LT, Nagahara L, et al. Flexible ultraviolet photodetectors based on one-dimensional gallium-doped zinc oxide nanostructures. ACS Applied Electronic Materials. 2020;**2**(11): 3522-3529

[197] Chu YL, Young SJ, Ji LW, Tang IT, Chu TT. Fabrication of ultraviolet photodetectors based on Fe-doped ZnO nanorod structures. Sensors. 2020;**20** (14):3861

[198] Boruah BD, Majjia SN, Misra A. Surface photo-charge effect in doped-ZnO nanorods for high-performance self-powered ultraviolet photodetectors. Nanoscale. 2017;**9**(13):4536-4543

[199] Jalal R, Ozel K, Atilgan A, Yildiz A. UV photodetectors based on W-doped ZnO thin films. Nanotechnology. 2024; **35**(26):265705

[200] Abbasi F, Zahedi F, Yousefi M. Performance improvement of UV photodetectors using Cd-doped ZnO nanostructures. Journal of Materials Science: Materials in Electronics. 2021; **32**:19614-19625

[201] Pineda-Reyes AM, Herrera-Rivera MR, Rojas-Chávez H, Cruz-Martínez H, Medina DI. Recent advances in ZnO-based carbon monoxide sensors: Role of doping. Sensors (Basel). 2021;**21**(13): 4425

[202] Du H, Li X, Yao P, Wang J, Sun Y, Dong L. Zinc oxide coated tin oxide nanofibers for improved selective acetone sensing. Nanomaterials. 2018;**8** (7):509

[203] Kang Y, Yu F, Zhang L, Wang W, Chen L, Li Y. Review of ZnO-based nanomaterials in gas sensors. Solid State Ionics. 2021;**360**:115544

[204] Li WZ, Wu MR, Tung CY, Huang CY, Tan CS, Huang YS, et al. Strain

control of a NO gas sensor based on Ga-doped ZnO epilayers. ACS Applied Electronic Materials. 2020;**2**(5): 1365-1372

[205] Abdelkarem K, Saad R, Sayed AME, Fathy MI, Shaban M, Hamdy H. Design of high-sensitivity La-doped ZnO sensors for CO_2 gas detection at room temperature. Scientific Reports. 2023;**13**: 18398

[206] Shingange K, Swart HC, Mhlongo GH. H2S detection capabilities with fibrous-like La-doped ZnO nanostructures: A comparative study on the combined effects of La-doping and post-annealing. Journal of Alloys and Compounds. 2019;**797**:284-301

[207] Xu XL, Chen Y, Ma SY, Li WQ, Mao YZ. Excellent acetone sensor of La-doped ZnO nanofibers with unique bead-like structures. Sensors and Actuators B: Chemical. 2015;**213**:222-233

[208] Santhosam AJ, Ravichandran K, Shkir M, Sridharan M. Effect of La incorporation on the NH3 sensing behaviour of ZnO thin films prepared using low-cost nebulizer spray technique. Journal of Materials Science: Materials in Electronics. 2020;**31**: 13240-13248

[209] Ramola RC, Negi S, Rawat M, Singh RC, Singh F. Annealing effects on gas sensing response of Ga-doped ZnO thin films. ACS Omega. 2021;**6**(17): 11660-11668

[210] Hjiri M, Dhahri R, Mir LE, Leonardi SG, Neri G. Excellent CO gas sensor based on Ga-doped ZnO nanoparticles. Journal of Materials Science: Materials in Electronics. 2015;**26**:6020-6024

[211] Wang T, Chen J, Chen J, Yao X, Chen G, Jiao Z, et al. UV-light enhanced gas sensor based on Ga doped ZnO for ultra-high sensitive and selective n-butanol detection. Applied Surface Science. 2023;**641**:158551

[212] Ramola RC, Negi S, Singh RC, Singh F. Gas sensing response of ion beam irradiated Ga-doped ZnO thin films. Scientific Reports. 2022;**12**:22351

[213] Jaballah S, Alaskar Y, AlShunaifi I, Ghiloufi I, Neri G, Bouzidi C, et al. Effect of Al and Mg doping on reducing gases detection of ZnO nanoparticles. Chem. 2021;**9**(11):300

[214] Qi J, Zhang H, Lu S, Li X, Xu M, Zhang Y. High performance indium-doped ZnO gas sensor. Journal of Nanomaterials. 2015;**16**(1):74-74

[215] Rahman F. Zinc oxide light-emitting diodes: A review. Optical Engineering. 2019;**58**(1):10901

[216] Frieiro J, Guillaume C, López-Vidrier J, Blázquez O, González-Torres S, Labbé C, et al. Toward RGB LEDs based on rare earth-doped ZnO. Nanotechnology. 2020;**31**(46):465207

[217] Rahman A, Mamun SMN, Hossain AKMA, Ton-That C. ZnO nanorods on Li-doped ZnO thin films for efficient p–n homojunction light-emitting diodes. ACS Applied Nano Materials. 2023;**6** (17):15757-15763

[218] Shafiqul IM, Yoshida T, Fujita Y. p-ZnO/n-ZnMgO nanoparticle-based heterojunction UV light-emitting diodes. Materials. 2022;**15**(23):8348

[219] Zhang L, Li Q, Shang L, Wang F, Qu C, Zhao F. Improvement of UV electroluminescence of n-ZnO/p-GaN heterojunction LED by ZnS interlayer. Optics Express. 2013;**21**(14):16578-16583

[220] Manzhi P, Kumari R, Alam MB, Umapathy GR, Krishna R, Ojha S, et al.

Mg-doped ZnO nanostructures for efficient organic light emitting diode. Vacuum. 2019;**166**:370-376

[221] Sandeep KM, Bhat S, Dharmaprakash SM. Structural, optical, and LED characteristics of ZnO and Al doped ZnO thin films. Journal of Physics and Chemistry of Solids. 2017;**104**:36-44

[222] Horng RH, Shen KC, Yin CY, Huang CY, Wuu DS. High performance of Ga-doped ZnO transparent conductive layers using MOCVD for GaN LED applications. Optics Express. 2013;**21**(12):14452-14457

Chapter 2

Recent Trends of Zinc Oxide Nanoparticles for Emerging Biomedical Application

Ajay Kumar Tiwari, Saket Jha, Ram Raseele Awasthi, Abhimanyu Kumar Singh, Abhishek Kumar Bhardwaj and Sharad Kumar Tripathi

Abstract

In the current scenario, various industries such as pharmaceuticals, biomedical sectors, cosmetics, photovoltaics, and automotive utilize zinc oxide nanoparticles (ZnO NPs) widely due to their exceptional potentials and high surface area-to-volume ratio. However, researchers are still working to improve the potential of ZnO NPs as antimicrobial, anticancer, antioxidant, antidiabetic, etc. This chapter highlighted plants and microbial extract-based synthesis methods of ZnO NPs and comparative understanding established with laser ablation, chemical reduction, milling, and sputtering. In contrast, the green synthesis of ZnO NPs offers an eco-friendly and chemical-free approach for biological applications. The green synthesis method involves a range of extract compositions, including secondary metabolites flavonoids, enzymes, proteins, and sugars, which reduce and stabilize ZnO NPs, influencing their structure, shape, size, and morphology. Biologically synthesized ZnO NPs, due to their cost-effective and eco-friendly nature, are significant for medication distribution and sensing applications.

Keywords: ZnO NPs, biological synthesis, eco-friendly, biomedical application, antioxidant

1. Introduction

The field of engineering and science known as nanotechnology, which plays with materials having dimensions smaller than 100 nanometers (nm), has significantly expanded possibilities for novel applications in the fields of agricultural industries and nanobiotechnology [1]. It is considered the application of nanoparticles (NPs), so it is described as microscopic particles that exhibit specific characteristics and modes of conveyance. It also has an enormous opportunity for providing researchers a chance to build prototype instruments to facilitate NPs incorporation into plants, which might be utilized to integrate prototype functionalities and complement existing ones. When NPs interact with plants, a number of morphological and

physiological changes take place. The efficiency of NPs resolves various aspects such as their size, surface coverage, reactivity, chemical composition, and, most significantly, their efficacy [2]. Conventional fertilizers are being used widely and at high rates to increase grain production in order to meet the rapidly expanding population's demands. Fertilizers are essential for plant growth and multiplication; however, most fertilizers that are given remain inaccessible to plants for a variety of reasons. These include leaching, photolysis-induced degradation, hydrolysis, and decomposition. As a result, it's necessary to reduce fertilization-related nutrient losses and increase crop yields by utilizing emerging approaches and applying nanotechnology and NPs [3]. The only metal present in all six groups of enzymes oxidoreductases, lyases, isomerases, transferases, hydrolases, and ligases is zinc (Zn), which is also essential to numerous essential metabolic activities [4]. In the end, zinc can boost the plant's photosynthetic machinery and increase the manufacture of carotenoids and chlorophylls [5]. ZnO NPs have superior optoelectrical, physical, and antibacterial qualities and present a significant deal of promise for increasing agricultural output [6]. Several investigations have reported strong absorption capacities for heavy metals, ZnO, and its NPs, as well as a variety of organic compounds [7]. When compared to the bulk material, ZnO NPs' incredibly large surface area-to-volume ratio increases the effectiveness of UV radiation blocking [8]. Numerous studies have assessed the effects of ZnO NPs on crop plants. In a variety of vegetable crops, nano-sized ZnO particles increased germination, pigments, sugar, and protein levels while also increasing the activity of antioxidant enzymes [9].

ZnO NPs internalize in the endodermal and vascular tissues, where they have a significant impact on the root epidermis and cortex of *Lolium perenne* [10]. ZnO NPs exhibit antibacterial action against a variety of pathogenic microorganisms, including *Campylobacter jejuni*, *Pseudomonas aeruginosa*, and *Escherichia coli* [11]. Increased yield has a direct correlation with the decline of some harmful microorganisms and the potential dietary value of the NPs themselves, primarily for the vital micronutrients required for host defense [12]. Numerous chemical techniques, including precipitation, vapor transport, and the hydrothermal process, can be used to create ZnO NPs (**Figure 1**). The use of various plant extracts or microorganisms in the biological synthesis of ZnO NPs is currently a developing field of study. When

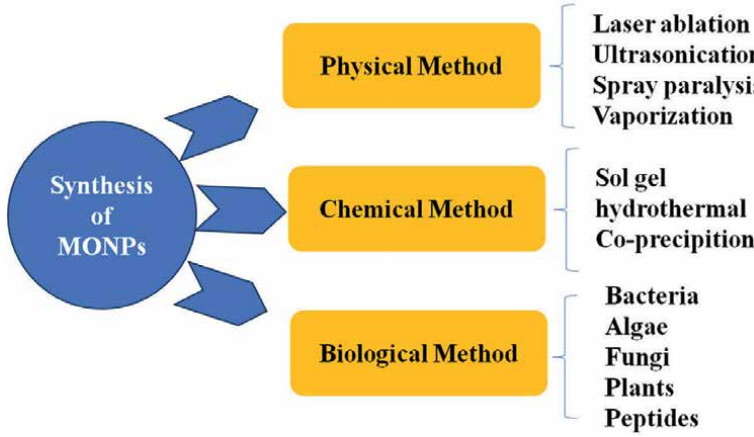

Figure 1.
Various methods for the synthesis of metal oxide nanoparticles.

compared to conventional chemical and physical approaches, the biological approach to NP synthesis provides an advantage [13]. ZnO NPs is an inorganic substance with a wide range of uses that is strategic, functional, promising, and diverse. Since Zn and O are confined to groups two and six of the periodic table, respectively, it is known as an II-VI semiconductor [14]. Unique optical, chemical sensing, electric conductivity, semiconducting, and piezoelectric characteristics are possessed by ZnO [15]. Its natural n-type electrical conductivity, a high excitonic binding energy of 60 meV at ambient temperature, and a relatively wide band gap of 3.3 eV in the near-UV spectrum are its distinguishing features. These properties make ZnO a fascinating material with a wide range of applications. ZnO's large band gap significantly influences its characteristics, including optical absorption and electrical conductivity. However, ZnO is doped with additional metals, the excitonic emission can persist longer at normal temperature, and the conductivity rises [16–21]. ZnO exhibits a weak covalent nature, although the Zn-O ionic bond is extremely strong. Inorganic and organic materials come before it in terms of heat resistance, selectivity, and longevity [22]. ZnO NPs production has prompted studies into its potential application as a prophylactic agent. ZnO NPs have strong photochemical and catalytic activities in addition to their distinct antibacterial and antifungal characteristics. ZnO NPs are used as a UV sentinel in cosmetics because of their strong optical absorption in the UVA (315–400 nm) and UVB (280–315 nm) wavelengths, which is advantageous for inhibiting bacterial growth [23]. The biological production of ZnO NPs and their biological applications are the main topics of this book chapter.

2. Biological synthesis of ZnO NPs

Nowadays, biological synthesis has become more popular due to its simple approach, cost effectiveness, and environmental friendliness. This method can be utilized without the involvement of any perilous and hazardous chemicals. Nowadays, either plant extract or microbe extract is utilized to synthesize the ZnO NPs.

2.1 Using the extract of the various parts of plants

Plant parts such as leaves, roots, rhizomes, bark, fruits, and flowers are utilized to synthesize ZnO NPs (**Table 1**). For their biosynthesis, a simple procedure is applied (**Figure 2**). Researchers collect these plant parts from different sources, wash them thoroughly with tap and distilled water to remove debris, and then either dry them, grind them into powder, or use them directly for extraction. They chop or grind the plant parts into small pieces or powder and boil them in different solvents (water, ethanol, etc.) at below 60°C to obtain the extract. To synthesize ZnO NPs, they use different concentrations of Zn salts as a metal precursor and extract at various pH levels and temperatures without needing external chemical stabilizers. Simply mixing the extract with a salt solution works because the biochemicals act as reducing and stabilizing agents for the ZnO NPs synthesis. Literature [21] describes a detailed protocol for synthesizing ZnO NPs using *Jacaranda mimosifolia* flower extract. The production of ZnO nanoparticles can be tracked through direct visual inspection or by utilizing a UV-visible spectrophotometer. After synthesis, the ZnO NPs solution is centrifuged at high rpm to separate the NPs, then washed thoroughly with solvents. **Figure 2** portrays the biological synthesis of ZnO NPs using different parts of various plants.

S. No.	Plants	Part of the plants	Size/shape of NPs	Application	Reference
1	*Calendula officinalis*	Petal extract	27.22 nm Spherical	Antioxidant	[22]
2	*Calendula officinalis*	Leaf extract	28.23 nm Hexagonal	Antioxidant and antimicrobial	[23]
3	*Citrus aurantifolia*	Fruit peel	35–45 nm Spherical	Good electrical and optical property	[24]
4	*Murraya paniculata*	Leaf extract	25–35 nm Spherical	Antimicrobial	[25]
5	*Parthenium hysterophorus*	Leaf extract	10 ± 5 nm Spherical	Antimicrobial	[26]
6	*Tectona grandis (L.)*	Leaf extract	22 ± 5 nm spherical	Anti-diabetic, Anti-inflammatory	[27]
7	*Citrus sinensis*	Peel Extract	10–20 nm spherical	Antibacterial	[28]
8	*WithaniaSomnifera*	Leaf Extract	70–90 nm spherical	Antimicrobial	[29]
9	*Euphorbia hirta*	Leaf extract	20–25 nm Hexagonal	Microbial	[30]
10	*Laurus nobilis*	Leaf extract	47.27 nm Hexagonal	Antioxidant and antimicrobial	[31]
11	*Cannabis sativa*	Leaf extract	46 nm Hexagonal	Antioxidant	[32]
12	*Syzygium Cumini*	Leaf extract	11.35 nm Hexagonal	Photocatalysis	[33]
13	*Borassus flabellifer*	fruit extract	39.83 nm Hexagonal	Photocatalysis	[34]
14	*Tabernaemontana divaricata*	Leaf extract	20–50 nm Spherical	Photocatalysis and antimicrobial	[35]
15	*loquat*	Seed extract	>50 nm Hexagonal	Photocatalytic degration	[36]
16	*Tabernaemontana divaricata*	flower extract	17.5–23.2 nm Hexagonal	Antimicrobial and Antioxidant	[37]
17	*Catharanthus roseus*	Leaf extract	36.83 nm Spherical	Antimicrobial	[38]
18	*Caesalpinia crista*	Seed extract	20–44 nm Irregular	Antimicrobial, antioxidant and anti- cancerous	[39]
19	*Tabernaemontana*	Leaf extract	20–50 nm Spherical	Photo catalytic and antimicrobial	[35]
20	*Borassus flabellifer*	Fruit extract	39.83 nm Hexagonal	Photo catalytic removal	[34]
21	*Coptidis rhizoma*	Leaf extract	2.9–25.2 nm Spherical	Antibacterial, antioxidant and cytotoxic	[40]

Table 1.
Biological synthesis of ZnO NPs using different plant sources.

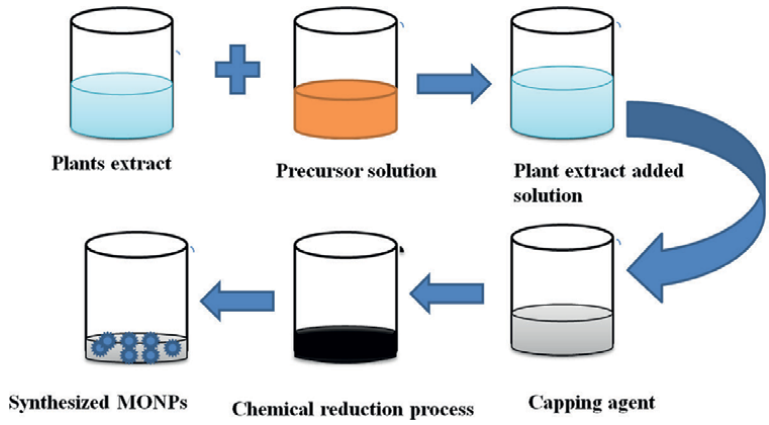

Figure 2.
Biological synthesis of MONPs using plant extract.

2.2 Using various microbes

The cultures grow as suspension cultures in sterilized distilled water containing culture media. After adding different concentrations of a ZnO to the freshly cultured

S. No.	Microbes	Precursor	Size(nm)	Shape	Reference
1	*S. nematodiphila*	Zinc sulfate	15–30	Roughly spherical	[41]
2	*L. plantarum*	Zinc nitrate	191–291	Flower-like and irregular	[42]
3	*B. cereus*	Zinc sulfate heptahydrate	21–35	Spherical	[43]
4	*Lactobacillus* spp.	Zinc acetate	32	Spherical	[44]
5	*Streptomyces* sp.	Zinc acetate dihydrate	16–25	Spherical	[45]
6	*S. plicatus*	Zinc sulfate	21.72	Spherical	[46]
7	*Pseudochrobactrum* sp.	Zinc acetate	90–110	Granular	[47]
8	*S. enisocaesilis*	Zinc sulphate	12–326	Needle shape	[48]
9	*A. niger*	Zinc nitrate	30–70	Spherical	[49]
10	*A. niger*	Zinc acetate	80–130	Rod and cluster	[50]
11	*Cordyceps militaris*	Zinc nitrate hexahydrate	10.15	Flower	[51]
12	*Fusarium keratoplasticum*	Zinc acetate	10–42	Hexagonal	[52]
13	*A. niger*	Zinc acetate	8–38	Nano-rod	
14	*Alternaria tenuissima*	Zinc sulphate	15.45	Spherical	[53]
15	*Penicillium corylophilum*	Zinc acetate dihydrate	9–51	Spherical	[54]
16	*Periconium* sp.	Zinc nitrate	16–78	Quasi spherical	[55]
17	*Agaricus bisporus*	Zinc acetate dehydrate	< 40 nm	Hexagonal	[56]
18	*Trichoderma harzianum*, and *T. reesei*	Zinc nitrate hexahydrate	60–70	Crystal planes	[57]
19	*Xylaria acuta*	Zinc nitrate hexahydrate	34–55	Hexagonal	[58]
20	*Acremonium potronii*	Zinc acetate hexahydrate	13–15	Spherical	[59]

Table 2.
Biological synthesis of ZnO NPs using various microbes.

microbes, keep it in an incubator for 24 hours until white deposition starts to form at the bottom of the flasks, indicating the initiation of transformation. The bioreduction of nanoparticles is monitored using a UV-visible spectrophotometer. The solution is then transferred into centrifuge tubes and centrifuged at 3000 rpm for 10–20 minutes to separate the synthesized nanoparticles. **Table 2** shows the various types of microbes that are utilized for the synthesis of the ZnO NPs. At the initial suspension, cultures are prepared in a sterile environment to ensure that no contamination affects the results. The culture media contain specific nutrients necessary for the growth and proliferation of the microbes. When different concentrations of ZnO are introduced to the cultures, the microbes start interacting with ZnO, leading to the deposition of ZnO at the bottom of the flasks. The incubation period of 24 hours allows enough time for this process to initiate visible changes. The use of a UV-visible spectrophotometer to monitor bioreduction assists in identifying the development and growth of nano-sized particles. UV-visible spectroscopy measures the absorbance or reflectance of light in the range of 200–800 nm, which provides key information about the size and concentration of the NPs produced. After monitoring, the solutions containing ZnO NPs are transferred into centrifuge tubes. The centrifugation process, which utilizes centrifugal force to separate materials based on their densities, is performed at 3000 rpm for 10–20 minutes. **Table 2** shows a detailed list of the various types of microbes that have been successfully used for the preparation of ZnO NPs.

3. Reduction of ZnO NPs by bio-reductants

ZnO NPs production involves the use of capping and stabilizing chemicals. It is possible to stabilize ZnO particles with varying shapes, sizes, and other characteristics using different capping agents. ZnO NPs are traditionally produced using a variety of surfactants; however, these are environmentally harmful and difficult to break down. Green capping agents are therefore desperately needed to synthesize ZnO NPs. Another option is to employ the biochemicals found in plant extracts.

4. Mechanism of biological synthesis of ZnO NPs

In recent years, researchers have used various microbes and plant extracts to biologically synthesize metal and metal oxide nanoparticles (NPs). The synthesis of ZnO NPs by plants relies on phytochemicals like alkaloids, phenols, flavonoids, tannins, saponins, terpenoids, and carbohydrates, which are crucial for NP formation. Microbe-mediated synthesis of NPs is categorized into extracellular and intracellular based on the NPs formation site. During intracellular synthesis, metal ions enter the microbial cell and form NPs with the cell's enzymes. Conversely, in extracellular biosynthesis, metal ions get trapped on the microbial cell surface and are reduced to NPs by surface enzymes. Karnan and his team created ZnO NPs using *Nephelium lappaceum* peel extract, discovering the extract's phenolic components act as a binding agent to zinc ions, forming a stable zinc-ellagate complex that decomposes into ZnO NPs at 450°C in static air. Sharma and colleagues produced ZnO NPs from *Carica papaya* milk through complex reaction, NP aggregation, and compound oxidation in the extract [60]. They found that the extract's interaction with Zn^{2+} ions form various ZnO morphologies [61]. Similarly, using *Vitex negundo* leaf extract, which contains polyphenolic compounds isoorientin and luteolin, leads to ZnO NP bioreduction through the formation of a

zinc-isoorientin complex in an acidic medium [62]. Azizi employed *Anchusa italica* flower extract, rich in certain essential oils, for ZnO NPs biosynthesis. He described the formation mechanism in which biomolecules complex with Zn^{2+}, stabilizing the nanoparticles and inhibiting crystal growth, followed by the thermal decomposition of $Zn(OH)_2$. In summary, recent research has successfully synthesized metal and metal oxide NPs using microbes and plant extracts, leveraging specific phytochemicals for NP formation [63]. This synthesis involves intricate biochemical processes, including metal ion complexation and reduction, enzyme interactions, and thermal decomposition, leading to the production of ZnO NPs with diverse structures and properties.

5. Application of biologically synthesized ZnO NPs

Biologically synthesized ZnO NPs have substantial biological activities, including antioxidant, antimicrobial, antibacterial, anti-diabetic, anti-inflammatory and anti-cancerous potential. **Figure 3** shows the application of the biologically synthesized ZnO NPs in divers' fields of nano and biotechnologies.

5.1 Antimicrobial activity

It is found that biologically synthesized ZnO NPs come in various shapes and exhibit remarkable antibacterial activity against a broad spectrum of microorganisms [64]. Previous studies demonstrate that the antibacterial efficacy of ZnO NPs improves as the powder concentration increases and diminishes as the particle size decreases [65]. This enhanced antibacterial property of ZnO NPs can be attributed to their enormous surface area-to-volume ratio, which allows more ligands to bind to their surface [66, 67]. The antibacterial action of ZnO NPs is primarily mediated through the generation of oxidative stress. This process occurs due to the interaction

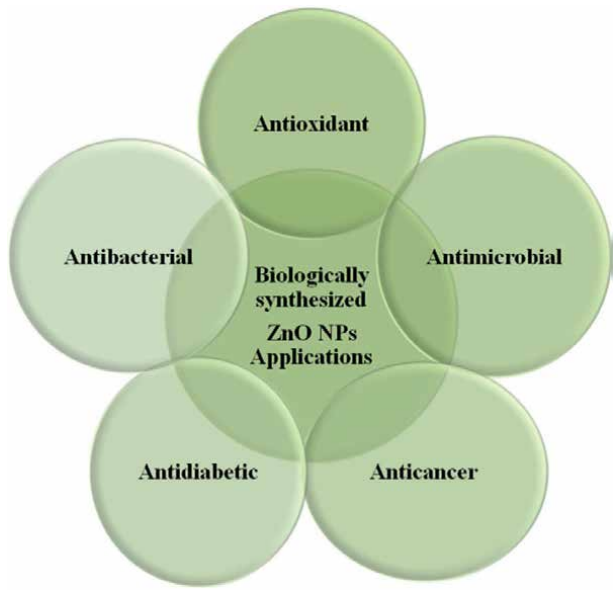

Figure 3.
Biomedical Application of the biologically synthesized ZnO NPs.

between the Zn^{+} ion and the thiol group of the bacterial respiratory enzyme. As a result of this interaction, oxidative stress is generated within the bacterial cells, leading to an increase in reactive oxygen species (ROS). These ROS are highly reactive molecules that can cause severe damage to bacterial cells, ultimately resulting in cell damage and death [68, 69]. This highlights the potential of ZnO NPs as effective antibacterial agents, especially in contexts where traditional antibiotics may fail due to resistance issues. By manipulating the concentration and size of nanoparticles, researchers can optimize their antibacterial properties for various applications in medicine, agriculture, and environmental protection. ZnO NPs have demonstrated potent antimicrobial activity, while the U.S. Food and Drug Administration (FDA) classifies ZnO as GRAS (Generally Recognized as Safe) [70]. Scientific literature abounds with reports showcasing the antibacterial activity of ZnO NPs against various model pathogens, including both Gram-positive and Gram-negative bacteria. Due to its strong photocatalytic properties, ZnO is anticipated to generate significant levels of reactive oxygen species (ROS) when exposed to light irradiation [71]. The combination of ZnO NPs with essential oils leads to synergistic interactions that result in either a significantly enhanced antimicrobial effect or a reduction in the quantity of active compounds needed to effectively combat a wide range of microorganisms. This innovative approach not only boosts the overall efficacy but also offers a more efficient and sustainable alternative in antimicrobial treatments. Such functionalized NPs can be applied in various fields, including the formulation of topical ointments for wound care and skin infections, as well as in other antimicrobial technologies, such as food packaging materials, where they help to extend shelf life by inhibiting microbial growth [72]. ZnO NPs demonstrate strong antibacterial activity due to the production of free radicals, particularly on their oxide surface [73]. ZnO NPs possess several advantages over organic antimicrobial agents, including stability under pressure, high temperatures, long shelf life, robustness, and other beneficial qualities. Researchers have utilized the antibacterial characteristics of biologically synthesized ZnO NPs as a foundational element in designing cosmetics, personal care items, and functional textiles [74]. ZnO NPs produce ROS that can damage bacterial cell membranes, leading to the death of harmful microorganisms and enhancing the efficacy of ZnO NPs as antibacterial agents. The stability of inorganic oxides like ZnO allows them to remain effective even under harsh conditions, which is a significant limitation for many organic compounds that can degrade or lose potency under similar circumstances. In the cosmetic industry, manufacturers incorporate ZnO NPs into products like sunscreens and moisturizers to not only provide antimicrobial protection but also to benefit from their UV-blocking properties. Personal care items such as toothpaste and deodorants also benefit from the inclusion of ZnO NPs due to their long-lasting and robust antimicrobial effects. Additionally, the textile industry uses ZnO NPs in the production of fabrics that resist bacterial growth, thereby reducing odor and increasing the material's lifespan. The application of ZnO NPs in these fields highlights their versatility and the ongoing research aimed at maximizing their beneficial properties [75]. ZnO NPs synthesized using the flower extract of *Trifoliumpratense* exhibit notable antibacterial activity against *Staphylococcus aureus* (ATCC 4163), *Escherichia coli* (ATCC 25922), and *Pseudomonas aeruginosa* (ATCC 6749) [76].

5.2 Antioxidant activity

Due to the transfer of electron density at oxygen and the dependence of these properties on the structural makeup of oxygen atoms, ZnO NPs exhibit significant

antioxidant properties [77]. Scientists have discovered this material in nature, highlighting its remarkable ability to provide antioxidant protection, which originates from higher plants. These antioxidant properties have proven to be highly effective in combating a range of chronic diseases that are closely linked to oxidative stress and processes. Oxidative stress occurs when there is an imbalance between the production of free radicals and the body's ability to counteract their harmful effects through antioxidants. Over time, this imbalance can lead to cellular damage, contributing to the development of various chronic conditions such as cardiovascular diseases, neurodegenerative disorders, and even cancer. One of the key components of this material is zinc, a trace element renowned for its multifaceted role in maintaining cellular health. Although zinc is known for its ability to produce free radicals under certain conditions, it paradoxically functions as a potent antioxidant. This dual capability is one of zinc's unique attributes, enabling it to act as a protective agent in preventing oxidative damage to cell membranes and other vital cellular components. By neutralizing ROS, zinc helps to minimize the destructive effects of oxidative stress, thereby supporting overall cell integrity and function. Beyond its direct antioxidant role, zinc is also integral to the activity of numerous enzymes involved in regulating oxidative processes. As either a cofactor or a structural component of these enzymes, zinc plays a critical role in enzymatic functions that manage the body's response to oxidative stress. These enzymes are crucial in various cellular pathways, including DNA repair, protein synthesis, and immune function, all of which are vital for maintaining cellular health and preventing oxidative damage. Zinc's involvement in these enzymatic processes further underscores its importance as a protective agent against oxidative stress-related diseases. Furthermore, long-term exposure to antioxidants like zinc can modulate the body's sensitivity to oxidative stress. This means that, over time, the presence of antioxidants can fine-tune how cells detect and respond to oxidative damage. This adaptive response may lead to improved resilience against oxidative threats as cells become more efficient at mitigating the damaging effects of free radicals. However, this increased sensitivity must be carefully balanced, as an overly sensitive oxidative stress response could potentially lead to unintended consequences, such as inflammation or other cellular dysfunctions [78]. In earlier studies, plant extracts from a variety of medicinal species, including liquorice (*Glycyrrhiza lepidota*), horsetail (*Equisetum* spp.), senega (*Polygalasenega*), echinacea (*Echinacea angustifolia*), and bearberry leaves (*Arctostaphylos uva-ursi*), were found to exhibit substantial antioxidant activity. These plants, known for their traditional therapeutic uses, contain bioactive compounds that help neutralize oxidative stress, further highlighting their potential for applications in health-promoting formulations. This adds to the growing body of evidence supporting the antioxidant properties of various botanical sources [79]. The synthesized ZnO NPs from *Polygala tenuifolia* root extract exhibited moderate antioxidant activity, demonstrated by a 45.47% DPPH radical scavenging capacity at a concentration of 1 mg/mL [80]. In summary, zinc plays a pivotal role in protecting against chronic diseases linked to oxidative processes by acting as a powerful antioxidant. Its ability to reduce cellular damage, particularly in cell membranes, and its critical involvement in the function of enzymes that regulate oxidative stress make it an essential element for maintaining health. Over time, the presence of antioxidants, including zinc, can enhance the body's ability to respond to oxidative stress, offering potential therapeutic benefits in preventing and managing chronic diseases associated with oxidative damage. This natural material, with its plant-derived antioxidant properties, represents a promising tool in the fight against oxidative stress-related conditions, further solidifying the importance of antioxidants in promoting long-term health.

5.3 Anticancer activity

ZnO NPs exhibit good anticancer action because of their greater toxicity, effective cell distribution, and superior solubility compared to individual medications. As ZnO NPs concentration rises, so do the levels of inhibition and cell viability [81]. Because ZnO NPs reduce ROS formation across the cell, they can elicit significant selective toxicity against cancer cells without damaging normal cells. This disruption to the mitochondrial membrane leads to the death of cancer tissue [82, 83]. Protons migrate from the particle surface into the aqueous medium at higher pH values, leaving behind partly bonded oxygen atoms with negatively charged surfaces. Protons from the surrounding environment transfer to the particle surface at lower pH levels, which is why under healthy conditions, NPs have a significant positive surface charge [84, 85]. Metal and metal oxide NPs derived from plants have gained significant attention as promising therapeutic agents in the fight against various types of cancers [86]. These NPs possess unique properties, such as high surface area and reactivity, which make them effective in targeting and destroying cancer cells. Their biocompatibility, derived from the eco-friendly synthesis using plant extracts, also makes them appealing for cancer treatment applications. However, despite the potential benefits, a major concern regarding the use of these synthesized cytotoxic NPs is their safety. While they have shown effectiveness in killing cancer cells, one of the biggest challenges lies in their non-selective nature. Anticancer agents, including NPs, can inadvertently affect healthy cells in addition to targeting cancerous ones. This off-target effect can lead to unintended damage to normal tissues, resulting in side effects that may compromise the overall health of the patient. The balance between efficacy and safety is crucial when using plant-derived metal or metal oxide NPs in cancer therapy. While their ability to induce cancer cell death is promising, further research is needed to improve their selectivity, minimize toxicity to healthy cells, and fully understand their long-term effects on the body. Ensuring that these NPs can selectively target cancer cells without harming healthy tissues will be key to their successful development as safe and effective treatments [87]. The anti-proliferative activity of the ZnO NPs was evaluated against the human skin cancer cell line A431 using the MTT assay, a widely accepted method for measuring cell viability. This assay revealed a significant reduction in the number of viable cancer cells, demonstrating that the compound effectively inhibits the growth and proliferation of A431 cells. This result suggests that the compound has potential as a therapeutic agent in the treatment of skin cancer by impeding the uncontrolled division of cancer cells. To further investigate the mechanisms underlying this anti-proliferative effect, additional studies were conducted, including cell cycle analysis and apoptosis assays. Using flow cytometry, a powerful technique for analyzing the physical and chemical properties of cells, researchers observed that the treatment caused a disruption in the normal progression of the cell cycle. This disruption likely played a role in halting cell division, thereby contributing to the observed reduction in cell proliferation. By disrupting the cell cycle, the compound was found to induce apoptosis, a form of programmed cell death that is critical for eliminating damaged or cancerous cells. The apoptosis assay, also performed using flow cytometry, revealed clear evidence of increased membrane permeability in treated cells, which is a common indicator of apoptosis. The loss of membrane integrity allows for the entry of various dyes and markers that can be used to identify cells undergoing programmed cell death. Moreover, DNA fragmentation analysis provided further confirmation of apoptosis induction. DNA fragmentation is a characteristic feature of apoptosis, where the cell's DNA is cleaved into smaller

fragments as part of the process leading to cell death. The analysis showed prominent DNA fragmentation in A431 cells treated with the compound, underscoring its effectiveness in promoting apoptosis. This is a critical finding, as apoptosis plays a vital role in the elimination of cancer cells, and therapies that induce apoptosis are highly sought after in cancer treatment. Overall, the combination of these findings—significant anti-proliferative activity, disruption of the cell cycle, increased membrane permeability, and prominent DNA fragmentation—highlights the potential of this compound as a promising candidate for further research and development in skin cancer therapy. By promoting apoptosis and inhibiting cancer cell growth, the compound could offer new avenues for targeted treatment of skin cancer [86].

5.4 Antidiabetic activity

ZnO NPs exhibit an impressive anti-diabetic impact, especially in terms of improved glucose tolerance, lower blood sugar, increased serum insulin, decreased non-esterified fatty acids, and decreased triglycerides [88]. The involvement of zinc in the biosynthesis of insulin production and storage is well known, given its influence on the structure of the hormone. Researchers have established that certain zinc transporters, such as zinc transporter-8, play a significant role in the release of insulin from pancreatic beta cells. This operates in several ways, including enhancing insulin signaling through zinc, increasing phosphoinositide 3-kinase activity, and promoting higher phosphorylation of insulin receptors. Consequently, there is a complex link between diabetes and zinc [88]. ZnO NPs have been shown to exert a remarkable effect on managing diabetes. For instance, individuals treated with ZnO NPs demonstrate not only improved glucose tolerance but also exhibit lower blood sugar levels. Additionally, these NPs contribute to increased levels of serum insulin while simultaneously reducing non-esterified fatty acids and triglycerides. Zinc's crucial involvement in insulin biosynthesis and storage arises from its impact on the structural integrity of the hormone. Zinc transporter-8, a specific type of zinc transporter, has been identified as playing a pivotal role in the insulin release process from pancreatic beta cells. The mechanism by which zinc influences insulin and glucose metabolism includes enhancing insulin signaling pathways, increasing the activity of phosphoinositide 3-kinase, and promoting higher phosphorylation rates of insulin receptors. The interplay between zinc and diabetes is multifaceted. Zinc directly affects insulin's structural formation, which is vital for its storage and release. These findings underscore the intricate relationship between zinc and diabetes, suggesting that zinc not only supports hormone synthesis but also influences the cellular mechanisms that control blood sugar levels [69]. Thus, understanding the role of zinc and ZnO NPs could be pivotal in developing advanced treatments for diabetes management.

ZnO nanoparticles (NPs) have shown remarkable potential in the treatment of diabetes, particularly in their ability to improve various markers associated with the disease [89]. These include enhanced glucose tolerance, reduced blood sugar levels, increased serum insulin concentrations, and lowered amounts of non-esterified fatty acids and triglycerides. Such effects suggest that ZnO NPs could play a crucial role in managing diabetes, a condition characterized by impaired glucose metabolism and insulin function. One of the primary reasons behind the beneficial impact of ZnO NPs is the well-established role of zinc in the biosynthesis, storage, and regulation of insulin. Insulin, a hormone produced by pancreatic beta cells, is essential for maintaining normal blood sugar levels. Zinc is directly involved in the structural stability of insulin, ensuring that it retains its functional form. Without sufficient zinc, insulin

may lose its structural integrity, which could impair its ability to regulate blood sugar levels effectively [90]. Research has further highlighted that certain zinc transporters, such as zinc transporter-8 (ZnT8), are critically important in the process of insulin secretion from the pancreatic beta cells. ZnT8 facilitates the movement of zinc ions into these cells, where they contribute to the proper packaging and release of insulin. The involvement of ZnT8 in insulin secretion is significant because it directly influences how well the body can respond to elevated blood sugar levels after meals. Moreover, the mechanism by which zinc, and in particular ZnO NPs, exert its anti-diabetic effects extends beyond simple insulin production. Zinc enhances insulin signaling within the body, which is a crucial pathway for glucose metabolism. For example, zinc has been found to increase the activity of phosphoinositide 3-kinase (PI3K), an enzyme involved in the intracellular signaling pathway that mediates the effects of insulin. This enzyme plays a pivotal role in the uptake of glucose by cells, enabling them to utilize sugar for energy, thereby lowering blood sugar levels. Additionally, zinc promotes greater phosphorylation of insulin receptors, a process that enhances the sensitivity of cells to insulin. Phosphorylation activates these receptors, allowing cells to better respond to the presence of insulin and efficiently manage blood sugar. This is particularly important in individuals with diabetes, where insulin resistance is a common issue. By improving the body's ability to respond to insulin, ZnO NPs could potentially reverse some of the damaging effects of insulin resistance. Thus, the relationship between zinc and diabetes is complex and multifaceted, involving not only the structural role of zinc in insulin formation but also its influence on the cellular pathways that regulate glucose metabolism. The promising effects of ZnO NPs on improving insulin function and blood sugar control suggest that they could be a valuable tool in the development of more effective treatments for diabetes. Understanding the full scope of zinc's involvement in these processes may open new avenues for therapeutic strategies aimed at better management of this chronic disease.

ZnO NPs have demonstrated significant antidiabetic properties, as seen in diabetic rats treated with these NPs along with insulin. Studies show that these NPs effectively reduce blood glucose levels, indicating their ability to improve glycemic control. Additionally, treated rats exhibited higher serum insulin levels, reflecting improved insulin production or secretion. Furthermore, ZnO enhanced glucokinase activity, an enzyme that plays a key role in glucose metabolism by promoting glucose utilization in the liver. This was accompanied by an increased expression of essential genes involved in glucose regulation, including insulin, insulin receptor, GLUT-2 (a glucose transporter), and glucokinase genes. The upregulation of these genes suggests that the NPs may improve insulin sensitivity and glucose uptake in diabetic conditions. In conclusion, ZnO NPs act as potent antidiabetic agents, not only by lowering blood glucose but also by enhancing insulin production, improving glucose metabolism, and upregulating key genes involved in glucose homeostasis. These findings underscore their potential as promising therapeutic tools in managing diabetes [91].

6. Conclusions and future prospective

This chapter reveals that, biological and chemical synthesis, biological synthesis emerges as a more favorable and sustainable approach. Chemical synthesis, while effective, leads to environmental pollution, which in turn poses significant health risks to humans, making it a less desirable option. Biological synthesis is found to be simpler, cost-effective, single pot, safer, and environmentally friendly. This process

makes use of natural resources such as plants and microbes as reducing and stabilizing agents, which significantly reduces the environmental footprint. Moreover, such synthesis is particularly efficient in the production of ZnO NPs for several applications. Its reliance on biological agents allows for better control over particle size and stability, which enhances its suitability for various biomedical applications. In contrast, the chemical synthesis, which may introduce impurities or harmful by-products, makes it less ideal for sensitive applications, especially in medical or environmental fields. Biological synthesis, with its use of natural, non-toxic, and biodegradable components, offers an edge not only in safety but also in the sustainability of the process. Furthermore, this method shows great potential for producing bioactive compounds that are vital for various industrial, medicinal, and agricultural applications. Therefore, biological synthesis makes an attractive option for industries and sustainable technologies. However, despite its many advantages, there is still a need for more in-depth research to fully unravel the biochemical and molecular mechanisms involved in the synthesis of ZnO NPs by different microbes and plant products. Understanding these mechanisms in greater detail will pave the way for optimizing biological synthesis processes and expanding their applications in a wide range of fields.

Acknowledgements

The authors would like to thank the management and the director of G H Raisoni International Skill Tech University for their constant encouragement.

Funding source

No funding sources are available.

Conflict of interest

No conflict of interest was reported by authors.

Author details

Ajay Kumar Tiwari[1*], Saket Jha[2], Ram Raseele Awasthi[3], Abhimanyu Kumar Singh[4], Abhishek Kumar Bhardwaj[5] and Sharad Kumar Tripathi[6]

1 Department of Physics, GH Raisoni International Skill Tech University, Pune, India

2 Department of Surgery, University of Illinois at Chicago (UIC), Chicago, Illinois, USA

3 Faculty of Engineering and Technology, Khwaja Moinuddin Chishti Language University, Lucknow, U.P., India

4 Department of Physics, Shyama Prashad Mukherjee Govt. Degree College, University of Allahabad, Phaphamau, Prayagraj, U.P., India

5 Department of Environmental Science, Amity School of Life Sciences, Amity University, Gwalior, M.P., India

6 Department of Life Sciences, Arni University, Kangra, H.P., India

*Address all correspondence to: ajayngbv@gmail.com

IntechOpen

References

[1] Bhardwaj AK, Naraian R, Sundaram S, Kaur R. Biogenic and non-biogenic waste for the synthesis of nanoparticles and their applications. In: Bioremediation. Boca Raton, FL, USA: CRC Press; 2022. pp. 207-218. DOI: 10.1201/9781003181224

[2] Rath P, Bhardwaj LK, Yadav P, Bhardwaj AK. A synthesis of biogenic nanoparticles (NPs) for the treatment of wastewater and its application: A review. In: Biogenic Wastes-Enabled Nanomaterial Synthesis: Applications in Environmental Sustainability. Amsterdam, The Netherlands: Elsevier; 2024. pp. 127-148. DOI: 10.1007/978-3-031-59083-2_5

[3] Krężel A, Maret W. The biological inorganic chemistry of zinc ions. Archives of Biochemistry and Biophysics. 2016;**611**:3-19. DOI: 10.1016/j.abb.2016.04.010

[4] Kaur H, Garg N. Zinc toxicity in plants: A review. Planta. 2021;**253**(6):129. DOI: 10.1007/s00425-021-03642-z

[5] Bayçu G, Gevrek-Kürüm N, Moustaka J, Csatári I, Rognes SE, Moustakas M. Cadmium-zinc accumulation and photosystem II responses of Noccaeacaerulescens to Cd and Zn exposure. Environmental Science and Pollution Research. 2017;**24**:2840-2850. DOI: 10.1007/s11356-016-8048-4

[6] Alqarni LS, Alghamdi MD, Alshahrani AA, Nassar AM. Green nanotechnology: Recent research on bioresource-based nanoparticle synthesis and applications. Journal of Chemistry. 2022;**2022**(1):4030999. DOI: 10.1155/2022/4030999

[7] Sharma P, Urfan M, Anand R, Sangral M, Hakla HR, Sharma S, et al. Green synthesis of zinc oxide nanoparticles using Eucalyptus lanceolata leaf litter: Characterization, antimicrobial and agricultural efficacy in maize. Physiology and Molecular Biology of Plants. 2022;**28**(2):363-381. DOI: 10.1007/s12298-022-01136-0

[8] Tania IS, Ali M. Coating of ZnO nanoparticle on cotton fabric to create a functional textile with enhanced mechanical properties. Polymers. 2021;**13**(16):2701. DOI: 10.3390/polym13162701

[9] Sarkhosh S, Kahrizi D, Darvishi E, Tourang M, Haghighi-Mood S, Vahedi P, et al. Effect of zinc oxide nanoparticles (ZnO-NPs) on seed germination characteristics in two Brassicaceae Family species: Camelina sativa and Brassica napus L. Journal of Nanomaterials. 2022;**2022**(1):1892759. DOI: 10.1155/2022/1892759

[10] Singh N, Singh MK, Yadav RK, Azim Z. Role of green synthesized nano iron oxide in alleviating the cadmium toxicity in Brassica oleracea var. italica seedlings. Plant Nano Biology. 2023;**6**:100055. DOI: 10.1016/j.plana.2023.100055

[11] Korotcenkov G. Cd-and Zn-based wide band gap II-VI semiconductors. In: Handbook of II-VI Semiconductor-Based Sensors and Radiation Detectors: Volume 1, Materials and Technology. Cham: Springer International Publishing; 2023. pp. 21-65. DOI: 10.1007/978-3-031-19531-0_2

[12] Saeed M, Marwani HM, Shahzad U, Asiri AM, Rahman MM. Recent advances, challenges, and future perspectives of ZnO nanostructure materials towards energy

applications. The Chemical Record. 2024;**24**(1):e202300106. DOI: 10.1002/tcr.202300106

[13] Rong P, Ren S, Yu Q. Fabrications and applications of ZnO nanomaterials in flexible functional devices-a review. Critical Reviews in Analytical Chemistry. 2019;**49**(4):336-349. DOI: 10.1080/10408347.2018.1531691

[14] Bhadwal N, Ben Mrad R, Behdinan K. Review of zinc oxide piezoelectric nanogenerators: Piezoelectric properties, composite structures and power output. Sensors. 2023;**23**(8):3859. DOI: 10.3390/s23083859

[15] Borysiewicz MA. ZnO as a functional material—A review. Crystals. 2019;**9**(10):505. DOI: 10.3390/cryst9100505

[16] Aspoukeh PK, Barzinjy AA, Hamad SM. Synthesis, properties and uses of ZnO nanorods: A mini review. International Nano Letters. 2022;**12**(2):153-168. DOI: 10.1007/s40089-021-00349-7

[17] Ayoub I, Kumar V, Abolhassani R, Sehgal R, Sharma V, Sehgal R, et al. Advances in ZnO: Manipulation of defects for enhancing their technological potentials. Nanotechnology Reviews. 2022;**11**(1):575-619. DOI: 10.1515/ntrev-2022-003

[18] Galdámez-Martinez A, Santana G, Güell F, Martínez-Alanis PR, Dutt A. Photoluminescence of ZnO nanowires: A review. Nanomaterials. 2020;**10**(5):857. DOI: 10.3390/nano10050857

[19] Shankar S, Rhim JW. Effect of Zn salts and hydrolyzing agents on the morphology and antibacterial activity of zinc oxide nanoparticles. Environmental Chemistry Letters. 2019;**17**:1105-1109. DOI: 10.1007/s10311-018-00835-z

[20] Dey A, Ray PG, Dhara S, Neogi S. Optically engineered ZnO nanoparticles: Excitable at visible wavelength and lowered cytotoxicity towards bioimaging applications. Applied Surface Science. 2022;**592**:153303. DOI: 10.1016/j.apsusc.2022.153303

[21] Al-darwesh MY, Ibrahim SS, Mohammed MA. A review on plant extract mediated green synthesis of zinc oxide nanoparticles and their biomedical applications. Results in Chemistry. 2024;**7**:101368. DOI: 10.1016/j.rechem.2024.101368

[22] Tiwari AK, Jha S, Tripathi SK, Awasthi RR, Bhardwaj AK, Singh AK, et al. Antioxidant response of *Calendula officinalis* L. assisted synthesized zinc oxide nanoparticles. Materials Research Express. 2024;**11**(8):085005. DOI: 10.1088/2053-1591/ad6ca9

[23] Tiwari AK, Jha S, Tripathi SK, Shukla R, Awasthi RR, Bhardwaj AK, et al. Spectroscopic investigations of green synthesized zinc oxide nanoparticles (ZnO NPs): Antioxidant and antibacterial activity. Discover Applied Sciences. 2024;**6**(8):399. DOI: 10.1007/s42452-024-06049-z

[24] Çolak H, Karaköse E. Green synthesis and characterization of nanostructured ZnO thin films using Citrus aurantifolia (lemon) peel extract by spin-coating method. Journal of Alloys and Compounds. 2017;**690**:658-662. DOI: 10.1016/j.jallcom.2016.08.090

[25] Tiwari AK, Jha S, Agrawal R, Mishra SK, Pathak AK, Singh AK, et al. Anti-bacterial efficacy of phyto-synthesized zinc oxide nanoparticles using murraya paniculata l. leaf extract. Sciences. 2022;**4**(7):464-471. DOI: 10.13040/IJPSR.0975-8232.13(2).864-71

[26] Umavathi S, Mahboob S, GovindarajanM,Al-GhanimKA,AhmedZ, Virik P, et al. Green synthesis of ZnO nanoparticles for antimicrobial and vegetative growth applications: A novel approach for advancing efficient high quality health care to human wellbeing. Saudi Journal of Biological Sciences. 2021;**28**(3):1808-1815. DOI: 10.1016/j.sjbs.2020.12.025

[27] Eswari KM, Asaithambi S, Karuppaiah M, Sakthivel P, Balaji V, Ponelakkia DK, et al. Green synthesis of ZnO nanoparticles using abutilon Indicum and Tectona Grandis leaf extracts for evaluation of anti-diabetic, anti-inflammatory and in-vitro cytotoxicity activities. Ceramics International. 2022;**48**(22):33624-33634. DOI: 10.1016/j.ceramint.2022.07.308

[28] Thi TU, Nguyen TT, Thi YD, Thi KH, Phan BT, Pham KN. Green synthesis of ZnO nanoparticles using orange fruit peel extract for antibacterial activities. RSC Advances. 2020;**10**(40):23899-23907. DOI: 10.1039/D0RA04926C

[29] Kiani BH, Haq IU, Alhodaib A, Basheer S, Fatima H, Naz I, et al. Comparative evaluation of biomedical applications of zinc nanoparticles synthesized by using Withaniasomnifera plant extracts. Plants. 2022;**11**(12):1525. DOI: 10.3390/plants11121525

[30] Ahmad W, Kalra D. Green synthesis, characterization and anti microbial activities of ZnO nanoparticles using Euphorbia hirta leaf extract. Journal of King Saud University-Science. 2020;**32**(4):2358-2364. DOI: 10.1016/j.jksus.2020.03.014

[31] Vijayakumar S, Vaseeharan B, Malaikozhundan B, Shobiya M. Laurus nobilis leaf extract mediated green synthesis of ZnO nanoparticles: Characterization and biomedical applications. Biomedicine & Pharmacotherapy. 2016;**84**:1213-1222. DOI: 10.1016/j.biopha.2016.10.038

[32] Shahzadi T, Rehman S, Riaz T, Zaib M. Eco-friendly synthesis of ZnO nanoparticles using Cannabis sativa and assessment of its activities as efficient dyes removal and antioxidant agent. International Journal of Environmental Analytical Chemistry. 2022;**102**(16):4738-4756. DOI: 10.1080/03067319.2020.1789610

[33] Sadiq H, Sher F, Sehar S, Lima EC, Zhang S, Iqbal HM, et al. Green synthesis of ZnO nanoparticles from Syzygium Cumini leaves extract with robust photocatalysis applications. Journal of Molecular Liquids. 2021;**335**:116567. DOI: 10.1016/j.molliq.2021.116567

[34] Mandal G, Bhattacharjee B. Biosynthesis of ZnO nanoparticles using the young fruit of Borassus flabellifer: Characterization and photocatalytic removal of biohazardous safranin-O dye using solar irradiation. The Scientific Temper. 2024;**15**(02):2092-2098. DOI: 10.58414/SCIENTIFICTEMPER.2024.15.2.19

[35] Raja A, Ashokkumar S, Marthandam RP, Jayachandiran J, Khatiwada CP, Kaviyarasu K, et al. Eco-friendly preparation of zinc oxide nanoparticles using Tabernaemontana divaricata and its photocatalytic and antimicrobial activity. Journal of Photochemistry and Photobiology B: Biology. 2018;**181**:53-58. DOI: 10.1016/j.jphotobiol.2018.02.011

[36] Shabaani M, Rahaiee S, Zare M, Jafari SM. Green synthesis of ZnO nanoparticles using loquat seed extract; biological functions and photocatalytic degradation properties. Lwt. 2020;**134**:110133. DOI: 10.1016/j.lwt.2020.110133

[37] Sarkar T, Kundu S, Ghorai G, Sahoo PK, Bhattacharjee A. Structural, spectroscopic and morphology studies on green synthesized ZnO nanoparticles. Advances in Natural Sciences: Nanoscience and Nanotechnology. 2023;**14**(3):035001. DOI: 10.1088/2043-6262/acd8b6

[38] Gupta M, Tomar RS, Kaushik S, Mishra RK, Sharma D. Effective antimicrobial activity of green ZnO nano particles of Catharanthus roseus. Frontiers in Microbiology. 2018;**9**:2030. DOI: 10.3389/fmicb.2018.02030

[39] Donga S, Chanda S. Caesalpinia crista seeds mediated green synthesis of zinc oxide nanoparticles for antibacterial, antioxidant, and anticancer activities. BioNanoScience. 2022;**12**(2):451-462. DOI: 10.1007/s12668-022-00952-8

[40] Nagajyothi PC, Sreekanth TV, Tettey CO, Jun YI, Mook SH. Characterization, antibacterial, antioxidant, and cytotoxic activities of ZnO nanoparticles using Coptidis Rhizoma. Bioorganic & Medicinal Chemistry Letters. 2014;**24**(17):4298-4303. DOI: 10.1016/j.bmcl.2014.07.023

[41] Jain D, Shivani BAA, Singh H, Daima HK, Singh M, Mohanty SR, et al. Microbial fabrication of zinc oxide nanoparticles and evaluation of their antimicrobial and photocatalytic properties. Frontiers in Chemistry. 2020;**8**:778. DOI: 10.3389/fchem.2020.00778

[42] Mohd Yusof H, Mohamad R, Zaidan UH, Rahman NA. Sustainable microbial cell nanofactory for zinc oxide nanoparticles production by zinc-tolerant probiotic lactobacillus plantarum strain TA4. Microbial Cell Factories. 2020;**19**:1-7. DOI: 10.1186/s12934-020-1279-6

[43] Ahmed T, Wu Z, Jiang H, Luo J, Noman M, Shahid M, et al. Bioinspired green synthesis of zinc oxide nanoparticles from a native Bacillus cereus strain RNT6: Characterization and antibacterial activity against rice panicle blight pathogens Burkholderiaglumae and B. Gladioli. Nanomaterials. 2021;**11**(4):884. DOI: 10.3390/nano11040884

[44] Suba S, Vijayakumar S, Vidhya E, Punitha VN, Nilavukkarasi M. Microbial mediated synthesis of ZnO nanoparticles derived from lactobacillus spp: Characterizations, antimicrobial and biocompatibility efficiencies. Sensors International. 2021;**2**:100104. DOI: 10.1016/j.sintl.2021.100104

[45] Shanmugasundaram T, Balagurunathan R. Bio-medically active zinc oxide nanoparticles synthesized by using extremophilic actinobacterium, Streptomyces sp.(MA30) and its characterization. Artificial Cells, Nanomedicine, and Biotechnology. 2017;**45**(8):1521-1529. DOI: 10.1080/21691401.2016.1260577

[46] Kalaba MH, Moghannem SA, El-Hawary AS, Radwan AA, Sharaf MH, Shaban AS. Green synthesized ZnO nanoparticles mediated by Streptomyces plicatus: Characterizations, antimicrobial and nematicidal activities and cytogenetic effects. Plants. 2021;**10**(9):1760. DOI: 10.3390/plants10091760

[47] Siddique K, Shahid M, Shahzad T, Mahmood F, Nadeem H, Saif ur Rehman M, et al. Comparative efficacy of biogenic zinc oxide nanoparticles synthesized by Pseudochrobactrum sp. C5 and chemically synthesized zinc oxide nanoparticles for catalytic degradation of dyes and wastewater treatment. Environmental Science and Pollution Research. 2021;**28**:28307-28318. DOI: 10.1007/s11356-021-12575-9

[48] Rajivgandhi G, Gnanamangai BM, Prabha TH, Poornima S, Maruthupandy M, Alharbi NS, et al. Biosynthesized zinc oxide nanoparticles (ZnO NPs) using actinomycetes enhance the anti-bacterial efficacy against K. Pneumoniae. Journal of King Saud University-Science. 2022;**34**(1):101731. DOI: 10.1016/j.jksus.2021.101731

[49] Es-haghi A, Soltani M, Karimi E, Namvar F, Homayouni-Tabrizi M. Evaluation of antioxidant and anticancer properties of zinc oxide nanoparticles synthesized using aspergillus Niger extract. Materials Research Express. 2019;**6**(12):125415. DOI: 10.1088/2053-1591/ab5f72

[50] Gao Y, Arokia Vijaya Anand M, Ramachandran V, Karthikkumar V, Shalini V, Vijayalakshmi S, et al. Biofabrication of zinc oxide nanoparticles from aspergillus Niger, their antioxidant, antimicrobial and anticancer activity. Journal of Cluster Science. 2019;**30**:937-946. DOI: 10.1007/s10876-019-01551-6

[51] Li JF, Rupa EJ, Hurh J, Huo Y, Chen L, Han Y, et al. Cordyceps militaris fungus mediated zinc oxide nanoparticles for the photocatalytic degradation of methylene blue dye. Optik. 2019;**183**:691-697. DOI: 10.1016/j.ijleo.2019.02.081

[52] Mohamed AA, Fouda A, Abdel-Rahman MA, Hassan SE, El-Gamal MS, Salem SS, et al. Fungal strain impacts the shape, bioactivity and multifunctional properties of green synthesized zinc oxide nanoparticles. Biocatalysis and Agricultural Biotechnology. 2019;**19**:101103. DOI: 10.1016/j.bcab.2019.101103

[53] Abdelhakim HK, El-Sayed ER, Rashidi FB. Biosynthesis of zinc oxide nanoparticles with antimicrobial, anticancer, antioxidant and photocatalytic activities by the endophytic Alternaria tenuissima. Journal of Applied Microbiology. 2020;**128**(6):1634-1646. DOI: 10.1111/jam.14581

[54] Fouda A, Salem SS, Wassel AR, Hamza MF, Shaheen TI. Optimization of green biosynthesized visible light active CuO/ZnO nano-photocatalysts for the degradation of organic methylene blue dye. Heliyon. 2020;**6**(9):1-13, e04896. DOI: 10.1016/j.heliyon.2020.e04896

[55] Ganesan V, Hariram M, Vivekanandhan S, Muthuramkumar S. Periconiumsp. (endophytic fungi) extract mediated sol-gel synthesis of ZnO nanoparticles for antimicrobial and antioxidant applications. Materials Science in Semiconductor Processing. 2020;**105**:104739. DOI: 10.1016/j.mssp.2019.104739

[56] Singh A, Dutta PK. Green synthesis, characterization and biological evaluation of chitin glucan based zinc oxide nanoparticles and its curcumin conjugation. International Journal of Biological Macromolecules. 2020;**156**:514-521. DOI: 10.1016/j.ijbiomac.2020.04.081

[57] Shobha B, Lakshmeesha TR, Ansari MA, Almatroudi A, Alzohairy MA, Basavaraju S, et al. Mycosynthesis of ZnO nanoparticles using Trichoderma spp. isolated from rhizosphere soils and its synergistic antibacterial effect against Xanthomonas oryzae pv. Oryzae. Journal of Fungi. 2020;**6**(3):181. DOI: 10.3390/jof6030181

[58] Ogunyemi SO, Abdallah Y, Zhang M, Fouad H, Hong X, Ibrahim E, et al. Green synthesis of zinc oxide nanoparticles using different plant extracts and their antibacterial activity against Xanthomonas oryzae pv. Oryzae. Artificial Cells, Nanomedicine, and

Biotechnology. 2019;**47**(1):341-352. DOI: 10.1080/21691401.2018.1557671

[59] Ameen F, Dawoud T, AlNadhari S. Ecofriendly and low-cost synthesis of ZnO nanoparticles from Acremonium potronii for the photocatalytic degradation of azo dyes. Environmental Research. 2021;**202**:111700. DOI: 10.1016/j.envres.2021.111700

[60] Karnan T, Selvakumar SA. Biosynthesis of ZnO nanoparticles using rambutan (Nephelium lappaceumL.) peel extract and their photocatalytic activity on methyl orange dye. Journal of Molecular Structure. 2016;**1125**:358-365. DOI: 10.1016/j.molstruc.2016.07.029

[61] Sharma SC. ZnO nano-flowers from Carica papaya milk: Degradation of alizarin red-S dye and antibacterial activity against Pseudomonas aeruginosa and Staphylococcus aureus. Optik. 2016;**127**(16):6498-6512. DOI: 10.1016/j.ijleo.2016.04.036

[62] Mekky AE, Farrag AA, Hmed AA, Sofy AR. Preparation of zinc oxide nanoparticles using aspergillus Niger as antimicrobial and anticancer agents. Journal of Pure and Applied Microbiology. 2021;**15**(3):1547-1566. DOI: 10.22207/JPAM.15.3.49

[63] Narayanan PM, Wilson WS, Abraham AT, Sevanan M. Synthesis, characterization, and antimicrobial activity of zinc oxide nanoparticles against human pathogens. BioNanoScience. 2012;**2**:329-335. DOI: 10.1007/s12668-012-0061-6

[64] Qi WH, Wang MP. Size and shape dependent lattice parameters of metallic nanoparticles. Journal of Nanoparticle Research. 2005;**7**:51-57. DOI: 10.1007/s11051-004-7771-9

[65] Kumar A, Dixit CK. Methods for characterization of nanoparticles. In: Advances in Nanomedicine for the Delivery of Therapeutic Nucleic Acids. New Delhi: Woodhead Publishing; 2017. pp. 43-58. DOI: 10.1016/B978-0-08-100557-6.00003-1

[66] Sathishkumar M, Sneha K, Won SW, Cho CW, Kim S, Yun YS. Cinnamon zeylanicum bark extract and powder mediated green synthesis of nano-crystalline silver particles and its bactericidal activity. Colloids and Surfaces B: Biointerfaces. 2009;**73**(2):332-338. DOI: 10.1016/j.colsurfb.2009.06.005

[67] Sirelkhatim A, Mahmud S, Seeni A, Kaus NH, Ann LC, Bakhori SK, et al. Review on zinc oxide nanoparticles: Antibacterial activity and toxicity mechanism. Nano-Micro Letters. 2015;**7**:219-242. DOI: 10.1007/s40820-015-0040-x

[68] Emami-Karvani Z, Chehrazi P. Antibacterial activity of ZnO nanoparticle on gram-positive and gram-negative bacteria. African Journal of Microbiology Research. 2011;**5**(12):1368-1373. DOI: 10.5897/AJMR10.159

[69] Agarwal H, Nakara A, Shanmugam VK. Anti-inflammatory mechanism of various metal and metal oxide nanoparticles synthesized using plant extracts: A review. Biomedicine & Pharmacotherapy. 2019;**109**:2561-2572. DOI: 10.1016/j.biopha.2018.11.116

[70] Aderibigbe BA. Zinc oxide nanoparticles in biomedical applications: Advances in synthesis, antimicrobial properties, and toxicity considerations. In: Nanoparticles in Modern Antimicrobial and Antiviral Applications. Cham: Springer International Publishing; 2024. pp. 119-149. DOI: 10.1007/978-3-031-50093-0_6

[71] Motelica L, Vasile BS, Ficai A, Surdu AV, Ficai D, Oprea OC, et al.

Influence of the alcohols on the zno synthesis and its properties: The photocatalytic and antimicrobial activities. Pharmaceutics. 2022;**14**(12):2842. DOI: 10.3390/pharmaceutics14122842

[72] Nikolova MP, Chavali MS. Metal oxide nanoparticles as biomedical materials. Biomimetics. 2020;**5**(2):27. DOI: 10.3390/biomimetics5020027

[73] Fontecha-Umaña F, Ríos-Castillo AG, Ripolles-Avila C, Rodríguez-Jerez JJ. Antimicrobial activity and prevention of bacterial biofilm formation of silver and zinc oxide nanoparticle-containing polyester surfaces at various concentrations for use. Food. 2020;**9**(4):442. DOI: 10.3390/foods9040442

[74] Souza RC, Haberbeck LU, Riella HG, Ribeiro DH, Carciofi BA. Antibacterial activity of zinc oxide nanoparticles synthesized by solochemical process. Brazilian Journal of Chemical Engineering. 2019;**36**:885-893. DOI: 10.1590/0104-6632.20190362s20180027

[75] Pasquet J, Chevalier Y, Pelletier J, Couval E, Bouvier D, Bolzinger MA. The contribution of zinc ions to the antimicrobial activity of zinc oxide. Colloids and Surfaces A: Physicochemical and Engineering Aspects. 2014;**457**:263-274. DOI: 10.1016/j.colsurfa.2014.05.057

[76] Dobrucka R, Długaszewska J. Biosynthesis and antibacterial activity of ZnO nanoparticles using Trifolium pratense flower extract. Saudi Journal of Biological Sciences. 2016;**23**(4):517-523. DOI: 10.1016/j.sjbs.2015.05.016

[77] Popescu T, Matei CO, Vlaicu ID, Tivig I, Kuncser AC, Stefan M, et al. Influence of surfactant-tailored Mn-doped ZnO nanoparticles on ROS production and DNA damage induced in murine fibroblast cells. Scientific Reports. 2020;**10**(1):18062. DOI: 10.1038/s41598-020-74816-0

[78] Stan M, Popa A, Toloman D, Silipas TD, Vodnar DC. Antibacterial and antioxidant activities of ZnO nanoparticles synthesized using extracts of Allium sativum, Rosmarinus officinalis and Ocimumbasilicum. Acta MetallurgicaSinica (English Letters). 2016;**29**:228-236. DOI: 10.1007/s40195-016-0380-7

[79] Nagajyothi PC, Cha SJ, Yang IJ, Sreekanth TV, Kim KJ, Shin HM. Antioxidant and anti- inflammatory activities of zinc oxide nanoparticles synthesized using Polygala tenuifolia root extract. Journal of Photochemistry and Photobiology B: Biology. 2015;**146**:10-17. DOI: 10.1016/j.jphotobiol.2015.02.008

[80] Danet AF. Recent Advances in Antioxidant Capacity Assays. London, UK: IntechOpen; 2021. DOI: 10.5772/intechopen.96654

[81] Zhao CY, Tan SX, Xiao XY, Qiu XS, Pan JQ, Tang ZX. Effects of dietary zinc oxide nanoparticles on growth performance and antioxidative status in broilers. Biological Trace Element Research. 2014;**160**:361-367. DOI: 10.1007/s12011-014-0052-2

[82] Jiang J, Pi J, Cai J. The advancing of zinc oxide nanoparticles for biomedical applications. Bioinorganic Chemistry and Applications. 2018;**2018**:1-18. DOI: 10.1155/2018/1062562

[83] Cruz DM, Mostafavi E, Vernet-Crua A, Barabadi H, Shah V, Cholula-Díaz JL, et al. Green nanotechnology-based zinc oxide (ZnO) nanomaterials for biomedical applications: A review. Journal of

Physics: Materials. 2020;**3**(3):034005. DOI: 10.1088/2515-7639/ab8186

[84] Akintelu SA, Folorunso AS. A review on green synthesis of zinc oxide nanoparticles using plant extracts and its biomedical applications. BioNanoScience. 2020;**10**(4):848-863. DOI: 10.1007/s12668-020-00774-6

[85] Mishra PK, Mishra H, Ekielski A, Talegaonkar S, Vaidya B. Zinc oxide nanoparticles: A promising nanomaterial for biomedical applications. Drug Discovery Today. 2017;**22**(12):1825-1834. DOI: 10.1016/j.drudis.2017.08.006

[86] Vidhya E, Vijayakumar S, Prathipkumar S, Praseetha PK. Green way biosynthesis: Characterization, antimicrobial and anticancer activity of ZnO nanoparticles. Gene Reports. 2020;**20**:100688. DOI: 10.1016/j.genrep.2020.100688

[87] Hanan NA, Chiu HI, Ramachandran MR, Tung WH, Mohamad Zain NN, Yahaya N, et al. Cytotoxicity of plant-mediated synthesis of metallic nanoparticles: A systematic review. International Journal of Molecular Sciences. 2018;**19**(6):1725. DOI: 10.3390/ijms19061725

[88] Wiesmann N, Tremel W, Brieger J. Zinc oxide nanoparticles for therapeutic purposes in cancer medicine. Journal of Materials Chemistry B. 2020;**8**(23):4973-4989. DOI: 10.1039/D0TB00739K

[89] Jagessar RC. Antioxidant properties of plant extracts. Pharmaceutica Analytica Acta. 2019;**1**:18-21. DOI: 10.33805/2689-9477.105

[90] Vinotha V, Iswarya A, Thaya R, Govindarajan M, Alharbi NS, Kadaikunnan S, et al. Synthesis of ZnO nanoparticles using insulin-rich leaf extract: Anti-diabetic, antibiofilm and anti-oxidant properties. Journal of Photochemistry and Photobiology B: Biology. 2019;**197**:111541. DOI: 10.1016/j.jphotobiol.2019.111541

[91] Alkaladi A, Abdelazim AM, Afifi M. Antidiabetic activity of zinc oxide and silver nanoparticles on streptozotocin-induced diabetic rats. International Journal of Molecular Sciences. 2014;**15**(2):2015-2023. DOI: 10.3390/ijms15022015

Chapter 3

ZnO Nanoparticles as a Catalyst for Water Purification

Maryam Basit, Muhammad Aftab Akram, Mohsin Saleem, Sofia Javed and Jung-Hyuk Koh

Abstract

The organic pollutants in industrial water require an effective and environment friendly approach to degrade. The major concern of textile industry is the synthetic dyes. Dyes are carcinogenic persistent organic pollutants and pose a huge threat to the aquatic life, hence destroying the ecosystem. The transition metal oxides are used as the photocatalyst to degrade them effectively at low cost. ZnO NPs has outstanding properties such as cost effectiveness, non-toxicity, structural variations, and capability of complete mineralization of organic pollutant making them ideal candidate for the photocatalytic degradation. However, the limiting factor of ZnO is the constrained photocatalytic reduced in visible light. This chapter investigates conventional and modern synthesis techniques with their consequent effects on the crystal growth, band gap, surface area, particle size, morphology, and the effect on the photocatalytic activity. This chapter discusses in detail the impact of doping with different elements, semiconductors, and supporting materials with the insight of the photocatalytic mechanism. Moreover, the degradation of azo dyes under visible light is studied. The parameters such as catalyst dose, radiation source, dye concentration, redox reaction duration, rate of reaction, and kinetics of photocatalytic activity have been studied in detail. The chapter also gives the insight into the current challenges and future prospectives of ZnO as a photocatalyst.

Keywords: photocatalysts, water purification, ZnO nanostructures, green synthesis, co-doping effects

1. Introduction

1.1 Overview of ZnO nanoparticles

The growing need for energy and a clean environment is a challenge for a modern man in the twentieth century and poses more significant arguments worldwide than ever. The growing industry at the global level has threatened both humans and animals. A lot of pollutants are pushed into the atmosphere daily [1]. Through the lens of this situation, the necessity of pure water and green energy is growing daily. According to the 2030 Agenda for Sustainable Development, the United Nations acknowledged the importance of environmental management of water and sanitation in Sustainable Development Goal 6 and the provision to shift to greener energy in Sustainable Development Goal 7 [2].

There are three fundamental approaches for degrading persistent organic pollutants (POPs) and dyes in water effluents: chemical, biological, and physical. The chemical approach encompasses ozonation, Fenton's reagent, and photocatalytic degradation. In contrast, the biological methodology includes fungal and anaerobic degradation, and the physical technique uses adsorption, filtration, ion exchange, and coagulation to remove pollutants [3]. The chemical approach uses advanced oxidation processes (AOPs), which involve highly reactive chemicals that decompose POPs and stubborn dyes [4].

Many scientists are trying to develop new and improved methods to treat contaminated water for significant water recycling. Compared to the rest of the wastewater treatment, photocatalysis has many upsides, as it is cost-effective and does not involve any secondary pollutants. Photocatalysis stands out in degrading organic contaminants due to the easy rector setup, no intermediate pollutants, and minimization of by-products. The photocatalysts have been well-studied for water treatment and spilling for the last few decades. Numerous researchers have investigated and developed new photocatalysts that are highly effective for water splitting to generate green energy, degrading POPs and organic dyes. The most common, durable, and effective photocatalyst reported in multiple studies is TiO_2 [5, 6]. ZnO has shown better performance due to the unique properties of high conductivity, non-toxic nature, tailored bandgap, and cost-effectiveness [4–7], as well as thermal and chemical stability [8–10].

It offers numerous morphologies in different dimensions [11]. 3-D nanostructures such as snowflakes [12, 13], flowers [14–16], dandelions [17, 18], and coniferous urchins-like structures [7, 19–21]; 2-D nanostructures such as nanosheets [22, 23] and nano-pellets [24, 25], 1-D nanostructures such as nanoneedles [26, 27], nanowires [28–30], and nanorods [31–33]; and 0-D nanostructures such as nanospheres [34, 35] are reported in various studies [36, 37]. The modification in the nanostructure has been reported as a better photocatalyst due to improved mechanical strength and charge mobility. Numerous studies have been carried out on the doping and decoration of ZnO with different metals, metal oxides, and carbon-based nanostructures [38–42]. This chapter discusses the pros of ZnO over other transition metal dichalcogenides (TMDs) as a photocatalyst. Modifications in ZnO nanostructures are studied by doping and decorating metals and non-metals. The heterojunction nanocomposites of ZnO are developed to enhance the photocatalytic performance in visible light. The synthesis technique, morphological changes, structural modification, optical properties, and photocatalytic studies of ZnO are discussed intensively in this chapter, providing detailed insight into the possible changes in photodegradation mechanisms.

1.1.1 Background

Photo means light, and catalyst refers to the materials which significantly reduce the activation energy of the reaction, hence increasing the rate of reaction. The photocatalyst increases the reaction rate in the presence of an optimized wavelength of light. In 1911, Alexander Eibner, a German chemist, experimented on Prussian blue with ZnO under UV light [43]. Later, in 1972, Fukushima and Honda discovered the photocatalytic effect of the TiO_2 electrodes under UV light [44]. Numerous research has been conducted to reduce carbon dioxide, degrade multiple pollutants, and generate green energy by exploiting the photocatalytic properties of semiconductors [45–47]. There are two types of photocatalysts: heterogeneous and homogeneous. The homogeneous photocatalyst is in the same phase as the reactant, whereas the heterogeneous photocatalyst is in a different phase than the reactant [48].

The heterogeneous photocatalysts are well investigated due to the better minimization capability of the POPs. These are mostly transition metal oxide semiconductors with an optimal bandgap to absorb the light. This absorption will generate a redox reaction on the surface of the photocatalyst, which will break the stubborn bonds of pollutants and degrade them effectively [49].

Transition metal oxides (TMO) show distinct optical and electronic properties with an effective number of reactive sites on the surface of nanoparticles. It allows them to absorb light and make explicit numbers of excitons, which initiate the photocatalytic reaction to degrade the organic pollutants, and under specific conditions, it can split water. Their environment-friendly nature, non-toxicity, high stability, cost-effectiveness, and high mechanical strength make them highly suitable for multiple applications [50]. The electron-hole pair will be generated when the light falls into the TMO semiconductor. The hydroxyl radicals (OH-) and superoxide ions (*O-2) are generated as the pollutants are adsorbed on the surface of the photocatalysts, which results in degradation [51]. ZnO [11, 46, 52], TiO_2 [8, 53], CeO_2 [54], CuO [55], SnO_2 [56, 57], WO_3 [58], Nb_2O_5 [59–61], and numerous others are explored in photocatalytic studies. ZnO and TiO_2 stand out due to their better comparability to sunlight absorption. ZnO provides higher quantum efficiency and is a cheaper source for large-scale photocatalytic water treatments.

Man has always been fascinated by colors regardless of their origin. Dyes are the major component of colors in leather, textile, cosmetics, paint, food, paper, and plastic industries but are not limited to these industries [62, 63]. The chromophore, auxochromes, and the length of the conjugating bond between them in organic dyes are primary components of the appearance of color. The length of the conjugating bond is increased with the increase in electron realization of auxochromes with an increase in electron withdrawal of chromophore, resulting in the variation of the color in different dyes [64, 65]. There are numerous chemical structures of dyes and multiple sources (natural or synthetic) and various compatibility levels with the fiber. Azo dyes are the foremost component of industrial dyes. Azo dyes are categorized as anionic and cationic dyes. **Table 1** describes the properties of Azo dyes used in textile industry They have chromophores with at least one nitrogen atom attached to an aromatic ring [66].

Anionic dyes have the sulfonic or carboxylic acid groups, which react with the positively charged ions in the aqueous medium. They are effective in acidic mediums due to the access presence of negative ions (O- anionic group). These dyes are effective in acidic mediums, which is why they are also called acidic dyes. Anionic dyes have electron affinity with positively charged proteins in natural fibers [67]. Methyl orange (I, II), methyl red (MR), congo red (CR), and indigo carmine (IC) are included in this category [68].

Cationic dyes have N+ ions that interact with negatively charged ions in an aqueous medium. They react to the negative components in the surfaces. Unlike anionic dyes, these dyes are effective in basic mediums. This class includes rhodamine-B (Rh-B), methylene blue (MB), basic red-18, basic red-46, crystal violet, and malachite green (MG) [64, 69]. Out of thousands of azo dyes, 130 are reported as carcinogenic. Some can cause increased heart rate, cyanosis, tissue necrosis, vomiting, skin irritation, and allergic dermatitis in humans. These dyes are very stable in an environment, making them challenging to degrade without generating intermediate pollutants. These intermediates are even more stubborn to decomposition and require advanced oxidation processes (AOPs) for further degradation, which includes the highly reactive chemicals for the breakdown. Photocatalysts are an effective solution to these issues as

Categorization	Nomenclature	Chemical Formula	Structural Formula	Molecular Weight (g/mol)	λmax (nm)	Adverse Effects
Anionic dyes	Methyl Orange (MO)	$C_{14}H_{14}N_3NaO_3S$		327.33	464	Carcinogenic, genotoxic, mutagenic, may cause gastrointestinal irritation [22]
	Methyl Red (MR)	$C_{15}H_{15}N_3O_2$		269.29	409	Irritation, allergic reaction, Respiratory Irritation, gastrointestinal irritation [22]
	Congo Red (CR)	$C_{32}H_{22}N_6Na_2O_6S_2$		696.66	497	Carcinogenic, mutagenic, neurotoxic [22]
	Indigo Carmine (IC)	$C_{16}H_8N_2Na_2O_8S_2$		466.36	610	Skin irritant, can cause hypertension and gastrointestinal disorders [22]
Cationic dyes	Rhodamine-B (Rh-B)	$C_{28}H_{31}ClN_2O_3$		479.02	554	Carcinogenic, neurotoxic, may cause skin and gastrointestinal irritation [23]
	Methylene Blue (MB)	$C_{16}H_{18}ClN_3S$		319.85	665	Carcinogenic, adverse effects on lymphoid organs and kidneys [23]
	Basic Red-18	$C_{19}H_{25}Cl_2N_5O_2$		426.34	509	Highly carcinogenic, gastrointestinal disorders, mutagenic, teratogenic, respiratory and orgain (liver and kidneys) toxicity [23]
	Basic Red-46	$C_{18}H_{21}BrN_6$		401.3	530	Carcinogenic, allergic Reactions, respiratory toxicity [23]
	Crystal Violet	$C_{25}N_3H_{30}Cl$		407.979	590	Respiratory toxicity, gastrointestinal distress, carcinogenicity, mutagenic, genotoxicity [23]
	Malachite Green (MG)			364.91	618	Carcinogenic, mutagenic, teratogenic, respiratory toxicity [23]

Table 1.
The properties of Azo dyes used in textile industry.

they degrade these dyes at low cost with maximum minimization of the organic pollutants. **Table 1** represent the properties of Azo dyes used in textile industry.

1.1.2 Significance as a catalyst

TMO semiconductor ZnO is extensively used in photocatalytic reactions due to its ability to generate an exciton pair upon exposure to light [70]. It has a band gap of 3.37 eV. ZnO conduction band (CB) is at −0.5 V vs. NHE, which is more negative than the redox potential of O_2/O_2^- -0.33 V vs. NHE. Consequently, the O_2 ready level is reduced to O_2^-. Moreover, the valance band is more positive +2.7 V vs. NHE than the redox potential of OH/H_2O (+2.53 V vs. NHE). The difference is responsible for the generation of hydroxyl radicals, as the holes in the valence band can oxidize the water molecule [71]. Besides the redox potential, ZnO has higher visible transmission, high charge mobility, high chemical and thermal stability, and a lesser environmental signature [72]. ZnO is an effective candidate for excessive use in water treatments and green energy generation [73]. The higher density of crystal defects on the interfaces and the surface of ZnO nanoparticles surges the photocatalytic redox reaction [74]. ZnO crystallite size, hexagonal wurtzite crystal structure, huge surface area, the porosity of the nanoparticles, phase purity, and dopant type are major components for the effective photocatalytic decomposition of the organic pollutants.

2. Synthesis of ZnO nanoparticles

The variation in particle size, phase difference, grain boundaries, crystallinity, lattice defects, and morphology of ZnO nanoparticles is reported to affect the band gap, charge separation, exciton recombination rates, and interface reactive sites [11, 75, 76]. Hence, the synthesis approach highly influences the photocatalytic properties.

Commonly, synthesis techniques are divided into two general approaches. The top-down physically breaks down the bulk material into small nanoparticles through mechanical milling, sputtering, laser ablation, etching, and lithography. At the same time, the bottom-up technique uses self-assembly, nucleation, and growth mechanisms in the presence of ions and bonds chemically, which include solution-based approaches such as sol-gel, co-precipitation, hydrothermal, combustion, microemulsion, chemical reduction, microwave-assisted, and green synthesis.

Morphological changes occur in ZnO nanoparticles due to synthesis techniques and parameter optimization variations. ZnO is reported to create numerous morphologies, including nanoflowers, nanorods, nanowires, nanoribbons, nano tetra-pods, nanospheres, and nanobelts [11, 77]. The effects of different synthesis methods on the photocatalytic activity of ZnO nanoparticles and their composites are difficult to describe in the following section. **Figure 1** illustrates the summary of the synthesis techniques.

2.1 Conventional techniques for the synthesis of ZnO NPs

2.1.1 Precipitation synthesis

The co-precipitation method is affordable, easy to handle, and energy efficient and offers a high purity of nanoparticles. Due to the low temperature and pressure conditions, the large-scale synthesis of TMO nanoparticles is possible, with better control

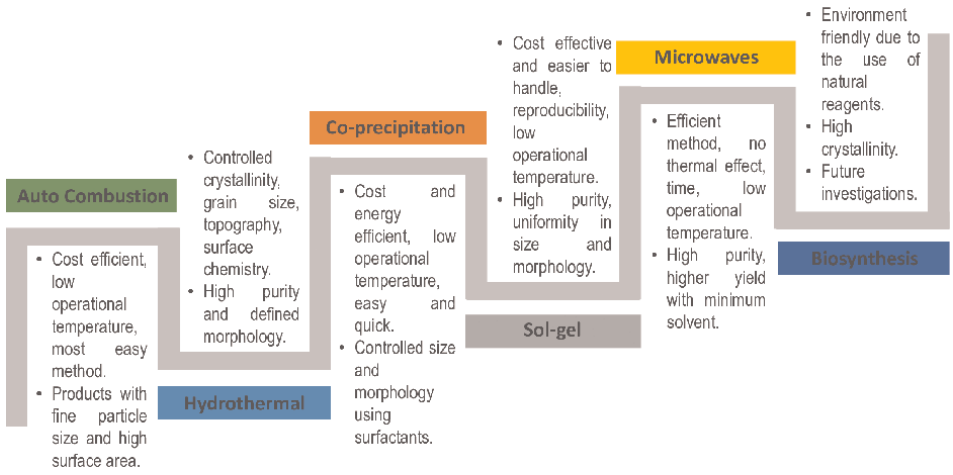

Figure 1.
Summary of the conventional and green synthesis techniques.

over the size and morphology with a sight change in the surfactants and dopants [78–81].

Lad et al. used zinc acetate dihydrate and zinc nitrate hexahydrate as precursors for synthesizing ZnO NPs [82]. Both the salts show well-arranged hexagonal structures in XRD peaks. The bandgap is reported as 2.6 and 2.915 eV for acetate and nitrate salts, respectively. At the same time, the quasi-spherical structure by acetate and ellipsoid by nitrate precursor lattice structure is observed in HD-TEM. MB was degraded under solar radiation up to 96.38 and 94.58% in 2 hours with acetate and nitrate salts, respectively. The higher photocatalytic response with acetate precursors is because of the lower band gap and higher oxygen defects in the ZnO nanostructures with an increased number of reactive sites on the surface.

Krobthong et al. compared the co-precipitation and combustion routes for the ZnO NPs structural and photocatalytic properties [83]. Both synthesis techniques give XRD peaks of hexagonal crystal structure with different crystallite sizes. The co-precipitation produces 45.5 nm crystallite sized nanoparticles, whereas the combustion synthesis gives 10.4 nm. The bigger crystallite size is due to the longer nucleation reaction in the precipitation method. Despite the size of the co-precipitation technique, it reduced the band gap by 3.18 eV compared to the combustion route which was 3.3 eV. The precipitation technique offers 90% photodegradation of MB, whereas the combustion gives 40% decay under UV light in an hour. The deviation in the band gap is attributed to crystal defects, lattice dislocations, oxygen vacancies, and impurities generated during the synthesis. The increased photocatalytic activity is due to the reduced band gap.

2.1.2 Sol-gel synthesis

Sol-gel has many benefits, including low cost, ease of handling, high reproducibility, low reaction temperatures, and better control over the surface morphology of synthesized ZnO NPs. Nanoparticles' uniform shape and size can be achieved with remarkably high purity [84–87].

Saravanan et al. synthesized ZnO NPs using zinc acetate as precursor salt and NaOH as a reducing agent by sol-gel method. Later, the ZnO NPs were calcinated for

30 minutes at 450°C [88]. The XRD peaks conformed to the hexagonal wurtzite crystal structure with the crystallite size of 16 nm. The synthesized ZnO NPs have an average particle size of 30–35 nm, with a band gap of 3.48 eV and a surface area of 10.5 m^2/g. Further testing by TEM reveals the uniform nanospheres. MO and MB were photo-decayed under UV light for 2 hours, up to 63 and 99%, respectively. The comparison is built with the thermal decomposition and co-precipitation synthesis methods, and it learned that the sol-gel prepared nanoparticles are more photocatalytic due to their high crystallinity and huge surface area.

M. Lal et al. prepared the ZnO NPs by sol-gel assisted with ultrasonic hydrothermal method at different temperatures (90, 190, and 550°C) [89]. The particle size increases with temperature whereas, the band gap is not significantly changed. Rh-B is degraded under UV-C up to 95% in 70 min by the sample prepared at 90°C. The higher degradation efficiency is due to higher surface area at the respective synthesis temperature.

2.1.3 Microwave-assisted synthesis

Scientists synthesize new nano-compounds using microwave assistance to speed up the reaction rate. This simple technique has no thermal effects and produces a highly pure product. It involves less reaction time and generates high yields [90–92].

Arellano-Cortaza et al. prepared ZnO NPs exploiting microwaves with various pHs of 5, 7, 8, 10, and 12 [93]. The pH of solutions was achieved by using a 4-molar solution of NaOH and KOH. The reaction mixtures were exposed to 400 W microwaves for 10 minutes; afterward, they were dried at 80°C for 12 hours. The band gap decreased with the increase in the pH values, whereas the surface area increased. Despite the reduction in particle size, the photocatalytic activity decreases with pH compared to the acidic pH samples or near isoelectric point pH. MB and Rh-B were degraded at 99% and 98% under UV light for 240 minutes by the sample prepared at pH 5. The high photocatalytic activity is due to the availability of reactive sites on the surface of ZnO NPs.

Ahammed et al. used ascorbic acid and PVA to encapsulate ZnO NPs synthesized by microwave-assisted growth [94]. The researcher explored the effects of capping agents and microwaves on crystal structure and photocatalytic properties. The lattice size of 22 nm and particle from 70 to 90 nm is observed with hexagonal phase peaks in XRD. The bandgap of the prepared sample is 3.35 eV. About 98% MB is photo—decayed within 210 minutes under solar light. The higher efficiency is achieved due to better charge separation and higher radical production during illumination.

From the above discussion, the direct influence of the synthesis method is evident in the photocatalytic activity of the nanoparticles. The choice of method, precursor, pH, temperature, and pressure optimization influence the material design. These parameters determine the morphology, surface area, bandgap, recombination rate, reactive site on the surface, and crystallite size of the nanoparticles, which influence the photocatalyst properties of the material.

2.1.4 Hydrothermal synthesis

In this technique, the inorganic precursors are pressurized and autoclaved to form nanocompounds. Stainless steel achieves high pressure and temperature. By adjusting the temperature, pressure, time, and ionic conductions within the steel vessel, the

product compounds are highly pure with optimized crystallinity, particle size, and surface functionalization [95–97].

Ghoderao et al. studied the effects of pH variation on the ZnO NPs at 8, 10, 11, and 12 [98]. The wurtzite hexagonal crystal structure is observed in all synthesized ZnO nanostructures. No prominent difference is observed in the photocatalytic ability of ZnO nanostructures, with a significant decrease in the crystallite size from 15 nm to 9.1 nm and an increase in the band gap from 3.21 to 3.3 eV. MB was photo-decayed under visible light, and 99% degradation was reported with pH 11 in 100 minutes. The increase in degradation is due to the excess OH radical that captured the holes in the conduction band.

A recent study by Sansenya et al. prepared ZnO NPs with the hydrothermal method with variation in molar ratio 1:5, 1:12, and 1:18 of Zn^{2+} and OH radicals [96]. XRD patterns confirmed the ZnO wurtzite hexagonal structure with increased lattice size 39.85 to 48.33 nm, whereas the band gap does not show much variation 3.19, 3.2, and 3.18 eV, respectively. Photocatalytic degradation of ZnO 1:5 is 100% of RR141, CR, and OFL in 20, 60, and 180 minutes under solar radiation in repetitive cycles. The increase in photodegradation is due to the decrease in particle size, an increase in surface area from 10.32 to 10.68 m^2/g, and high crystal defects, which significantly decrease the recombination rate.

2.1.5 Combustion synthesis

This is the simplest method to synthesize the metal oxide nanoparticles and ceramics. There are multiple routes in combustion, such as solution combustion, gas phase combustion, and auto combustion. All of them offer fine particle size with high surface area. The benefits of this technique are size homogeneity, simplicity of execution, cost-effectiveness, and easy component adjustments. This method is based on the exothermic reaction of metal salts as precursors with oxide in the presence of suitable reducing agents such as glycine, urea, citric acid, or tartaric acid. The choice of the reducing agent and the fuelling agent is also crucial to generating adequate energy for the combustion process [99–102].

Kotkar et al. employed the auto-combustion method to synthesize ZnO NPs for the photo decay of MB in solar irradiation [103]. The hexagonal crystal is observed in an XRD pattern with a crystallite size of 41.58 nm. A slight reduction in the bandgap of 3.07 eV is observed compared to bulk ZnO. HR-TEM results expressed the unclear mass of the hexagonal shape, while the SAED shows plans of (100) and (101). The MB is photo-catalytically decayed by 98% within 45 minutes under sunlight.

Bhapkar et al. use glycine nitrate as a combustion agent in reaction to prepare ZnO NPs to decay MB in visible light [104]. The particle size of 18.54 nm is reported with a band gap of 3.21 eV. The SEM images express the quasi-spherical spheres of 93 nm. A photocatalytic study was done on MB as a probe dye, which decays up to 97% in 2 hours with 5 mg/L of MB concentration and catalyst dose of 0.1 mg/L. The high performance of the nanoparticles is due to the oxygen defects and intrinsic defects in the crystal structure. The properties of recently synthesized ZnO NPs by conventional techniques are discussed in **Table 2**.

2.2 Recent advances in synthesis techniques

The synthesis techniques mentioned earlier are physical or chemical routes requiring elevated temperatures and pressure. Some even include high vacuum conditions

Synthesis Technique	Photocatalyst synthesis conditions	Morphology	Particle size (nm)	Crystallite Size (D) (nm)	Band gap (eV)	Surface Area (m^2/g)	Light Source	Probe pollutant	Dye Dose (mg/L)	Catalyst Dose (mg/L)	Degradation %	Rate Constant (k) $(min)^{-1}$	Exposure Time (min)	Ref.
Coprecipitation	ZnO (acetate & nitrate precursor)	Quasi spherical, ellipsoid	42	—	2.6, 2.915	—	—	MB	—	—	96.38 & 94.58	—	120	[24]
	ZnO	Quasi spherical	1022	45.5	3.18	—	UV & solar	MB	5	1	90%	0.00374, 0.03531	60	[25]
	ZnO	Nanospindles	25	22	3.31	9.4	UV-C	MB, MO	—	1000	98, 61	—	120	[26]
	ZnO	sea urchin, CTAB coated nanostructure	1500, 80–100	4–6, 80	3.71, 3.54	17.7, 26.9	UV	RhB, IC, MB	10	250	96, 99, 86	0.0534, 0.076, 0.0305	60	[34]
	ZnO	nanoparticles	140	—	3.00	—	Vis	CR	20	500	85	—	120	[35]
Sol-gel	ZnO	Nanospheres	30–35	16	3.48	10.5	UV-C	MB, MO	—	1000	99, 63	—	120	[26]
	ZnO	Nanospheres	21	21.13	3.26	—	UV-C	RhB	25	2	95	—	70	[27]
Microwave assisted	ZnO	Semi spherical	57	18	3.16	—	UV-A	MB, Rh-B	10	300	99, 98	0.017, 0.0095	240	[28]
	ZnO	Spherical	70–90	22,	3.35	—	Sloar	MB,	50	1000	98%,	0.01	210	[29]
Hydrothermal	ZnO pH (8, 10, 11 & 12)	Nanorods, Nano particles, Nanoplates	4000 by 700, 46–60, 150–40	15, 14.06, 10.2, 9.1	3.21, 3.28, 3.32, 3.3	—	Vis	MB	10	1000	91, 96, 99, 97	0.0177, 0.0252, 0.045, 0.0246	100	[30]
	Zn^{2+}/OH^{-} mole ratio (1:5, 1:12 & 1:18)	Nanoplates, nanorods	580, 420, 580–380	39.85, 45.53 & 48.33	3.19, 3.2, 3.18	10.59, 10.68, 10.32	UV & solar	RR141, CR and OFL	10	250	100%	UV (0.0671, 0.0157 & 0.007) Vis (0.1432, 0.0494 & 0.0304)	UV (40, 40,240) Vis (20, 60, 180)	[31]

Synthesis Technique	Photocatalyst synthesis conditions	Morphology	Particle size (nm)	Crystallite Size (D) (nm)	Band gap (eV)	Surface Area (m^2/g)	Light Source	Probe pollutant	Dye Dose (mg/L)	Catalyst Dose (mg/L)	Degradation %	Rate Constant (k) $(min)^{-1}$	Exposure Time (min)	Ref.
	ZnO (0.0, 0.1, 0.2 of Molar wt of Urea)	Dumbbell, nano roses, floral nanostructure	4000, 2000	24, 22, 17	3.18,3.15,3.11		Vis	MO	10	1000	59, 87, 92		30	[32]
Combustion	ZnO	Irregular	1462	10.4	3.3	—	UV & solar	MB	5	1	40	0.00227, 0.00856	60	[25]
	ZnO (pH 5, 7, 9, 11)	particles	216	—	3.07 7	—	Solar	MB	10	1000	89.9, 90.45, 97.61, 94.36	0.0211, 0.227, 0.0398, 0.0276	45	[32]
	ZnO (pH 9)	particles	216	—	3.07 7	—	Solar	MB	10	200, 600, 1000, 1400	84.95, 86.68, 97.61, 90.74	0.0191, 0.0209, 0.0398, 0.0252	45	[32]
	ZnO	Quasi spherical	93	18.54	3.21	—	Visible	MB	5,10, 15	100	97, 90.6, 84.12	0.0318, 0.0222, 0.0209	120	[33]
	ZnO	Quasi spherical	93	18.54	3.21	—	Visible	MB	5	50, 100, 150	95.16, 97.16, 94.46	—	120	[33]

Table 2.
Overview of conventional synthesis methods on ZnO on crystal structural and photocatalytic activity.

Part of Plant	Plant Sourcee	Morphology	Particle size (nm)	Crystallite Size (D) (nm)	Band gap (eV)	Surface Area (m^2/g)	Light Source	Probe pollutant	Dye Dose (mg/L)	Catalyst Dose (mg/L)	Degradation %	Rate Constant (k) $(min)^{-1}$	Exposure Time (min)	Ref
Leaves	*Ipomoea pes-caprae*	Dumbbell	25	20	3.19		Solar	MB			30%	—	30	[43]
	Lepidagathis ananthapuramensis	Hexagonal	14.72	28.12	3.01	1.44	Solar	MB	500	100, 200	84.1%, 95.01%	—	90	[44]
	Lepidagathis ananthapuramensis, precursor concentrations of $Zn(NO_3)_2{\cdot}6H_2O$ (0.025 M, 0.1 M and 1 M)	Hexagonal	14.72	28.12	3.00–3.01	1.44	Solar	MB	500	100	82.99%, 84.1% & 89.12%	—	90	[44]
	Lepidagathis ananthapuramensis (concentration of LA extrac 5 mL, 10 mL, 25 mL)	Hexagonal	14.72	28.12	3.01	1.44	Solar	MB	500	100	84.1%, 92.36%, 92.36%, & 98.50%	—	90	[44]
	Lepidagathis ananthapuramensis (Effect of calcinations temperature500, 700 & 900)	Hexagonal	14.72	28.12	3.01	1.44	Solar	MB	500	100	84.10%, 96.02% and 90.06%	—	90	[44]
	Lepidagathis ananthapuramensis (Effect of calcinations hours 2, 4 & 6)	Hexagonal	14.72	28.12	3.01	1.44	Solar	MB	500	100	84.10%, 84.10% and 86.05%	—	90	[44]
	Cinnamomum tamala	Polygonal	35–40	35	3.24	—	Solar	MB	0.2	100–300	93.89%	—	90	[45]
	Cinnamomum tamala (Effect of Calcination Temperature 300, 500 & 700)	Polygonal	35–40	35	3.24	—	Solar	MB	0.2	100	82.41%, 87.45% & 93.89%	—	90	[45]

Part of Plant	Plant Sourcee	Morphology	Particle size	Crystallite Size (D)	Band gap	Surface Area	Light Source	Probe pollutant	Dye Dose	Catalyst Dose	Degradation %	Rate Constant (k)	Exposure Time	Ref
			(nm)	(nm)	(eV)	(m^2/g)			(mg/L)	(mg/L)		$(min)^{-1}$	(min)	
	Cinnamomum tamala (Effect of Precursor Concentration 0.1, 0.025 & 0.05 M)	Polygonal	35–40	25..51, 30.44, 49.95	3.24	—	Solar	MB	0.2	100	87.45%, 98%	—	90	[45]
	Alchemilla vulgaris	Cauliflower shaped	120		3.27	—	Solar	RhB	125	500	75%	—	120	[46]
	Origanum vulgare (0.1, 0.5, 4% of plant extract)	Spherical	60, 50, 10	37.3, 35.6, 8.4	2.29, 2.77, 2.94	—	Solar	RhB,	15	1000	88%, 93%, 94.24%	0.0171. 0.0299, 0.0377	100	[47]
	Ruellia tuberosa	Rod-shaped	40–50				Solar	MB, MG	10, 10	200	94%, 92%		150	[48]
	Salvadora persica (different routes of synthesis A1 & B1)	Spheres, Rod-shaped	30–50, 25–35	—	3.26, 3.3	—	UV	MB	5	10	75%, 95%	—	150	[49]
	Azadirachta indic (5, 10, 15 ml of extrat))	Nanorods	100–200	19.6, 18.5, 13.2	3.05, 3, 2.99	—	UV	MG	16	—	96.30, 97.9%, 99%	—	160	[50]
Eucalyptus	Distorted spherical	—	23.5	3.6	—	UV 254 nm	MG	20	240	95%	0.016	240	[51]	
	Carica papaya	Semi-spherical, nanorods	40	19.6	2.88	34	UV	CR,	120	150, 200	99%, 90%	0.07527	180	[52]
	Simarouba Glauca ZnO	nanoparticles	—	10	3.2	—	Solar	CR	10	100	85	—	150	[53]

Part of Plant	Plant Sourcee	Morphology	Particle size	Crystallite Size (D)	Band gap	Surface Area	Light Source	Probe pollutant	Dye Dose	Catalyst Dose	Degradation %	Rate Constant (k)	Exposure Time	Ref
			(nm)	(nm)	(eV)	(m^2/g)			(mg/L)	(mg/L)		$(min)^{-1}$	(min)	
Fruit	*Myristica fragrans*	Elliptical	35.5	29	2.57	—	UV	MB,	—	—	88%	—	140	[54]
	Averrhoe Carrambola	Nano flakes	20	19.6	3.2	—	UV-Visible	CR	40, 60, 80, 100	1000	93%	0.0005, 0.0014, 0.0015, 0.002	180	[55]
Chili	*Capsicum annuum* var. Anaheim	Quasi spherical	40	17	2.93	—	UV	MB, MO, RhB	300	1000	100%, 85%, 92%	0.064, 0.01, 0.013	60, 180, 180	[56]
Pods	*Peltophorum pterocarpum*	Nanoflowers	59	17.79	3.43	19.61	Solar	MB	25	40	88.4%	0.0114	180	[57]
Peels	*Passiflora foetida*	Hexagonal	58	23.8	3.16	30.83	Solar	MB, RhB	10, 10	1	93.25%, 91.06%	0.0337, 0.0347	70, 70	[58]
Shells	*Peanut*	Rods	—	—	—	—	Solar	IC	10	2000	97	—	120	[59]
Photosynthetic bacteria	*Anabaena variabilis* ARM 441	Polygonal	150	33.31	3.21	38.718	UV	BG, IC	500, 500	500	98.07%, 808%	0.7623, 0.85349	130	[60]

Table 3.
Overview of Green synthesis methods on ZnO on crystal structural and photocatalytic activity.

that are time-consuming, and high energy is consumed for maintaining or following chemical reactions for quicker routes. However, these reactions generate toxic by-products, which are environmental hazards. Scientists are developing new methods that are more eco-friendly and have a minimal impact on the environment. Green synthesis involves plants, animals, bacteria, fungi, and algae for the synthesis of nanoparticles [34, 105–107]. Green fabrication is also called biosynthesis. It is an advanced method that gives highly effective photocatalyst ZnO NPs. This technique adheres unique organic molecules to the surface of the prepared ZnO NPs. For green synthesis, biochemicals present in a plant's various parts, such as roots, flowers, leaves, shoots, and fruits, are used as reducing, stabilizing, and encapsulating agents. These agents influence the surface area, morphology, and stability of the NPs [106]. The widespread practice is synthesis from dried leaves and flower petals; then washing and crushing them; separating the plant part by Mili-Q H_2O; adding zinc precursors; and then boiling and filtering the mixture at various temperatures, pH, and times to get the ZnO NPs [34].

2.2.1 Green synthesis methods

Rosa canina fruit extract is used in a study to synthesize ZnO NPs using Jafarirad's microwave-assisted growth and temperature method [35]. The microwaves speed up the rate of reaction with low cytotoxicity. However, the optimization of size, morphology, and crystal defects is to be studied further for synthesized ZnO NPs.

Chaudhuri et al. used a green synthesis technique for ZnO NPs from *calotropis* leaf extract, using zinc acetate as a precursor and NaOH as a reducing agent [108]. The ZnO NPs are reported with an ideal dispersion of 20 nm of ZnO crystalline size. This can be used as a growth agent in plants such as Milkwood pine, Karanj, and Neem.

The team of Mirza et al. used *Lupinus albus* as a precursor for ZnO and *Lupinus pilosus* as an encapsulating agent to prepare ZnO NPs [109]. The bioactive chemicals (phenol, alkanes, alkaloids, and different organic acids) play a significant role in the redox reaction of the synthesis. These ZnO NPs degraded MB up to 61% under UV light in 160 mins.

Souza et al. separated the phytochemicals from different plants by GC MS spectroscopy. The neem and eucalyptus extracts play an efficient role as reducing and capping agents and reduce ZnO NPS's agglomeration [110].

Another study by Supin and Vasundhara confirmed the above results by studying both plants separately [111]. It is reported that combining both plant extracts can disturb the photocatalytic efficiency due to the decrease in crystallinity. The ZnO NP synthesis by neem extract performs better due to the better crystallinity and lower bandgap.

Khalid et al. synthesized Mo-doped ZnO by the green method, photocatalytic decaying Rh-B to 89.6% in 180 minutes under sunlight [112]. MO-doped ZnO performed better due to its stability, with a lower charge recombination rate and lower band gap.

Priyadharshini et al. studied the biosynthesized ZnO NPs from coconut husk extracts using a novel combustion process for large-scale synthesis. Coconuts have high polyphenols, cellulose, lignin, and pentosans [113]. The XRD peaks confirm the presence of a hexagonal crystal structure of 48 nm crystallite size with a reduced bandgap of 2.93 eV. The FESEM images show bipyramid morphology. MB is photodegrade up to 99% in 100 minutes.

Vinayagam et al. used *Peltophorum pterocarpum* pod extract to synthesize the ZnO NPs [114]. XRD peaks agree with the JCPDS 36-1451, having a crystallite size of

17.79 nm with a bandgap of 3.43 eV with the morphology of morphology and particle size of 59 nm. MB is degraded up to 88.39% in solar light within hours. The high porosity creates a high surface area, which results in the high performance of photocatalysts [114].

The above studies show that biosynthesis is an eco-friendly synthesis technique for nanoparticles with low-cost and green by-products, controlled particle size, and reduced agglomeration in an aqueous medium. The literature shows that ZnO NPs perform well as photocatalysts under solar light and better than under UV radiation. However, limited studies express the photocatalytic activity in visible light. To enhance photocatalytic efficiency, many adjustments are required in nanoparticles' morphology, bandgap, and surface interfaces. These modifications are discussed in **Table 3**.

3. Influence of structural parameters

The modification in ZnO NPs boosts the photocatalytic decay of synthetic dyes in solar and visible light. The limitation of the transition metal oxide is that the photoactive decay is limited by a wide bandgap, due to which they are only responsive in UV light response [115]. Scientists are trying to reduce the bandgap and make the designed photocatalyst active and visible by doping and co-doping with metal and non-metals. Moreover, nanocomposites can be fabricated with metal oxides, polymers, membranes, and carbon and its allotropes to optimize the bandgap [116–118]. The charge recombination rate is very crucial for the efficiency of the photocatalyst. The longer the charge separation, the higher the probability of the electron and holes interacting with the reactive species, increasing the efficiency of the TMO. ZnO NPs with effective exciton separation reduce energy losses and increase the quantum yield [119]. Interfacial charge transfer on the surface of the nanoparticles influences the absorbance of wavelengths by optimizing the surface properties of the nanoparticles [120].

Modification in ZnO NPs primarily aims to tune the optimized band gap for enhanced light absorption. Create the surface defects and decrease the recombination rate to increase the reactive site and effective ions for redox reaction.

3.1 Effects of doping on photocatalytic efficiency

The doping created an extra band level or localized state below the conduction band of the dopant is n-type and an extra band level above the valance band if the dopant is p-type. Doping reduces the bandgap to the visible range and shifts the absorbance spectrum to a longer wavelength. The ZnO NPs improve the photocatalytic activity in the visible range after doping due to increased surface area with reduced lattice size and tailoring in the bandgap. Doping from every group of periodic table causes meaningful change in the physical properties in ZnO NPs and their photocatalytic activity [69, 76, 121].

The alkaline metal ions are studied to create the interstitial crystal defects in ZnO NPs. Moreover, unlike transition metals, these metal ions do not have any localized d-orbital, which results in effective high photon absorption in the visible range [122]. Shirdel et al. prepared the pristine ZnO NPs and Ba-doped ZnO NPs by sol-gel method [123]. The effects of calcination temperature along the Ba-doping were studied to degrade Rh-B dye under visible light. 0.1% doping of Ba with a calcination

temperature of 400°C decayed the Rh-B dye up to 98.4% within an hour. The high efficiency is associated with oxygen vacancies, which reduce the electron-hole recombination rate.

Another study by Pradeep et al. synthesized the Mg-doped ZnO NPs by co-precipitation technique for photocatalysis of Rh-B [124]. XRD patterns show that increased Mg doping results in a larger crystallite size. The bandgap was reduced to 3.04 eV due to the strain in the crystal lattice in 7.5% Mg-doped ZnO NPs. The red shift in bandgap is due to the quantum confinement and high defect in the lattice crystal structure. Mg-doped ZnO NPs photocatalytic decay of RHB was up to 78%, whereas the pure ZnO NPs decayed 13% in 2 hours. The increase in the photo response is due to the excess cations on the surface of the prepared ZnO NPs.

Bashir et al. doped ZnO NPs with the Sr. atom to enhance the photocatalytic effect [125]. The dopants create lattice defects in the crystal, generating a higher affinity to the reactive radicals. Selvaraj et al. prepared the doped Sr-doped ZnO NPs with 1%, 3%, and 5% wt. ratios by hydrothermal technique [126]. XRD patterns show the decrease in crystallite size with the percentage increase of Sr. Likewise, the decrease is observed in the bandgap from 3.09 to 2.93 eV for 5% doping of Sr. The Sr-doped ZnO NPs degraded MB and Rh-B dye up to 99 and 90% in 1.5 hours in solar radiation. The high performance is due to the high concentration of OH^- ion, a primary species that interacts with the probe dyes. The increased light absorbance of visible light creates better ion separation and generates excess exciton pairs.

However, the transition metal ions generate an extended separation in the electron-hole pair, decreasing the recombination rate because of the electron trapped in the d-shell. The decrease in the recombination rate increases the overall photocatalytic efficiency of the NPs. The transition metals have a similar atomic radius to the Zn, which makes them ideal for doping. The rapid charge transfer from CB to VB due to the partially filled d-shell results in a decrease in the bandgap of ZnO NPs [127]. Mondal et al. synthesized the Fe, Co, and Ni-doped ZnO NPs by co-precipitation [128]. The prepared NPs decayed MB in UV and visible light to 94.5% by Fe-doped ZnO NPs. The Co-doped ZnO NPs decayed by 81% and Ni-doped ZnO NPs by up to 83%. The degradation of MB is due to the structural defects and reduced bandgap.

Karthik et al. used a green synthesis technique for Cu-doping ZnO nanocrystals [129]. Leaf extract of *Synadium* granite is used with $Zn(NO_3)_3$ and Cu $(NO_3)_3$ to degrade the MB, IC, and Rh-B under UV light up to 91.3, 92.2, and 90.1%, respectively. The bandgap increases with the increase in the doping percentage. The highest photodegradation is observed with 3% Cu doping for MB and IC, whereas the 5% doped ZnO NPs degraded the highest Rh-B. The enhanced photocatalytic decay is due to the lattice strain and decreased recombination rates.

Elamin et al. prepared the 5% Cr-doped ZnO NPs by sol-gel wet method for photodegradation of CR [130]—the difference in annealing temperature redshifts the bandgap from 3.16 to 3.09 eV at 500°C. The change in the bandgap is the attribute of the sublevels created by Cr-doping and crystal defects. The CR decays up to 94% in an hour under visible light. The same method was used to prepare the pristine ZnO NPs, decayed CR 64% in similar conditions.

The noble metals are well known to create an effective electron trap due to the Schottky barriers at the interface of nanoparticles. The difference in the work function of TMO and noble metals makes them attractive candidates for creating the ideal modifications and preventing repaid neutralization of the electron-hole pair. The noble metal ion captures these photogenerated electrons, and light absorbance is

enhanced due to the surface plasmon resonance (SPR). The reactive sites on the surface are more responsive to the present radicals and hence show improved photocatalytic activity [131].

Ahmed et al. prepared the Au-doped ZnO NPs by sol-gel method with hydrogen tetra chloruretic as AU precursor salts and polyvinylpyrrolidone to control the surface of the ZnO NPs [132]. The Au-doping reduced the crystallite size to 42 nm from 53 nm, with the redshift in the bandgap to 3.08 eV. ZnO electrons trap in the d-shell of the Au within the CB and VB, enhancing light absorption in the visible range. MB degraded up to 82.1% in 180 minutes under UV light.

Ahmad et al. conducted another study to prepare the Au-doped ZnO NPs using the biosynthesis technique. Carya illusoriness leaf extract is used as a reducing agent during the synthesis [133]. The prepared Au-doped ZnO NPs degraded Rh-B up to 95% under UV light in 180 minutes. Pathak et al. compared the ZnO NPs doped with Ag and Au using combustion [134]. The results show better performance with Ag doping in the photocatalytic degradation of MB.

The Au and Ag doping gives high photocatalytic performance due to the surface plasmon effect and higher conductivity in both electrical and thermal mediums. Their enhanced stability and environmental nature make them a suitable candidate for water treatment. Oxygen deficiency and interstitial defects will increase the e−/h + separation [135].

Furthermore, the rare earth metals are reported to change the electronic structure of ZnO nanoparticles. Therefore, they enhance the absorption of visible light hence, increasing the photo response to generate a pair of excitons which increases the photocatalytic performance. Rare earth metal ions have “f” shell electrons which reduce the band gap [136].

Lu et al. synthesized Ta-doped ZnO NPs using the hydrothermal method for the photocatalytic degradation of MB [137]. The structural variation in crystallite size and bandgap is observed with the difference in the synthesis temperature. Nanocomposite synthesized at 150°C performed well compared to the rest synthesized at 110 and 170° C. The synthesized Ta-doped ZnO has photodegraded 97.8% of probe dye due to the oxygen defects. The reduced recombination rate is primarily responsible for the enhanced degradation.

Palanivel et al. used the co-precipitation method to prepare the Gd/La co-doped ZnO and compared it with the dopants separately Gd-doped ZnO and La-doped ZnO nanostructure [138]. The Rh-B was degraded to study the photocatalytic activity under solar light. Samples were doped with 5 moles percent and La 3 moles percent. The XRD pattern shows the increase in the amorphous phase in the sample due to the difference in the atomic radii. The band gap is reduced and doped ZnO becomes responsive at 401 nm with co-doping of ZnO with RE metal ions. The Rh-B photodegraded is highest up to 91% with Gd/La @ ZnO. The reduction CB potential value is observed to be increased to −0.74 eV rather than −0.3 eV which reduces the oxygen to superoxide radical. The VB potential is also increased to 2.42 eV from 1.98 eV from the standard oxidation potential of ZnO NPs which oxidize water to OH^-. Hydroxyl ions and superoxide ions behave as the reactive species in photocatalytic reactions.

ZnO NPs are doped with many nonmetals to reduce the bandgap and enhance the photocatalytic response to visible light. The crystal and surface defects are generated by substituting oxygen atoms in the lattice with carbon, nitrogen, and sulfur dopants [139]. These atoms are small and intercalate to the crystal structure by oxidation process which defects expedite the rate of reaction in doped ZnO NPs.

The intermediate energy level is introduced which drastically reduces the rate of recombination. The difference in the properties of these nonmetals and their high electron affinity with oxygen atoms within the lattice enables tailoring of the optical and structural properties [140].

Carbon is well known for its high mechanical strength, chemical stability, and electrical properties. The ZnO-doped carbon is reported to significantly reduce the bandgap, hence increasing the visible light response NPs. Zhang et al. prepared C-doped ZnO NPs by pyrolysis of MOFs and degraded the Rh-B in visible light [141]. The crystallite size increases with the doping of C while its bandgap decreases. The doping of C is effective in increasing the charge life and their availability on the surface for the photodegradation degradation of Rh-B. Moreover, there is effective cyclic reusability of these photocatalysts.

Photocatalytic activity is majorly depending on the surface aera, crystal defects, bandgap, and crystallinity of the ZnO NPs. Every dopant atom has a significant effect on the crystal defects and photo-response by shifting the bandgap. Smaller percentage of doping is reported to perform better than the higher doping percentages. Due to the induced stresses, strains, oxygen vacancies and dislocations in the crystal structures interdiction of a new crystallize phase within the nanocomposite is observed multiple studies.

3.2 Effect of size and surface area on photocatalytic efficiency

Particle size and surface area are directly associated with catalytic response. The surface area determines the absorption of pollutant molecules on the photocatalyst. The highest the surface area and smaller the size of the NPs will give higher absorption area which enables the effective transmission of the exitron for redox reaction.

Khalid et al. prepared the Cu and Co-doped ZnO NPs by hydrothermal method [142]. FESEM shows that the Cu-doped ZnO NPs have the smallest particle sizes. MB is photo-decayed up to 80 and 94% by Co-doped and Cu-doped ZnO NPs in 100 minutes, respectively. The Cu-doped ZnO NPs show a high photocatalytic effect due to the smaller particle, higher surface area, high crystal defects ratio, and longer charge separation.

Another study by Ma et al. to synthesize Cu-doped ZnO NPs by co-precipitation [143]. The crystallite increases with the increase of Cu ions, but the sudden decrease is observed at 5% doping with the decrease in bandgap value from 3.24 to 3.17 eV. The 3% Cu-doped ZnO NPs photo-decayed the MB up to 95% in 240 minutes.

Using the co-precipitation method, Kareem et al. conducted co-precipitation of ZnO NPs [144]. The sudden increase observed in the crystallite size is due to the separate phase of Ag in XRD. The Ag doping reduced the bandgap, resulting in a red shift in DRS spectra with a slight increase over 0.75% Ag doping. The Ag-doped nanoparticles are used to degrade the MB. About 1% doped Ag photo decayed dye to 98% within 2 hours under solar light. The higher efficiency is due to the increased surface area and induced defects.

Bhosale et al. doped the Ag using the co-precipitation method for the degradation study of MO [145]. In this study, the scientists observed the smaller size of Ag-doped at 1%, which degraded the MO up to 96.7%. Meanwhile, the pristine ZnO NPs show 70.7% degradation. The trapping experiment exhibits that O_2^* is the reactive species in the reaction process.

The Sm, Nd, and Dy doped ZnO NPs were prepared by sol-gel method by Dhiman et al. to degrade the MG under visible light [146]. Citric acid is used as a fuel during

the sol-gel reaction. The crystallite size is smaller than the pristine ZnO NPs. The Dy-doped ZnO has the smallest crystallite size and narrowed band gap due to which it exhibits the highest photocatalytic degradation, 97.1%, of MG in 2 hours. The cyclic study shows the sustainable retention of the catalytic response. The induced crystal defects and extended charge separations are the primary factors for the highest photocatalytic activity.

Rodwihok et al. synthesized the Ce-doped ZnO NPs by hydrothermal method with 3, 5, and 7% doping [147]. Ce reduced the size and band gap of the doped ZnO NPs. The MO is degraded photocatalytic up to 94.06% with 7% Ce-doped ZnO NPs. The exponential increase in photocatalytic activity is due to the electron trapping within the Ce^{4+} ions which reduced the charge recombination rate significantly.

Selvaraj et al. prepared the Sm-doped ZnO NPs by co-precipitation method at different doping concentrations (1, 3, and 5%) [148]. The crystallite is increased with the doping of Sm. The redshift is seen in the band gap of doped samples because of the induction of intermediate energy level between the CB and VB of the ZnO band gap. The intermediate level is introduced due to the 4 f of Sm. The MB is degraded by up to 96% in 90 minutes under sunlight with 5% Sm-doping in ZnO NPs. The Sm ions are ascribed as the electron traps and limit the charge recombination within the ZnO NPs.

Sukriti et al. synthesized the Sm-doped ZnO with different percentages to degrade the MB. The highest photo response was observed in 4% Sm-doped in ZnO NPs in visible light to degrade the MB. The crystallite size was reduced with a reduction in the band gap is the major attribute of the Sm-doped ZnO NPs. The defects in the crystal structures and f subshell electron traps significantly reduced the recombination rate. Sm was reported to be the most effective doping of rare earth metals to enhance the photocatalytic studies [149].

Mirzaeifard et al. used a hydrothermal method for the synthesis of S-doped ZnO NPs at different doping percentages using thiourea as a precursor for S [150]. Unlike C doping, the S doping is reported to increase the crystallite size with increasing the doping. The highest photocatalytic activity is observed with 0.5 wt.% doping of S in ZnO NPs to degrade Rh-B under visible light up to 95% in five cycles. The high specific surface area and large pore volume provide a larger number of reactive sites for photocatalytic reaction.

The above studies show that the higher surface area plays a significant role in the efficiency of the photocatalytic reaction as the number of effective reactive sites increases for the redox reaction of pollutants.

3.3 Effect of crystallinity and morphology on photocatalytic efficiency

The crystallinity of crystal structure and morphology of ZnO NPs has significant implications on the photocatalytic reactions. The reduction in the crystallinity usually result in the increase of charge separation which results in the increment in the exitron life span.

The most effective photocatalytic activity was observed by nitrogen-doped ZnO Nps. The nitrogen radii and p orbital are almost comparable to O which leads to the formation of oxygen vacancies and high solubility [151]. Prabakaran et al. reported the N-doped ZnO NPs synthesized by hydrothermal method, where the hydrazine is used as a source of N atom [72]. The NPs have the morphology of cabbage with a reduction in the crystallite size and bandgap of N-doped ZnO NPs. The effective decay of MB is observed under UV and visible light up to 98 and 96%, respectively. The catalyst is stabilized for four consecutive cycles.

Kabir et al. synthesized N-doped ZnO with the combustion method at different doping percentages, using urea as the source of N [152]. The crystallite and particle size were reduced with doping. Rod-like morphology is observed in SEM images which are exploited for the photo-degradation of MB and Rh-B under solar light. The rate of photocatalytic activity is effectively high with 7% N-doping in ZnO NPs. MB is decayed up to 98%, and Rh-B is decayed up to 86% under sunlight. The higher crystallinity of N-doped ZnO NPs with low recombination rate is the prime reason for the better performance.

In another study, R Mahdavi et al. used the sol-gel method for the synthesis of ZnO and Al-doped ZnO NPs using the same precursor and reduction agent with aluminum nitrate salt to dope Al^{+3} ions later calcinated at 200°C for 2 hours [153]. The XRD shows the well-aligned peaks with the hexagonal structure of ZnO, with no discrete peak of Al or Al_2O_3. Moreover, the decrease in crystal size is seen with Al doping. The TEM exhibits the change in morphology with the increase in Al doping. The pristine ZnO NPs have hexagonal polyhedral structures with increased Al doping till 3% of the nanoparticles appear spherical. Further, the increase creates nanorods. This change in morphology is due to the quantum changes on the surface caused by adding an extra positive charge of the Al^{+3} ion. The band gap is also reduced to 2.93 with 7% Al doping. MO is degraded to 65% with 5% Al-doped ZnO nanoparticles in 3 hours, slightly higher than in the previous study.

A recent work by Peerakiatkhajohn et al. prepared ZnO and Al-doped ZnO NPs using the same precursor and reducing agent with sol-gel technique at three different calcination temperatures: 200, 300, and 400°C for the photodegradation of MO [154]. The increase in particle size is observed with the increase in the calcination temperature from 28 to 71 nm, with a slight decrease in the band gap from 3.34 to 3.28 eV. The XRD is in good agreement with the hexagonal structure and high crystallinity. The calcination temperature generates different morphologies. The lowest calcination temperature gives the highest surface area and effective light absorbance. Hence, the sample with 200°C calcification temperature gives the highest MO photocatalytic decay up to 80% in 4 hours under UV light. With Al doping, the ZnO NPs were active in the visible range due to the reduction in the band gap. The most responsive doping in visible light was 5% Al in ZnO NPs, which has a band gap of 2.23 eV and degrades MO by up to 99% in 40 minutes under UV radiation. The decrease in the band gap, change in the ionic surface of the nanoparticles, and increased light absorbance result in the effective photo decay of the MO.

The morphological changes are due to the growth of polar surface in ZnO NPs which is an attribute of the hexagonal crystal structure. The variation in nanostructures of the ZnO NPs and crystallinity effectively influence the photocatalytic rate of reaction. The enhanced charge separation within the nanocomposite and reduced recombination rates result in the increase of photocatalytic activity.

3.4 Effects of co-doping with metal oxides on photocatalytic efficiency

Combining the two different metal oxides is another approach to designing an effective photocatalyst responsive to visible light. The metal oxide of two different band gap composites constructs heterogeneous photocatalysts with relatively low recombination rates [155]. Two semiconductors of different band gaps in a composite are exposed to appropriate wavelength. They generate the pair of exciton under wide bandwidth [156].

In semiconductors, the charge flows toward the low potential, respectively. In type-I heterojunction, the first semiconductor has more negative potential CB and more positive potential VB than the second semiconductor. So, the pair of exciton transfer to SC-II and a redox reaction occurs. In type-II heterojunction, the CB of SC-I is more negative than the CB of SC-II; however, the VB is less positive than the SC-II. The electrons in CB of SC-I transfer to the SC-II, and the holes transport from SC-II to SC-I. Hence, the exciton pair is effectively separated which results in the better performance of the photocatalysts. However, the Z-scheme heterogeneous photocatalyst is like the type-II heterojunction, but the electrons in the CB of the SC-II are absorbed by the holes in the VB of the SC-I. The smaller potential difference in the VB of SC-I and CB of the SC-II enables such recombination. However, Z-scheme photocatalysts are more effective than type-II because of the better charge separation and high redox capability [157].

Shanmugam et al. synthesized the nanocomposite of ZnO/CuO by hydrothermal method with different percentages of CuO [158]. XRD patterns show the hexagonal wurtzite structure of ZnO and the monoclinic structure of CuO. The energy band gap decreases with the increase in the CuO in the nanocomposite. The synthesized samples were tested for the degradation of MB as a probe pollutant under UV-visible irradiation up to 98% within 150 mins. Despite the smaller band gap of ZnO/CuO (20%), the ZnO/CuO (10%) performs better as a photocatalyst. The high performance is an attribute of effective charge transfer, better charge separation, and high crystallinity of the ZnO/CuO (10%). Moreover, the stability and reusability are reported for five cycles.

Elshypany et al. prepared a ZnO/Fe_3O_4 composite with different ratios by the co-precipitation method [159]. The band gap decreases with the increase in the Fe_3O_4. The PL results exhibit the induced defects and stress in crystallite. MB is photo-decayed under visible light in 4 hours by the 8:1 of ZnO/Fe_3O_4 composite. The photocatalyst remains stable in five cycles.

Wahba et al. developed the ZnO/ZrO_2 composite with various percentages of ZrO_2 by sol-gel method [160]. The crystallite increases as the ZrO_2 in composite, whereas the band gap decreases. The best performance is of 50:50 ratio to photo degrade the MB up to 97% in 150 minutes and IC up to 99% in 300 minutes. The higher performance is due to the strong interfacial interaction between the semiconductors.

Munawar et al. designed the ternary composite CuO-MgO-ZnO using co-precipitation [161]. The rod-like structure was achieved with intrinsic defects in the crystal structure. Outstanding degradation efficiencies are reported for the decay of MB, MO, and Rh-B up to 88.5, 93.5, and 75.9%, respectively, in 100 minutes under sunlight.

Zhang et al. designed a nanocomposite of ZnO/SnO_2 with different mass ratios (1:1, 1:3, and 1:5) using the hydrothermal-assisted ultrasonic method [162]. The flower-like nanocomposites were used to photo-decay MG under visible light. The 1:1 ratio has performed well and decayed the dye up to 98% in 150 minutes. The O_2^- trapping exposes that O_2^- major reactive species in photocatalytic reaction. The type-II heterojunction formation enables a decrease in the charge recombination rate which has extended the possibility of redox reaction.

Sayadi et al. use green chemistry to synthesize ZnO/SnO_2 composite using *Viscum album L* extract as a surface-active agent [163]. The XRD pattern shows significant changes in the peak position and intensities. Moreover, the pattern agrees with the formation of heterojunction within the semiconductor. The CR was used as a probe pollutant for photo decay under visible light. The heterojunction is an effective photocatalyst due to the prolonged charge separation.

The introduction of Z-scheme in the heterogeneous photocatalyst is an effective way to prolong the life span of the charges and provide large number of reactive sites. The co-doping technique improves the light response and makes the photocatalyst to work on two wide range of wavelengths which means larger number of exitron production over the same time of irradiation of light.

3.5 Effects of carbonaceous 2-D material on photocatalytic efficiency

The ZnO NPs were decorated on the 2-D supporting material such as graphene, GO and rGO, and g-C_3N_4 nanosheets. The researchers are investigating the effects of graphene and other carbonaceous materials supporting the TMO NPs due to their ability to disperse the active sites on the surface of the photocatalyst. Such composites have large surface area which makes them the responsive to visible light with better charge separations which is supportive for the effective photocatalytic degradation [164]. The sp2 in carbonation 2-D nanosheets with honey comb structure is the prime attraction for researchers [165]. The light response of carbonaceous 2-D materials is remarkably high in visible range which assist the exciton generation in the nanocomposite. Moreover, it provides better charge separation which result in the reduction of the charges recombination rate. The flow of charge is enhanced by the presence of carbonaceous material due to their reported high conductivity [166].

Zheng et al. supported that the ZnO NPs on the graphene reported the better mechanical strength and high porous structure to assist the cay to the pollutant [167]. Hummer's method assists to increase the interplanar distance by oxidizing the pi-bond between the layers resulting in the production of the GO. The rGO is achieved by adjusting the pH of solution during the synthesis of GO. This rGO stabilizes by the post thermal treatment [168].

Oyewo et al. synthesized nanocomposites of 10% Sn doped ZnO NPs anchored on the GO surface [169]. The reduction in the bandgap is due to the formation of defects in the ZnO crystal lattice. PL indicates the intrinsic defects and better charge separation within the complex. The Sn-doped ZnO NPs are reported to be less photocatalytic active than the Sn-ZnO/GO complex. MO was photo-decayed up to 96% under visible light in 2 hours. The significant increase is due to the outstanding electronic and thermal properties of GO with large effective surface area. Moreover, the GO was contributing to the prolong charge separation.

The g-C_3N_4 is investigated as a support material due to its stability and simple synthesis technique. Moreover, it has high corrosion resistance. Ngullie et al. prepared ZnO/g-C_3N_4 complex with different wt.% of ZnO hydrothermal method used to degrade MB [170]. The 75% ZnO/g-C_3N_4 shows higher photocatalytic response and decayed the MB in 2 hours up to 91% which is higher than the pristine ZnO (26%). The reduced charge recombination within the complex is a major reason for the better performance. Furthermore, the scavenging testing express hole as the primary reactive species in photocatalytic reaction. The prepared sample was reported to be responsive after five cycles.

Bhosale et al. developed ZnO-gC_3N_4 composite with different ratio weights 4:1, 3:1, and 2:1 by using co-precipitation [171]. The crystallite size increases from 19.07 to 26.71 nm. The bandgap decreases to 2.95 eV from 3.13 eV with the increase in the gC_3N_4 in composite. The decrease in band gap increases the visible light response in generation of the exciton. The BET shows it has a larger surface area than either of the pristine in the components in the composite. The increased in the surface area results in decent availability of reactive sites for photocatalytic reaction for the decay of MO.

The pristine sample exhibits 70% decay, whereas the nanocomposite degrades the MO up to 99.51% in 90 minutes under visible light. The scavenger test shows that the O_2^- >. *OH* > H^+ reactive response of the ions.

Girish et al. designed the ZnO-gC_3N_4 Z-scheme heterogeneous photocatalyst by using the co-precipitation method with different weight ratios (5:1,1:5 and 1:1) [172]. The MB is 71% decayed by gC_3N_4 and pristine ZnO NPs decayed 52% whereas the composite is reported to decay MB up to 92% under visible light in 120 minutes. The trapping experiment exhibits that O_2^- is a reactive species in the reaction.

The carbonaceous 2-D nanostructures are more likely to produce the high porosity, better charge separation, high mechanical strength, and wide range photo response due to the shift in the bandgap. The above properties result in the enhanced performance of the nanocomposites.

4. Mechanisms and pathways as photocatalyst in water purification

The degradation of the ZnO NPs follows the following route.

1. The adsorption of pollutants on the surface of the ZnO NPs.

2. The redox reaction occurs due to the photon absorbance, which desorbs the intermediates of the pollutants.

3. The pollutants are degraded at the interface of ZnO NPs.

The absorbance of specific energy of photon will generate the exitron pair within the NPs. Leaving holes in VB and electrons on CB. The charges travel to the surface of the ZnO NPs and react simultaneously with the organic pollutants with the reactive species (OH and O_2^-). The electron reduces at the CB, by interacting with the oxygen molecules present nearby and generate superoxide anion. Later, the superoxide reacts with H_2O molecules and gives out hydrogen superoxide radical (HO_2^*). Hydrogen superoxide then interact with H_2O molecules resulting in the formation of hydrogen peroxide (H_2O_2). The H_2O_2 reacts with superoxide ion and give hydroxyl radical (OH). These ions of hydroxyl are vital oxidizing radicals for the decomposition of pollutants [173].

$$ZnO + hv \rightarrow ZnO\left(h^+\right)_{VB} + ZnO\left(e^-\right)_{CB}$$
$$\left(e^-\right)_{CB} + O_2 \rightarrow O_2^-$$
$$O_2^- + H_2O \rightarrow HO_2^*$$
$$HO_2^* + H_2O \rightarrow H_2O_2$$
$$H_2O_2 + O_2^- \rightarrow OH$$

However, the holes oxidize at VB and get trapped by H_2O molecules subsequently generating hydroxyl radicals (OH) [174]. The equation is represented as follows:

$$H_2O \leftrightarrow \left(H^+ + OH^-\right) + \left(h^+\right)_{VB} \leftrightarrow H^+ + OH$$

Eventually, these hydroxyl ions oxidize to produce CO_2 and H_2O as products:

$$\text{Dye} + \text{OH} \rightarrow \text{minimization product } (CO_2 \text{ and } H_2O)$$

The degradation rate is measured by spectrophotometric measurements. Every organic dye has it is characteristic absorbance peak. The absorbance peak is observed by UV-visible spectrophotometer after the time interval of irrigation of light. The rate to degradation is calculated by evaluating the decrease in the maximum absorbance peak. **Figure 2** represents the schematic diagram of conventional mechanism of pristine ZnO NPs during photocatalytic reaction.

The photocatalytic reaction mechanism changes with the addition of dopants. Moreover, the dopant electron vacancy, atomic radii, and induced crystal defects are the major factors to affect the photodegradation process.

Dopant from alkaline earth metals such as Mg, Sr., or Ba doping in ZnO NPs respond to the incident photon of respective energy. The pair of electron and hole is produced like the pure ZnO NPs. Electron are led to the CB and holes move to the VB. The introduction of interstitial sites within the crystal structure results in the creation of an energy level within the region of forbidden zone of semiconductor ZnO NPs. The extra energy level introduces doping which reduces the recombination rate in photocatalysts hence increase the life span of the exitron pair. Therefore, the probability of surface reaction increases, resulting in the enhanced photocatalytic response. The alkaline metals attract the electrons to $Sr.^{+2}/Ba^{+2}/Mg^{+2}$ ions from the CB of the ZnO NPs. These electrons get reduced to the available oxygen molecules and produce the superoxide ions. However, holes get oxidized with water molecules at the VB and generate the hydroxyl ions. These reactive radicals interact with the dye molecules and degrade them [175].

$$\text{ZnO} + \text{hv} \rightarrow \text{ZnO}\left(h^+\right)_{VB} + \text{ZnO}\left(e^-\right)_{CB}$$

$$\left(e^-\right)_{CB} + \left(Sr^{+2}/Ba^{+2}/Mg^{+2}\right) \rightarrow Sr^{+}/Ba^{+}/Mg^{+}$$

$$O_2 + \left(Sr^{+}/Ba^{+}/Mg^{+}\right) \rightarrow O_2^- + \left(Sr^{+2}/Ba^{+2}/Mg^{+2}\right)$$

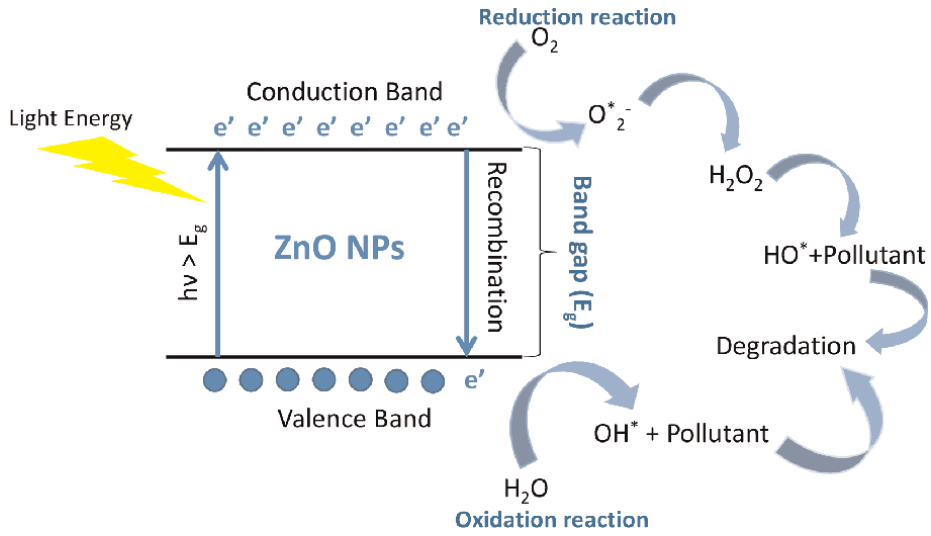

Figure 2.
The schematic of conventional mechanism of pristine ZnO NPs photocatalytic reaction.

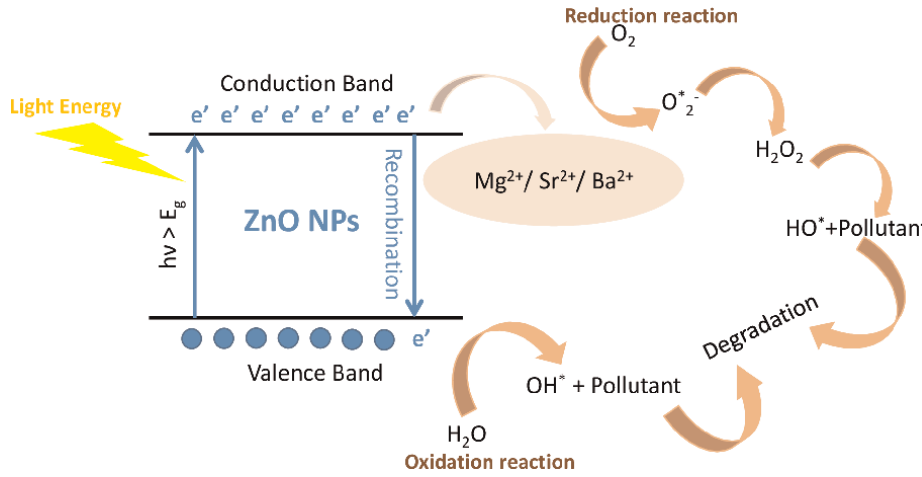

Figure 3.
The schematic of alkali metal-doped ZnO NP reaction mechanism of photocatalytic degradation.

$$H_2O \rightarrow (H^+ + OH^-) + (h^+)_{VB} \rightarrow OH$$

$$\text{Dye} + (OH/O_2^-) \rightarrow \text{minimization product } (CO_2 \text{ and } H_2O)$$

Figure 3 represents the schematic diagram of alkali metal-doped ZnO NP reaction mechanism of photocatalytic degradation.

The transition metals (TM) such as Cr, Fe, Cu, Mn, and Co doping significantly reduce the band gap of doped ZnO NPs, hence becoming photo-responsive in visible ranges. The doping of TM creates the pronounced changes in the optical and electrical properties along with the defects in crystal structure [176]. TM-doped ZnO NPs release the exitron when irradiation under light. The photoelectrons move to CB leaving the holes in VB. In the pristine ZnO NPs recombination for electron occurs more frequently. However, the doping of TM increases the charge separation, and the excited electrons are captured by the acceptor level of the respective dopant atom, which reduces the TM ions. The recombination rate is reduced by the reduction process, and the hole in VB reacts to produce the hydroxyl ions. These ions reduce the dye molecules and degrade them in H_2O and CO_2 [143].

$$ZnO + hv \rightarrow ZnO\,(h^+)_{VB} + ZnO\,(e^-)_{CB}$$

$$(e^-)_{CB} + (Sr^{+2}/Ba^{+2}/Mg^{+2}) \rightarrow Sr^+/Ba^+/Mg^+$$

$$O_2 + (Sr^+/Ba^+/Mg^+) \rightarrow O_2^- + (Sr^{+2}/Ba^{+2}/Mg^{+2})$$

$$H_2O \rightarrow (H^+ + OH^-) + (h^+)_{VB} \rightarrow OH$$

$$\text{Dye} + (OH/O_2^-) \rightarrow \text{minimization product } (CO_2 \text{ and } H_2O)$$

Figure 4 represents the schematic diagram of transition metal-doped ZnO NP reaction mechanism of photocatalytic degradation.

The noble metals always stand out due to their localized surface plasmon resonance (LSPR). Doping of ZnO NPs with noble magnifies the photocatalytic performance. The charge transfer to the noble metals to the ZnO NPs creates the better charge separation

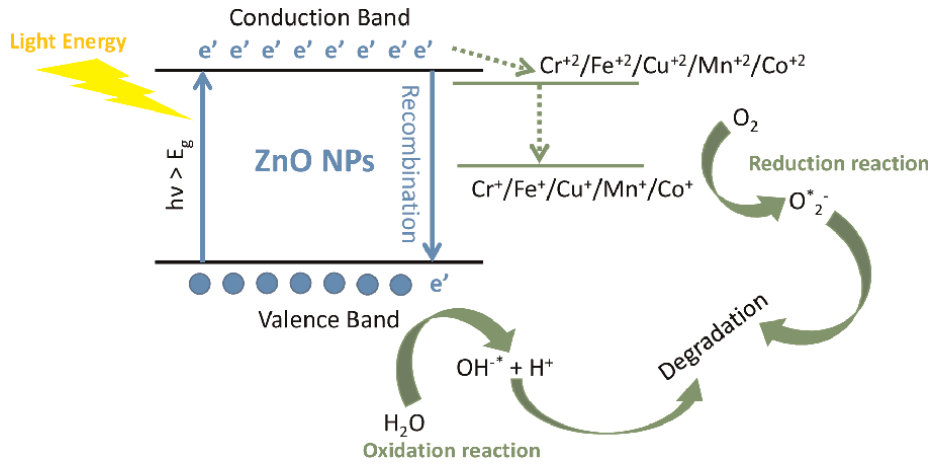

Figure 4.
The schematic of transition metal-doped ZnO NP reaction mechanism of photocatalytic degradation.

and absorbs the effective energy. The introduction of Schottky barrier between the CB and VB enables the electron from the Ag/Au/Pd metals ions to ZnO crystal structure to achieve the equilibrium within the system and create a fermi energy level (E_f). E_f is a bit lower than the CB of ZnO which creates an extra band in the forbidden region, and the Ag/Au/Pd metals capture the photogenerated electron and get charged which is responsible for the delay of the photogenerated electron hole recombination and extending life span, thus increasing the redox reactions at the surface of NPs. The oxygen molecule reduces to super oxide ion and water molecules to hydroxyl ion [69, 135, 177]. However, the noble metal doping rises the cost of the photocatalytic production which limits their production of the catalyst. Moreover, its excess loss of catalyst during the processing at large scale adding the cost value of the purification process.

$$\mathrm{ZnO} + \mathrm{hv} \rightarrow \mathrm{ZnO}\left(\mathrm{h}^{+}\right)_{\mathrm{VB}} + \mathrm{ZnO}\left(\mathrm{e}^{-}\right)_{\mathrm{CB}}$$

$$\left(\mathrm{e}^{-}\right)_{\mathrm{CB}} + \left(\mathrm{Cr}^{+2}/\mathrm{Fe}^{+2}/\mathrm{Cu}^{+2}/\mathrm{Mn}^{+2}/\mathrm{Co}^{+2}\right) \rightarrow \mathrm{Cr}^{+}/\mathrm{Fe}^{+}/\mathrm{Cu}^{+}/\mathrm{Mn}^{+}/\mathrm{Co}^{+}$$

$$\mathrm{O}_2 + \left(\mathrm{Cr}^{+}/\mathrm{Fe}^{+}/\mathrm{Cu}^{+}/\mathrm{Mn}^{+}/\mathrm{Co}^{+}\right) \rightarrow \mathrm{O}_2^{-}$$

$$\mathrm{H_2O} \leftrightarrow \left(\mathrm{H}^{+} + \mathrm{OH}^{-}\right) + \left(\mathrm{h}^{+}\right)_{\mathrm{VB}} \rightarrow \mathrm{OH}$$

$$\mathrm{Dye} + \left(\mathrm{OH}/\mathrm{O}_2^{-}\right) \rightarrow \text{minimization product } \left(\mathrm{CO_2 \text{ and } H_2O}\right)$$

Figure 5 represents the schematic diagram of noble metal-doped ZnO NP reaction mechanism of photocatalytic degradation and charge transfers.

The ZnO electronic structure can be altered by the doping of rare earth metals (RE) and make them responsive in the visible light. The charge transfer mechanism began as the visible light fall on the ZnO NPs and generate the exitron pair. RE metals have f orbitals and 3^{+} oxidation state which capture the electrons further creating an extended separation within the charge. The RE^{3+} ion reduces to RE^{2+} and later reduces the oxygen molecule to superoxide ion. However, the holes oxidize at the VB and produce the hydroxyl ion upon interaction with water molecules. The reactive radicals react with dye molecules resulting in their degradation. The RE metals enhance the photoresponsivity in the NPs, yet the price factor is extremely high which limits their use at larger scales due to inadequate recycling of the of nanocatalysts.

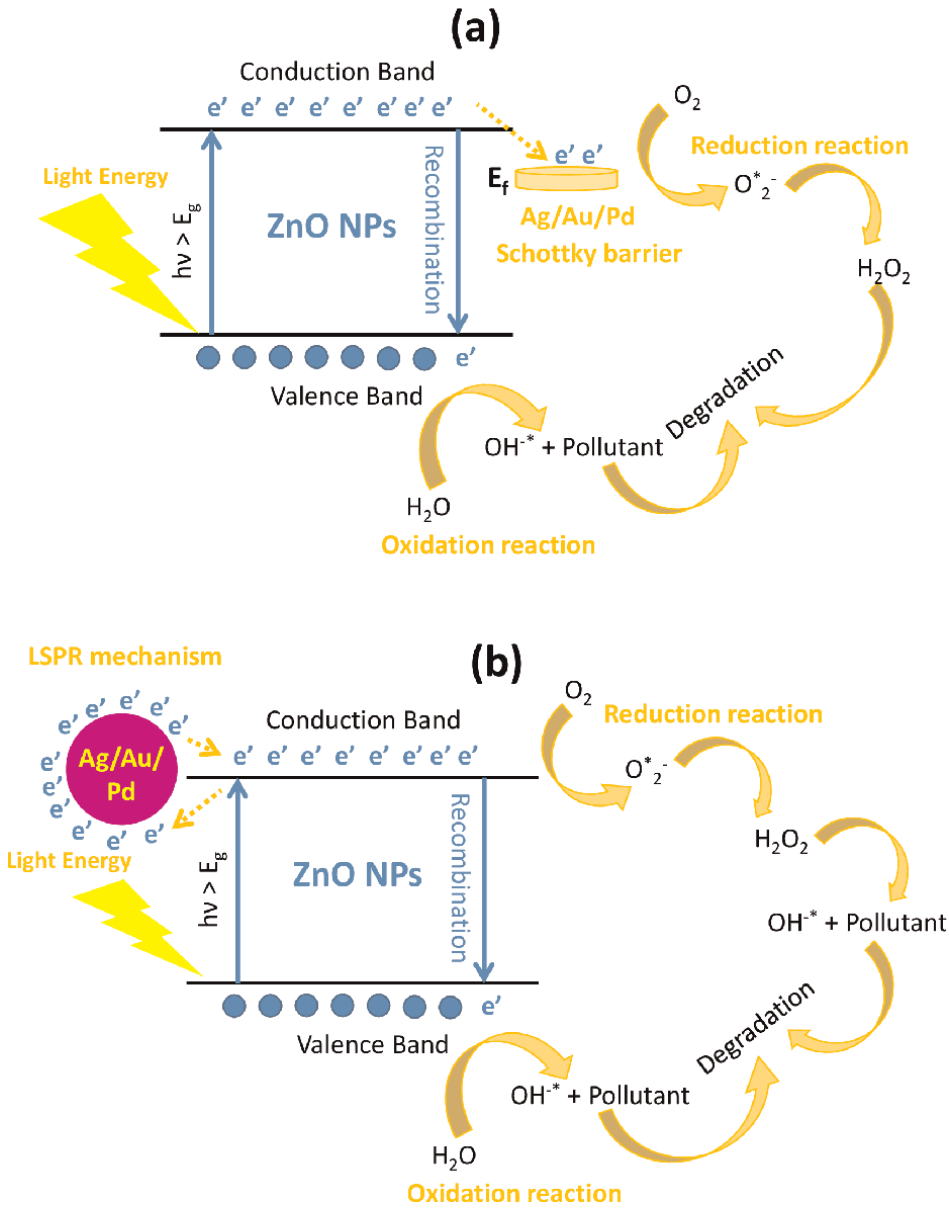

Figure 5.
The schematic of noble metal-doped ZnO NPs reaction mechanism of photocatalytic degradation. (a) Schottky barrier formation. (b) LSPR mechanism.

$$\mathrm{ZnO} + \mathrm{hv} \rightarrow \mathrm{ZnO}\left(\mathrm{h}^{+}\right)_{\mathrm{VB}} + \mathrm{ZnO}\left(\mathrm{e}^{-}\right)_{\mathrm{CB}}$$

$$(\mathrm{Ag/Au/Pd}) + \mathrm{hv} \rightarrow \left(\mathrm{Ag}^{+}/\mathrm{Au}^{+}/\mathrm{Pd}^{+}\right) + \left(\mathrm{e}^{-}\right)_{\mathrm{SPR}}$$

$$\mathrm{O_2} + \left(\mathrm{e}^{-}\right)_{\mathrm{SPR}} \rightarrow \mathrm{O_2^{-}}$$

$$\left(\mathrm{e}^{-}\right)_{\mathrm{CB}} + \left(\mathrm{Ag}^{+}/\mathrm{Au}^{+}/\mathrm{Pd}^{+}\right) \rightarrow (\mathrm{Ag/Au/Pd})$$

$$\mathrm{H_2O} \leftrightarrow \left(\mathrm{H}^{+} + \mathrm{OH}^{-}\right) + \left(\mathrm{h}^{+}\right)_{\mathrm{VB}} \rightarrow \mathrm{OH}$$

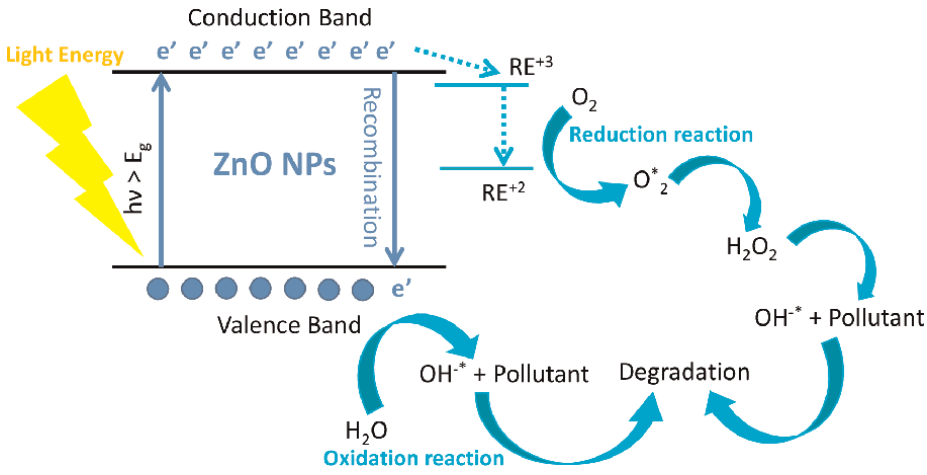

Figure 6.
The schematic of rare earth metal (RE)-doped ZnO NP reaction mechanism of photocatalytic degradation.

$$\text{Dye} + \left(\text{OH}/\text{O}_2^-\right) \rightarrow \text{minimization product } (\text{CO}_2 \text{ and } \text{H}_2\text{O})$$

Figure 6 represents the schematic diagram of rare earth metal (RE)-doped ZnO NP reaction mechanism of photocatalytic degradation and charge transfers.

The route of photocatalytic reaction in ZnO NPs doped with a non-metallic element (C, N, and S) exhibits the absorbance of incident light. The incident light generates the exitron in the ZnO NPs which get captured by the induced crystal defects by the dopant atoms such as substitutional and interstitial defects. These defects act as the energy band and slightly rise in the VB, hence reducing the band gap and responding to the visible light energies. The excited electron reduces to produce the superoxide ion and holes in VB oxide to form OH ions. Both reactive species degrade the probe dye and organic pollutant.

$$\text{ZnO} + \text{hv} \rightarrow \text{ZnO}\left(\text{h}^+\right)_{\text{VB}} + \text{ZnO}\left(\text{e}^-\right)_{\text{CB}}$$

$$\left(\text{e}^-\right)_{\text{CB}} + \left(\text{RE}^{3+}\right) \rightarrow \left(\text{RE}^{2+}\right)$$

$$\text{O}_2 + \left(\text{RE}^{2+}\right) \rightarrow \text{O}_2^-$$

$$\text{H}_2\text{O} \leftrightarrow \left(\text{H}^+ + \text{OH}^-\right) + \left(\text{h}^+\right)_{\text{VB}} \rightarrow \text{OH}$$

$$\text{Dye} + \left(\text{OH}/\text{O}_2^-\right) \rightarrow \text{minimization product } (\text{CO}_2 \text{ and } \text{H}_2\text{O})$$

As doping of different elements results in the better charge separation and effectively enhance the photocatalytic activity, over doping creates excess traps for the charges which limits the generation of reactive species. Hence, the redox reaction gets limited. The composite of ZnO with other semiconductors creates the Z-scheme to work effectively to degrade the organic pollutants.

Generalising the mechanism of ZnO-based nanocomposites is not possible due to the difference in the bandgap of each metal oxide in compression of the ZnO NPs. However, the synthesis of nanocomposite supports the functionalization in visible and UV ranges due to the different photo response of the wavelength of every material. **Figure 7**

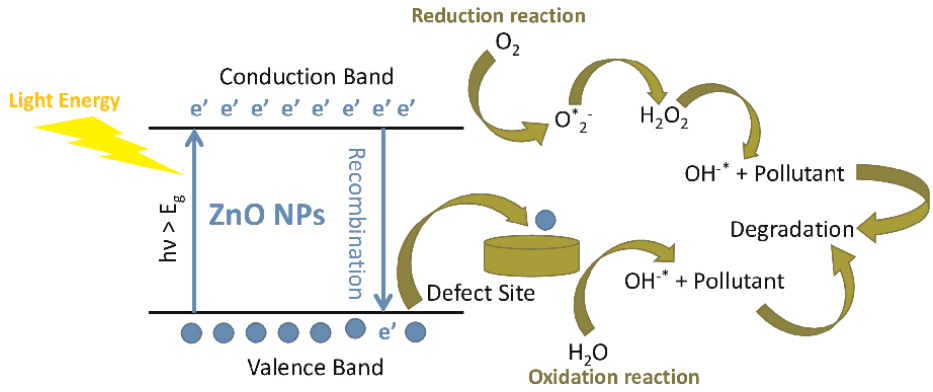

Figure 7.
The schematic of non-metallic element (C, N, and S)-doped ZnO NP reaction mechanism of photocatalytic degradation.

represents the schematic diagram of non-metallic element (C, N, and S)-doped ZnO NP reaction mechanism of photocatalytic degradation and charge transfers.

However, the supporting material assists with the charge separation along with the mechanical strength to the system. Upon the irradiation with light, the exitron pair is generated within the ZnO/carbonaceous nanocomposite. The charges produced at the heterojunction migrate to the surface and degrade to the organic pollutant.

In case of the potential of in g-C_3N_4 VB is lower than the oxidation standard potential (1.22 eV) which will limit the oxidation of the holes at the lower level, the electrons from CB of ZnO would not be able to reduce at the lower energy levels then the standard reduction levels. (−0.877 eV). The position of energy levels of both materials makes it a Z-scheme heterogeneous photocatalyst. The electron from the CB of the ZnO NPs moves to the CB of g-C_3N_4 where they reduce the oxygen molecules to the super oxide ion. However, the hole transfers from the VB of the g-C_3N_4 to the VB of the ZnO and oxidize water molecules to OH ions. The reactive species interact with

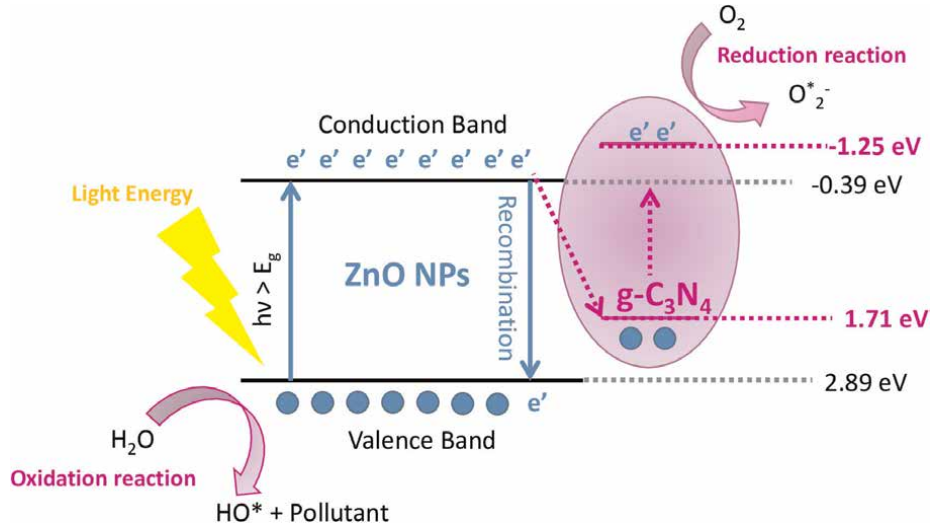

Figure 8.
The schematic diagram of nanocomposite of the g-C_3N_4 @ ZnO nanocomposite photocatalytic mechanism.

the organic pollutants and degrade them effectively. Hence, the difference in the energy levels and their response to the different wavelengths of light make these nanocomposites highly effective in visible light. **Figure 8** represents the schematic diagram of nanocomposite of the g-C_3N_4 @ ZnO nanocomposite reaction mechanism of photocatalytic degradation and charge transfers.

5. Challenges and future perspectives

The following are the current challenges in the design of ZnO-based photocatalysts.

5.1 Challenges in ZnO catalysis

The synthetic dyes are used as the permanent coloring agent in the textile industry. Such dyes are mostly toxic and carcinogenic which are extremely fatal for health and the environment. The untreated dye hinders the natural activities such as photosynthesis and reduces or aborts the underwater vegetation which results in an ecological imbalance. The treatment for these dyes before entering to the main water bodies reduces such threat.

Photocatalytic degradation is a time saving and cost-effective technique without any toxic by-products. ZnO is proven photocatalyst over the last few decades due to its nontoxicity and large-scale practical synthesis techniques. However, the there are some challenges with ZnO NPs be used as photocatalytic in large scale treatment plants.

5.1.1 Stability and reusability

An exceptionally large variety of morphology and nanocomposites is designed by ZnO NPs by using different synthesis techniques. Yet there is not accurate mechanism advanced for the morphological changes which makes the use of the designed very tricky. Every morphological structure responds differently light and to the probe pollutant as they have different reactive sites and polar surface. Such difference makes the ZnO more challenging to handle the stability during the synthesis.

The reusability is particularly an important parameter to upscale the use of any photocatalyst in the treatment plant. The recycling is a limiting factor as the reduced amount of nanomaterial will disturb the reaction kinetics. Moreover, the used material will flow to the mainstream raising another environmental concern.

5.1.2 Efficiency limitations

The limitation over the efficiency of the photocatalyst is also a mitigating factor for the practical application of them in the large scale. The efficiency gets limited if there is a small surface area or the pore size is not accessible by the subjected pollutant molecule. The availability of reactive radicals to the pollutant is very fundamental for the redox reaction. The larger surface area and effective pore sizes enable photocatalysts to degrade organic waste effectively.

5.1.3 Cost-effective scaling

The cost is always a primary factor for the scale up of any scientific advancement. The above factors are the restricting factors for ZnO NPs and nanocomposites to be used at the larger scale. The unsupervised overflow of the catalyst and recycling is also a crucial factor to be addressed to industrialize the setup.

5.2 Future perspective of ZnO catalysis

The current study includes the experimental methods of trial-and-error analysis. The modern approach of modeling and computational analysis will enable scientists to save time and energy while precisely designing the photocatalyst using the current database. It will also give insights into the research to address the issue beforehand in the upscaling of this technology. The possibility of exploring and developing an effective photocatalyst is endless.

The toxicity and other environmental concerns of the synthesis techniques can be limited by using the green chemistry. The further research is needed to improve this synthesis technique and develop an effective photocatalyst. Moreover, it develops the photocatalyst that is responsive to the visible range and increase light harvesting factor.

The difference in the performance of photocatalysts over different organic pollutants despite having the same functional group needs more investigation. The insight will enable scientists to develop the more sensitive site over the photocatalyst which will allow the specific degradation of the pollutants. There is huge gap to develop the insight of photodegradation phenomena and predict the interactions between catalyst and organic pollutants.

The combination of ZnO NPs with different semiconductors, carbonaceous material, 2-D supports, and conductive polymers has been the recent areas to investigate. The possibility of such systems is endless.

6. Conclusion

The chapter gives the comprehensive view about the recent synthesis technique of ZnO and its nanocomposites with the improved photocatalytical degradation of textile dyes. However, this article only gives the overview of the scientific work and the insight of the shift of synthesis approach in the last few years. The possible mechanisms are discussed to develop better insight for the improvement in the design systems. The impact of different doping are well studied, and moreover, the support materials are also included. The changes in the bandgap, morphology, and particle size have their limitation. The increase in the surface area is viewed in the perspective of photocatalytic performance. The modern technique of synthesis of ZnO NPs and its composites by green chemistry is investigated while keeping the environmental signature in mind. The organic plants, bacterial and other animal sources are used as precursors during the synthesis which are easily accessible or extracted. Many of them act as reducing agent in the reaction process. Some may act as capping agents to limit the agglomeration and helps retaining the small size with a large surface area. The present bottle neck of the prepared ZnO NPs is discussed in detail with their suggested solutions. The possible approaches to increase light harvesting for efficient photocatalysis by doping and designed heterogeneous photocatalyst by the combining

with other semiconductors or decorating ZnO NPs on carbonaceous materials as absorbate. The support materials not only enable the composite to respond in visible light but also the enable the better charge separation, with an increase in charge between the materials as the Z-scheme, hence enhancing the performance. The oxidation and reduction potential of both materials are chosen with careful study to assist the generation of the reactive radicals for the redox reaction. The supporting materials have a large surface area to provide the spread of charges and provide an effective surface area for the dye molecules to interact with the surface of the photocatalyst and degrade. Moreover, these supporting materials act as cocatalysts which further increase the efficiency. The choice of dopant, levels of dopant percentages, and synthesis approach are major parameters for crystal structures, induced defects, tailor bandgap, surface area, and particle size which influence the photocatalytic efficiency. The literature review gives us that the comprehension view of morphological and structural changes in ZnO has significantly increased the efficiency of the photocatalytic activity under visible light.

Many parameters of photocatalytic reaction determine the rate and effectivity of the redox reaction other than the material modification of the ZnO photocatalyst. The structure of organic pollutant, dose of pollutant and the catalyst, pH of the mixture, temperature, the integrity of the light, the source of the radiation, and the number of the redox radical produced at the surface significantly affect the degradation of dyes. The chapter details the azonic dye degradation by ZnO NPs and its nanocomposites as photocatalyst. Numerous factors that are mentioned above are taken into account while studying the variation of results and trends. This chapter can be a huge help for the scientists to understand the challenges and future perspectives of ZnO as photocatalysts under the lens of recent research advancements.

Acknowledgements

This research was supported by the MSIT (Ministry of Science and ICT), Korea, under the ITRC (Information Technology Research Center) support program (IITP-2024-2020-0-01655) supervised by the IITP (Institute of Information and Communications Technology Planning and Evaluation).

DOI: http://dx.doi.org/10.5772/intechopen.1007849

Author details

Maryam Basit[1], Muhammad Aftab Akram[2], Mohsin Saleem[1,3,4], Sofia Javed[1*] and Jung-Hyuk Koh[3,4*]

1 School of Chemical and Materials Engineering, National University of Sciences and Technology, SCME, NUST, Islamabad, Pakistan

2 Pak-Austria Fachhochschule: Institute of Applied Sciences, Department of Materials Science and Engineering, Mang, Khanpur Road, Haripur, KPK, Pakistan

3 School of Electrical and Electronic Engineering, Chung-Ang University, Seoul, Republic of Korea

4 Graduate School of Intelligent Energy and Industry, Chung-Ang University, Heukseok-ro, Seoul, Republic of Korea

*Address all correspondence to: sofia.javed@scme.nust.edu.pk; jhkoh@cau.ac.kr

IntechOpen

References

[1] Kishore S et al. A comprehensive review on removal of pollutants from wastewater through microbial nanobiotechnology -based solutions. Biotechnology and Genetic Engineering Reviews. 2024;**40**(4):3087-3112. DOI: 10.1080/02648725.2022.2106014

[2] Naghdi S, Shahrestani MM, Zendehbad M, Djahaniani H, Kazemian H, Eder D. Recent advances in application of metal-organic frameworks (MOFs) as adsorbent and catalyst in removal of persistent organic pollutants (POPs). Journal of Hazardous Materials. 2023;**442**:130127

[3] Ruan W, Hu J, Qi J, Hou Y, Zhou C, Wei X. Removal of dyes from wastewater by nanomaterials: A review. Advanced Materials Letters. 2019;**10**(1): 9-20

[4] Jiang T et al. Degradation of organic pollutants from water by biochar-assisted advanced oxidation processes: Mechanisms and applications. Journal of Hazardous Materials. 2023;**442**:130075

[5] Andronic L, Lelis M, Enesca A, Karazhanov S. Photocatalytic activity of defective black-titanium oxide photocatalysts towards pesticide degradation under UV/VIS irradiation. Surfaces and Interfaces. 2022;**32**:102123

[6] Qiao X, Xiong Z, Wang Y, Wang R, Zhang Z, Qiu S. Double shelled titanium dioxide@ mesoporous organosilica nanotube as an amphiphilic photoactive nanoreactor for efficient photocatalytic oxidation of styrene. Journal of Colloid and Interface Science. 2023;**651**:235-242

[7] Karajz D, Szilágyi IM. Review of photocatalytic ZnO nanomaterials made by atomic layer deposition. Surfaces and Interfaces. 2023;**40**:103094

[8] Zheng F et al. Au-sensitised TiO2 and ZnO nanoparticles for broadband pharmaceuticals photocatalytic degradation in water remediation. Colloids and Surfaces A: Physicochemical and Engineering Aspects. 2023;**671**:131594

[9] Puri N, Gupta A. Water remediation using titanium and zinc oxide nanomaterials through disinfection and photo catalysis process: A review. Environmental Research. 2023;**227**: 115786

[10] Agarwal H, Menon S, Kumar SV, Rajeshkumar S. Mechanistic study on antibacterial action of zinc oxide nanoparticles synthesized using green route. Chemico-Biological Interactions. 2018;**286**:60-70

[11] Basit M, Javed S, Ali S, Qureshi AA, Gul IH, Akram MA. Recent innovations in low dimensional ZnO nanostructures/ nanocomposites for photocatalytic degradation. Materials Innovafions. 2022;**2**(9):225-254

[12] Li Q, Cui Y, Lin J, Zhao C, Ding L. Synthesis of carbon microsphere-assisted snowflake-like ZnO nanomaterials for selective detection of NO2 at room temperature. Journal of Industrial and Engineering Chemistry. 2022;**110**: 542-551

[13] Suganya Josephine GA, Jayaprakash K, Meenakshi G, Sivasamy A, Nirmala Devi G, Viswanath RN. Photocatalytically active ZnO flaky nanoflowers for environmental remediation under solar light irradiation: Effect of morphology on photocatalytic activity. Bulletin of Materials Science. 2021;**44**(4):247. DOI: 10.1007/s12034-021-02531-1

[14] Bi T, Du Z, Chen S, He H, Shen X, Fu Y. Preparation of flower-like ZnO photocatalyst with oxygen vacancy to enhance the photocatalytic degradation of methyl orange. Applied Surface Science. 2023;**614**:156240

[15] Kaliraj L, Ahn JC, Rupa EJ, Abid S, Lu J, Yang DC. Synthesis of panos extract mediated ZnO nano-flowers as photocatalyst for industrial dye degradation by UV illumination. Journal of Photochemistry and Photobiology B: Biology. 2019;**199**:111588. DOI: 10.1016/j.jphotobiol.2019.111588

[16] Araujo FP et al. Eco-friendly synthesis and photocatalytic application of flowers-like ZnO structures using Arabic and Karaya gums. International Journal of Biological Macromolecules. 2020;**165**:2813-2822. DOI: 10.1016/j.ijbiomac.2020.10.132

[17] Jorge FE, Tienne LGP, de Marques MFV, Monteiro SN. Evaluation of thermoelectric properties of hybrid polyaniline nanocomposites incorporated with graphene oxide and zinc oxide with different morphologies. Journal of Materials Research and Technology. 2023;**27**:6822-6832

[18] Negi A, Gangwar R, Kumar Vishwakarma R, Singh Negi D. Antibacterial, antioxidant and photodegradation potential of ZnO nanoparticles mediated via roots of Taraxacum officinale radix. Materials Today: Proceedings. 2022;**57**:2435-2443. DOI: 10.1016/j.matpr.2022.02.019

[19] Ong CB, Ng LY, Mohammad AW. A review of ZnO nanoparticles as solar photocatalysts: Synthesis, mechanisms and applications. Renewable and Sustainable Energy Reviews. 2018;**81**:536-551

[20] Raha S, Ahmaruzzaman M. ZnO nanostructured materials and their potential applications: Progress, challenges and perspectives. Nanoscale Advances. 2022;**4**(8):1868-1925

[21] Noureen L, Wang Q, Humayun M, Shah WA, Xu Q, Wang X. Recent advances in structural engineering of photocatalysts for environmental remediation. Environmental Research. 2023;**219**:115084

[22] Gang R et al. Fabrication of MoS2 QDs/ZnO nanosheet 0D/2D heterojunction photocatalysts for organic dyes and gaseous heavy metal removal. Journal of Colloid and Interface Science. 2020;**579**:853-861. DOI: 10.1016/j.jcis.2020.06.116

[23] Singh R, Verma K, Patyal A, Sharma I, Barman PB, Sharma D. Nanosheet and nanosphere morphology dominated photocatalytic & antibacterial properties of ZnO nanostructures. Solid State Sciences. 2019;**89**:1-14. DOI: 10.1016/j.solidstatesciences.2018.12.011

[24] Choudhury SP, Nakate UT. Study of improved VOCs sensing properties of boron nitride quantum dots decorated nanostructured 2D-ZnO material. Ceramics International. 2022;**48**(19):28935-28941

[25] Sowbhagya NPS, Pasha M. Novel bio-mediated preparation of ZnO-ZnS binary nanocomposite from Zn (NO3) 2·6H2O, musk melon pulp and waste chicken feathers: A comparative study of enhanced photocatalytic and biological activities. Social Science Research Network, Rochester, NY. 2023:4367852. DOI: 10.2139/ssrn.4367852

[26] Ballesteros-Balbuena M et al. Photocatalytic urchin-like and needle-like ZnO nanostructures synthetized by thermal oxidation. Materials Chemistry and Physics. 2020;**244**:122703. DOI: 10.1016/j.matchemphys.2020.122703

[27] Wang Y, Zhang X, Hou C. Facile synthesis of Al-doping 1D ZnO nanoneedles by co-precipitation method for efficient removal of methylene blue. Nano-Structures & Nano-Objects. 2018; **16**:250-257. DOI: 10.1016/j.nanoso.2018.07.001

[28] Smazna D et al. Mutual interplay of ZnO micro- and nanowires and methylene blue during cyclic photocatalysis process. Journal of Environmental Chemical Engineering. 2019;**7**(2):103016. DOI: 10.1016/j.jece.2019.103016

[29] Azzouz I et al. Zinc oxide nano-enabled microfluidic reactor for water purification and its applicability to volatile organic compounds. Microsystems & Nanoengineering. 2018; **4**(1):1-7. DOI: 10.1038/micronano.2017.93

[30] Choudhary S, Sahu K, Bisht A, Satpati B, Mohapatra S. Rapid synthesis of ZnO nanowires and nanoplates with highly enhanced photocatalytic performance. Applied Surface Science. 2021;**541**:148484. DOI: 10.1016/j.apsusc.2020.148484

[31] De Peres ML, Delucis RDA, Amico SC, Gatto DA. Zinc oxide nanoparticles from microwave-assisted solvothermal process: Photocatalytic performance and use for wood protection against xylophagous fungus. Nanomaterials and Nanotechnology. 2019;**9**: 184798041987620. DOI: 10.1177/1847980419876201

[32] Tumram SK, Bandyopadhyaya R. Zinc oxide nanostructures: Experiments probing their transformation to nanorods. Materials Science and Engineering: B. 2023;**296**:116569

[33] Mohammed R, Ali MEM, Gomaa E, Mohsen M. Green ZnO nanorod material for dye degradation and detoxification of pharmaceutical wastes in water. Journal of Environmental Chemical Engineering. 2020;**8**(5):104295. DOI: 10.1016/j.jece.2020.104295

[34] Thi TUD, Nguyen TT, Thi YD, Thi KHT, Phan BT, Pham KN. Green synthesis of ZnO nanoparticles using orange fruit peel extract for antibacterial activities. RSC Advances. 2020;**10**(40): 23899-23907

[35] Jafarirad S, Mehrabi M, Divband B, Kosari-Nasab M. Biofabrication of zinc oxide nanoparticles using fruit extract of Rosa canina and their toxic potential against bacteria: A mechanistic approach. Materials Science and Engineering: C. 2016;**59**:296-302

[36] Abou Zeid S, Leprince-Wang Y. Advancements in ZnO-based Photocatalysts for water treatment: A comprehensive review. Crystals. 2024;**14**(7):611

[37] Raizada P, Sudhaik A, Singh P. Photocatalytic water decontamination using graphene and ZnO coupled photocatalysts: A review. Materials Science for Energy Technologies. 2019;**2**(3):509-525. DOI: 10.1016/j.mset.2019.04.007

[38] Dimapilis EAS, Hsu C-S, Mendoza RMO, Lu M-C. Zinc oxide nanoparticles for water disinfection. Sustainable Environment Research. 2018;**28**(2):47-56

[39] Rezaei A, Katoueizadeh E, Zebarjad SM. Investigating of the influence of zinc oxide nanoparticles morphology on the properties of electrospun polyvinyl alcohol/chitosan (PVA/CS) nanofibers. Journal of Drug Delivery Science and Technology. 2023;**86**:104712

[40] Widiyandari H, Al Ja'farawy MS, Parasdila H, Astuti Y, Arutanti O, Mufti

N. Temperature impact on the morphological evolution of nitrogen-doped carbon quantum dot-decorated zinc oxide and its influence on highly efficient visible-light photocatalyst. Physica B: Condensed Matter. 2023;**669**: 415293

[41] Zheng ALT, Abdullah CAC, Chung ELT, Andou Y. Recent progress in visible light-doped ZnO photocatalyst for pollution control. International journal of Environmental Science and Technology. 2023;**20**(5):5753-5772. DOI: 10.1007/s13762-022-04354-x

[42] Dejam L et al. ZnO, Cu-doped ZnO, Al-doped ZnO and Cu-Al doped ZnO thin films: Advanced micro-morphology, crystalline structures and optical properties. Results in Physics. 2023;**44**: 106209

[43] Belousov AS. Theoretical foundations of photocatalysis. In: Fukina DG, Belousov AS, Suleimanov EV, editors. Pyrochlore Oxides, Green Chemistry and Sustainable Technology. Cham: Springer Nature Switzerland; 2024. pp. 61-95. DOI: 10.1007/978-3-031-46764-6_3

[44] Fujishima A, Honda K. Electrochemical photolysis of water at a semiconductor electrode. Nature. 1972; **238**(5358):37-38

[45] Kiwaan HA, Atwee TM, Azab EA, El-Bindary AA. Efficient photocatalytic degradation of acid red 57 using synthesized ZnO nanowires. Journal of the Chinese Chemical Society. 2019;**66** (1):89-98. DOI: 10.1002/jccs.201800092

[46] Commandeur D, Brown G, Hills E, Spencer J, Chen Q. Defect-rich ZnO Nanorod arrays for efficient solar water splitting. ACS Applied Nano Materials. 2019;**2**(3):1570-1578. DOI: 10.1021/acsanm.9b00047

[47] Deng H et al. S-scheme heterojunction based on p-type ZnMn2O4 and n-type ZnO with improved photocatalytic CO_2 reduction activity. Chemical Engineering Journal. 2021;**409**:127377

[48] Kumar N, Yadav S, Mittal A, Kumari K. Photocatalysis by zinc oxide- based nanomaterials. In: Nanostructured Zinc Oxide. Synthesis, properties and application, Metal Oxides. Elsevier. 2021. pp. 393-457. DOI: 10.1016/B978-0-12-818900-9.00005 -X

[49] Dörr TS et al. Ordered mesoporous TiO_2 gyroids: Effects of pore architecture and Nb-doping on photocatalytic hydrogen evolution under UV and visible irradiation. Advanced Energy Materials. 2018;**8**(36):1802566. DOI: 10.1002/aenm.201802566

[50] Belver C, Bedia J, Gómez-Avilés A, Peñas-Garzón M, Rodriguez JJ. Semiconductor photocatalysis for water Purification., Nanoscale Materials in Water Purification., Micro and Nano Technologies. Elsevier; 2019. pp. 581-651. DOI: 10.1016/B978-0-12-813926-4.00028-8

[51] Russo V, Hmoudah M, Broccoli F, Iesce MR, Jung O-S, Di Serio M. Applications of metal organic frameworks in wastewater treatment: A review on adsorption and photodegradation. Frontiers in Chemical Engineering. 2020;**2**:581487

[52] Nandi P, Das D. Photocatalytic degradation of Rhodamine-B dye by stable ZnO nanostructures with different calcination temperature induced defects. Applied Surface Science. 2019;**465**: 546-556

[53] Tichapondwa SM, Newman JP, Kubheka O. Effect of TiO2 phase on the photocatalytic degradation of methylene

blue dye. Physics and Chemistry of the Earth, Parts A/B/C. 2020;**118**:102900

[54] Fauzi AA et al. A critical review on relationship of CeO2-based photocatalyst towards mechanistic degradation of organic pollutant. Chemosphere. 2022;**286**:131651

[55] Raizada P et al. Engineering nanostructures of CuO-based photocatalysts for water treatment: Current progress and future challenges. Arabian Journal of Chemistry. 2020;**13** (11):8424-8457

[56] Sun C et al. Recent intensification strategies of SnO2-based photocatalysts: A review. Chemical Engineering Journal. 2022;**427**:131564

[57] Prakash K, Senthil Kumar P, Pandiaraj S, Saravanakumar K, Karuthapandian S. Controllable synthesis of SnO_2 photocatalyst with superior photocatalytic activity for the degradation of methylene blue dye solution. Journal of Experimental Nanoscience. 2016;**11**(14):1138-1155. DOI: 10.1080/17458080.2016.1188222

[58] Shandilya P, Sambyal S, Sharma R, Mandyal P, Fang B. Properties, optimized morphologies, and advanced strategies for photocatalytic applications of WO3 based photocatalysts. Journal of Hazardous Materials. 2022;**428**:128218

[59] Souza RP et al. Photocatalytic activity of TiO2, ZnO and Nb2O5 applied to degradation of textile wastewater. Journal of Photochemistry and Photobiology A: Chemistry. 2016;**329**:9-17

[60] Jin F, Ma X, Guo S-Q. F-doped hierarchical Nb2O5: Structural, optical and photocatalytic performance. Materials Letters. 2023;**347**:134664

[61] Abreu E et al. Degradation of emerging contaminants: Effect of thermal treatment on nb2o5 as photocatalyst. Journal of Photochemistry and Photobiology A: Chemistry. 2021; **419**:113484

[62] Kumar S, Kaushik RD, Purohit LP. Novel ZnO tetrapod-reduced graphene oxide nanocomposites for enhanced photocatalytic degradation of phenolic compounds and MB dye. Journal of Molecular Liquids. 2021;**327**:114814

[63] Tavker N, Sharma M. Designing of waste fruit peels extracted cellulose supported molybdenum sulfide nanostructures for photocatalytic degradation of RhB dye and industrial effluent. Journal of Environmental Management. 2020;**255**:109906

[64] Affat SS. Classifications, advantages, disadvantages, toxicity effects of natural and synthetic dyes: A review. University of Thi-Qar Journal of Science. 2021;**8**(1): 130-135

[65] Hitam CN, Jalil AA. A review on exploration of Fe2O3 photocatalyst towards degradation of dyes and organic contaminants. Journal of Environmental Management. 2020;**258**:110050

[66] Zafar MN, Dar Q, Nawaz F, Zafar MN, Iqbal M, Nazar MF. Effective adsorptive removal of azo dyes over spherical ZnO nanoparticles. Journal of Materials Research and Technology. 2019;**8**(1):713-725

[67] Yu C-X et al. Highly efficient and selective removal of anionic dyes from aqueous solution by using a protonated metal-organic framework. Journal of Alloys and Compounds. 2021;**853**:157383

[68] Azam K et al. A review on activated carbon modifications for the treatment of wastewater containing anionic dyes. Chemosphere. 2022;**306**:135566

[69] Sanakousar FM, Vidyasagar CC, Jiménez-Pérez VM, Prakash K. Recent progress on visible-light-driven metal and non-metal doped ZnO nanostructures for photocatalytic degradation of organic pollutants. Materials Science in Semiconductor Processing. 2022;**140**:106390

[70] Davis K, Yarbrough R, Froeschle M, White J, Rathnayake H. Band gap engineered zinc oxide nanostructures via a sol-gel synthesis of solvent driven shape-controlled crystal growth. RSC Advances. 2019;**9**(26): 14638-14648

[71] Qi K, Cheng B, Yu J, Ho W. Review on the improvement of the photocatalytic and antibacterial activities of ZnO. Journal of Alloys and Compounds. 2017;**727**:792-820

[72] Prabakaran E, Pillay K. Synthesis of N-doped ZnO nanoparticles with cabbage morphology as a catalyst for the efficient photocatalytic degradation of methylene blue under UV and visible light. RSC Advances. 2019;**9**(13):7509-7535

[73] Schmidt-Mende L, MacManus-Driscoll JL. ZnO–nanostructures, defects, and devices. Materials Today. 2007;**10**(5):40-48

[74] Etacheri V, Roshan R, Kumar V. Mg-doped ZnO nanoparticles for efficient sunlight-driven Photocatalysis. ACS Applied Materials & Interfaces. 2012;**4**(5):2717-2725. DOI: 10.1021/am300359h

[75] Prakash T, Jayaprakash R, Espro C, Neri G, Ranjith Kumar E. Effect of Sn doping on microstructural and optical properties of ZnO nanoparticles synthesized by microwave irradiation method. Journal of Materials Science. 2014;**49**(4):1776-1784. DOI: 10.1007/s10853-013-7865-9

[76] Kadhim MJ, Mahdi MA, Selman AM, Al-Ani SJ, Hassan JJ, Ahmed NM. The most important parameters that affect the photocatalytic activity of ZnO nanostructures against organic dyes: A review. Iranian Journal of Catalysis. 2023;**13**(1):1-21

[77] Basit M, Abbas M, Ahmad N, Javed S, Shah NA. Synthesis of ZnO/CNT nanocomposites for ultraviolet sensors. Frontiers in Materials. 2022;**9**:835521

[78] Rangel WM, Santa RAAB, Riella HG. A facile method for synthesis of nanostructured copper (II) oxide by coprecipitation. Journal of Materials Research and Technology. 2020;**9**(1): 994-1004

[79] Kotresh MG, Patil MK, Inamdar SR. Reaction temperature based synthesis of ZnO nanoparticles using co-precipitation method: Detailed structural and optical characterization. Optik. 2021;**243**:167506

[80] Vasantharaj S et al. Enhanced photocatalytic degradation of water pollutants using bio-green synthesis of zinc oxide nanoparticles (ZnO NPs). Journal of Environmental Chemical Engineering. 2021;**9**(4):105772

[81] Adam RE, Pozina G, Willander M, Nur O. Synthesis of ZnO nanoparticles by co-precipitation method for solar driven photodegradation of congo red dye at different pH. Photonics and Nanostructures-Fundamentals and Applications. 2018;**32**:11-18

[82] Lad P, Pathak V, Thakkar AB, Thakor P, Deshpande MP, Pandya S. ZnO nanoparticles synthesized by precipitation method for solar-driven photodegradation of methylene blue dye and its potential as an anticancer agent. Brazilian Journal of Physics. 2023;**53**(3): 63. DOI: 10.1007/s13538-023-01278-w

[83] Krobthong S, Rungsawang T, Wongrerkdee S. Comparison of ZnO nanoparticles prepared by precipitation and combustion for UV and sunlight-driven photocatalytic degradation of methylene blue. Toxics. 2023;**11**(3):266

[84] Chen X, Wu Z, Liu D, Gao Z. Preparation of ZnO photocatalyst for the efficient and rapid photocatalytic degradation of azo dyes. Nanoscale Research Letters. 2017;**12**(1):143. DOI: 10.1186/s11671-017-1904-4

[85] Köse H, Karaal Ş, Aydın AO, Akbulut H. A facile synthesis of zinc oxide/multiwalled carbon nanotube nanocomposite lithium ion battery anodes by sol–gel method. Journal of Power Sources. 2015;**295**:235-245

[86] Arya S et al. Review—Influence of processing parameters to control morphology and optical properties of sol-gel synthesized ZnO nanoparticles. ECS Journal of Solid State Science and Technology. 2021;**10**(2):023002. DOI: 10.1149/2162-8777/abe095

[87] Ben Amor I, Hemmami H, Laouini SE, Mahboub MS, Barhoum A. Sol-gel synthesis of ZnO nanoparticles using different chitosan sources: Effects on antibacterial activity and photocatalytic degradation of AZO dye. Catalysts. 2022; **12**(12):1611:1-16. Art. no. 12. DOI: 10.3390/catal12121611

[88] Saravanan R, Gupta VK, Narayanan V, Stephen A. Comparative study on photocatalytic activity of ZnO prepared by different methods. Journal of Molecular Liquids. 2013;**181**:133-141

[89] Lal M, Sharma P, Singh L, Ram C. Photocatalytic degradation of hazardous Rhodamine B dye using sol-gel mediated ultrasonic hydrothermal synthesized of ZnO nanoparticles. Results in Engineering. 2023;**17**:100890

[90] Manuchehri QS, Assi N, Pourmand S, Darwish M, Pakzad A. Photocatalytic activity of ZnO nanoparticles prepared by a microwave method in ethylene glycol and polyethylene glycol media: A comparative study. Journal of Nano Research. 2016;**42**:53-64

[91] Al-Gharibi MA, Kyaw HH, Al-Sabahi JN, Zar Myint MT, Al-Sharji ZA, Al-Abri MZ. Silver nanoparticles decorated zinc oxide nanorods supported catalyst for photocatalytic degradation of paracetamol. Materials Science in Semiconductor Processing. 2021;**134**:105994. DOI: 10.1016/j.mssp.2021.105994

[92] Bhapkar AR, Bhame S. A review on ZnO and its modifications for photocatalytic degradation of prominent textile effluents: Synthesis, mechanisms, and future directions. Journal of Environmental Chemical Engineering. 2024;**12**(3):112553. DOI: 10.1016/j.jece.2024.112553

[93] Arellano-Cortaza M, Ramírez-Morales E, Pal U, Pérez-Hernández G, Rojas-Blanco L. pH dependent morphology and texture evolution of ZnO nanoparticles fabricated by microwave-assisted chemical synthesis and their photocatalytic dye degradation activities. Ceramics International. 2021; **47**(19):27469-27478

[94] Ahammed KR et al. Microwave assisted synthesis of zinc oxide (ZnO) nanoparticles in a noble approach: Utilization for antibacterial and photocatalytic activity. SN Applied Sciences. 2020;**2**(5):955. DOI: 10.1007/s42452-020-2762-8

[95] Resende Leite R et al. Precursor effect on the hydrothermal synthesis of pure ZnO nanostructures and enhanced photocatalytic performance for norfloxacin degradation. Chemical Engineering Journal. 2024;**496**:154374. DOI: 10.1016/j.cej.2024.154374

[96] Sansenya T et al. Hydrothermal synthesis of ZnO photocatalyst for detoxification of anionic azo dyes and antibiotic. Journal of Physics and Chemistry of Solids. 2022;**160**:110353

[97] Lal M, Sharma P, Ram C. Optical, structural properties and photocatalytic potential of Nd-ZnO nanoparticles synthesized by hydrothermal method. Results in Optics. 2023;**10**:100371. DOI: 10.1016/j.rio.2023.100371

[98] Ghoderao KP, Jamble SN, Kale RB. Influence of pH on hydrothermally derived ZnO nanostructures. Optik. 2018;**156**:758-771

[99] Srinatha N, Kumar KJR, Kumar MRS, Pattar KV, Madhu A, Angadi B. Combustion synthesis of Al- doped ZnO nanoparticles using a new fuel and the study of its structural, micro-structural and optical properties. Applied Nanoscience. 2021;**11**:1197-1209. DOI: 10.1007/s13204-021-01689-8

[100] Gowthambabu V, Balamurugan A, Bharathy RD, Satheeshkumar S, Kanmani SS. ZnO nanoparticles as efficient sunlight driven photocatalyst prepared by solution combustion method involved lime juice as biofuel. Spectrochimica Acta Part A: Molecular and Biomolecular Spectroscopy. 2021; **258**:119857. DOI: 10.1016/j. saa.2021.119857

[101] Lutukurthi DNVVK, Dutta S, Behara DK. Effect of ignition temperature and fuel amount on photocatalytic activity of solution combustion synthesized ZnO. Ceramics International. 2020;**46**(14):22419-22428. DOI: 10.1016/j.ceramint.2020.05.324

[102] Al-Namshah KS, Shkir M, Ibrahim FA, Hamdy MS. Auto combustion synthesis and characterization of Co doped ZnO nanoparticles with boosted photocatalytic performance. Physica B: Condensed Matter. 2022;**625**:413459. DOI: 10.1016/j.physb.2021.413459

[103] Kotkar SN, Prasad S, Gadekar GP, Rewatkar SB. Auto combustion synthesis of ZnO for degradation of organic dye under natural solar light with bactericidal activity. Inorganic Chemistry Communications. 2022;**144**: 109830

[104] Bhapkar A, Prasad R, Jaspal D, Shirolkar M, Gheisari K, Bhame S. Visible light driven photocatalytic degradation of methylene blue by ZnO nanostructures synthesized by glycine nitrate auto combustion route. Inorganic Chemistry Communications. 2023;**148**: 110311

[105] Rani M, Yadav J, Shanker U, Sillanpää M. Green synthesized zinc derived nanocomposites with enhanced photocatalytic activity: An updated review on structural modification, scientific assessment and environmental applications. Inorganic Chemistry Communications. 2023;**147**:110246

[106] Agarwal H, Kumar SV, Rajeshkumar S. A review on green synthesis of zinc oxide nanoparticles–An eco-friendly approach. Resource-Efficient Technologies. 2017;**3**(4):406-413

[107] Panchal P, Sharma R, Reddy AS, Nehra K, Sharma A, Nehra SP. Eco-friendly synthesis of Ag-doped ZnO/MgO as a potential photocatalyst for antimicrobial and dye degradation applications. Coordination Chemistry Reviews. 2023;**493**:215283

[108] Chaudhuri SK, Malodia L. Biosynthesis of zinc oxide nanoparticles using leaf extract of *Calotropis gigantea*: Characterization and its evaluation on tree seedling growth in nursery stage.

Applied Nanoscience. 2017;**7**(8):501-512. DOI: 10.1007/s13204-017-0586-7

[109] Mirza S et al. Photocatalytic and antibacterial activities of ZnO nanoparticles synthesized from *Lupinus albus* and *Lupinus pilosus* plant extracts via green synthesis approach. Inorganic Chemistry Communications. 2023;**155**: 111124

[110] D'Souza JN, Nagaraja GK, Navada KM, Kouser S, Nityasree BR, Manasa DJ. An ensuing repercussion of solvent alteration on biological and photocatalytic efficacy of *Emilia sonchifolia* (L.) phytochemicals capped zinc oxide nanoparticles. Colloids and Surfaces A: Physicochemical and Engineering Aspects. 2021;**627**:127162

[111] Supin KK, Vasundhara M. Green synthesis of ZnO nanoparticles from neem and eucalyptus leaves extract for photocatalytic applications. Materials Today: Proceedings. 2023;**92**: 787-795

[112] Khalid NR et al. Green synthesis and characterizations of bi-functional Mo-doped ZnO nanostructures for antimicrobial and photocatalytic applications. Materials Chemistry and Physics. 2023;**296**:127306

[113] Priyadharshini SS et al. Photocatalytic degradation of methylene blue and metanil yellow dyes using green synthesized zinc oxide (ZnO) nanocrystals. Crystals. 2021;**12**(1):22

[114] Vinayagam R, Pai S, Murugesan G, Varadavenkatesan T, Selvaraj R. Synthesis of photocatalytic zinc oxide nanoflowers using Peltophorum pterocarpum pod extract and their characterization. Applied Nanoscience. 2023;**13**(1):847-857. DOI: 10.1007/s13204-021-01919-z

[115] Gnanasekaran L et al. The influence of heterostructured TiO2/ZnO nanomaterials for the removal of azo dye pollutant. Chemosphere. 2022;**308**: 136161

[116] El-Samak AA, Ponnamma D, Hassan MK, Al-Maadeed MAA. A stable porous vessel for photocatalytic degradation of Azocarmine G dye. Microporous and Mesoporous Materials. 2022;**341**:111994

[117] Prabhuraj T et al. Bifunctional ZnO sphere/r-GO composites for supercapacitor and photocatalytic activity of organic dye degradation. Diamond and Related Materials. 2021; **120**:108592

[118] Kumar SG, Kavitha R. Lanthanide ions doped ZnO based photocatalysts. Separation and Purification Technology. 2021;**274**:118853

[119] Das A, Patra M, Bhagavathiachari M, Nair RG. Role of type II heterojunction in ZnO–In2O3 nanodiscs for enhanced visible-light photocatalysis through the synergy of effective charge carrier separation and charge transport. Materials Chemistry and Physics. 2021; **263**:124431

[120] Abdo DM, El-Shazly AN, Hamza MA. Effect of acidic and basic leachants on the synthesis of ZnO nanoparticles from Egyptian zinc ore, their optical/surface characteristics and photocatalytic performance. Materials Letters. 2024;**364**:136377

[121] Muktaridha O, Adlim M, Suhendrayatna S, Ismail I. Progress of 3d metal-doped zinc oxide nanoparticles and the photocatalytic properties. Arabian Journal of Chemistry. 2021;**14** (6):103175. DOI: 10.1016/j.arabjc.2021.103175

[122] Beevi AF, Sreekala G, Beena B. Synthesis, characterization and photocatalytic activity of SnO2, ZnO nanoparticles against Congo red: A comparative study. Materials Today: Proceedings. 2021;**45**:4045-4051

[123] Shirdel B, Behnajady MA. Visible-light-induced degradation of Rhodamine B by Ba doped ZnO nanoparticles. Journal of Molecular Liquids. 2020;**315**: 113633

[124] Pradeev Raj K et al. Influence of Mg doping on ZnO nanoparticles for enhanced photocatalytic evaluation and antibacterial analysis. Nanoscale Research Letters. 2018;**13**(1):229. DOI: 10.1186/s11671-018-2643-x

[125] Bashir M, Batool M, Arif N, Tayyab M, Zeng Y-J, Zafar MN. Strontium-based nanomaterials for the removal of organic/inorganic contaminants from water: A review. Coordination Chemistry Reviews. 2023;**492**:215286

[126] Selvaraj S et al. Effect of Sr doping in ZnO microspheres for solar light-driven photodegradation of organic pollutants. Journal of Materials Science: Materials in Electronics. 2022;**33**:8777-8788

[127] Potan R, Srivastav PK. Review on synthesis, characterisation and properties of transition metal doped ZnO nanostructures. In: AIP Conference Proceedings. Vol. 2986. No. 1. AIP Publishing; 2024. p. 030156. DOI: 10.1063/5.0196537

[128] Mondal A, Giri N, Sarkar S, Majumdar S, Ray R. Tuning the photocatalytic activity of ZnO by TM (TM= Fe, Co, Ni) doping. Materials Science in Semiconductor Processing. 2019;**91**:333-340

[129] Karthik KV et al. Green synthesis of Cu-doped ZnO nanoparticles and its application for the photocatalytic degradation of hazardous organic pollutants. Chemosphere. 2022;**287**: 132081

[130] Elamin N, Modwi A, Aissa MB, Taha KK, Al-Duaij OK, Yousef TA. Fabrication of Cr–ZnO photocatalyst by starch-assisted sol–gel method for photodegradation of Congo red under visible light. Journal of Materials Science: Materials in Electronics. 2021;**32**:2234-2248

[131] Vaiano V, Jaramillo-Paez CA, Matarangolo M, Navío JA, del Carmen Hidalgo M. UV and visible-light driven photocatalytic removal of caffeine using ZnO modified with different noble metals (Pt, Ag and Au). Materials Research Bulletin. 2019;**112**:251-260

[132] Ahmed MA, Abou-Gamra ZM, Alshakhanbeh MA, Medien H. Control synthesis of metallic gold nanoparticles homogeneously distributed on hexagonal ZnO nanoparticles for photocatalytic degradation of methylene blue dye. Environmental Nanotechnology, Monitoring & Management. 2019;**12**:100217

[133] Ahmad M et al. Phytogenic fabrication of ZnO and gold decorated ZnO nanoparticles for photocatalytic degradation of rhodamine B. Journal of Environmental Chemical Engineering. 2021;**9**(1):104725

[134] Pathak TK, Kroon RE, Swart HC. Photocatalytic and biological applications of Ag and Au doped ZnO nanomaterial synthesized by combustion. Vacuum. 2018;**157**:508-513

[135] Mohammadzadeh Kakhki R, Tayebee R, Ahsani F. New and highly efficient Ag doped ZnO visible nano photocatalyst for removing of methylene blue. Journal of Materials Science:

Materials in Electronics. 2017;**28**(8): 5941-5952. DOI: 10.1007/s10854-016-6268-5

[136] Pascariu P, Homocianu M, Cojocaru C, Samoila P, Airinei A, Suchea M. Preparation of La doped ZnO ceramic nanostructures by electrospinning–calcination method: Effect of La3+ doping on optical and photocatalytic properties. Applied Surface Science. 2019;**476**:16-27

[137] Luu TVH, Dao NN, Le Pham HA, Nguyen QB, Nguyen VC, Dang PH. One-step hydrothermal preparation of Ta-doped ZnO nanorods for improving decolorization efficiency under visible light. RSC Advances. 2023;**13**(8):5208-5218

[138] Palanivel B et al. Rare earth (Gd, La) co-doped ZnO nanoflowers for direct sunlight driven photocatalytic activity. Journal of Rare Earths. 2023;**41** (1):77-84

[139] Aftab S et al. Highly efficient visible light active doped ZnO photocatalysts for the treatment of wastewater contaminated with dyes and pathogens of emerging concern. Nanomaterials. 2022;**12**(3):486

[140] Kumari V, Mittal A, Jindal J, Yadav S, Kumar N. S-, N- and C-doped ZnO as semiconductor photocatalysts: A review. Frontiers of Materials Science. 2019;**13** (1):1-22. DOI: 10.1007/s11706-019-0453-4

[141] Zhang Y, Zhou J, Chen X, Feng Q, Cai W. MOF-derived C-doped ZnO composites for enhanced photocatalytic performance under visible light. Journal of Alloys and Compounds. 2019;**777**: 109-118

[142] Khalid A et al. Structural, optical, and renewable energy-assisted photocatalytic dye degradation studies of ZnO, CuZnO, and CoZnO nanostructures for wastewater treatment. Separations. 2023;**10**(3):184

[143] Ma Q, Yang X, Lv X, Jia H, Wang Y. Cu doped ZnO hierarchical nanostructures: Morphological evolution and photocatalytic property. Journal of Materials Science: Materials in Electronics. 2019;**30**:2309-2315

[144] Kareem MA, Bello IT, Shittu HA, Sivaprakash P, Adedokun O, Arumugam S. Synthesis, characterization, and photocatalytic application of silver doped zinc oxide nanoparticles. Cleaner Materials. 2022;**3**:100041

[145] Bhosale A, Kadam J, Gade T, Sonawane K, Garadkar K. Efficient photodegradation of methyl orange and bactericidal activity of Ag doped ZnO nanoparticles. Journal of the Indian Chemical Society. 2023;**100**(2):100920

[146] Dhiman P, Rana G, Kumar A, Dawi EA, Sharma G. Rare earth doped ZnO nanoparticles as spintronics and photo catalyst for degradation of pollutants. Molecules. 2023;**28**(6):2838

[147] Rodwihok C, Wongratanaphisan D, Tam TV, Choi WM, Hur SH, Chung JS. Cerium-oxide-nanoparticle-decorated zinc oxide with enhanced photocatalytic degradation of methyl orange. Applied Sciences. 2020;**10**(5):1697

[148] Selvaraj S, Vangari GA, Mohan MK, Ponnusamy S, Muthamizchelvan C. Facile synthesis of Sm doped ZnO nanoflowers by Co-precipitation method for enhanced photocatalytic degradation of MB dye under sunlight irradiation. Ceramics International. 2022;**48**(19): 29049-29058

[149] Chand P, Singh V. Enhanced visible-light photocatalytic activity of

samarium-doped zinc oxide nanostructures. Journal of Rare Earths. 2020;**38**(1):29-38

[150] Mirzaeifard Z, Shariatinia Z, Jourshabani M, Rezaei Darvishi SM. ZnO Photocatalyst revisited: Effective photocatalytic degradation of emerging contaminants using S-doped ZnO nanoparticles under visible light radiation. Industrial and Engineering Chemistry Research. 2020;**59**(36):15894-15911. DOI: 10.1021/acs.iecr.0c03192

[151] Zeljković S et al. Mechanochemically induced synthesis of N-ion doped ZnO: Solar photocatalytic degradation of methylene blue. Green Chemistry Letters and Reviews. 2022;**15**(4):869-880. DOI: 10.1080/17518253.2022.2108343

[152] Kabir R, Saifullah MAK, Ahmed AZ, Masum SM, Molla MAI. Synthesis of n-doped zno nanocomposites for sunlight photocatalytic degradation of textile dye pollutants. Journal Of Composites Science. 2020;**4**(2):49

[153] Mahdavi R, Talesh SSA. Sol-gel synthesis, structural and enhanced photocatalytic performance of Al doped ZnO nanoparticles. Advanced Powder Technology. 2017;**28**(5):1418-1425

[154] Peerakiatkhajohn P, Butburee T, Sul J-H, Thaweesak S, Yun J-H. Efficient and rapid photocatalytic degradation of methyl orange dye using Al/ZnO nanoparticles. Nanomaterials. 2021;**11**(4):1059

[155] Mohamed KM, Benitto JJ, Vijaya JJ, Bououdina M. Recent advances in ZnO-based nanostructures for the photocatalytic degradation of hazardous, non-biodegradable medicines. Crystals. 2023;**13**(2):329

[156] Pan J et al. The enhancement of photocatalytic hydrogen production via Ti3+ self-doping black TiO2/g-C3N4 hollow core-shell nano-heterojunction. Applied Catalysis B: Environmental. 2019;**242**:92-99

[157] Salazar-Marín D et al. Distinguishing between type II and S-scheme heterojunction materials: A comprehensive review. Applied Surface Science Advances. 2024;**19**:100536

[158] Shanmugam P, Ngullie RC, Smith SM, Boonyuen S, Boddula R, Pothu R. Visible-light induced photocatalytic removal of methylene blue dye by copper oxide decorated zinc oxide nanorods. Materials Science for Energy Technologies. 2023;**6**:359-367

[159] Elshypany R et al. Elaboration of Fe3O4/ZnO nanocomposite with highly performance photocatalytic activity for degradation methylene blue under visible light irradiation. Environmental Technology & Innovation. 2021;**23**:101710

[160] Wahba MA, Yakout SM, Mohamed WA, Galal HR. Remarkable photocatalytic activity of Zr doped ZnO and ZrO2/ZnO nanocomposites: Structural, morphological and photoluminescence properties. Materials Chemistry and Physics. 2020;**256**:123754

[161] Munawar T et al. Sunlight-induced photocatalytic degradation of various dyes and bacterial inactivation using CuO–MgO–ZnO nanocomposite. Environmental Science and Pollution Research. 2021;**28**(31):42243-42260. DOI: 10.1007/s11356-021-13572-8

[162] Zhang Y et al. Synthesis of SnO2/ZnO flowerlike composites photocatalyst for enhanced photocatalytic degradation of malachite green. Optical Materials. 2022;**133**:112978

[163] Sayadi MH, Ghollasimood S, Ahmadpour N, Homaeigohar S. Biosynthesis of the ZnO/SnO2 nanoparticles and characterization of their photocatalytic potential for removal of organic water pollutants. Journal of Photochemistry and Photobiology A: Chemistry. 2022;**425**: 113662

[164] Zheng Y, Liu J, Cheng B, You W, Ho W, Tang H. Hierarchical porous Al2O3@ ZnO core-shell microfibres with excellent adsorption affinity for Congo red molecule. Applied Surface Science. 2019;**473**:251-260

[165] Arif N et al. Design and fabrication of biomass derived black carbon modified g-C_3N_4/$FeIn_2S_4$ heterojunction as highly efficient Photocatalyst for wastewater treatment. Small. 2024;**20** (20):2308908. DOI: 10.1002/smll.202308908

[166] Ahmad I et al. Recent progress in rare earth oxides and carbonaceous materials modified ZnO heterogeneous photocatalysts for environmental and energy applications. Journal of Environmental Chemical Engineering. 2022;**10**(3):107762. DOI: 10.1016/j.jece.2022.107762

[167] Zheng ALT, Ohno T, Andou Y. Recent Progress in photocatalytic efficiency of hybrid three-dimensional (3D) graphene architectures for pollution remediation. Topics in Catalysis. 2022;**65**(19–20):1634-1647. DOI: 10.1007/s11244-022-01610-9

[168] Asgharian M, Mehdipourghazi M, Khoshandam B, Keramati N. Photocatalytic degradation of methylene blue with synthesized rGO/ZnO/Cu. Chemical Physics Letters. 2019;**719**:1-7

[169] Oyewo OA, Ramaila S, Mavuru L, Onwudiwe DC. Enhanced photocatalytic degradation of methyl orange using Sn-ZnO/GO nanocomposite. Journal of Photochemistry and Photobiology. 2022; **11**:100131

[170] Ngullie RC, Alaswad SO, Bhuvaneswari K, Shanmugam P, Pazhanivel T, Arunachalam P. Synthesis and characterization of efficient ZnO/g-C3N4 nanocomposites photocatalyst for photocatalytic degradation of methylene blue. Coatings. 2020;**10**(5):500

[171] Bhosale A, Gophane A, Kadam J, Sabale S, Sonawane K, Garadkar K. Fabrication of visible-active ZnO-gC3N4 nanocomposites for photodegradation and cytotoxicity of methyl orange and antibacterial activity towards drug resistance pathogens. Optical Materials. 2023;**136**:113392

[172] Girish YR et al. Rapid and facile synthesis of Z-scheme ZnO/g-C3N4 heterostructure as efficient visible light-driven photocatalysts for dye degradation and hydrogen evolution reaction. Journal of Hazardous Materials Advances. 2023;**9**:100230

[173] Dutta V, Sharma S, Raizada P, Hosseini-Bandegharaei A, Gupta VK, Singh P. Review on augmentation in photocatalytic activity of CoFe2O4 via heterojunction formation for photocatalysis of organic pollutants in water. Journal of Saudi Chemical Society. 2019;**23**(8):1119-1136

[174] Saikia L, Bhuyan D, Saikia M, Malakar B, Dutta DK, Sengupta P. Photocatalytic performance of ZnO nanomaterials for self sensitized degradation of malachite green dye under solar light. Applied Catalysis A: General. 2015;**490**:42-49

[175] Raj KP, Sadaiyandi K, Kennedy A, Thamizselvi R. Structural, optical, photoluminescence and photocatalytic

assessment of Sr-doped ZnO nanoparticles. Materials Chemistry and Physics. 2016;**183**:24-36

[176] Mahajan BK, Kumar N, Chauhan R, Srivastava VC, Gulati S. Mechanistic evaluation of heterocyclic aromatic compounds mineralization by a Cu doped ZnO photo-catalyst. Photochemical & Photobiological Sciences. 2019;**18**:1540-1555

[177] Güy N, Çakar S, Özacar M. Comparison of palladium/zinc oxide photocatalysts prepared by different palladium doping methods for Congo red degradation. Journal of Colloid and Interface Science. 2016;**466**:128-137

Chapter 4

Perspective Chapter: Vertically Aligned 1D ZnO Nanostructures – Influence of Synthesis Parameters on the Nanomaterials' Properties

Maria Morais, Mariana Cortinhal, Ana Rovisco, Jorge Martins, Rodrigo Martins and Pedro Barquinha

Abstract

Zinc oxide (ZnO) is a widely explored semiconductor metal oxide. This material has interesting properties for several research areas, including energy storage and harvesting, sensing and electronic applications. Its versatility has led to the development of various approaches for synthesizing nanostructures with different morphologies according to the application. In this chapter, a literature review on vapor phase and solution phase synthesis approaches for synthesizing one-dimensional (1D) ZnO nanostructures on different substrates will be provided to establish a comparison between different processes' parameters. Since hydrothermal synthesis is the most widely used approach for growing ZnO on different substrates due to its simplicity and cost-effectiveness, the principles of this technique will be detailed. As an experimental demonstration of such technique, novel results obtained at CENIMAT on microwave-assisted hydrothermal synthesis of ZnO nanorods, exploring the influence of seed layer thickness, ultraviolet/ozone (UVO) treatment to this layer, and synthesis time and temperature on the nanostructures' morphology, will be presented. The nanostructures' length, diameter and density were measured to establish a correlation between synthesis conditions and nanostructures' features. A seed layer thickness of 100 nm, a 5 min UVO treatment, and a synthesis time and temperature of 60 min and 100°C led to the formation of ZnO nanorods with increased length and aspect ratio.

Keywords: zinc oxide, vertically aligned nanostructures, vapor phase synthesis, solution phase synthesis, hydrothermal synthesis

1. Introduction

Zinc oxide (ZnO) is an inorganic II-VI n-type semiconductor with a wide and direct band gap (around 3.37 eV) and large exciton binding energy (approximately

60 meV) [1, 2]. Additionally, this metal oxide presents high electron mobility (205 to 300 $cm^2 V^{-1} s^{-1}$) and tunable conductivity [3–6].

Zinc oxide nanostructures present good physicochemical and electrochemical properties [1], chemical and thermal stability [2, 7, 8], and high mechanical strength [8]. Besides, this metal oxide also presents biocompatibility and non-toxicity [8, 9].

Zinc oxide can crystallize into one of the three structures depicted in **Figure 1**: rock salt (cubic), zinc-blend (cubic), or wurtzite (hexagonal) [1, 11]. The rock salt can only be produced at high temperatures, whereas the zinc-blend is stabilized by cubic structures [11]. As such, crystallization in the wurtzite structure is the most thermodynamically favorable [4]. Oxygen atoms tetrahedrally coordinated to four zinc cations (and *vice versa*) compose the hexagonal wurtzite crystal structure that comprises alternating planes of zinc and oxygen atoms stacked along the *c*-axis [2, 4]. The net positively charged zinc-terminated planes and the negatively charged oxygen-terminated planes have high energy and act as basal facets of the hexagonal structure, where a zinc-terminated plane is at the top while an oxygen-terminated plane is at the bottom [12]. In contrast, the prismatic lateral faces of the metal oxide crystal are non-polar and present lower energy [2, 4].

A crystal's preferential growth is determined by the energy of each surface and the amount of active sites [1]. In ZnO, the polar planes have higher energy than the unit cell's lateral surfaces because polar surfaces are more susceptible to electrostatic interactions [1, 13]. As such, the growth along the direction parallel to the *c*-axis is favorable since it decreases the free surface energy [1, 2], which is also favored by the increase of the non-polar surfaces' area during growth [1]. It is worth mentioning that the growth along the *c*-axis is often promoted by moderate temperatures (at least 80°C), as the growth medium reaches an energy level sufficiently high to allow the attachment of molecules to the crystal's surfaces [14].

Interestingly, ZnO presents spontaneous polarization due to the noncentrosymmetric nature of its wurtzite structure and the presence of zinc and oxygen basal planes [4, 12]. As there is no center of inversion along the *c*-axis in a ZnO hexagonal crystal, which leads to asymmetry, the metal oxide nanostructures present piezoelectric properties [1, 4, 9]. Besides the piezoelectricity, ZnO's properties have led to its use in several applications, including photocatalytic degradation of organic contaminants present in water [14, 15], surface acoustic wave devices [16], solar cells [3, 17], photodetectors [5, 7, 8, 12], scintillator applications [2], photoelectrochemically related applications [18–20], gas sensors [21], field-emission devices [22], energy

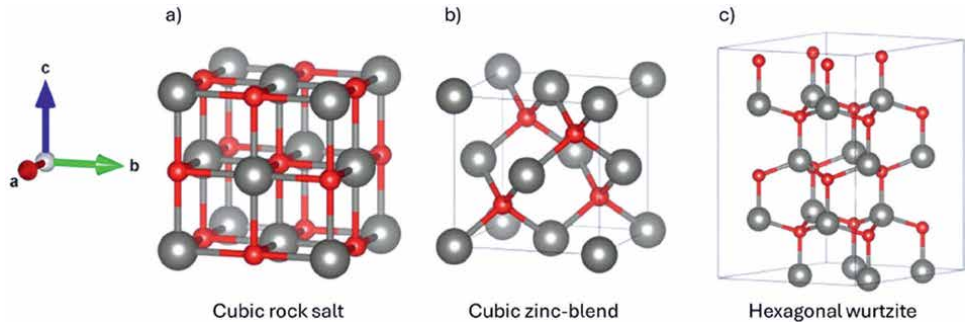

Figure 1.
Different crystal structures of ZnO: (a) rock salt, (b) zinc-blend, and (c) wurtzite. Adapted with permission [10]. Copyright 2023. Advanced Energy and Sustainability Research published by Wiley-VCH GmbH.

storage [23], or radiation absorption [24]. The properties of the ZnO nanostructures, such as the aspect ratio, crystallinity, growth orientation, vertical alignment, density, and lateral ordering, will influence their performance [12, 25]. As such, precise tuning of the nanostructures' properties by determining their synthesis method and controlling their synthesis kinetics is decisive in the final performance [12].

2. Approaches for the synthesis of vertically aligned ZnO nanostructures

The variety of fabrication techniques to synthesize ZnO has led to a wide assortment of nanostructures [2]. ZnO nanostructures can be synthesized in different morphologies, such as nanotubes, nanowires, nanorods (NRs), nanocombs, nanoneedles, nanorings, microspheres, nanobelts, nanosheets, tetrapods, and nanohelices, depending on the synthesis parameters [1, 17, 18].

Among the several ZnO nanostructures, one-dimensional (1D) ZnO materials have been the focus of many research groups due to their physical, mechanical, and electronic properties [12, 25] and improved optical performance compared to bulk form [2]. Namely, when compared with films, 1D nanostructures present lower recombination rates and larger surface-to-volume ratio, desirable features in several areas such as electronics and sensing [12, 20, 26]. Moreover, ZnO nanowires, nanorods, and nanotubes' features also promote electron conduction in the uniaxial direction [5, 26].

Several approaches have been reported to synthesize aligned ZnO nanostructures, including synthesis from both solution and vapor phases [4] techniques, such as pulsed laser deposition (PLD), chemical vapor deposition (CVD), and vapor-liquid-solid (VLS) [25, 27]. On the other hand, these materials have also been synthesized using chemical bath deposition (CBD) and electrodeposition [25, 27].

2.1 Vapor phase synthesis of ZnO nanostructures

VLS, PLD, CVD, and microwave-plasma assisted thermal evaporation (MPATE) have been employed to grow ZnO nanostructures under vacuum and at high temperatures, as summarized in **Table 1**. These techniques offer versatility in tailoring the nanostructure's properties, making them valuable for applications in electronics, sensors, and optoelectronics [1].

2.1.1 Vapor-liquid-solid method

Vapor-liquid-solid is a widely utilized method where a metal catalyst acts as a seed for the nanostructures' growth, guiding the vapor phase precursor to solidify into the desired morphology on the catalyst surface [38].

One-dimensional nanorods can be fabricated through a process known as the vapor phase method. This method produces vapor through chemical and gaseous reactions and evaporation. The targeted vapor undergoes rapid heating before slowly cooling on the substrate, forming 1D nanomaterials. Although the theory makes the procedure look straightforward, it must be done at extremely high temperatures of around 1000°C to evaporate the source materials, such as zinc or ZnO powder. It is essential to analyze this process's additional reactions and breakdown [39]. You *et al*. reported the fabrication of vertically aligned ZnO nanowire arrays by the vapor phase transport approach to be employed as self-driven solar-blind photodetectors

Synthesis technique	Substrate	Growth				Ref
		Seed layer	Source material	Carrier gas	Conditions	
VLS	Sapphire	None	ZnO and carbon powders	Ar and O_2	1050°C, 20 min	[28] (2019)
	Sapphire	50 nm ZnO (RF sputtering)	ZnO and graphite powders	Ar and O_2	1050°C, 30 min	[6] (2019)
PLD	c-cut Al_2O_3 (0001)	None	Au/ZnO target	O_2	500°C; 45° laser angle; 420 mJ laser energy; 5 Hz pulsed laser frequency	[29] (2020)
	n-doped Si (111) wafer; ITO coated on glass; Al_2O_3 substrate	None	ZnO target	O_2	500–600°C; laser energy density between 3 and 4 J cm^{-2}; 10 Hz pulsed laser frequency; pulse duration of 20 ns	[30] (2018)
CVD	AlN film on a Si substrate	70 nm ZnO (ALD)	ZnO and graphite powders	Ar and O_2	750°C (Sample) 950°C (Furnace)	[31] (2023)
	ITO	1 mM ZAD (spin-coating)	None	Ar and O_2	600°C, 10 min	[22] (2021)
	Si/SiO_2 wafers	None	ZnO and graphite powders	Ar	270°C (Sample) 930°C (Furnace) 100 min	[32] (2021)
	Pt-coated Si wafer (p-type)	None	Bulk zinc wire	Ar and O_2	700°C, 1 min	[33] (2021)
	Si/SiO_2 substrates	450 nm ZnO (PLD)	ZnO and carbon powders	Ar and O_2	850°C, 30 min	[34] (2019)
	Glass	5 mM ZAD (drop-coating)	Zinc	Ar and acetone vapor	400 to 500°C (Sample) 850°C (Furnace) 30 min	[35] (2019)
	p-GaN/ sapphire	None	ZnO and graphite powders	Ar	1150°C, 45 min	[36] (2020)

Synthesis technique	Substrate	Growth				Ref
		Seed layer	Source material	Carrier gas	Conditions	
MPATE	Glass	None	Zinc powder	Ar and H_2O_2	RT, 7 min	[37] (2018)

RF: radio frequency; ITO: indium tin oxide; AIN: aluminum nitride; PLD: pulsed laser deposition; ALD: atomic layer deposition; ZAD: zinc acetate dihydrate; p-GAN: p-type gallium nitride; RT: room temperature.

Table 1.
Vapor-based synthesis approaches to produce 1D ZnO nanostructures.

with superior sensitivity. This study used a mixture of ZnO and carbon powders as precursors that were heated at 1050°C for 20 min. The produced arrays were then homogeneously coated with 20 nm thick monoclinic gallium oxide (Ga_2O_3) through sputtering methods to form vertically aligned ZnO/Ga_2O_3 core/shell nanowire arrays [28]. Also in 2019, You *et al*. reported a similar process; however, before the powder evaporation, a thin 50 nm ZnO seed layer was deposited by radio frequency (RF) sputtering. Here, the evaporation of ZnO and graphite powders at 1050°C for 30 min produced nanowires of around 300 nm in diameter. Finally, a zinc tellurium (ZnTe) layer was grown as a shell on the ZnO nanorod array surface by RF sputtering, creating a self-powered photodetector that relied on the coupling between the photovoltaic and pyroelectric effects [6].

2.1.2 Pulsed laser deposition

Pulsed laser deposition of ZnO nanowires uses a femtosecond pulsed laser to ablate a ZnO target, creating a plume of material that subsequently condenses on a substrate to form nanowire structures [30]. It is worth noting that this process requires high temperatures (between 500 and 600°C) [30]. The femtosecond laser pulses enable precise control over the deposition process, offering advantages, such as high spatial resolution and minimal damage to the substrate. Zhang *et al.* reported the use of this approach to grow ZnO nanowires with good crystallinity and reasonably uniform diameters, which can be attributed to the homogeneity of femtosecond laser-produced precursor vapor in which micron-sized particulates are minimal [40].

2.1.3 Chemical vapor deposition

Chemical vapor deposition involves the controlled deposition of ZnO on a substrate through chemical reactions in the vapor phase [41]. It is a vapor route process frequently used to manufacture ZnO nanorods on horizontal tube furnace systems, where oxygen gas is required. Zinc [42] and ZnO powder [43] are typical precursors used in forming ZnO nanorods by CVD, where temperatures between 450 and 900°C or up to 1200°C (respectively) are required to perform the synthesis. Zinc vapor is deposited on the surface of the heated substrate and reacts with oxygen to form ZnO nanorods. Synthesis parameters, such as substrate type, vacuum pressure, type of carrier gas, and synthesis temperature, are essential factors affecting ZnO nanorods' structural and piezoelectric properties [44]. Schaper *et al*. reported in 2021 the fabrication of a novel and advanced approach to directly grow ZnO

nanowires on single-walled carbon nanotubes and graphene surfaces through successfully forming 1D-1D and 1D-2D (two-dimensional) heterostructure interfaces. In this study, a mixture of ZnO and graphite precursors was placed in a small quartz boat that was heated up to 930°C, while the samples were heated to 270°C, using only Argon [32]. Kolhelp *et al*. reported a similar method but with two modifications. An initial 70 nm ZnO seed layer was deposited by atomic layer deposition (ALD), and the nanostructures' growth was performed employing a controlled oxygen flow. The procedure led to the formation of nanowires with lengths up to 12 μm [31]. Furthermore, Swathi *et al.* reported the fabrication of branched ZnO nanorods by adding a second step after the initial ZnO growth by CVD, in which zinc seeds were coated on the obtained nanorods through spin-coating [22]. The versatility of CVD is mirrored in the wide choice of precursors. In this scope, it is worth mentioning the synthesis of ZnO nanostructures using a bulk zinc wire precursor reported by Kim *et al*. [33].

Metal-organic chemical vapor deposition (MOCVD) has been reported to grow ZnO nanorods using the free catalytic-agent process, with a temperature between 400 and 500°C, which is far from the CVD-based reported studies, carried out using higher temperatures [39].

2.1.4 Microwave plasma-assisted thermal evaporation

Although VLS, CVD, and PLD offer the possibility of carefully controlling the ZnO nanorods' growth and tuning their properties, they require long processing times, high temperatures, and complex and high-cost equipment. In addition, catalysts and seed layers are essential for growing vertically aligned ZnO nanorods on substrates. Therefore, developing a simple, catalyst-free, fast, and economical approach to growing vertically aligned ZnO nanorods remains a significant challenge. In this scope, Thongsuksai *et al*. reported successful growth of vertically aligned ZnO nanorods on glass substrates by MPATE. The nanorods' growth was carried out at room temperature using only zinc powder as the source material. The growth lasted 7 min, which is much faster than other methods and resulted in nanowires with diameters of 319 nm [37].

2.2 Solution phase synthesis of ZnO nanostructures

Solution phase syntheses are also called CBD and include approaches, such as emulsion methods, sol-gel, precipitation from saturated solutions of zinc salts, spray pyrolysis, and hydrothermal synthesis [4]. These wet chemical approaches offer the possibility of synthesizing ZnO without vacuum and at relatively low temperatures (around 80°C) [2] through simple, time- and cost-effective routes [1, 2, 4]. Moreover, they pose no limitation regarding substrate material and scalability [2–4]. The properties of the resulting material and the nanostructures' distribution on the substrate can be tuned by controlling the growth parameters of different synthesis approaches, including growth time and temperature or nature and concentration of precursors [4, 25].

Being 1D ZnO nanostructures vastly explored materials, several synthesis techniques, such as electrochemical and sonochemical methods, ultrasonic spray pyrolysis, and hydrothermal synthesis, have been developed and optimized over the years. **Table 2** presents relevant information regarding some synthesis procedures of nanorods and nanowires reported in the literature.

Synthesis technique	Substrate	Seed layer		Growth		Ref
		Deposition techniques	Conditions	Solution	Conditions	
Anodization	Zinc foil	Non-applicable	Non-applicable	Zinc foil Electrolyte: $KHCO_3$ (50 mM–230 mM)	5 to 15 V RT, 5 to 20 min	[20] (2020)
CBD synthesis	FTO	Sol-gel Spin-coating	0.5 M ZAD	0.081 M ZAD 1.2 M NaOH PVP (5 wt%)	70°C, time up to 15 min	[3] (2020)
	Si (100) wafer	Sol-gel Dip-coating	375 mM ZAD 375 mM ME	50 mM $Zn(NO_3)_2{\cdot}6H_2O$ 50 mM HMTA	95°C, 2 h	[25] (2020)
	Glass	Dip-coating	0.22 M ZAD 0.1 M PVA NH_3 (pH between 7 and 8)	0.05 M $Zn(NO_3)_2{\cdot}6H_2O$ 0.05 M HMTA	90°C for 2, 4, and 6 h	[14] (2020)
	Stainless steel	Drop-casting	0.5 mM ZAD	0.1 M $Zn(NO_3)_2{\cdot}6H_2O$ 0.1 M HMTA NH_4OH (pH ≈ 6)	70°C, 3 to 6 h	[23] (2020)
	Glass	DC magnetron reactive sputtering	Non-applicable	$Zn(NO_3)_2{\cdot}6H_2O$ HMTA (equimolar)	97°C, 4 h	[45] (2019)

Synthesis technique	Substrate	Seed layer		Growth		Ref
		Deposition techniques	Conditions	Solution	Conditions	
Electrodeposition	ITO-coated glass	None	None	5×10^{-3} M $ZnCl_2$ 5×10^{-3} M H_2O_2 0.1 M KCl	−1.0 V 65°C, 40 min	[15] (2019)
	FTO-coated glass	Sol-gel Spin-coating	0.3 M ZAD 0.3 M ME	0.01 M $Zn(NO_3)_2{\cdot}6H_2O$ 0.1 M KCl HMTA (0 to 9 mM)	−1.3 V 70°C, 10 min	[17] (2018)
	Au electrodes of AT-cut QCM	J = 0.012 mA cm^{-2} 2000 s	5 mM $ZnCl_2$ 0.1 M KCI	1.5 to 12 mM KCl 1.25 to 10 mM $ZnCl_2$	- 0.9 V 80°C, 3000 s	[21] (2020)
	ITO-coated glass	None	None	5×10^{-4} M $ZnCl_2$ 0.1 M KCl	−0.9 to −1.1 V 80°C, 4600 and 9700 s	[19] (2018)
	FTO-coated glass	−1.3 V 80°C, 10 to 90 s	1 mM $Zn(NO_3)_2{\cdot}6H_2O$ 0.1 M $NaNO_3$ 1 mM HMTA HNO_3 (pH ≈ 6)	1 mM $Zn(NO_3)_2{\cdot}6H_2O$ 0.1 M $NaNO_3$ 1 mM HMTA HNO_3 (pH ≈ 6)	−1.0 V 80°C, 30 min	[46] (2020)

Synthesis technique	Substrate	Seed layer		Growth		Ref
		Deposition techniques	Conditions	Solution	Conditions	
Hydrothermal synthesis	ITO-coated glass	Sol-gel Spin-coating	0.1 M ZAD 0.1 M ME	25 mM ZAD 25 mM HMTA	95°C, 24 h	[13] (2020)
	ITO	Sol-gel Dip-coating	0.1 to 0.7 M ZAD 0.1 to 0.7 M Et_3N	$Zn(NO_3)_2{\cdot}6H_2O$ HMTA (equimolar)	90°C, 2 h	[12] (2020)
	(100) Si wafer	Spray pyrolysis	50 mM ZAD	25 mM $Zn(NO_3)_2{\cdot}6H_2O$ 25 mM HMTA (molar ratios of 3:1, 2:1, 1:1, 1:2, and 1:3)	85°C, 180 min	[2] (2018)
	ITO	Sol-gel Dip-coating	0.2 M ZAD 0.2 M DE	0.04 M $Zn(NO_3)_2{\cdot}6H_2O$ 0.04 M HMTA	90–130°C, 4 h	[18] (2018)
	Au precoated glass	Sol-gel Spin-coating	157 g L^{-1} ZAD 4% ME	0.03 M $Zn(NO_3)_2{\cdot}6H_2O$ 0.05 M HMTA	80°C, 5 h	[8] (2020)
	Glass	Sol-gel Spin-coating	1 M ZAD 0.395 M Et_3N	0.01 M $Zn(NO_3)_2{\cdot}6H_2O$ 0.01 M HMTA	90°C, 4 h	[27] (2020)
	Glass	Sol-gel Spin-coating	0.05 M ZAD 0.06 M DE ZnO nanorods (up to 0.01 g)	0.001 M $Zn(NO_3)_2{\cdot}6H_2O$ 0.1 M NaOH	70°C, 90 min	[5] (2019)
	Flexible carbon cloth	None	None	16 mM $Zn(NO_3)_2{\cdot}6H_2O$ or 25 mM $ZnCl_2$ or 10 mM ZAD 16 mM HMTA 1 mL of ammonia (25%)	105°C, 20 h	[24] (2019)
Sonochemical method	Glass	RF sputtering	Non-applicable	0.05 M $Zn(NO_3)_2{\cdot}6H_2O$ 0.05 M HMTA	2 h at 40% amplitude (maximum of 27 W)	[7] (2019)

Synthesis technique	Substrate	Seed layer		Growth		Ref
		Deposition techniques	Conditions	Solution	Conditions	
Ultrasonic spray pyrolysis	Glass	Ultrasonic spray pyrolysis	0.5 M ZAD 0.5 M ME	0.1M $Zn(NO_3)_2{\cdot}6H_2O$ 0.1 M HMTA	400°C, 2 min	[11] (2023)
	Glass	Ultrasonic spray pyrolysis	0.5 M ZAD 0.5 M ME	0.5 M $Zn(NO_3)_2{\cdot}6H_2O$ 0.5 M HMTA	400°C, 2 min	[26] (2023)

ZAD: zinc acetate dihydrate; ME: monoethanolamine; ITO: Indium tin oxide; DE: diethanolamine; FTO: fluorine-doped tin oxide; DC: direct current; HMTA: hexamethylenetetramine; Et_3N: trimethylamine; PVA: polyvinyl alcohol; PVP: polyvinylpyrrolidone; AT-cut QCM: AT-cut quartz crystal microbalance; RT: room temperature.

Table 2.
Solution-based synthesis approaches to produce 1D ZnO nanostructures.

2.2.1 Electrochemical anodization

Zinc oxide nanowires can be synthesized through electrochemical anodization of a zinc foil. A two-electrode electrochemical cell with a graphite rod as a counter electrode and an electrolyte is required for the synthesis. The working electrode is zinc foil that acts as a source of zinc cations. At the beginning of the reaction, the current reaches maximum values, as the resistance offered by the zinc foil is very low. As the reaction continues, the current decreases due to the formation of an oxide layer.

Tantray and Shah produced nanowires with diameters of around 99 nm at room temperature, under an applied potential between 5 and 15 V, for different periods of time (5–20 min) via electrochemical anodization. Anodization time and temperature, electrolyte characteristics (nature and concentration), and applied voltage were reported to influence the properties of the resulting nanowire films, which determined the final samples' optoelectric properties [20].

2.2.2 Electrodeposition

Nanostructures can be synthesized on conductive substrates at atmospheric pressure and low temperature without substrate dimension limitations using electrodeposition [19, 46]. Furthermore, a high growth rate can be achieved using this simple and cost-effective technique [46].

Generally, the electrochemical growth of ZnO nanorods is carried out in an electrolyte with dissolved oxygen [19]. This electrochemical-assisted growth depends on the electroreduction of nitrate and molecular oxygen [17]. The oxygen and nitrate reduction reactions form hydroxyl radicals, which react with zinc cations, forming zinc hydroxide that later produces ZnO when the temperature is adequate (at least 70°C) [17, 46]. In general, pure and highly crystalline phases can be obtained without posttreatment [46]. It is important to note that different ZnO morphologies can be synthesized by tuning the growth solution concentration and the deposition potential of the electrochemical process, as these parameters condition the nitrate reduction reaction and the subsequent formation of hydroxyl radicals [17] whose origin has also been proposed to derive from hydrogen peroxide reduction [15]. A metal catalyst or templates can also be used to tune the nanostructures' morphology [46].

The seed layer features have also proven fundamental in determining the properties of the synthesized nanorod arrays, such as diameter, morphology, and density. Additionally, increasing the electrodeposition time for producing a seed layer on fluorine-doped tin oxide (FTO) substrates affected the nanostructures' crystallinity. It also led to a decrease in their diameter and an increase in the nanorods' density due to a higher number of nucleation sites [46].

Marimuthu *et al*. reported the synthesis of ZnO nanostructures (agglomerated flowers and rods) without metallic zinc phase by a potentiostatic method (−1.3 V) using a 0.01 M zinc nitrate hexahydrate and 0.1 M potassium chloride solution to which hexamethylenetetramine (HMTA, 9 mM) was added. The results underlined HMTA's essential role in determining the crystallinity of the produced nanostructures [17].

Yang's work highlighted the importance of the voltage used in the electrochemical process on the ZnO properties [19]. The electrodeposition-assisted growth of ZnO nanorods on indium tin oxide (ITO)-coated glass was performed by a potentiostatic method at three different potentials (−0.9, −1.0, and −1.1 V (saturated calomel electrode (SCE)). Although the dimensions of the ZnO nanostructures were similar

for the three tested voltage values, their density and, consequently, the surface area decreased with decreasing deposition potential. Moreover, at −1.1 V (SCE), the nanorods' growth was random and unordered. The aligned growth along the *c*-axis was promoted only during syntheses at −0.9 and −1.0 V (SCE). These observations were pointed to be associated with the formation of a zinc hydroxide depletion layer near the interface between the substrate and the electrolyte, which limited the supply of zinc ions and consequently hindered the nanorods' growth [19].

2.2.3 Sonochemical synthesis

Sonochemical synthesis is a simple and cost-effective approach for producing nanostructures with a uniform size distribution, high surface area, and purity [7]. Hammed *et al*. reported the synthesis of ZnO nanostructures using this approach. During this process, ultrasounds are applied to the growth solution through acoustic cavitation, creating specific conditions of high temperature and pressure (up to 5000 K and 1000 atm) where ZnO can be formed. The underlying reactions include zinc precursor decomposition and subsequent reaction with hydroxyl radicals, leading to the formation of ZnO. Nanorods with 529 and 668 nm lengths were grown on glass substrates based on this approach by using a zinc nitrate and HMTA equimolar growth solution [7].

2.2.4 Ultrasonic spray pyrolysis

Ultrasonic spray pyrolysis is a valuable alternative for the fast synthesis of ZnO nanostructures. During this process, films are produced by spraying a precursor solution onto a heated substrate [26]. This technique is a time- and cost-effective approach for producing nanostructures on large areas without resorting to expensive apparatus [11, 26]. By tuning the deposition parameters, the film growth kinetics can be tailored according to the intended application [26]. Reports on the ultrasonic spray pyrolysis growth of ZnO nanorods with lengths between 0.9 and 1.45 μm and diameters ranging from 20 to 70 nm on glass substrates have already been presented in the literature [11, 26]. Although the synthesis is fast (2 min), high temperatures (around 400°C) are required for the crystallization of the precursors [11, 26].

2.2.5 Hydrothermal synthesis

Hydrothermal synthesis is the most used technique to synthesize ZnO nanostructures due to its cost-effectiveness, simplicity [8, 9], and environmental friendliness [9]. Besides, the synthesis can be carried out at relatively low growth temperatures of at least 100°C [5, 7, 8].

During a hydrothermal synthesis, the thermal decomposition of the precursors and, subsequently, of the newly formed intermediate products takes place [2, 5]. Briefly, the precursors decompose, originating zinc cations and ammonia (NH_3). Then, the latter reacts with water, producing hydroxyl radicals that react with zinc cations to form zinc hydroxide ($Zn(OH)_2$). Zinc hydroxide, in turn, dehydrates due to increasing temperature, forming ZnO crystals [2, 5]. Since the chemical principles leading to the formation of ZnO are similar for different precursors, as an example, the reactions leading to the formation of ZnO from zinc acetate and HMTA are presented next:

$$\left(CH_2\right)_6 N_4 + 6H_2O \leftrightarrow 6HCHO + 4NH_3 \quad (1)$$

$$Zn\left(CH_3COO\right)_2 \cdot 2H_2O \leftrightarrow Zn^{2+} + 2CH_3COO^- + 2H_2O \quad (2)$$

$$NH_3 + H_2O \leftrightarrow NH_4^+ + 2OH^- \quad (3)$$

$$Zn^{2+} + 2OH^- \leftrightarrow Zn\left(OH\right)_2 \quad (4)$$

$$Zn\left(OH\right)_2 \underset{\leftrightarrow}{\Delta} ZnO + H_2O \quad (5)$$

The growth rate of each crystal plane is as follows: v(0001) > v(0111) > v(0110) > v(0001). Since v(0001) is the highest, the ZnO nanostructures grow along this direction [2, 5].

Similarly to other CBD approaches, the hydrothermal synthesis conditions, such as synthesis time and temperature, precursors' nature and concentration, and the characteristics of the seed layer (thickness and orientation), strongly influence the properties of the resulting nanostructures [2, 7, 9]. For example, the aspect ratio of hydrothermally synthesized nanostructures can be tuned by controlling the growth kinetics [4].

Several research groups have investigated the role of the hydrothermal synthesis parameters in the properties of the produced nanostructures. Remarks regarding the importance of the seed layer properties, the growth solution composition, and synthesis time and temperature will be presented next. Given that the controlled growth of 1D nanostructures has become a central research focus, an innovative alternative for density-controlled growth will also be described.

2.2.5.1 Seed layer properties

The crystallographic surface quality of the substrate influences the growth of ZnO nanorods through CBD, i.e., the properties of the substrate determine the lattice mismatch between this material and ZnO, which creates structural defects that hinder the growth of high-quality ZnO nanostructures [4, 7, 25]. One of two approaches can be followed to minimize this mismatch: use of a single crystalline substrate (gallium nitride, alumina, or ZnO) with a heteroepitaxial ZnO film or resort to non-epitaxial substrates coated with a seed layer. Single crystalline substrates are expensive, so the seed layer approach is the most explored [4, 25].

The deposition of a seed layer is fundamental to the growth of vertically aligned ZnO nanostructures, which encompasses three steps: the deposition of a seed layer followed by nucleation and growth phases [1, 7]. The seed layer decreases the interfacial mismatch between ZnO and the substrate [5, 7]. As such, this layer provides nucleation sites and thus reduces the thermodynamic barrier to crystallization [1, 2].

Several techniques have proven efficient in depositing seed layers for the subsequent growth of aligned ZnO nanostructures [1, 17]. These approaches include physical vapor methods, such as PLD [47], sputtering [48], and thermal evaporation and wet chemical procedures, including sol-gel/spin-coating [49] and electrochemical deposition [17].

It is worth mentioning that the properties of the seed layer influence those of hydrothermally synthesized ZnO nanostructures. The seed layer's thickness, orientation, and crystallinity determine the aspect ratio, crystal structure, crystallinity,

optical properties, alignment, and density of ZnO nanostructures [7, 12, 50]. In particular, the concentration of the seed layer was reported to improve the density of ZnO nanorods, leading to a decrease in their diameter [51].

The growth of vertically aligned ZnO nanorods requires high-quality seed layers [4]. In this scope, Basinova *et al*. studied changes in morphology and crystallinity caused by the seed layer preheating and annealing. Changes in these two properties influenced the vertical alignment of the ZnO nanorods grown on silicon substrates where zinc acetate seed layers were deposited via dip-coating. The dip-coating was repeated 3 times, and the preheating step was performed after each cycle at temperatures between 300 and 400°C. Higher temperatures, besides degrading by-products of the deposited xerogel, also promoted the coalescence of the seed layer crystallites, which stimulated the vertical alignment of the nanostructures grown by CBD as the seed layer presented lower roughness and porosity. After the three dip-coating cycles, an annealing step was carried out to decrease the number of structural defects and promote ZnO crystallization. This step was performed in an argon atmosphere and in the air at 600 and 800°C. The annealing in air improved the properties of the seed layer by decreasing its roughness [4].

2.2.5.2 Growth solution composition

The nature and concentration of the precursors used for the synthesis of ZnO nanostructures have a vital role to play in the growth kinetics, i.e., varying the precursors' concentration alters the properties of the hydrothermally synthesized ZnO nanostructures [2].

Generally, two precursors are required in a ZnO hydrothermal synthesis: one to provide zinc cations and the other to supply hydroxyl radicals. The zinc precursor (such as zinc nitrate, chloride, sulfate, or acetate) provides cations that will integrate ZnO nanostructures [1]. On the other hand, the non-polar chelating agent HMTA is often used as the pH buffer [2], as it functions as a hydroxyl radicals' source [14, 46], and it also acts as a complexing agent [17]. HMTA hydrolyzes at elevated temperatures [46] and preferentially attaches to the non-polar faces of ZnO crystals, promoting the nanostructures' growth along the *c*-axis since radial growth is hindered [1, 2]. As such, a higher concentration of HMTA leads to longer and thinner 1D nanostructures, whereas the reverse is observed when HMTA concentration is lower compared to zinc concentration [2]. These morphological features will influence other properties, such as the nanostructures' optical properties [2].

Gill *et al*. studied the influence of ammonia addition on the properties of hydrothermally synthesized ZnO nanorods on ITO glass substrates. Ammonia addition promoted the nanostructures' growth along the *c*-axis since this species reacts with zinc cations, forming complexes such as $Zn(NH_3)_2^+$ and $Zn(NH_3)_3^{2+}$. These complexes increase the nanorods' density and stimulate their growth as their solubility in water is higher than that of zinc hydroxide, translating into a decreased tendency to precipitate [13].

The solvent properties, namely its polarity, also influence the hydrothermal synthesis growth kinetics, as depending on the solvent's overall charge, its molecules attach to different crystal facets and can act as structure-directing agents [52].

Several additives can be added to the growth solution to promote the formation of the intended ZnO crystal morphology. In this scope, polymeric surfactants such as poly(vinyl alcohol) have been proven to interact with zinc cations, producing zinc hydroxide, which is then confined in the polymer's structure. Although heating leads

to polymer decomposition, carbon backbone grids with ZnO nanoparticles can stay in solution, leading to the growth of aligned nanorod arrays along the *c*-axis [14].

2.2.5.3 Synthesis time and temperature

The variation of the hydrothermal synthesis time has also been reported to influence ZnO nanorods' properties [3, 18]. A study of the impact of the reaction time proved that longer nanorods could be produced by increasing the synthesis duration [3]. In this work, a zinc acetate seed layer was primarily deposited on FTO substrates through spin-coating. Afterward, syntheses with different durations (up to 15 min) were performed using a zinc acetate, sodium hydroxide, and polyvinylpyrrolidone growth solution. Nanostructures with lengths between 300 and 1500 nm were obtained [3].

The growth of ZnO nanorods at several temperatures and at different times on ITO glass precoated with a zinc acetate layer through dip-coating has also been reported [18]. First, the syntheses were performed at 120°C with variable durations (1–4 h), and the results revealed a band gap decrease with increasing synthesis time (3.24 and 3.13 eV, for 1 and 4 h synthesis time). Then, the temperature was varied from 90 to 130°C, and the results indicate that a 130°C synthesis temperature might lead to the vaporization of zinc nitrate hexahydrate, which could inhibit the nanorods' growth. As such, in the study mentioned above, a temperature of 120°C and a synthesis duration of 4 h were considered optimal as they maximized the nanorods' length, leading to improved photoresponse [18].

2.2.5.4 Filling ratio

Efafi and colleagues presented a study on the influence of the filling volume on the properties of ZnO nanorods grown on glass substrates. Samples were prepared by filling 25, 50, and 75% of an autoclave volume with a zinc nitrate and HMTA growth solution. The samples resulting from the synthesis with the highest filling percentage presented an increased number of charge carriers and reduced band gap energy. Moreover, these samples' XRD patterns presented an enhanced intensity of the (002) peak, pointing to a higher growth along the *c*-axis. Additionally, the ZnO nanorods produced with the highest solution volume demonstrated higher density and improved alignment, which are attributed to the higher pressure and, consequently, temperature inside the autoclave ($PV = nRT$) [27].

2.2.5.5 Controlled growth-patterning

Chalangar and co-workers proposed an approach to grow density-controlled ZnO nanorod arrays on silicon substrates. First, a zinc acetate seed layer was deposited on the substrate through dip-coating, followed by the deposition of a poly(methyl methacrylate) sacrificial layer and a photoresist film. Then, the samples were covered with poly(diallyl dimethylammonium) to promote the electrostatic adhesion of polystyrene nanobeads. These nanobeads were posteriorly removed, creating nanoholes where ZnO nanorods were selectively hydrothermally grown. Nanobeads with different sizes were tested: while smaller beads led to heterogeneous growth, larger ones caused the growth of star-shaped structures and ZnO nanorods. The reported results indicate that choosing an appropriate nanohole size makes it possible to grow a single aligned ZnO nanorod on each hole [25].

Having in mind the influence of the hydrothermal synthesis parameters on the properties of the synthesized materials, in this work, a thorough study was carried out on the impact of seed layer properties and synthesis time and temperature on the morphological features of nanorod arrays grown on glass substrates by microwave-assisted hydrothermal synthesis. The length, diameter, aspect ratio, and density of nanorods synthesized under different conditions were estimated in order to establish a correlation between the synthesis conditions and each of these features. Therefore, the study carried out in this work becomes an essential tool when producing ZnO nanostructures by microwave-assisted hydrothermal synthesis since it presents itself as a guide of synthesis conditions for obtaining nanostructures with morphological features suited to the intended application.

3. Synthesis and characterization of aligned ZnO nanorods grown on glass substrates by microwave-assisted hydrothermal synthesis

3.1 Materials and methods

At CENIMAT, ZnO nanorod arrays were synthesized on Corning Eagle XG glass (Goodfellow, Cambridge, United Kingdom) by microwave-assisted hydrothermal synthesis. Prior to the nanostructures' growth, the substrate was coated with a seed layer by RF magnetron sputtering in an AJA ATC-1300F system without intentional substrate heating. A ceramic oxide target of ZnO supplied by Alineason Materials Technology GmbH, with a purity of 99.99%, was used for the deposition. First, the chamber was evacuated to a base pressure of 10^{-6} Torr, and then the process was performed with a power density of 4.2 W cm^{-2} and a pressure of 2.3 mTorr under an argon and oxygen atmosphere. The target and substrate were spaced by 18 cm.

After uniformly coating the Corning glass with the seed layer, ZnO nanorod arrays were synthesized by hydrothermal synthesis using a Discover SP Microwave Reaction System from CEM. For the ZnO nanorods growth, an equimolar (25 mM) aqueous mixture was prepared by combining zinc nitrate hexahydrate ($Zn(NO_3)_2{\cdot}6H_2O$; 98%; CAS: 10196-18-6) and HMTA ($(C_6H_{12}N_4)_2$; 99%; CAS: 100-97-0), both from Sigma-Aldrich. Before the synthesis, 25 mL of this solution was transferred to a 35 mL Pyrex vessel, and then, the substrate (25 × 12.5 mm) was placed at an angle against the inside vessel wall with the seed layer facing down. Different synthesis durations (15, 30, or 60 min) and temperatures (80, 100, or 120°C) were tested. A maximum pressure of 280 psi and a power of 100 W were kept for all syntheses. After each synthesis, the substrates were cleaned with deionized water and isopropyl alcohol and dried with nitrogen.

Ultraviolet/ozone (UVO) treatment with different durations (up to 30 min) was performed on the seed layer before the hydrothermal synthesis to analyze possible changes in this layer and the resulting nanostructures. The treatment was performed using a Novascan system equipped with two ultraviolet (UV) lamps with 185 nm and 254 nm wavelengths. The distance between the substrates and UV lamps was kept at 10 cm.

The morphological characterization of the seed layers and the ZnO nanorods was done by scanning electron microscopy (SEM) using either a Carl Zeiss AURIGA CrossBeam Workstation instrument or a Hitachi Regulus 8220 Scanning Electron Microscope. The nanorods' features, such as length, diameter, and density, were estimated using the ImageJ software and the SEM images. It is important to highlight that the nanorod density for each sample was calculated on a 0.2 μm^2 area from the SEM images. A Dektak XT stylus profilometer was used to determine seed layer thicknesses.

3.2 Results and discussion

3.2.1 ZnO seed layer thickness

The deposition of the ZnO seed layer on Corning glass was carried out by RF magnetron sputtering. A growth rate of 1.49 nm min^{-1} was estimated based on the data obtained by profilometry. Seed layers with 50, 100, and 400 nm thicknesses were produced using a 33, 67, and 268 min deposition time, respectively. **Figure 2** shows the secondary electrons (SE) scanning electron microscopy images of the surface morphology of the seed layers.

Considering the images presented in **Figure 2**, it can be concluded that an increase in the seed layer thickness causes the coalescence of the sputtered seed layer particles, as observed in the 400 nm ZnO layer image. This coalescence effect has been reported Ghayour et al. [53], where a regular grain distribution with a spherical shape was observed to grow in size with increasing deposition time. A decrease in deposition time, reaching 100 nm thickness, leads to a regular grain distribution, forming a smoother surface. Discontinuities are observed in the 50 nm seed layer surface.

Zinc oxide nanorods were successfully grown from the seed layers with different thicknesses by a 30 min and 100°C hydrothermal synthesis. Before the synthesis, the seed layer underwent a 5 min UVO treatment to promote growth along the *c*-axis [54]. The SEM images of the obtained samples are presented in **Figure 3**.

As the seed layer thickness duplicates from 50 to 100 nm, an increase in the nanorods' length can be observed (from 244 to 317 nm), as depicted in **Table 3**, presented at the end of the chapter. Upon increasing the seed layer thickness to 400 nm, a decrease in the nanorods' mean length (122 nm) is observed. This decrease is associated with the heterogeneity of the seed layer, which hinders the nanorods' growth. As such, regarding the length of the produced 1D nanostructures, the highest value was reached for a 100 nm seed layer.

It is well known that the diameter of ZnO nanorods strongly depends on the size of the seed layer particles. With an increase in seed layer thickness, the size of its grains and particles increases, which is expected to cause an increase in the nanorods' diameter as this layer acts as a template for their growth [55]. However, no significant differences were detected in the diameter of the nanorods (about 40 nm) produced from the different seed layers, which might be associated with the effect of the UVO treatment in stimulating the nanostructures' growth.

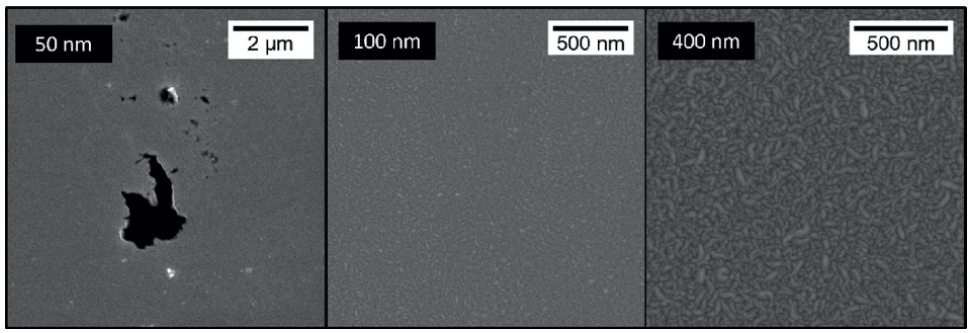

Figure 2.
SE mode SEM image of surface morphology of the 50, 100, and 400 nm ZnO seed layers (power = 85 W).

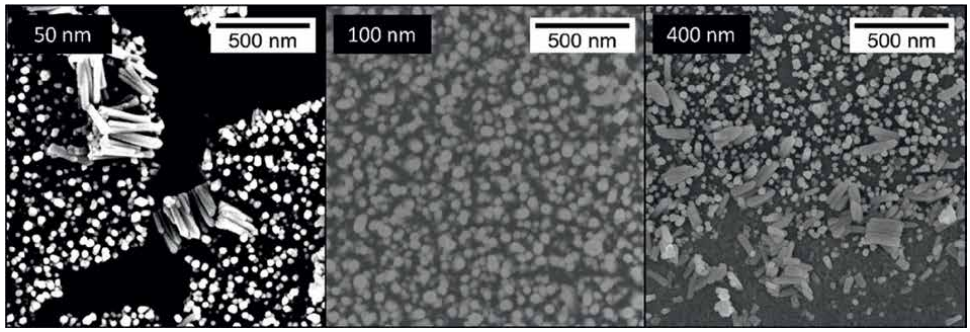

Figure 3.
SE mode SEM image of ZnO nanorods produced by hydrothermal synthesis from seed layers with different thicknesses (50, 100, and 400 nm).

The nanorods' density is expected to decrease with increasing seed layer thickness as the number of nucleation sites on the surface of this layer decreases [56]. As such, as expected, a decrease in the seed layer thickness from 400 to 100 nm prompted an increase in nanorod density from 533 to 754 NRs μm^{-2}. A lower nanorod density (306 NRs μm^{-2}) was obtained when the seed layer thickness was further reduced to 50 nm. The decrease in nanorod density can be ascribed to a lower number of nucleation sites, i.e., thinning of the seed layer might result in an uneven or discontinuous surface, which hinders the vertical growth of ZnO nanorods, as shown in **Figure 2**.

It is worth mentioning that the inverse relation between nanorod density and diameter for samples produced from seed layers with different thicknesses listed in **Table 3** was similar to the results reported by Song *et al.* [57].

3.2.2 UVO treatment to the seed layer prior to the synthesis

Before the hydrothermal growth of ZnO nanorods, a UVO treatment was performed on 100 nm thick seed layers to induce polarity in their surface and consequently promote the nanorods' vertical alignment [54]. The ZnO nanorods successfully grown from seed layers that underwent 5, 15, and 30 min UVO treatments and without this treatment are presented in **Figure 4**. The syntheses were carried out at 100°C for 30 min.

By exposing the ZnO seed layer to UV radiation, the oxygen adsorbed to its surface will decompose, and the surface will become more polar, promoting the growth of ZnO nanorods with a direction perpendicular to the seed layer surface [54]. The UVO treatment stimulated growth was observed in the prepared samples as the nanorods resulting from a seed layer without UVO treatment presented a mean length of 187 nm, whereas the nanostructures grown from a layer that underwent 5 and 15 min treatments exhibited higher lengths of 317 and 225 nm, respectively, as listed in **Table 3**. In turn, the length of the nanorods produced from a seed layer that underwent a 30 min UVO treatment was similar to that of the nanostructures produced from the sample that received no treatment. As such, a 5 min UVO treatment was considered the optimal condition to maximize the nanorods' length.

Changes in aspect ratio were also observed, as the nanorods' diameter decreased from 50 (no UVO treatment) to around 37 nm for a UVO treatment duration of up to 15 min. Further increasing the UVO treatment duration led to the formation of

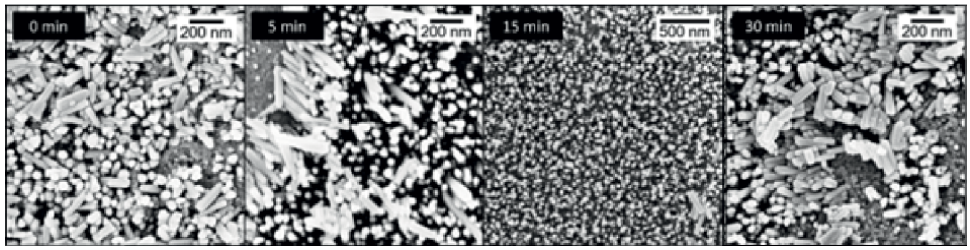

Figure 4.
SE mode SEM image of ZnO nanorods produced by hydrothermal synthesis from 100 nm seed layers that underwent UVO treatments with different durations (0, 5, 15, and 30 min).

nanorods with diameters of approximately 44 nm. A similar trend was reported by Song *et al.* [57].

The UVO treatment also influenced the density of nanorod arrays. The samples grown from a 5 min UVO-treated layer presented a density twice higher than that of the nanostructures produced from the seed layer without UVO treatment (from 344 to 754 NRs μm^{-2}). Increasing the UVO treatment duration from 5 to 15 min caused a decrease in the nanorods' density to 524 NRs μm^{-2}.

As can be seen from the studies above, the duration of UVO treatment is not proportionally related to these features, indicating that the UVO treatment's dynamics might change for longer durations. Thus, the UV radiation penetration depth might increase, leading to the effects of the UVO treatment being more significant in depth than at the surface of the seed layer. Moreover, the possible increase in penetration depth also allows the reabsorption of oxygen molecules on the seed layer surface, which lowers the induced polarization of this layer by the UVO treatment.

3.2.3 Synthesis time

Zinc oxide nanorods were grown at 100°C in syntheses whose duration varied between 15 and 60 min. A 100 nm seed layer, which underwent a 5 min UVO treatment, was used to grow the nanostructures presented in **Figure 5**.

The average diameter of the ZnO nanorods decreased from 48 nm to 35 nm for increasing synthesis time (15–60 min), resulting in a continuous increase in the nanorods' aspect ratio, as presented in **Table 3**.

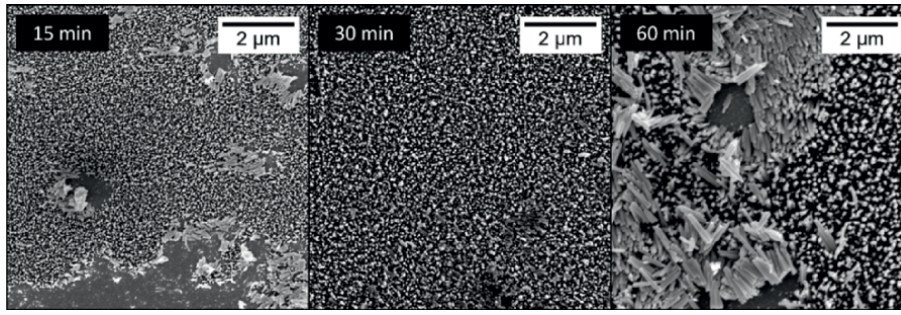

Figure 5.
SE mode SEM image of ZnO nanorods produced by hydrothermal synthesis with different durations (15, 30, and 60 min) from a 100 nm seed layer.

The nanorods' mean length and density values for each synthesis duration are presented in **Figure 6**.

The nanorods' mean length increases with increasing synthesis time, i.e., nanorods resulting from a 15 min synthesis present a 220 nm length. In contrast, nanostructures resulting from a 60 min synthesis have a 395 nm length.

The data presented in **Figure 6** depict a decrease in growth per minute, directly impacting the nanorods' density. For synthesis durations of up to 15 min, the growth rate presents a value of around 15 nm min^{-1}. However, for intervals between 15 and 30 min, the growth rate is about 7 nm min^{-1}, and a nanorod density increase from 375 to 754 NRs μm^{-2} is detected. Finally, a decrease in nanorod density, from 754 to 435 NRs μm^{-2}, was observed when the synthesis time was increased from 30 to 60 min. This decrease in density and the continuous increase in the nanorods' mean length with increasing synthesis time can be attributed to the Ostwald ripening process. During this process, small nanorods dissolve, and larger ones keep growing until an equilibrium is reached [58].

3.2.4 Synthesis temperature

The ZnO nanorods' growth is a thermo-activated process, so the temperature significantly conditions the nanorods' formation and growth along the *c*-axis [59]. In this scope, ZnO nanorods were grown at different temperatures of 80, 100, and 120°C from a 100 nm seed layer that underwent a 5 min UVO treatment prior to the synthesis. The synthesis duration was fixed at 30 min. The SEM images of the nanorods produced at different temperatures are presented in **Figure 7**.

The image of the nanorods grown at 120°C shows the detachment of the seed layer from the substrate in specific areas, which hinders the nanorods' growth. In turn, when the synthesis temperature was decreased from 120 to 100°C, the nanorods' length duplicated from 153 to 317 nm (**Table 3**), with a growth rate of around 8 nm°C^{-1}. However, when the temperature was further decreased to 80°C, the nanorods' mean length decreased to 220 nm, which was associated with the lower energy level of the

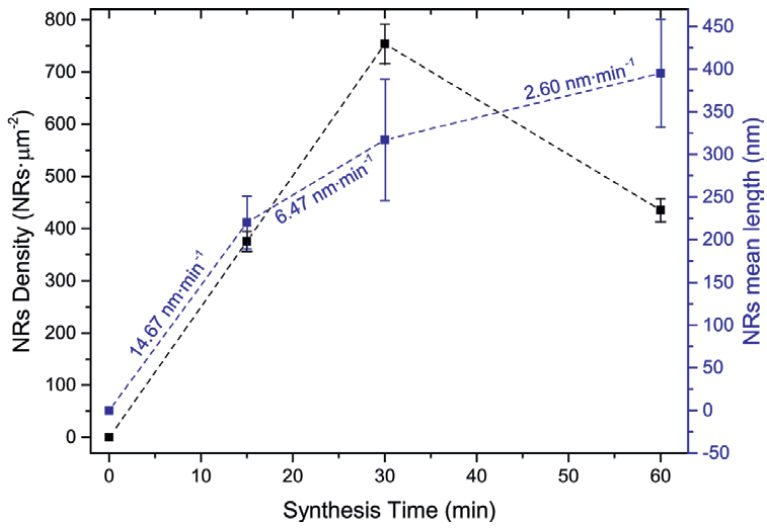

Figure 6.
Plot representing the evolution of ZnO nanorods' average density (black) and length (blue) as a function of synthesis time.

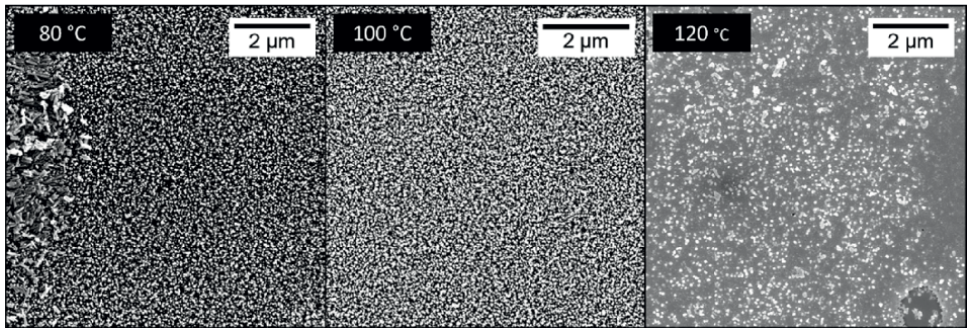

Figure 7.
SE mode SEM images of ZnO nanorods produced by hydrothermal synthesis at several temperatures (80, 100, and 120°C) for 30 min.

reaction medium derived from the lower temperature. Regarding the growth rate, a value of about 5 nm°C^{-1} is reached for synthesis temperatures between 80 and 100°C.

The nanorods' diameter presented a minimum value for a 100°C temperature, which would be expected since this sample presents nanostructures with the highest length. By varying the synthesis temperature, the energy state of the reaction medium is controlled, which promotes or hinders the growth of the nanorods along the *c*-axis [14]. In turn, higher growth in the direction normal to the substrate tends to lead to a decrease in the nanostructures' diameter.

The nanorod density increased when the synthesis temperature was varied between 80 and 100°C. However, when the temperature was further increased, the nanorods' density decreased, which is probably associated with the seed layer detachment from the Corning glass substrate.

Feature		NRs density (NRs µm^{-2})	NRs mean diameter (nm)	NRs mean length (nm)	NRs aspect ratio
Seed layer thickness	50 nm	158 ± 8	45 ± 10	244 ± 54	5
	100 nm	754 ± 38	37 ± 9	317 ± 71	8
	400 nm	533 ± 26	37 ± 8	122 ± 68	3
Seed layer UVO treatment time	0 min	344 ± 18	50 ± 11	187 ± 28	4
	5 min	754 ± 38	37 ± 9	317 ± 71	8
	15 min	524 ± 27	38 ± 9	225 ± 32	6
	30 min	437 ± 22	44 ± 10	184 ± 41	4
Synthesis time	15 min	375 ± 19	48 ± 17	220 ± 31	5
	30 min	754 ± 38	37 ± 9	317 ± 71	8
	60 min	435 ± 22	35 ± 4	395 ± 63	11
Synthesis temperature	80°C	438 ± 22	42 ± 6	220 ± 42	5
	100°C	754 ± 38	37 ± 9	317 ± 71	8
	120°C	443 ± 22	56 ± 22	153 ± 43	3

Table 3.
Summary of the obtained ZnO nanorods' morphological features according to the synthesis conditions.

The obtained results establish a clear relation between the nanorods' morphological features and the hydrothermal synthesis conditions. As such, the data presented in **Table 3** can serve as guidelines for future work where tailoring the nanostructures' properties according to the application in question might be needed since maximizing different parameters such as surface area or density might be fundamental depending on the research area.

4. Conclusions

Zinc oxide (ZnO) nanostructures present non-toxicity, which, jointly with their other properties such as piezoelectricity, high stability, and mechanical strength, make them attractive materials for use in several applications such as water splitting, sensing, or energy harvesting and storage. Among the several nanostructures, one-dimensional (1D) materials have been widely used due to their properties, such as improved optical performance and high surface-to-volume ratio, desirable features in electronic and optoelectronics. Vapor- and solution-based synthesis approaches have been proposed to grow these nanostructures on different substrates. Vapor phase approaches, such as VLS, PLD, CVD, and MPATE, offer precise control of the nanostructures' growth and allow the careful tuning of their properties, a valuable tool for (opto)electronic and sensing applications. On the other hand, solution phase syntheses, such as spray pyrolysis, emulsion methods, and hydrothermal synthesis, offer the possibility of producing ZnO through time- and cost-effective approaches, where ZnO properties can be tailored by controlling the reaction kinetics. Therefore, the method for synthesizing ZnO nanostructures should be chosen depending on the final application and the available equipment.

Since hydrothermal synthesis is a simple, cost- and time-effective method, it is the most used for growing ZnO nanorods on substrates. In this scope, a study was conducted on the influence of various parameters on the morphological properties of 1D ZnO nanostructures. In this work, ZnO nanorods were grown from seed layers with different thicknesses, which underwent an ultraviolet/ozone treatment prior to the hydrothermal synthesis. Synthesis time and temperature were also varied. Nanorods with lengths up to 317 nm were obtained using Corning glass precoated with a 100 nm seed layer that underwent a 5 min ultraviolet/ozone treatment to induce polarization on its surface. The aligned nanorods with improved aspect ratio were synthesized at 100°C for 60 min. The highest nanorod density values were obtained in the same conditions but for a synthesis time of 30 min. Thus, the obtained data indicate that each parameter impacts the synthesized nanostructures' properties. As such, the growth process details must be carefully selected depending on the final application aiming to optimize the nanostructures' performance.

The described results are the cornerstone for developing high-performance electronic three-dimensional (3D) devices and pressure sensors for monitoring human movements, as they provide a detailed report on the procedure to obtain nanorods with the desirable morphology, directly impacting the devices' operation.

Acknowledgements

This work was financed by national funds from FCT—Fundação para a Ciência e a Tecnologia, I.P., under the scope of the projects LA/P/0037/2020, UIDP/50025/2020

and UIDB/50025/2020 of the Associate Laboratory Institute of Nanostructures, Nanomodelling and Nanofabrication—i3N, and by the European Union's Horizon 2020 Research and Innovation Programme under the EMERGE project (N° 101008701) and the SYNERGY project (N° 952169). M.M and M.C. acknowledge funding from FCT-MCTES, I.P., through the PhD Grants 2022.13806.BD and 2022.09516.BD.

Conflict of interest

The authors declare no conflict of interest.

Author details

Maria Morais†, Mariana Cortinhal†, Ana Rovisco, Jorge Martins, Rodrigo Martins and Pedro Barquinha*
Department of Materials Science, CENIMAT|i3N, NOVA School of Science and Technology, NOVA University Lisbon and CEMOP/UNINOVA, Caparica, Portugal

*Address all correspondence to: pmcb@fct.unl.pt

† These authors contributed equally to this work.

References

[1] Abubakar S, Tan ST, Liew JYC, Talib ZA, Sivasubramanian R, Vaithilingam CA, et al. Controlled growth of semiconducting ZnO Nanorods for piezoelectric energy harvesting-based Nanogenerators. Nanomaterials. 2023;**13**(6):1025

[2] Angub MCM, Vergara CJT, Husay HAF, Salvador AA, Empizo MJF, Kawano K, et al. Hydrothermal growth of vertically aligned ZnO nanorods as potential scintillator materials for radiation detectors. Journal of Luminescence. 2018;**203**:427-435. Available from: https://linkinghub.elsevier.com/retrieve/pii/S002223131732135X

[3] Yun S, Guo T, Li Y, Gao X, Huang A, Kang L. Well-ordered vertically aligned ZnO nanorods arrays for high-performance perovskite solar cells. Materials Research Bulletin. 2020;**130**:110935. Available from: https://linkinghub.elsevier.com/retrieve/pii/S0025540820308941

[4] Basinova N, Cernohorsky O, Grym J, Kucerova S, Faitova H, Yatskiv R, et al. Highly textured seed layers for the growth of vertically oriented ZnO Nanorods. Crystals. 2019;**9**(11):566. Available from: https://www.mdpi.com/2073-4352/9/11/566

[5] Rastialhosseini SMAA, Khayatian A, Shariatzadeh R, Almasi KM. Three-dimensional ZnO nanorods growth on ZnO nanorods seed layer for high responsivity UV photodetector. Applied Physics A: Materials Science & Processing. 2019;**125**(12):829. Available from: http://link.springer.com/10.1007/s00339-019-3123-6

[6] You D, Xu C, Zhang W, Zhao J, Qin F, Shi Z. Photovoltaic-pyroelectric effect coupled broadband photodetector in self-powered ZnO/ZnTe core/shell nanorod arrays. Nano Energy. 2019;**62**:310-318. Available from: https://linkinghub.elsevier.com/retrieve/pii/S2211285519304562

[7] Hammed NA, Aziz AA, Usman AI, Qaeed MA. The sonochemical synthesis of vertically aligned ZnO nanorods and their UV photodetection properties: Effect of ZnO buffer layer. Ultrasonics Sonochemistry. 2019;**50**:172-181. Available from: https://linkinghub.elsevier.com/retrieve/pii/S1350417718309271

[8] Zheng H, Jiang Y, Yang S, Zhang Y, Yan X, Hu J, et al. ZnO nanorods array as light absorption antenna for high-gain UV photodetectors. Journal of Alloys and Compounds. 2020;**812**:152158. Available from: https://linkinghub.elsevier.com/retrieve/pii/S0925838819334048

[9] Kammel RS, Sabry RS. Effects of the aspect ratio of ZnO nanorods on the performance of piezoelectric nanogenerators. Journal of Science: Advanced Materials and Device. 2019;**4**(3):420-424. Available from: https://linkinghub.elsevier.com/retrieve/pii/S2468217919302102

[10] Han Y, Guo J, Luo Q, Ma C. solution-processable zinc oxide for printed photovoltaics: Progress, challenges, and prospect. Advanced Energy and Sustainability Research. 2023;**4**:2200179. DOI: 10.1002/aesr.202200179

[11] Çolak H, Karaköse E, Sungür Ç. Niobium doping effect on electrical and optical properties of ZnO nanorods produced by ultrasonic spray pyrolysis. Physica B: Condensed Matter. 2023;**671**:415455. Available from: https://

linkinghub.elsevier.com/retrieve/pii/S0921452623008220

[12] Gu P, Zhu X, Yang D. Vertically aligned ZnO nanorods arrays grown by chemical bath deposition for ultraviolet photodetectors with high response performance. Journal of Alloys and Compounds. 2020;**815**:152346. Available from: https://linkinghub.elsevier.com/retrieve/pii/S0925838819335923

[13] Gill R, Ghosh S, Sharma A, Kumar D, Nguyen VH, Vo DVN, et al. Vertically aligned ZnO nanorods for photoelectrochemical water splitting application. Materials Letters. 2020;**277**:128295. Available from: https://linkinghub.elsevier.com/retrieve/pii/S0167577X20310004

[14] Kardeş M, Öztürk K. Photocatalyst ZnO nanorod arrays on glass substrates: The critical role of seed layer in nanorod alignment and photocatalytic efficiencies. Chemical Engineering Communications. 2020;**207**(11):1522-1535. Available from: https://www.tandfonline.com/doi/full/10.1080/00986445.2019.1660651

[15] Henni A, Harfouche N, Karar A, Zerrouki D, Perrin FX, Rosei F. Synthesis of graphene–ZnO nanocomposites by a one-step electrochemical deposition for efficient photocatalytic degradation of organic pollutant. Solid State Sciences. 2019;**98**:106039. Available from: https://linkinghub.elsevier.com/retrieve/pii/S1293255819304698

[16] Heo YW, Norton DP, Tien LC, Kwon Y, Kang BS, Ren F, et al. ZnO nanowire growth and devices. Materials Science and Engineering: R: Reports. 2004;**47**(1-2):1-47. Available from: https://linkinghub.elsevier.com/retrieve/pii/S0927796X04001135

[17] Marimuthu T, Anandhan N, Thangamuthu R. Electrochemical synthesis of one-dimensional ZnO nanostructures on ZnO seed layer for DSSC applications. Applied Surface Science. 2018;**428**:385-394. Available from: https://linkinghub.elsevier.com/retrieve/pii/S0169433217327654

[18] Mohd Fudzi L, Zainal Z, Lim H, Chang SK, Holi A, Sarif@Mohd Ali M. Effect of temperature and growth time on vertically aligned ZnO Nanorods by simplified hydrothermal technique for Photoelectrochemical cells. Materials (Basel). 2018;**11**(5):704. Available from: http://www.mdpi.com/1996-1944/11/5/704

[19] Yang Y, Cheng YF. One-step facile preparation of ZnO nanorods as high-performance photoanodes for photoelectrochemical cathodic protection. Electrochimica Acta. 2018;**276**:311-318. Available from: https://linkinghub.elsevier.com/retrieve/pii/S0013468618309915

[20] Mateen Tantray A, Shah MA. Photo electrochemical ability of dense and aligned ZnO nanowire arrays fabricated through electrochemical anodization. Chemical Physics Letters. 2020;**747**:137346. Available from: https://linkinghub.elsevier.com/retrieve/pii/S000926142030261X

[21] Alev O, Sarıca N, Özdemir O, Arslan LÇ, Büyükköse S, Öztürk ZZ. Cu-doped ZnO nanorods based QCM sensor for hazardous gases. Journal of Alloys and Compounds. 2020;**826**:154177 Available from: https://linkinghub.elsevier.com/retrieve/pii/S0925838820305405

[22] Swathi S, Babu ES, Yuvakkumar R, Ravi G, Chinnathambi A, Alharbi SA, et al. Branched and unbranched ZnO nanorods grown via chemical vapor deposition for photoelectrochemical water-splitting applications. Ceramics

International. 2021;**47**(7):9785-9790. Available from: https://linkinghub.elsevier.com/retrieve/pii/S0272884220337202

[23] Chen HC, Lyu YR, Fang A, Lee GJ, Karuppasamy L, Wu JJ, et al. The design of ZnO Nanorod arrays coated with MnOx for high electrochemical stability of a Pseudocapacitor electrode. Nanomaterials. 2020;**10**(3):475. Available from: https://www.mdpi.com/2079-4991/10/3/475

[24] Wang L, Li X, Li Q, Yu X, Zhao Y, Zhang J, et al. oriented polarization tuning broadband absorption from flexible hierarchical ZnO arrays vertically supported on carbon cloth. Small. 2019;**15**:1900900. DOI: 10.1002/smll.201900900

[25] Chalangar E, Nur O, Willander M, Gustafsson A, Pettersson H. Synthesis of vertically aligned ZnO Nanorods using sol-gel seeding and colloidal lithography patterning. Nanoscale Research Letters. 2021;**16**(1):46. Available from: https://link.springer.com/10.1186/s11671-021-03500-7

[26] Çolak H, Karaköse E. Fabrication and investigation of zinc oxide nanorods doped with molybdenum via ultrasonic spray pyrolysis. International Journal of Applied Ceramic Technology. 2023;**21**(1):114-123. Available from: https://ceramics.onlinelibrary.wiley.com/doi/10.1111/ijac.14498

[27] Efafi B, Mazandarani H, Ara MHM, Ghafary B. Improvement in photoluminescence behavior of well-aligned ZnO nanorods by optimization of thermodynamic parameters. Physica B: Condensed Matter. 2020;**579**:411915. Available from: https://linkinghub.elsevier.com/retrieve/pii/S092145261930794X

[28] You D, Xu C, Zhao J, Zhang W, Qin F, Chen J, et al. Vertically aligned ZnO/Ga 2 O 3 core/shell nanowire arrays as self-driven superior sensitivity solar-blind photodetectors. Journal of Materials Chemistry C. 2019;**7**(10):3056-3063. Available from: http://xlink.rsc.org/?DOI=C9TC00134D

[29] Paldi RL, Sun X, Wang X, Zhang X, Wang H. Strain-driven In-plane ordering in vertically aligned ZnO–Au nanocomposites with highly correlated metamaterial properties. ACS Omega. 2020;**5**(5):2234-2241. Available from: https://pubs.acs.org/doi/10.1021/acsomega.9b03356

[30] Karnati P, Haque A, Taufique M, Ghosh K. A systematic study on the structural and optical properties of vertically aligned zinc oxide Nanorods grown by high pressure assisted pulsed laser deposition technique. Nanomaterials. 2018;**8**(2):62. Available from: http://www.mdpi.com/2079-4991/8/2/62

[31] Kolhep M, Bläsing J, Strittmatter A, Zacharias M. Spontaneous and position-controlled epitaxial growth of ZnO nanowires on AlN/Si by CVD. Crystal Growth & Design. 2023;**23**(10):7095-7102. Available from: https://pubs.acs.org/doi/10.1021/acs.cgd.3c00320

[32] Schaper N, Alameri D, Kim Y, Thomas B, McCormack K, Chan M, et al. Controlled fabrication of quality ZnO NWs/CNTs and ZnO NWs/gr Heterostructures via direct two-step CVD method. Nanomaterials. 2021;**11**(7):1836. Available from: https://www.mdpi.com/2079-4991/11/7/1836

[33] Kim Y, Deshmukh PR, Shin WG. Enhanced photoelectrochemical performance of vertically aligned ZnO nanowires. Materials Letters. 2021;**297**:129871. Available from: https://linkinghub.elsevier.com/retrieve/pii/S0167577X2100567X

[34] Cao P, Yang Z, Navale ST, Han S, Liu X, Liu W, et al. Ethanol sensing behavior of Pd-nanoparticles decorated ZnO-nanorod based chemiresistive gas sensors. Sensors and Actuators B: Chemical. 2019;**298**:126850. Available from: https://linkinghub.elsevier.com/retrieve/pii/S0925400519310494

[35] Rodwihok C, Choopun S, Ruankham P, Gardchareon A, Phadungdhitidhada S, Wongratanaphisan D. UV sensing properties of ZnO nanowires/nanorods. Applied Surface Science. 2019;**477**:159-165. Available from: https://linkinghub.elsevier.com/retrieve/pii/S0169433217332993

[36] Miao C, Jiang M, Xu H, Ji J, Kan C. Vertically-aligned ZnO microrod for high-brightness light source. CrystEngComm. 2020;**22**(39):6453-6464. Available from: http://xlink.rsc.org/?DOI=D0CE00933D

[37] Thongsuksai W, Panomsuwan G, Rodchanarowan A. Fast and convenient growth of vertically aligned ZnO nanorods via microwave plasma-assisted thermal evaporation. Materials Letters. 2018;**224**:50-53. Available from: https://linkinghub.elsevier.com/retrieve/pii/S0167577X18306542

[38] Ramgir NS, Subannajui K, Yang Y, Grimm R, Michiels R, Zacharias M. Reactive VLS and the reversible switching between VS and VLS growth modes for ZnO nanowire growth. Journal of Physical Chemistry C. 2010;**114**(23):10323-11039. Available from: https://pubs.acs.org/doi/10.1021/jp909377b

[39] Aspoukeh PK, Barzinjy AA, Hamad SM. Synthesis, properties and uses of ZnO nanorods: A mini review. International Nano Letters. 2022;**12**(2):153-168. Available from: https://link.springer.com/10.1007/s40089-021-00349-7

[40] Zhang Y, Russo RE, Mao SS. Femtosecond laser assisted growth of ZnO nanowires. Applied Physics Letters. 2005;**87**(13):1-3. Available from: https://pubs.aip.org/apl/article/87/13/133115/117229/Femtosecond-laser-assisted-growth-of-ZnO-nanowires

[41] Wan H, Ruda HE. A study of the growth mechanism of CVD-grown ZnO nanowires. Journal of Materials Science: Materials in Electronics. 2010;**21**(10):1014-1019. Available from: http://link.springer.com/10.1007/s10854-010-0118-7

[42] Barreca D, Bekermann D, Comini E, Devi A, Fischer RA, Gasparotto A, et al. 1D ZnO nano-assemblies by plasma-CVD as chemical sensors for flammable and toxic gases. Sensors and Actuators B: Chemical. 2010;**149**(1):1-7. Available from: https://linkinghub.elsevier.com/retrieve/pii/S0925400510005393

[43] Phan TL, Yu SC, Vincent R, Dan NH, Shi WS. Photoluminescence properties of various CVD-grown ZnO nanostructures. Journal of Luminescence. 2010;**130**(7):1142-1146. Available from: https://linkinghub.elsevier.com/retrieve/pii/S0022231310000499

[44] Le AT, Ahmadipour M, Pung SY. A review on ZnO-based piezoelectric nanogenerators: Synthesis, characterization techniques, performance enhancement and applications. Journal of Alloys and Compounds. 2020;**844**:156172. Available from: https://linkinghub.elsevier.com/retrieve/pii/S0925838820325366

[45] Ranjith Kumar D, Ranjith KS, Nivedita LR, Asokan K, Rajendra Kumar RT. Swift heavy ion induced effects on structural, optical and photo-catalytic properties of

Ag irradiated vertically aligned ZnO nanorod arrays. Nuclear instruments and methods in physics research section B: Beam interactions with materials and atoms. 2019;**450**:95-99. Available from: https://linkinghub.elsevier.com/retrieve/pii/S0168583X1830185X

[46] Hssi AA, Atourki L, Labchir N, Ouafi M, Abouabassi K, Elfanaoui A, et al. Electrodeposition of oriented ZnO nanorods by two-steps potentiostatic electrolysis: Effect of seed layer time. Solid State Sciences. 2020;**104**:106207. Available from: https://linkinghub.elsevier.com/retrieve/pii/S1293255820302314

[47] Sakai D, Nagashima K, Yoshida H, Kanai M, He Y, Zhang G, et al. Substantial narrowing on the width of "concentration window" of hydrothermal ZnO nanowires via ammonia addition. Scientific Reports. 2019;**9**(1):14160. Available from: https://www.nature.com/articles/s41598-019-50641-y

[48] Morais M, Marques AC, Ferreira SH, Pinheiro T, Pimentel A, Macedo P, et al. Visible Photoluminescent zinc oxide Nanorods for label-free nonenzymatic glucose detection. ACS Applied Nano Materials. 2022;**5**(3):4386-4396. Available from: https://pubs.acs.org/doi/10.1021/acsanm.2c00474

[49] Parize R, Garnier JD, Appert E, Chaix-Pluchery O, Consonni V. Effects of Polyethylenimine and its molecular weight on the chemical Bath deposition of ZnO nanowires. ACS Omega. 2018;**3**(10):12457-12464. Available from: https://pubs.acs.org/doi/10.1021/acsomega.8b01641

[50] Son NT, Noh JS, Park S. Role of ZnO thin film in the vertically aligned growth of ZnO nanorods by chemical bath deposition. Applied Surface Science. 2016;**379**:440-445. Available from: https://linkinghub.elsevier.com/retrieve/pii/S0169433216308595

[51] Fraleoni-Morgera A, Cesini I, Kumar P, Oddo CM. Hydrothermally grown ZnO Nanorods as promising materials for low cost electronic skin. ChemNanoMat. 2020;**6**(1):15-31. Available from: https://onlinelibrary.wiley.com/doi/10.1002/cnma.201900620

[52] Pimentel A, Rodrigues J, Duarte P, Nunes D, Costa FM, Monteiro T, et al. Effect of solvents on ZnO nanostructures synthesized by solvothermal method assisted by microwave radiation: A photocatalytic study. Journal of Materials Science. 2015;**50**(17):5777-5787

[53] Gonçalves RS, Barrozo P, Brito GL, Viana BC, Cunha F. The effect of thickness on optical, structural and growth mechanism of ZnO thin film prepared by magnetron sputtering. Thin Solid Films 2018;**661**(December 2017):40-45. Available from: https://linkinghub.elsevier.com/retrieve/pii/S0040609018304632

[54] Pimentel A, Samouco A, Nunes D, Araújo A, Martins R, Fortunato E. Ultra-fast microwave synthesis of ZnO nanorods on cellulose substrates for UV sensor applications. Materials (Basel). 2017;**10**(11):4-10

[55] Ghayour H, Rezaie HR, Mirdamadi S, Nourbakhsh AA. The effect of seed layer thickness on alignment and morphology of ZnO nanorods. Vacuum. 2011;**86**(1):101-105. Available from: https://linkinghub.elsevier.com/retrieve/pii/S0042207X11001679

[56] Pokai S, Limnonthakul P, Horprathum M, Eiamchai P, Pattantsetakul V, Limwichean S, et al. Influence of seed layer thickness on well-aligned ZnO nanorods via hydrothermal method. Materials Today Proceedings.

2017;**4**(5):6336-6341. Available from: https://linkinghub.elsevier.com/retrieve/pii/S2214785317309252

[57] Song J, Lim S. Effect of seed layer on the growth of ZnO Nanorods. Journal of Physical Chemistry C. 2007;**111**(2):596-600. Available from: https://pubs.acs.org/doi/10.1021/jp0655017

[58] Alshehri NA, Lewis AR, Pleydell-Pearce C, Maffeis TGG. Investigation of the growth parameters of hydrothermal ZnO nanowires for scale up applications. Journal of Saudi Chemical Society. 2018;**22**(5):538-545. Available from: https://linkinghub.elsevier.com/retrieve/pii/S1319610317301114

[59] Chevalier-César C, Capochichi-Gnambodoe M, Leprince-Wang Y. Growth mechanism studies of ZnO nanowire arrays via hydrothermal method. Applied Physics A: Materials Science & Processing. 2014;**115**(3):953-960. Available from: http://link.springer.com/10.1007/s00339-013-7908-8

Chapter 5

Zinc Oxide: Wurtzite Structure Properties under Isobaric and Isothermal Ensembles – A Computational Calculation

Yahia Chergui

Abstract

Zinc oxide is a promised component in Technology and Nanotechnology due to its practical properties especially under extended temperature and pressure. In this work parallel and equilibrium molecular dynamics technique (MD) (Raven Supercomputer of Cardiff University, UK) and DL_POLY 4 are used to study the effect of extended pressure and temperature; the system is composed from 2916 atoms of wurtzite type (1458 atoms of Oxygen and 1458 atoms of Zinc) under the range of pressure 0–200 GPa and the range of temperature 300–3000 K; the properties and chemical bonds of ZnO are analysed under isobaric and isothermal ensembles. These results are in the vicinity of available data of theoretical and experimental information. This work is very important in many industrial fields in nanoscale and macroscale fields.

Keywords: pressure, temperature, ZnO, chemical bonds, MD

1. Introduction

Zinc oxide is a very important material that can be used in a variety of applications such as gas sensors [1–5], photocatalyst [6, 7], nanowires [8–15], nanorods [16–20], tetra ped, nanowhiskers [21], nano combs [22, 23], nano pins [24, 25], and nano helices [26, 27]. At ambient conditions, the most stable phase of ZnO is wurtzite (B4) [28–31]. The parameters of the unit cell of B4 are; a = 3.242 (Å), c = 5.188 (Å), and μ = 3/8 where c/a = 1.633. The structure is formed by two interpenetrating zinc and oxygen hexagonal sublattices. Each atom of Zn is surrounded by four atoms of oxygen [32]. Due to its importance, ZnO has been the subject of many simulated investigations using different approaches. Under low and high pressures and temperatures, Hartree–Fock (HF) and density functional theory (DFT) have been used to simulate zinc oxide structure [33, 34], phase transition and elastic properties

[28, 29, 35–39], phonon-dispersion and defects [28, 40, 41], and structural stability [29, 34, 36, 42–52].

Classical force fields permit the study of physical properties and the temperature impact with consideration of anharmonicities using large systems [28, 42, 53], which can be investigated using molecular dynamics (MD). Although many experimental and theoretical investigations on ZnO have been conducted, there is still a need for more investigations in order to determine and predict possible scenarios of phase and structural transitions of different ZnO structures using the MD approach [16, 35]. This approach (MD) has been used to simulate isobaric and isothermal ensembles of ZnO at different temperatures and pressures [54–58], where the Buckingham potential is employed because it is binary as ZnO interactions [35, 59]. In this work, we focus on analysing isobaric-isothermal behaviours of the ZnO wurtzite phase to calculate the molar volume, its variation versus time, standard error of volume, fluctuations, total temperatures, total energy, equilibrium time of total energy, total temperature, and volume of the unit cell, bond-length of Zn-O, Zn-Zn, and O-O, and enthalpy of the system in the range of 0–200 GPa and up to 3000 K, where experimental and theoretical data under used conditions of pressures and temperatures are not available to our knowledge.

2. Numerical procedures

The present MD simulations on the ZnO B4 phase were achieved by the mean of the Raven supercomputer (Cardiff University, Chemistry Department, Wales, UK). We investigated the behaviour of our system at different temperatures and pressures. The atomic interactions of the system are given by Coulomb–Buckingham potential, with a cut-off radius of r_{cut} = 12 Å. Outside this distance, the short-range interactions are insignificant [4, 5]. To control the temperature and pressure, the Nose–Hoover constant NST ensemble was used (N number of atoms, S is the stress, and T is the temperature of the system) [6], with a thermostat relaxation time of 10 ps and a pressure (barostat) relaxation time of 10 ps (required time of thermostat).

The MD technique consists of numerically solving a group of differential equations of Newton's laws over all atoms of a simulation box. Thus, given an initial configuration of positions and velocities at the time (t), the positions, velocities, and accelerations can be calculated at a later time t + δt [7], where the time step was δt = 1 fs, and Verlet algorithm was employed for integration.

Each run is made up of 300,000 time steps (300 ps), enough to reach the equilibrium state of the system. The simulation box, with periodic boundary conditions, contains 2916 atoms of ZnO (1458 Zn^{2+} ions and 1458 O^{2-} ions), which is equivalent to a box of size 9 × 9 × 9 (according to x, y and z), with a = 3.242 Å, and c = 5.188 Å, see **Figure 1(a–d)**.

For long-range Coulomb interactions, the Ewald Sum method was applied [8]. The atomic positions in unit cell are (1/3, 2/3, 0), (2/3, 1/3, 1/2) for Zn^{2+}, and they are (1/3, 2/3, 0.381), (2/3, 0.335, 0.881) for O^{2-} ions. The error bar of molar volume calculations is between 0.0027 and 0.0064 $Å^3$.

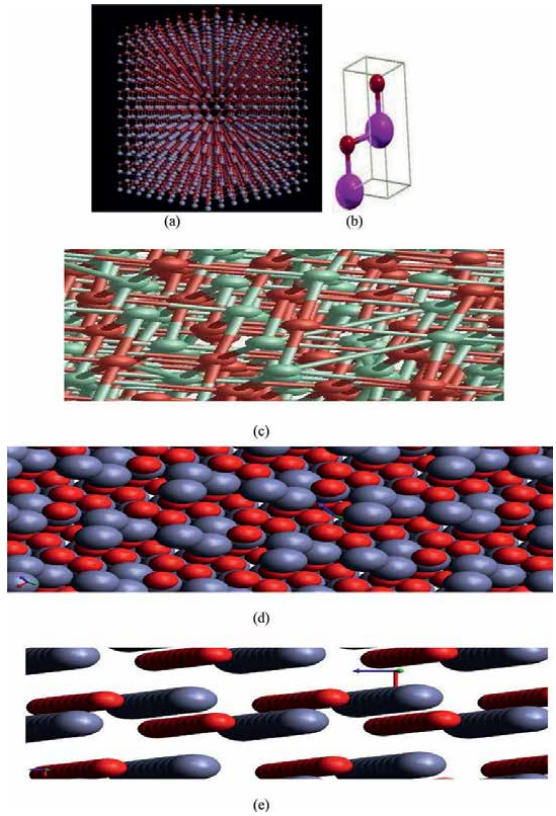

Figure 1.
(a) Simulation box 9a × 9b × 9c *supercell of ZnO B4 with 2916 atoms, under 0GPa and 300 K, the zinc and oxygen are grey and red spheres, respectively. (b) Unit cell of ZnO B4 (NASA Goddard Space Institute Collaboration), the zinc and oxygen atoms are magenta and red spheres, respectively.*

3. Results and discussion

3.1 Total energy of ZnO Wurtzite phase under different pressures and temperatures

3.1.1 Evolution of total energy in time under high pressure and different temperatures

In order to know the behaviour of total energy versus time, the equilibrium time of total energy is analysed to confirm the validity of Buckingham's potential under different temperatures and pressures. We study the system of 2916 atoms of ZnO-W phase under the range of 0–200 GPa and 300–3000 K, as shown in **Figures 2–12**. In **Figure 2**, under 0GPa and 300–3000 K ranges of temperatures, there is instability of the system due to the fluctuations from 0 ps to 100 ps at 1500, 2000, and 2500 K, especially at 3000 K because of the effect of temperature more than that of the pressure (around melting degree).

However, from 100 ps to 300 ps, the fluctuations become insignificant due to the equilibrium state; the system is more stable, and the total energy is linear and

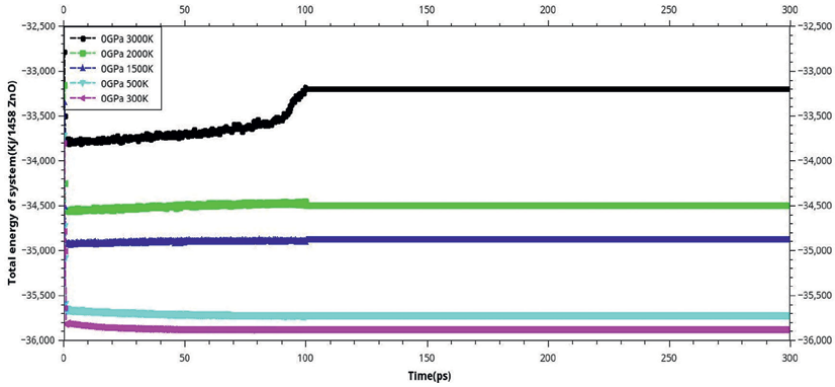

Figure 2.
Total energy of system of ZnO-W phase under 0 GPa and the range of 300–3000 K.

constant at 300–3000 K. While at 3000 K, we notice an important jump of the total energy in the vicinity of 100 ps; this means that the solid phase of the wurtzite ZnO is not stationary at this temperature, the most likely phase steady under these conditions (3000 K and 2500GPa) is the liquid phase, Chergui et al. [60].

Under 20 GPa and the range of temperature1500–3000 k, the total energy reaches its equilibrium value of around 100 ps with noteworthy fluctuations at 1500–3000 K, while at 300 K and 500 K, the fluctuations are slender, and the equilibrium time is around 10 ps.

The total energy rises with rising the temperature and pressure, and becomes smooth, see **Figure 3**.

The same behaviour can be seen in the case of the pressure 40–60 GPa, where the equilibrium time drops with rising temperature; besides that, there is a reduction of fluctuations and growth of total energy, see **Figures 4** and **5**. Under 20 GPa and the range of temperature 1500–3000 k, the total energy reaches its equilibrium value of around 100 ps with noticeable fluctuations at 1500–3000 K, while at 300 K and 500 K, the fluctuations are minor, and equilibrium time is around 10 ps. The total energy gets bigger with the extension of temperature and pressure and becomes smoother.

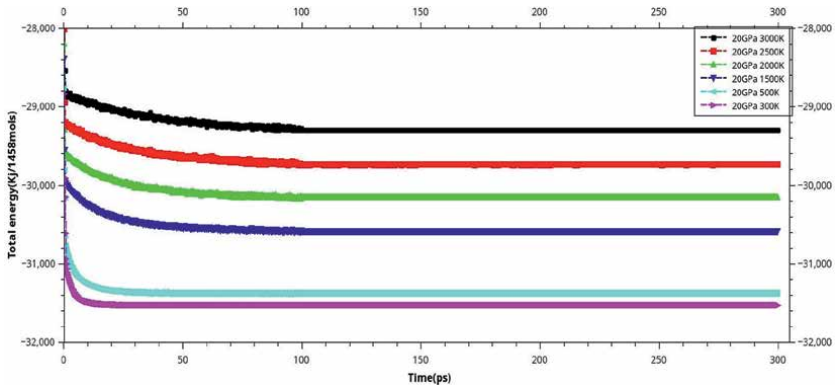

Figure 3.
Total energy of system of ZnO-W phase under 20 GPa and the range of 300–3000 K.

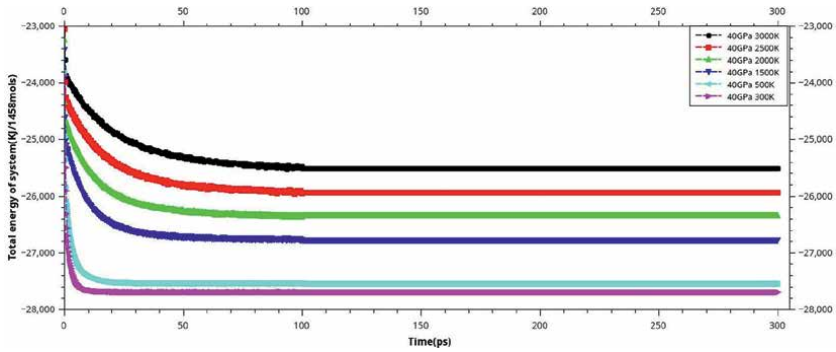

Figure 4.
Total energy of system of ZnO-W phase under 40GPa and the range of 300–3000 K.

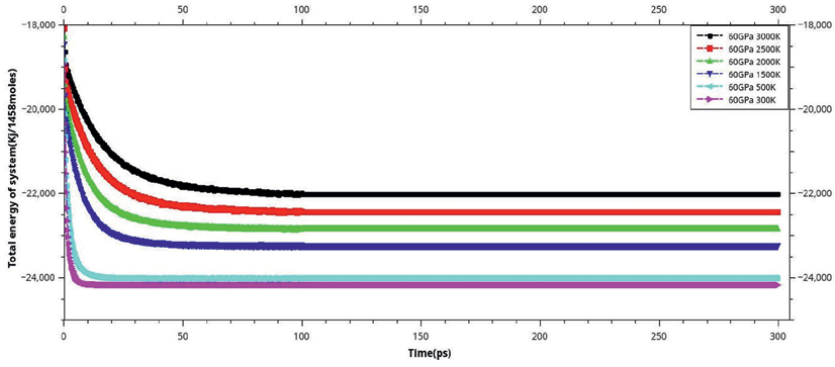

Figure 5.
Total energy of system of ZnO-W phase under 60 GPa and the range of 300–3000 K.

In the range of 80–200 GPa, the effect of pressure is more crucial; the total energy reaches its equilibrium value very quickly compared to the case of low pressures. Actually, we see from **Figures 6–12** that the bigger the pressure, the shorter the equilibrium time and vice versa.

The relationship between equilibrium time of total energy, under low and high temperatures and pressures is that; the equilibrium time increases with increasing

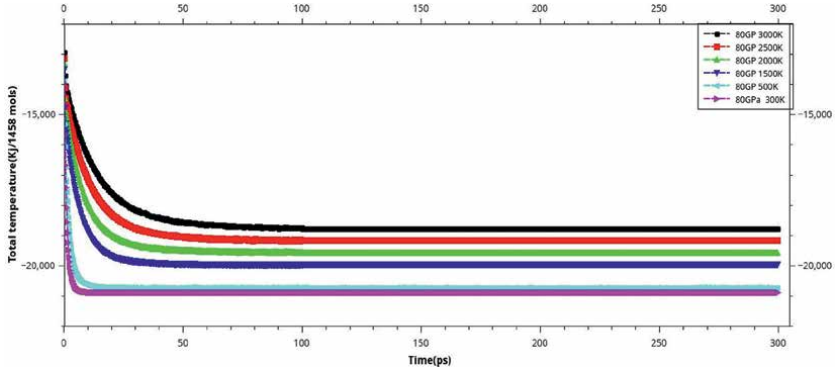

Figure 6.
Total energy of system of ZnO-W phase under 80GPa and the range of 300–3000 K.

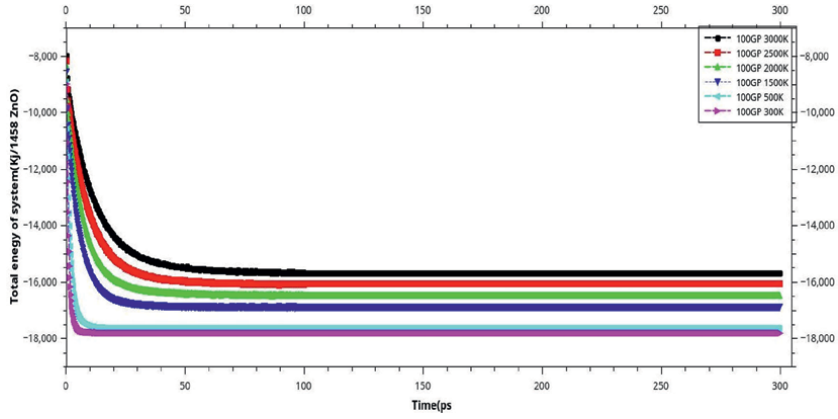

Figure 7.
Total energy of system of ZnO-W phase under 100GPa and the range of 300–3000 K.

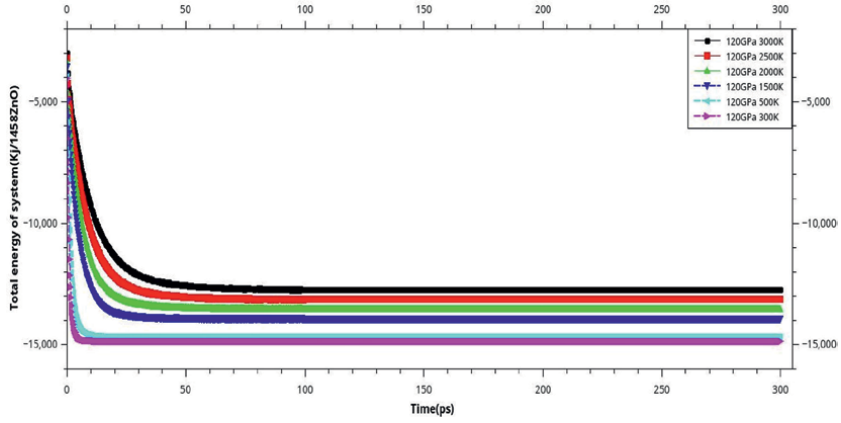

Figure 8.
Total energy of system of ZnO-W phase under 120GPa and the range of 300–3000 K.

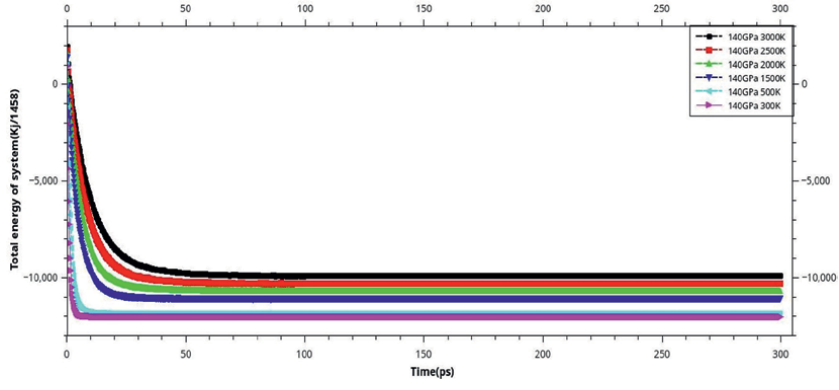

Figure 9.
Total energy of system of ZnO-W phase under 140GPa and the range of 300–3000 K.

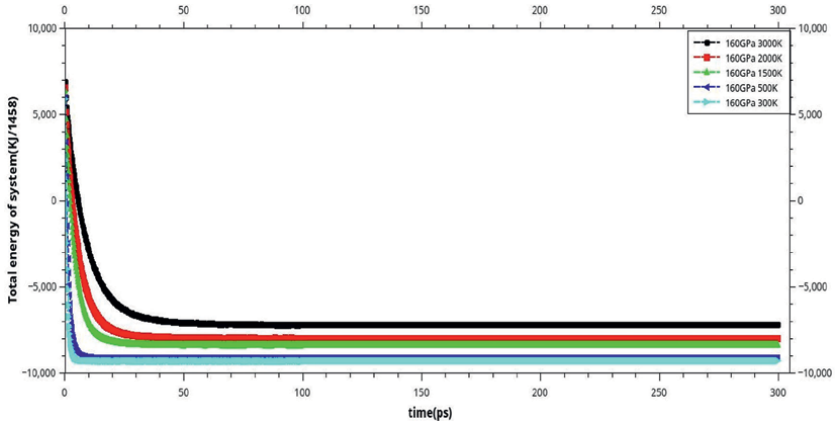

Figure 10.
Total energy of system of ZnO-W phase under 160GPa and the range of 300–3000 K.

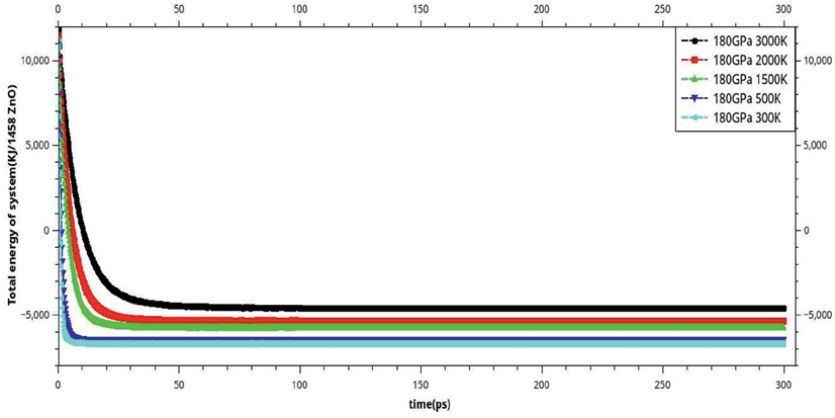

Figure 11.
Total energy of system of ZnO-W phase under 180GPa and the range of 300–3000 K.

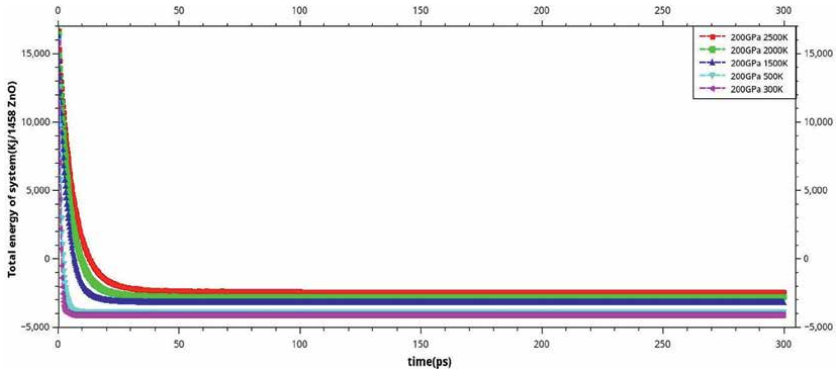

Figure 12.
Total energy of system of ZnO-W phase under 200GPa and the range of 300–3000 K.

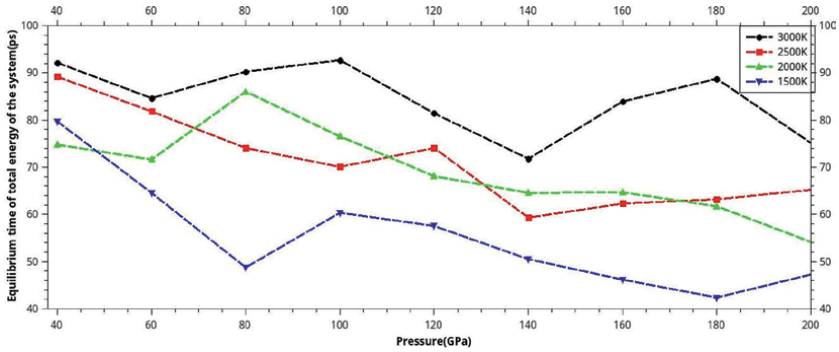

Figure 13.
Equilibrium time behaviour of total energy versus pressure under 40–200GPa and high temperature 1500–3000 K in isothermal ensemble.

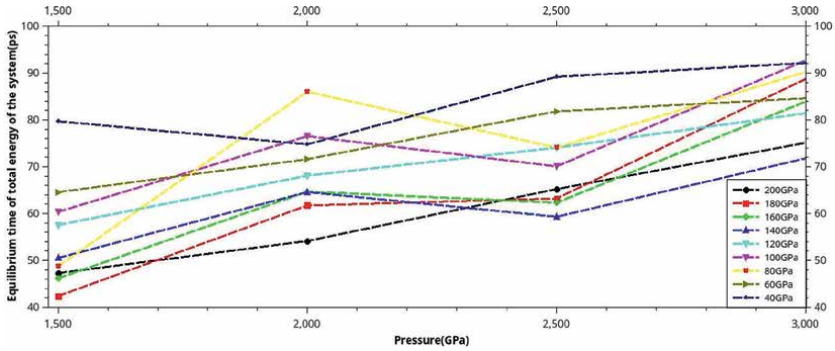

Figure 14.
Equilibrium time of total energy of ZnO-W type versus pressure under high pressure (40–200GPa) and high temperature (1500–3000 K) in an isobaric ensemble.

the temperature and decreases with increasing the pressure as shown in **Figure 13** (isothermal system) and in **Figure 14** (Isobaric system).

In isothermal or isobaric ensemble, each jump of the equilibrium means a phase transition which corresponds to a variation of volume as mentioned in part 3 (Molar Volume [60]). Under 2000 K and 2500 K (**Figure 15**) approximately, we have the same variation of equilibrium time due to melting degree of ZnO [60]. The same variation appears in isobaric ensemble for 2000 K and 2500 K, and under 40, 80,100, 160, and 180GPa, see **Figure 14**. Where at 60, 120, and 200GPa at all temperature the equilibrium time of total energy is linear, which means the same structure of B1. However, under 140GPa between 1500 and 2000 K, there is a phase transition where the structure maintains the same till 3000 K.

So from previous figures and under different ranges of pressures and temperatures, we can conclude and confirm that there is a phase transition when there is a jump in equilibrium time of total energy versus temperature at 2000 K and 2500 K (melting degree) under all pressures. It is approximately the same phenomena in molar volume variation versus pressure or temperature (part 3); see **Figures 16** and **17**. It needs to confirm the value of equilibrium time variation as in volume to have accuracy about phase transition under low temperature and high pressure.

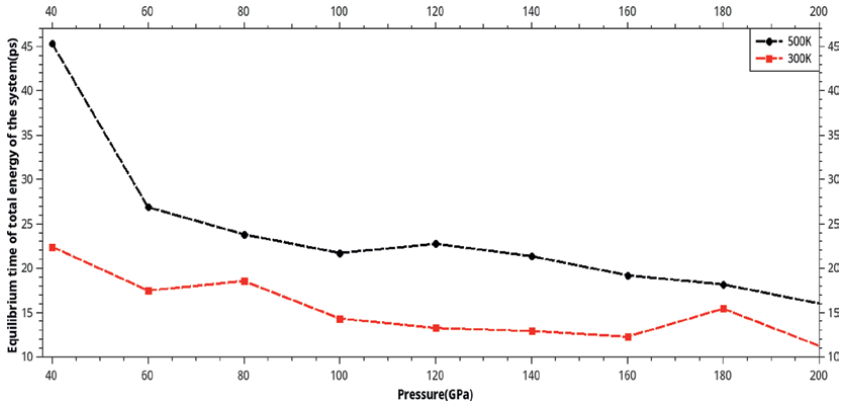

Figure 15.
Total energy of system of ZnO-W phase versus time under 15GPa and 300–3000 K range.

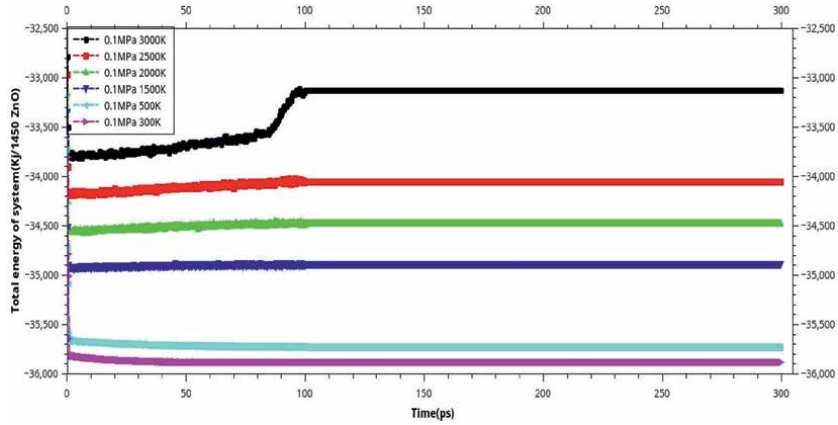

Figure 16.
Equilibrium time behaviour of total energy of ZnO-W type under high pressure (40–200GPa) and 300 K and 500 K.

3.1.2 Evolution in time of total energy under low pressure and different temperatures

Under low pressures (0.1, 5, 10, and 15GPa) see **Figures 15–18**, and low and high temperatures, the total energy remains constant after 100 (ps) due to the equilibrium of the system. While the fluctuations appear at 1500 K and increase with increasing temperature, where at 3000 K (2228 K is the melting degree), there is a bit of increase in total energy due to the effect of temperature, Chergui et al. [60].

Under 0.1 MPa, 5, and 10GPa and 300–3000 K ranges, the total energy is linear and approximately constant due to the effect of pressure, see **Figures 18–20**. Under 15GPa, the effect of pressure is clear, where the equilibrium time and the fluctuation are decreased since the total energy is decreased, as mentioned in **Figure 15**.

Under 15GPa, the total energy decreases a bit and starts to be smooth because the effect of pressure is more than temperature, which decreases the fluctuations. The equilibrium time of total energy under 0.–30GPa range and at low temperatures (300

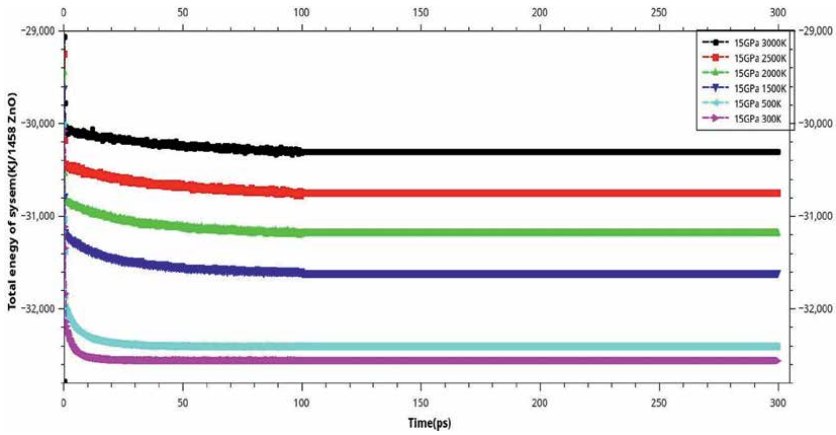

Figure 17.
Equilibrium time behaviour of total energy of ZnO-W type under high pressure (40–200GPa) and low temperature (300 K and 500 K) in an isobaric ensemble (isobaric ensemble).

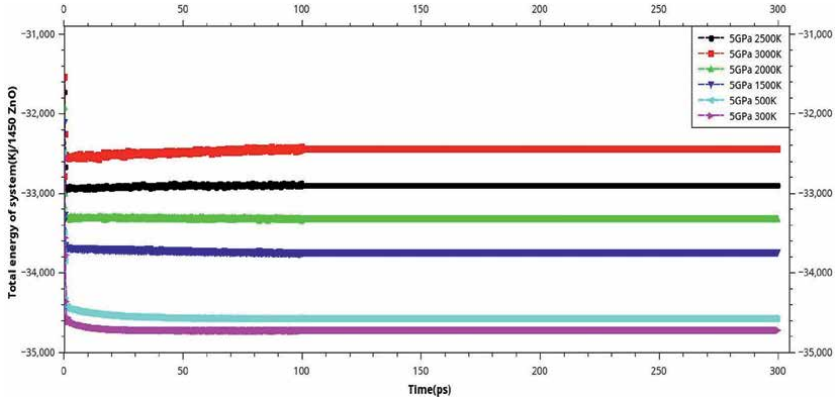

Figure 18.
Total energy of system versus time of ZnO-W phase under 0.1 MPa and the range of 300–3000 K.

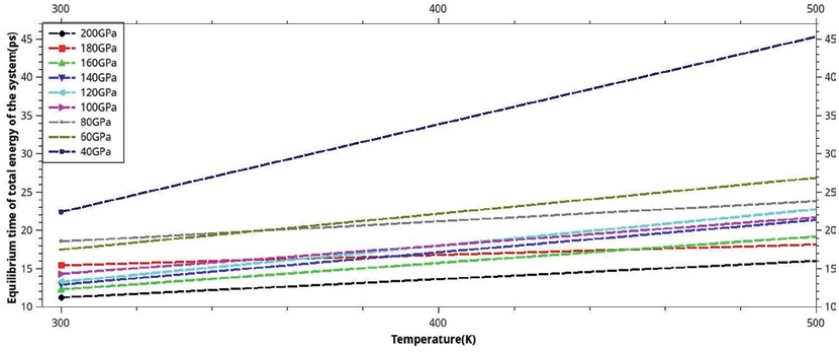

Figure 19.
Total energy of system versus time of ZnO-W phase under 5GPa and the range of 300–3000 K.

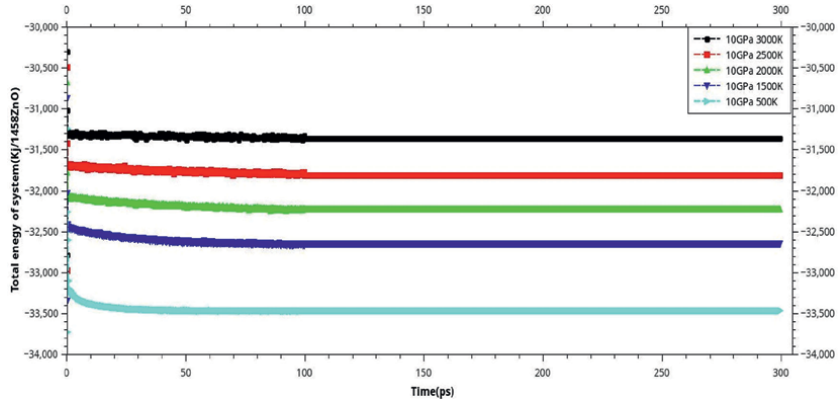

Figure 20.
Total energy of system versus time of ZnO-W phase under 10GPa and the range of 300–3000 K.

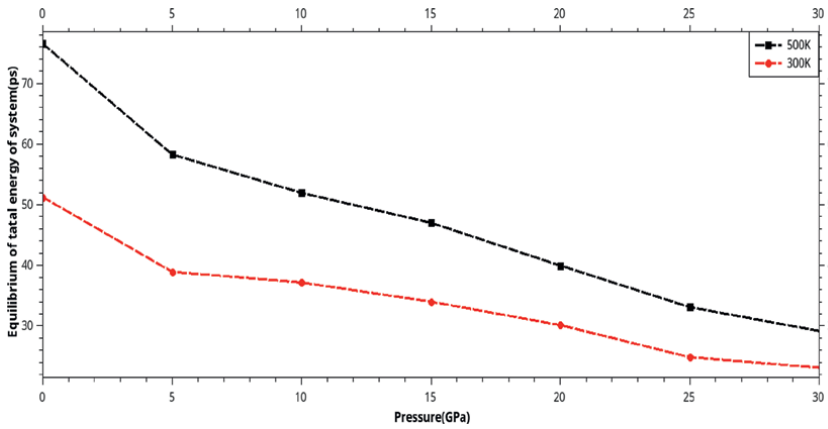

Figure 21.
Equilibrium time of total energy versus pressure of ZnO-W under 0–30GPa and at 300 K and 500 K in an isothermal ensemble.

and 500 K) in an isothermal ensemble has nearly the same variation. These curves have the shape of molar volume versus pressure under the same range of pressure and temperatures, where there were phase transitions between 5 and 15GPa at 300 K. This means that the rock salt type starts at 5GPa and finishes at 15GPa. However, the equilibrium time of total energy at 500 K has the same shape as the equilibrium time of total energy at 300 K (the same phase transitions as shown in **Figure 21**).

In an isobaric ensemble under the previous ranges of pressure and temperatures, the equilibrium time of total energy is linear and increases with increasing temperatures and decreases with increasing pressure, as mentioned in **Figure 22**.

The shape of this curve (**Figure 22**) has the same variation as the curve of equilibrium of molar volume versus the pressure at 300 K and 500 K and under 0–30GPa. In the literature on the molar volume of ZnO-W, there is a phase transition which starts at 5GPa and finishes at 15GPa [28, 29, 35–39]. This means that the equilibrium time of total energy versus pressure can prove and confirm this phase transition because there is a physical link between the change in volume and the change in total energy according to the interatomic and molecular distance change.

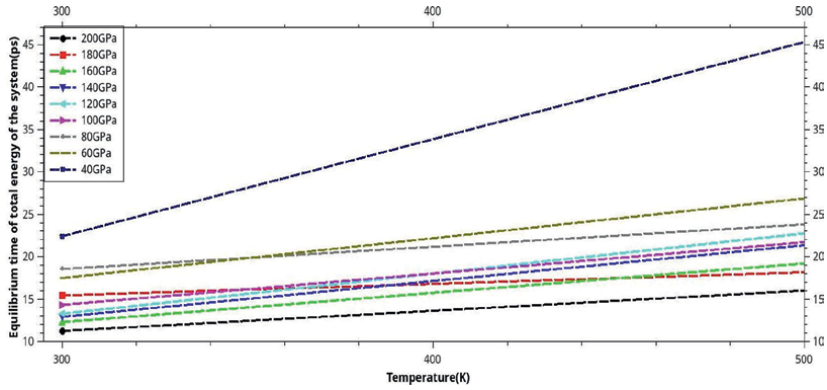

Figure 22.
Equilibrium time of total energy versus temperature of ZnO-W under 0–30GPa and at 300 K–500 K in an isobaric ensemble.

Figure 22 shows an isobaric ensemble of the equilibrium time of total energy versus temperatures under high pressure and low temperature, where the curves are linear and the equilibrium time is decreased with increasing pressure and increases with increasing temperature.

In order to clarify the effect of high temperature (1500–3000 K) and low pressure (0–20GPa) on the equilibrium time of total energy in an isobaric and isothermal ensemble, **Figures 23** and **24** show this behaviour. In isothermal ensemble (1500–3000 K and 0–20GPa), as shown in **Figure 23**, we note that the equilibrium time of total energy decreases with increasing the pressure till 10GPa and increases due to the effect of high temperature of 3000 K (solid–liquid phase) [35, 61–64]. While at 2500 K, the equilibrium time increases with increasing temperature due to the starting of melting of ZnO-W (2228 K), it is the same behaviour approximately at 2000 K.

At 1500 K, the equilibrium time of total energy is nearly linear between 0 and 10GPa and bit increases from 10GPa to 20GPa, which means that there are two phases of ZnO-W type [28, 29, 35–39].

we can note that; at 5GPa the equilibrium time of total energy is decreased from 1500 K to 2000 K and increased to 2500 K, which is the area of melting of ZnO-W

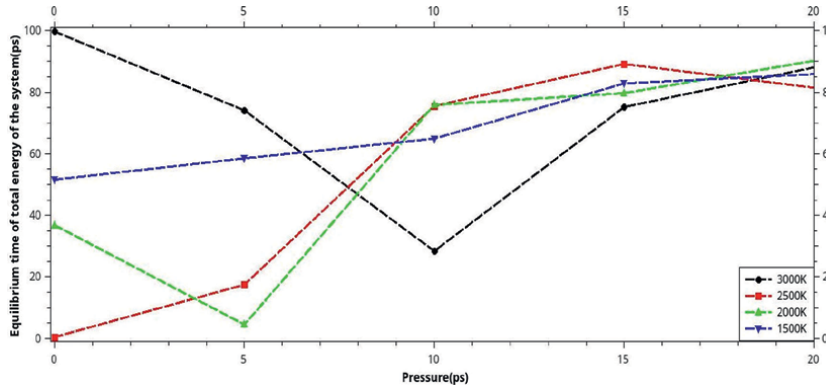

Figure 23.
Equilibrium time of total energy versus pressure of ZnO-W under 0–20GPa and at 1500–30,000 K in an isothermal ensemble.

and increased from 2500 K to 3000 K, which is the solid–liquid state. At 0GPa, the same behaviour is observed under 5GPa. Under 10GPa, the equilibrium time of total energy is linear between 1500 K and 2500 K, where it decreases till 3000 K, which means the effect of pressure is more than the effect of temperature. The variation of equilibrium time of total energy under 15GPa and at 20GPa is approximately the same at all temperatures, which means the same phase [28, 29, 35–39], (see **Figure 24**).

3.1.3 Total energy under high pressure and different temperatures

In an isothermal ensemble, the total energy under the range of 0–200GPa and 300–3000 K of the ZnO wurtzite phase is linear at all temperatures and increases with increasing pressure. Under low pressures is around –350,000 (Kj/1458mols), while under high pressure, it is around –50,000 (Kj/1458mols). See **Figure 25**; the increase in total energy is proportional to the rising of the pressure and temperature.

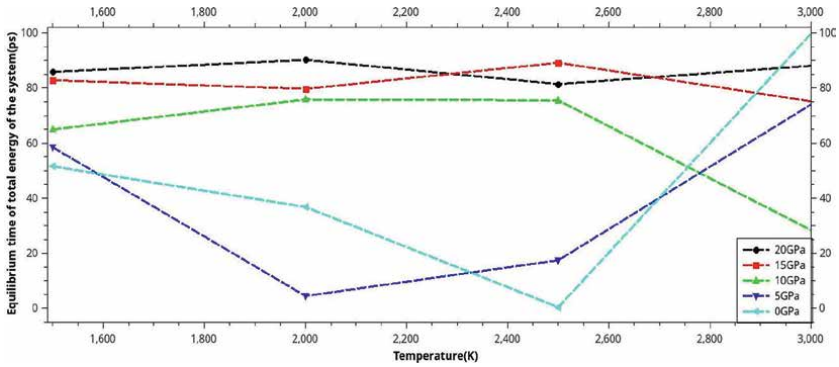

Figure 24.
Equilibrium time of total energy versus temperature of ZnO-W under 0–20GPa and at 1500–3000 K in an isobaric ensemble.

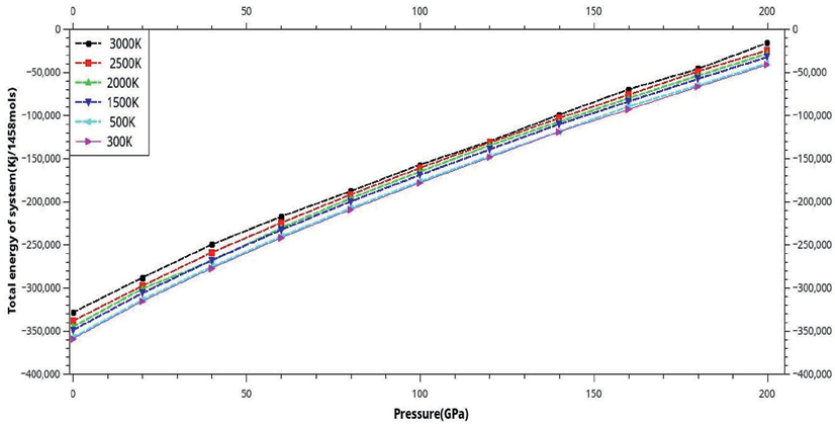

Figure 25.
The total energy variation versus pressure of ZnO-W phase under the range of 0–200GPa and at 300–3000 K (isothermal ensemble).

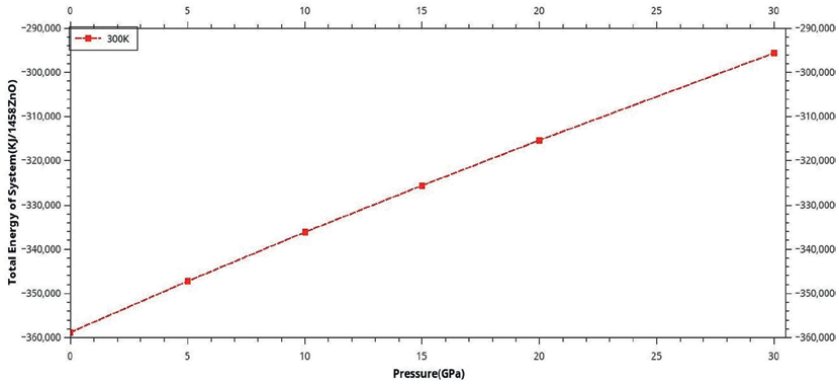

Figure 26.
Total energy of system versus pressure of ZnO-W phase under 0–30GPa and at 300 K.

3.1.4 Total energy under low pressure and different temperatures

At 300 K and the pressure is in the range of 0–30GPa (**Figure 25**), the total energy of ZnO wurtzite structure versus the pressure is linear; there is a proportionality between the increase of the total energy and the increase of the pressure, as shown in **Figure 26**.

4. Conclusion

The molecular dynamics technique and DL_POLY_4 are investigated to study the behaviour of total energy of ZnO wurtzite structure, equilibrium time, and the phase transition compared with literature data. The total energy, equilibrium time, and the fluctuations are increased with rising the temperature and drop with increasing pressure. The extraction of phase transition from the curves of equilibrium time versus pressure or temperature is a new approach compared with available data.

Acknowledgements

Parts of this chapter were previously published in the doctoral thesis by the same author, Yahia Chergui. Genetic Characterisation of Contribution to the Study of Some Properties of ZnO by Molecular Dynamics Method. 2019 Unpublished doctoral thesis. Badji Mokhtar University, Available from: https://biblio.univ-annaba.dz/wp-content/uploads/2021/12/These-Chergui-Yahia.pdf

Author details

Yahia Chergui[1,2]

1 IGEE Institute, University M'Hamad Bougara of Boumerdes, Boumerdes, Algeria

2 Physics Department, Badji Mokhtar University, Annaba, Algeria

*Address all correspondence to: y.chergui@univ-boumerdes.dz

IntechOpen

References

[1] Zhigang ZHU et al. Theoretical study on electronic and electrical properties of nano structural ZnO. The Japanese Journal of Applied Physics. 2008;**47**:2999-3006

[2] Sberveglieri G, Groppelli S, Nelli P, Tintinelli A, Giunta G. A Novel Method for the Preparation of NH3 Sensors Based on ZnO-In thin films Sensors Actuators B25-588. 1995

[3] Chu X, Jiang D, Djurisic AB, Leung YH. Gas-sensing properties of thick film based on ZnO nano-tetrapods. Chemical Physics Letters. 2005;**401**:426

[4] Liao L, Lu HB, Li JC, He H, Wang DF, Fu DJ, et al. Size dependence of gas sensitivity of ZnO nanorods. Journal of Physical Chemistry C. 2007;**111**:1900

[5] Tien LC, Sadik PW, Norton DP, Voss LF, Pearton SJ, Wang HT, et al. Hydrogen sensing at room temperature with Pt-coated ZnO thin films and nanorods. Applied Physics Letters. 2005;**87**:222106

[6] Jing L, Wang B, Xin B, Li S, Shi K, Cai W, et al. Investigations on the surface modification of ZnO nanoparticle photocatalyst by depositing Pd. Journal of Solid State Chemistry. 2004;**177**:4221

[7] Rodriguez JA, Jirsak T, Dvorak J, Sambasivan S, Fischer D. Reaction of NO_2 with Zn and ZnO: Photoemission, XANES, and density functional studies on the formation of NO_3. The Journal of Physical Chemistry. B. 2000;**104**:319

[8] Wan Q, Li QH, Chen YJ, Wang TH, He XL, Li JP, et al. Fabrication and ethanol sensing characteristics of ZnO nanowire gas sensors. Applied Physics Letters. 2004;**84**:3654

[9] Li QH, Liang YX, Wan Q, Wang TH. Oxygen sensing characteristics of individual ZnO nanowire transistors. Applied Physics Letters. 91, 2004;**85**:6389

[10] Fan ZY, Wang DW, Chang PC, Tseng WY, Lu JG. ZnO nanowire field-effect transistor and oxygen sensing property. Applied Physics Letters. 2004;**85**:5923

[11] Wan Q, Li Q, Chen HYJ, Wang TH, He XL, Gao XG, et al. Positive temperature coefficient resistance and humidity sensing properties of Cd-doped ZnO nano wires. Applied Physics Letters. 2004;**84**:3085

[12] Zhang YS, Yu K, Jiang DS, Zhu ZQ, Geng HR, Luo LQ. Zinc oxide nanorod and nanowire for humidity sensor. Applied Surface Science. 2005;**242**:212

[13] Kind H, Yan HQ, Messer B, Law M, Yang PD. Nanowire ultraviolet photodetectors and optical switches. Advanced Materials. 2002;**2**:14-158

[14] Yang PD, Yan HQ, Mao S, Russo R, Johnson J, Saykally R, et al. Controlled growth of ZnO nanowires and their optical properties. Advanced Functional Materials. 2002;**12**:323

[15] Zhang J, Sun L, Pan H, Liao C, Yan C. ZnO nanowires fabricated by a convenient route. New Journal of Chemistry. 2002;**26**:33

[16] Yi G, Wang C, Park W. ZnO nanorods: Synthesis, characterization and applications. Semiconductor Science and Technology. 2005;**20**:22

[17] Wang XD, Summers CJ, Wang ZL. Large-scale hexagonal-patterned growth of aligned ZnO nanorods for

nano-optoelectronics and nanosensor arrays. Nano Letters. 2004;**4**:423

[18] Pan N, Wang X, Zhang K, Hu H, Xu B, Li F, et al. An approach to control the tip shapes and properties of ZnO nanorods. Nanotechnology. 2005;**16**:1069

[19] Cho PS, Kim KW, Lee JH. NO_2 sensing characteristics of ZnO nanorods prepared by hydrothermal method. Journal of Electroceramics. 2006;**17**:975

[20] Al-Hilli SM, Mofarji RT, Willander M. Zinc oxide nano rod for intracellular pHpH sensing. Applied Physics Letters. 2006;**89**:173119

[21] Xu CX, Sun XW. Zinc oxide nanodisk. Applied Physics Letters. 2004;**85**:3878-3880

[22] Wang JX, Sun XW, Wei A. Zinc oxide nano comb biosensor for glucose detection. Applied Physics Letters. 2006;**88**:233106

[23] Lao CS, Gao PX, Yang RS, Zhang Y, Dai Y, Wang ZL. Formation of double-side teethed nano combs of ZnO and self-catalysis of Zn-terminated polar surface. Chemical Physics Letters. 2006;**417**:358

[24] Xu C, Sun X. Formation of double-side teethed nanocombs of ZnO and self-catalysis of Zn-terminated polar surface. International Journal of Nanotechnology. 2004;**1**:452

[25] Xu CX, Sun XW. Field emission from zinc oxide nano pins. Applied Physics Letters. 2003:**83**(18):3806

[26] Gao H, Zhang XT, Zhou MY, Zhang ZG, Wang XZ. Growth of novel ZnO nanohelices modified by SiO_2-sheathed ZnO discs. Nanotechnology. 2007;**18**:065601

[27] Yang RS, Ding Y, Wang ZL. Deformation-free single-crystal nanohelixes of polar nanowires. Nano Letters. 2004;**4**:1309

[28] Mujica A, Angel R, Munoz A, Needs RJ. High-pressure phase of group-IV, III–V, and II–VI compounds. Reviews of Modern Physics. 2003;**75**:863-912

[29] Timoshenko J, Anspoks A, Kalinko A, Kuzmin A. Temperature dependence of the local structure and lattice dynamics of wurtzite-type ZnO. Acta Materialia. 2014;**79**:194-202

[30] Morgan BJ. First-principles study of epitaxial strain as a method of B4<BCT stabilization in ZnO, ZnS, and CDs. Physical Review B. 2010;**82**:153408

[31] Morgan BJ. Preferential stability of the d-BCT phase in ZnO thin films. Physical Review B. 2009;**80**:174105

[32] Carasco J, Illas F, Bromley S. Ultralow-density nanocage-based metal-oxide polymorphs. Physical Review Letters. 2007;**99**:235502

[33] Jaffe JE, Snyder JA, Lin Z, Hess AC. LDA and GGA calculations for high-pressure phase transitions in ZnO and MgO. Physical Review B. 2000;**62**:1660

[34] Limpijumnong S, Jungthaw S. First-principles study of the wurtzite-to-rocksalt homogeneous transformation in ZnO: A case of a low-transformation barrier. Physical Review B. 2004;**70**:054104

[35] Dong X, Liu F, Xie Y, Shi WZ, Ye X, Jiang JZ. Pressure-induced structural transition of ZnO nanocrystals studied with molecular dynamics. Computational Materials Science. 2012;**65**:450-455

[36] Jiang JZ, Olsen JS, Gerward L, Frost D, Rubie D, Peyronneau J. Europhysics Letters. 2000;**50**:48-53

[37] Decremps F, Pellicer-Pores J, Macro Saitta A, Chervin JC, Polian A. High-pressure Raman spectroscopy study of wurtzite ZnO. Physical Review B. 2002;**65**:092101

[38] Uddin J, Scuseria GE. Theoretical study of ZnO phases using a screened hybrid density functional. Physical Review B. 2006;**74**:245115

[39] Jaffe JE, Harrison NM, Hess AC. Ab initio study of ZnO (101-bar0) surface relaxation. Physical Review B. 1994;**49**:11153

[40] Kresse G, Dulub O, Diebold U. Competing for stabilization mechanism of the polar ZnO (0 0 0 1)-Zn surface. Physical Review B. 2003;**68**:245409

[41] Jaffe JE, Hess AC. Hartree–fock study of phase changes in ZnO at high-pressure. Physical Review B. 1993;**48**:7903

[42] Ahuja R, Fast L, Eriksson O, Wills JM, Johansson B. Elastic and high-pressure properties of ZnO. Journal of Applied Physics. 1998;**83**:8065

[43] Serrano J, Romero AH, Manjon FJ, Lauck R, Cardona M, Rubio A. Pressure dependence of the lattice dynamics of ZnO; an ab initio approach. Physical Review B. 2004;**69**:094306

[44] Kohan AF, Ceder G, Morgan D, Van de Walle CG. Physical Review B. 2000;**61**:15019

[45] Wang S, Fan Z, Koster RS, Fang C, van Huis MA, Yalcin AO, et al. New ab initio based pair potential for accurate simulation of phase transitions in ZnO. Journal of Physical Chemistry C. 2014;**118**:11050-11061

[46] Sarasamak K, Limpijumnong S, Lambrecht WRI. Pressure-dependent elastic constants and sound velocities of wurtzite SiC, GaN, InN, ZnO, and CdSe, and their relation to the high-pressure phase transition: A first-principles study. Physical Review B. 2010;**82**:035201

[47] Seko A, Oba F, Kuwabara A, Tanaka I. Pressure-induced phase transition in ZnO and ZnO–MgO pseudobinary system: a first-principles lattice dynamics study. Physical Review B. 2005;**72**:024107

[48] Cai J, Chen N. First-principles study of the wurtzite-to-rocksalt phase transition in zinc oxide. Journal of Physics: Condensed Matter. 2007;**19**:266207

[49] Zwijnenburg MA, Illas F, Bromley ST. Apparent scarcity of low-density polymorphs of inorganic solids. Physical Review Letters. 2010;**104**:175503

[50] Schleife A, Fuchs F, Furthmiller J, Bechstedt F. First-principles study of ground and excited-state properties of MgO, ZnO, and CdO polymorphs. Physical Review B. 2006;**73**:245212

[51] Li C, Guo W, Kong Y, Gao H. First-principles study of the dependence of ground- state structural properties on the dimensionality and size of ZnO nanostructures. Physical Review B. 2007;**76**:035322

[52] Topsakal M, Cahangirov S, Bekaroglu E, Ciraci S. First-principles study of zinc oxide honeycomb structure. Physical Review B. 2009;**80**:235119

[53] Li Z, Xu Y, Gao G, Cui T, Ma Y. Tetragonal high-pressure phase of ZnO predicted from first principles. Physical Review B. 2009;**79**:193201

[54] Sun XW, Chen QF, Chu YD, Wang C. Structural and thermodynamic properties of GaN at high pressures

and high temperatures. Physica B. 2005;**368**:243

[55] Sun XW, Chen QF, Chu YD, Wa CW. Properties of MgO at high pressures: Shell- model molecular dynamics simulation. Physica B. 2005;**370**:186

[56] Sun XW, Chu YD, Liu ZJ, Liu YX, Wang CW, Liu WM. Molecular dynamics study on the structural and thermodynamic properties of the zinc-blende phase of GaN at high pressures and high temperatures. Acta Physica Sinica. 2005;**54**:5830 (in Chinese

[57] Hong ZH, Fang TH, Hwang SF. Atomic-level stress and induced growth of wurtzite zinc oxide using molecular dynamics simulation. Journal of Physics D: Applied Physics. 2011;**44**:505301

[58] Chen QF, Cai LC, Duan SQ, Chen DQ. Melting and Grüneisen parameters of NaCl at high-pressure. Chinese Physics. 2004;**13**(7):1091-1095

[59] Fincham D. Leapfrog rotational algorithms. Molecular Simulation. 1992;**8**:165

[60] Chergui Y, Aouaroun T, Hadley HJ, Chemam R, Ouatizerga A. Behavior of phasetransition of ZnO in nano scale of time a molecular dynamics computation. 2021;**8**(035905)

[61] Albertson J, Abrahams SC, Kvick A. Atomic displacement, anharmonic thermal vibration, expansivity and pyroelectric coefficient thermal dependencies in ZnO. Acta Crystallographica B. 1989;**45**:34

[62] Kisi EH, Elcombe M. u parameters for the wurtzite structure of ZnS and ZnO using powder neutron diffraction. Acta Crystallographica, Section C. CODEN ACSCE. 1989;**45**(12):1867-1870

[63] Every A, McCurdy A. Second and Higher Order Elastic Constants, Landolf-[8]

[64] Bornstein. In: Nelson DF, Madelung O, editors. New Series III. 29th ed. Berlin: Springer; 1992

Chapter 6

Defect-Induced Ferromagnetism in ZnO Nanoparticles

Bhagaban Kisan and Rajat Kumar Das

Abstract

ZnO nanoparticles of different sizes were produced using a high-energy mechanical milling process. The average crystallite size drops from ~28 to ~11 nm after milling for 60 hours, the effective strain rises, and both the unmilled and milled powders exhibit a wurtzite structure. The crystallite size value increases (~20–26 nm) with air annealing at 600°C. The pure ZnO powders show paramagnetism and eventually reveal ferromagnetism with moderate moment and large coercivity at ambient temperature. For the t_m = 40 hours, ZnO powder generated a moment of ~0.9 emu/g at 12 kOe applied field and a coercivity value of ~172 Oe. Further, H_c and M_s increase with decreasing temperature. ZFC and FC curve shows the ferromagnetic in nature. Furthermore, oxygen (V_O) and zinc vacancies (V_{Zn}) were the primary causes of intrinsic defects, supported by Raman scattering spectra. Therefore, ZnO nanoparticles with magnetic characteristics that may be adjusted show promise for use in multipurpose spintronic devices.

Keywords: nanoparticles, mechanical milling, ferromagnetism, defect, spintronics

1. Introduction

The ferromagnetic (FM) properties at room temperature in diluted magnetic semiconductors (DMS) with reduced band gaps have recently attracted much interest as a possible path toward realizing semiconductor-based and multifunctional spintronic devices. As a result, one of the primary methods for producing transition metal (TM) oxide nanocrystalline powders is based on DMS with a Curie temperature (T_C) higher than room temperature for usage in spintronic applications [1–5]. The first report on Mn-doped ZnO-produced room temperature ferromagnetism (RTF) at temperatures of approximately 700°C was reported by Sharma et al. [6]. Comparably, large-scale RTF oxide materials doped with TM-like (HfO_2, MgO, TiO_2, and SnO_2) have been described [7, 8]. Beyond stability and reproducibility concerns, there is an ongoing debate on the intrinsic vs. extrinsic causes of RTF, including the creation of clusters of magnetic nanoparticles and the presence of other phases by doping in the sample. It should be mentioned that these items are inappropriate for use with DMS. However, recent research on the ZnO system has shown that RTF can be realized in

two ways: in pure ZnO and doping with non-magnetic like C, H, Mg, and N [9, 10]. This is comparable to the RTF reported in SnO_2, TiO_2, and MgO, known as d^0 FM [11]. On the other hand, a comprehensive research analysis indicates inconsistent findings about the evolution of RTF in pristine ZnO systems. According to Bartolome et al. [12], the ball milling approach used to prepare ZnO-based particles led to a significant decrease in the average crystal size without causing any ferromagnetic characteristics to be induced. Furthermore, Sanyal et al. [13] observed that the ZnO treated by ball milling did not exhibit FM nature, even with the creation of Zn vacancy (V_{Zn}). However, Potzger et al. [14] described a simple mechanical method for producing ferromagnetic defect ZnO, which they connected with flake-like formations in planarly crushed powder fragments. According to Xing et al. [15], in ZnO nanowires manufactured *via* vapor transport, the oxygen vacancies increase the room temperature FM and cause distinctive photoluminescence. Additionally, Podila et al. [16] observed that the preparation of the sample and the annealing conditions affect the production of RTF in ZnO films. Theoretical computational work, such as Ab-initio research also reported how surface defects affect ZnO nanoparticles' magnetic characteristics. According to Banerjee et al. [17], the creation of oxygen vacancy clusters during thermal annealing of pure ZnO powder increases FM. It was suggested by Phan et al. [18] and Ghose et al. [19] that ZnO nanoparticles with induced defect-related ferromagnetism might be produced by mechanical milling from original paramagnetic ZnO powders. The room temperature ferromagnetism (RTFM) resulting from a shift in the quantity of oxygen defect and Zn interstitials was reported by Rainey et al. [20]. These investigations demonstrated that the defect density of either Zn (V_{Zn}) or oxygen (V_O) was the cause of the generation of FM in pristine ZnO nanoparticles. According to numerous investigations, oxygen vacancies (V_O) are the only ones thought to be crucial in mediating ferromagnetism at RTFM in ZnO [21–25]. Additionally, there have been studies indicating that other defects like zinc interstitials [26, 27], zinc vacancies (V_{Zn}) [28], and some extended defects [29–31] may be the cause of the RT ferromagnetic response. The researchers continue to face significant difficulties in determining the type of defects causing the observed FM. Since both zinc and oxygen vacancies were suggested to cause the FM in undoped ZnO, it is unclear which defects are attributed to the magnetic moments. However, theoretical and experimental research revealed that RTFM is caused by defect-related oxygen or zinc vacancies. In particular, both theoretical and practical results point to a strong relationship between oxygen vacancies and magnetism in undoped ZnO [23, 32–36]. With size variation and defect-induced effect in ZnO powders, only a small number of studies have examined RTFM [14–18]. Here is a simple ball milling technique for room-temperature ferromagnetism in ZnO. For ferromagnetic, optoelectronic uses of ZnO are highly helpful. It is widely acknowledged that by simply varying the milling duration, mechanical milling can introduce a significant amount of defect into the powders [37–41]. In-depth research has been done on the band gap alteration that is produced in ZnO powders when strain and oxygen vacancy defects or zinc vacancy work together. So, the observed RTF in ZnO powders is intrinsic. The defects associated with oxygen and zinc vacancies play a vital part in the presence of ferromagnetism. This was further validated by Raman scattering spectrometer measurement. Nevertheless, comprehensive papers describing the size effect on RTF formation and its stability of magnetism higher than ambient temperature in ZnO nanoparticles are lacking. Therefore, a report on the investigation into the effects of varying sizes on room temperature-dependent magnetic, vibrational, and structural characteristics of ZnO particles that are generated by mechanical milling is needed.

DOI: http://dx.doi.org/10.5772/intechopen.1006296

2. Experimental details

A planetary high-energy ball mill was used to produce ZnO (>99.9%, Merck) nanopowders that showed paramagnetic (*PM*) characteristics at ambient temperature. The ZnO powder was processed mechanically at 500 rpm using a 10:1 ball-to-powder weight ratio for the milling period t_m = 0–60 hours. The nanopowders were prepared in an environment of extreme purity using argon. The mill was set up to shut down for 15 minutes following every 15 minutes of operation to prevent overheating. **Figure 1** shows the schematic view of the milling process inside the vial and the photographic view of the horizontal support disc on which vials are mounted (Insmart, India). Then, these nanopowders were air annealed at 600°C for 3 hours. For crystal structure analysis, a high-power X-ray diffractometer of Cu-Kα radiation was used (Rigaku TTRAX III 18 kW). The XRD data were gathered at 0.05 °/s scan rate to investigate the creation of nanostructured ZnO, and the Williamson Hall Plot (WHP) method was used for crystallite analysis [37, 42]. A field emission scanning electron microscope (FESEM, Sigma Zeiss, Germany) was measured to study the surface morphology. A vibrating sample magnetometer (VSM, LakeShore Model 7410) was used to study the magnetic characteristics at room and low temperatures (25–300 K). The *M-T* investigation (*ZFC* and *FC*) was measured using a superconducting quantum interference device at various temperatures (SQUID, Quantum Design MPMS XL7). Micro-Raman spectroscopy (LabRam HR800, Jobin Yvon) was used to measure the Raman spectra, with an excitation wavelength of 488 nm.

3. Results and discussion

A room temperature X-ray diffraction (XRD) spectrum of unmilled and milled ZnO powders at various milling times (t_m = 0–60 hours) is shown in **Figure 2**, and

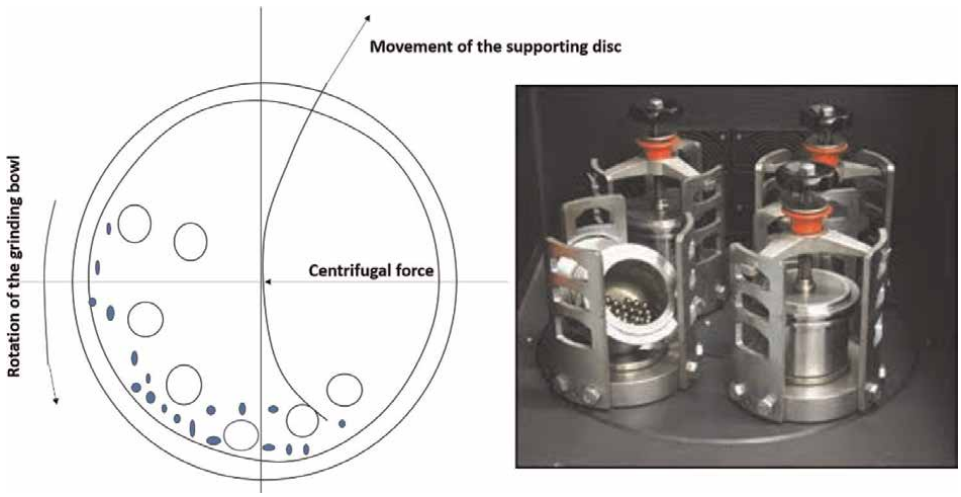

Figure 1.
(Left) Schematic diagram of the horizontal section of the ball milling process and the (right) photographic view of the horizontal support disc on which vials are mounted.

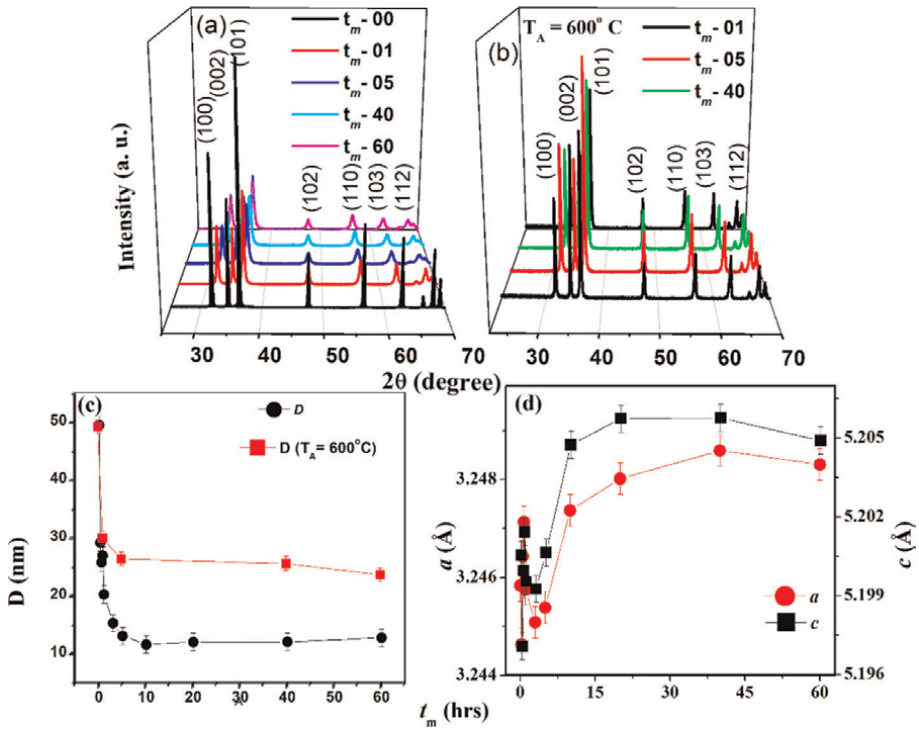

Figure 2.
(a) XRD patterns of (a) t_m = 0–60 hours milled, (b) XRD pattern of annealed (t_m = 01, 05, 60) sample at T_A = 600°C, (c) variation D for as-milled and annealed with milling time (t_m) of ZnO powders, and (d) variation of a and c value with milling period (t_m) for milled ZnO powders [43].

annealed ZnO powder (t_m = 01, 05, and 60 hours) samples at 600°C are observed in **Figure 2(b)**. The XRD patterns show the absence of any further impurity phases, all pure ZnO that has been ground and annealed exhibits all the reflections that accord with the wurtzite structure's hexagonal form. When the t_m is increased from 0 to 60 hours, the wurtzite structure remains unchanged during milling. Nonetheless, there is a noticeable increase in the width of the XRD peaks found for milled ZnO. The reduction in the crystallite size, and strain, and the existence of extra defects are the causes of this peak broadening. The large strain and atomic modification in ZnO nanocrystalline powders are unavoidable due to the milling process, which leads to significant fragmentation, cold welding, and deformation in a particularly strong grinding media.

Conversely, **Figure 2(b)** shows that the peak width of the XRD diffraction of the samples after annealed T_A at 600°C at 3 hours gradually decreases. The reduction in the width of the peak with annealing T_A in the sample can be attributed to the formation of ZnO with the absorption of oxygen from the atmosphere and due to the relaxation of strain that is accumulated in the as-milled powders. Williamson-Hall plot (*WHP*) method [37, 42] was used to examine XRD patterns to thoroughly assess the structural refinement, as stated in Eq. (1),

$$\frac{(\Delta\theta_B)\cos\theta_B}{\lambda} = \frac{k}{D} + \eta\frac{\sin\theta_B}{\lambda} \tag{1}$$

where η is effective strain, k is Scherrer's constant (given as 0.9 for the spherical nature of particles), and D is the average crystallite size. $\Delta\theta_B$ is defined as the full width at half maximum (*FWHM*) of the Bragg reflections (in radians). The X-ray wavelength is denoted as λ = 1.5406 Å. The D value (derived from the inverse of the intercept) and the η (derived from the slope of the fit) are obtained by fitting the data with a straight-line process, by the *WHP* approach, which calls for a straight line to connect ($\Delta\theta_B \cos\theta_B/\lambda$) and ($\sin\theta_B/\lambda$). The average crystallite size (D) for both the milled and annealed samples is displayed in **Figure 2(c)**. As the milling time increases, the average crystallite size is found to decrease with increasing t_m = 60 hours, reaching a value of approximately 10.5 nm for 40 hours. For powder milled for 60 hours, there was a modest rise in crystallite size, which can be associated with repeated milling. Additionally, it is evident that, as a result of strain relaxation, the average crystallite size grows with air-annealed T_A at 600°C, reaching a value of roughly 26 nm for powders milled for 05 hours and 24 nm for powders milled for 60 hours. The calculated value of lattice constants (a, c) using Eq. (2) with milling time t_m is displayed in **Figure 2(d)** [44], for the calculation of the lattice constant for as-milled ZnO powders.

$$\sin^2\theta = \frac{\lambda^2}{4}\left[\frac{4}{3}\left(\frac{h^2+hk+k^2}{a^2}\right)\frac{l^2}{c^2}\right] \tag{2}$$

Plotting the predicted lattice parameters (a, c) against t_m in **Figure 2(d)** reveals that the lattice constant, which is derived from XRD peaks, increases gradually for the t_m = 01 hours of milling and then gradually drops over the next 03 hours. The lattice constant grows significantly up to t_m = 20 hours of milling on further increasing t_m, after which it shows a modest relationship. This may be explained by the fact that as milling times increase, defect densities and size reductions occur. When t_m increases, ZnO nanoparticles' average crystallite size decreases and defect density increases according to structural characterizations. Using the FE-SEM technique, the pure ZnO and milled ZnO powders were analyzed to comprehend the change in the surface morphology. The FE-SEM images of milled ZnO powders for unmilled and t_m = 40 hours milled ZnO powders are shown in **Figure 3**. In pure unmilled ZnO powders, a distinct particle morphology is found between 0.1 and 1 μm particle size. Furthermore, it was discovered that the particle shapes are essentially random. The average size of milled ZnO drops significantly below 100 nm as t_m increases. Concurrently, the fine particle agglomeration intensifies, resulting in aggregated particles, a characteristic of powders that have been ball-milled [45, 46]. This is mostly caused by the frequent cold welding and powder breakage that occurs during milling.

The usual plane-view bright-field TEM (BF-TEM) pictures and selected area electron diffraction (SAED) patterns for pristine unmilled ZnO powder and milled ZnO powders at t_m = 05 and t_m = 40 hours are reported in our earlier paper [43]. The pure ZnO powder's BF-TEM image shows a distinct particle shape with crystal sizes varying between 50 and 100 nm. The ZnO diffraction rings in the SAED pattern clearly show the polycrystalline nature of the crystals, despite their seemingly random size and form. Similarly, irregularly shaped fine nanocrystalline microstructure is confirmed by BF-TEM images of milled ZnO particles. Furthermore, the SAED patterns exhibit diffraction rings, which support the polycrystalline nature and hexagonal wurtzite structure of ZnO. After milling for t_m = 5 hours and t_m = 40 hours, the average crystal size as determined by BF-TEM images at random places decreases from 50 to 100 nm to around 13 and 11.5 nm, respectively. The ZnO crystallite size fluctuations seen by

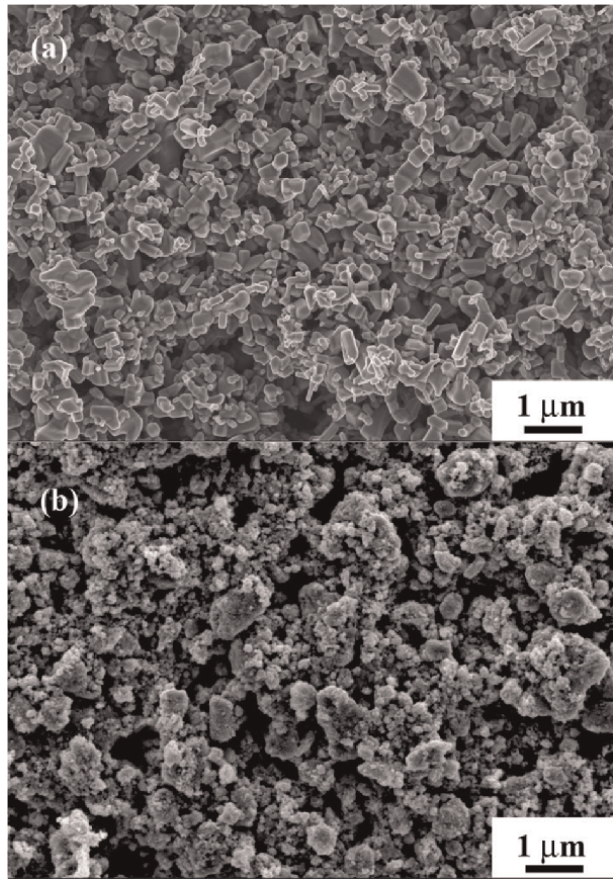

Figure 3.
FESEM images of (a) pure unmilled ZnO powder (b) and t_m = 40 hours of ZnO powders.

TEM show a similar behavior that is nearly identical to the XRD findings. However, the powders at the nanoscale have a wide range of sizes and asymmetrical forms. Therefore, there is good agreement between the analyses of TEM and XRD findings, and it is anticipated that these structural variations in ZnO powders will result in significant changes to their physical properties.

3.1 Raman study

The room temperature Raman spectra were measured for unmilled and milled ZnO powders, as shown in **Figure 4** to explore the crystallinity and defects structure present in the milled powders [47, 48]. The Raman spectra were subjected to curve fitting analysis using various band combinations to determine the area under the curves, peak position, and peak breadth. The fitted curves are also displayed in an earlier paper [43]. As well-documented in literature [3, 49–52], wurtzite ZnO belongs to the space group C_{6v}^4 using two formula units in the primitive cell, the irreducible representations can be used to categorize the zone-center optical phonons: $\Gamma_{opt} = A_1 + 2E_2 + E_1 + 2B_1$. Silent modes make up the B_1 modes. Both the transverse-optical (TO) and longitudinal-optical (LO) components of the polar, Raman, and infrared active A_1 and E_1 modes divide at distinct frequencies. The two frequencies of

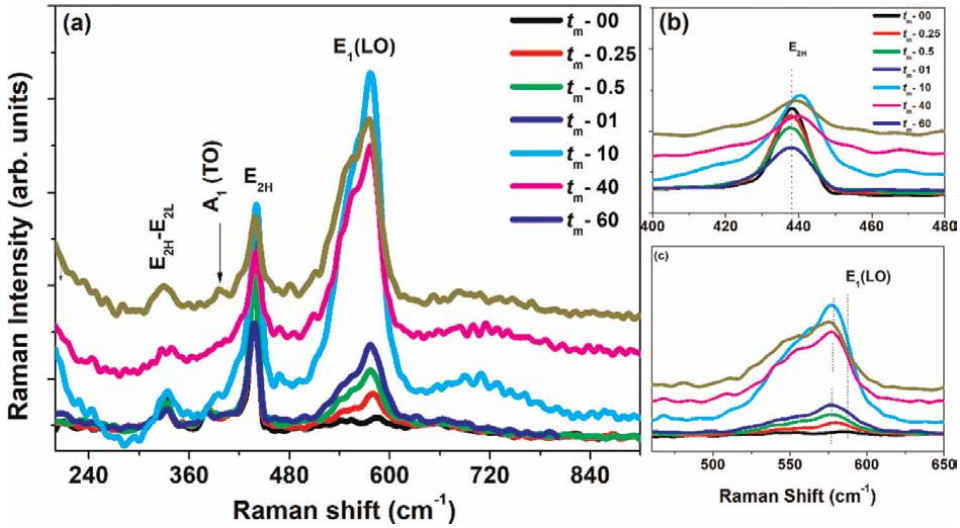

Figure 4.
(a) Raman spectra of unmilled and milled t_m = 0–60 hours. (b) Enlarged view of E_1(LO) mode and (c) enlarged view of Raman shift for E_{2H} mode of ZnO sample [43].

the nonpolar E_2 modes are E_2 (high) and E_2 (low), which correspond to the vibration of the zinc (Zn) sublattice and the motion of oxygen (O) atoms, respectively [50, 52, 53]. A large peak was discovered at 438 cm^{-1} for pristine un-milled ZnO, as shown in **Figure 4(a)**. This peak is ascribed to the E_2 (high) (E_{2H}) mode. The A_1(TO), A_1(LO), E_1(LO), and 2(E_{2H}-E_{2L}) modes, respectively, could be responsible for the smaller peaks that were also seen at ~330, ~381, ~543, ~581, and ~660 cm^{-1} [3, 47, 50, 54–57]. The E_1(LO) peak is more prominent after increasing milling time. The E_{2H} mode at ~438 cm^{-1} broadens asymmetrically and drops dramatically with increasing t_m. However, for the milled ZnO powders, the weak peak A_1(LO) and E_1(LO) modes in pure ZnO powders are more noticeable. The presence of different defects (surface and bulk defects) due to Zn interstitial defect states, oxygen vacancies, size effects, reduced crystallinity, etc., may be the source of A_1(LO) and E_1(LO) peak [58–62]. Furthermore, when t_m grows, the A_1(LO) and E_1(LO) modes move noticeably toward lower frequencies, as shown in **Figure 4(c)** and **(d)**. This lower wavenumber shift is due to the expansion in the lattice constant. This is consistent with the XRD data, which showed that ball-milled ZnO particles exhibit an increase in *c*-axis length. The unit cell's expansion results in the corresponding bonds' elongation along the *c*-axis, which weakens the force constant and softens the phonons' lower vibration frequency mode. These findings unequivocally demonstrate that, as t_m increases, the ball milling method causes defects and a decrease in particle size in ZnO powders. The milling conditions have a noteworthy influence on the relative strengths of the peaks. These findings closely match the vibration characteristics of the samples that are currently being studied.

Figure 5 shows the Raman spectra for annealed at 600°C for t_m = 01, 03, 05, and 40 hours milled sample. The high-intensity peak is only E_{2H} and other peak intensities show very low and the absence of a peak was observed. This absence and low-intensity peak were observed after annealing at 600°C due to the relaxation in the strain and absorption of oxygen from the atmosphere. So, from this observation, large defects like oxygen (V_O) are generated with increasing milling t_m and disappear with air annealing.

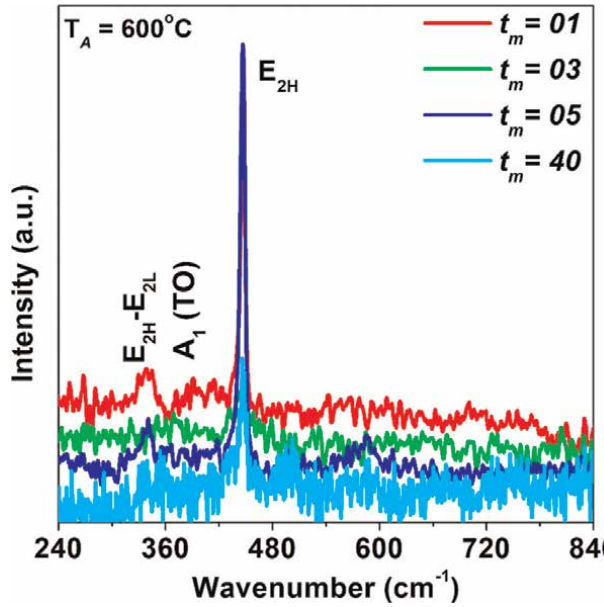

Figure 5.
Raman spectra of annealed ZnO milled samples at 600°C.

3.2 Magnetic study

To investigate the effects of size on the magnetic characteristic of ZnO sample measured the (i) initial magnetization (*IM*) and *M-H* loops in a wide temperature range, for the un-milled and milled ZnO samples. **Figure 6** shows the *M-H* loops and

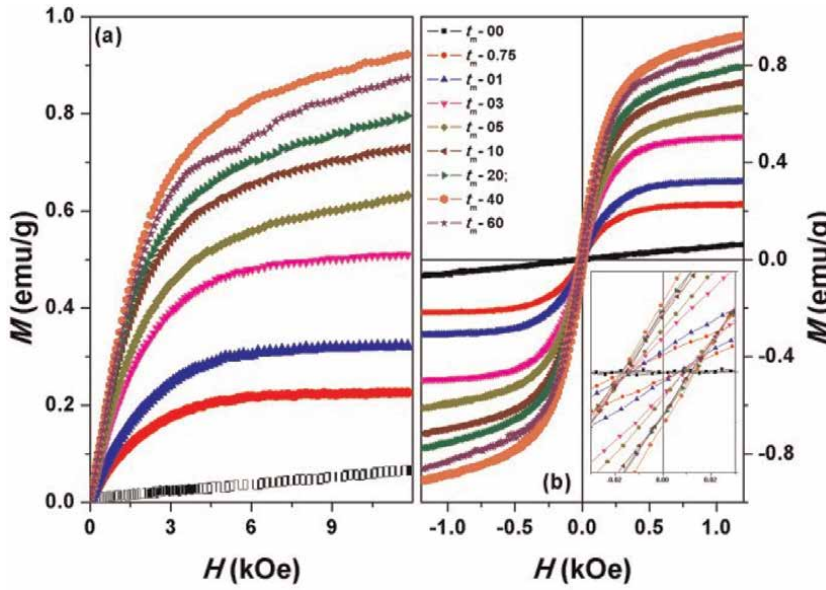

Figure 6.
(a) Initial curve, (b) M-H loop at 12 kOe, for pristine and milled ZnO samples at room temperature. (The inset figure represents the enlarged view) [41].

IM curves at room temperature, as well as an enlarged view of the *M-H* loops near the origin (inset), at various t_m for both unmilled and milled ZnO powders. It is noted that (i) unmilled ZnO powder shows a paramagnetic (PM) in nature as *M-H* loop crosses through the origin, which responds weakly to applied fields (see inset). (ii) In contrast, the milled ZnO powder responds to applied fields in a different way; at lower applied fields, magnetization increases somewhat, while at higher applied fields, it increases gradually. The magnetization value of 0.9 emu/g is obtained for 40 hours milled sample. When the t_m is increased up to t_m = 40 hours, the rate of magnetization rises steadily. After that, it dramatically declines when t_m is increased beyond 40 hours. Conversely, following the first milling, the H_C of pure ZnO, which was initially recorded as zero because of its PM nature, has greatly grown ($\sim$ 100 Oe). After 40 hours of milling, H_C rises to around $\sim$172 Oe with rising t_m, and then somewhat decreases for t_m = 60 hours. Here, it links the structural, vibrational, and magnetic properties to comprehend the origin of the FM found in the milled ZnO particles. The *M-H* loop goes from the origin, and the pure, unmilled ZnO responds weakly to the applied magnetic field. It is commonly known that the procedure for ball milling significantly increases the number of defects in the beginning material through repetitive cold welding and fracturing to create different nanoparticles. Thus, as can be shown in the current instance, size reduction and vacancy creation take place in milled ZnO powders. This is in good accord with previous findings [14, 18, 63, 64] for comparable materials. It is anticipated that the FM order will rise in tandem with defect density if the ball milling process causes the defect density to increase as t_m increases. Further, this could be correlated with the results of the Raman spectra, displayed in our earlier paper [43]. However, because longer milling causes a minor increase in average crystal size, a t_m increase beyond t_m = 40 hours leads to a slight drop in magnetization. These findings imply that the size-varying ZnO in the nanoscale range, with oxygen vacancies and/or Zn interstitials formed in this milling process, is the cause of FM in the ZnO under investigation. These findings support a strong relationship between ZnO powders' structural, vibrational, and magnetic characteristics. At least to the detection limit of this method, contaminants in the milled ZnO could not be found from EDS and X-ray photoelectron spectra (XPS) shown in earlier paper [43]. Remarkably, as t_m grows, the percentage of O_V rises significantly and the O_C component rises somewhat at the expense of the O-Zn component. This demonstrated that significant oxygen vacancies are introduced during the ZnO milling process, resulting in oxygen deficiency present in the ZnO particles [43].

To investigate how structural refinement affects magnetic characteristics, *M-H* loops were monitored under various temperatures ranging from 30 K to 300 K, as shown in **Figure** 7. It is found that (i) pure ZnO powder, because of its PM nature, responds weakly to applied fields and that the nature of the loops remains constant at low temperatures. (ii) In a similar vein, the milled powder loops' characteristics remain unchanged as the temperature of measurement drops. (iii) For all of the milled powders, however, the area under the loops grows significantly as the temperature drops. To comprehend how temperature affects different magnetic characteristics, **Figure 8** shows the values of H_C and is displayed with temperature. The milled ZnO powders' H_C(T) rises when the temperature drops, although the rate of increase in H_C is mostly dependent on t_m and ZnO crystal size. For the ZnO particles that are milled for 01 hour, H_C(T) varies roughly linearly. The linear fluctuation of H_C(T) transforms into a nonlinear form with increasing t_m, especially at lower temperatures. This may be connected to the distinct magnetic characteristics of tiny ZnO nanocrystals with

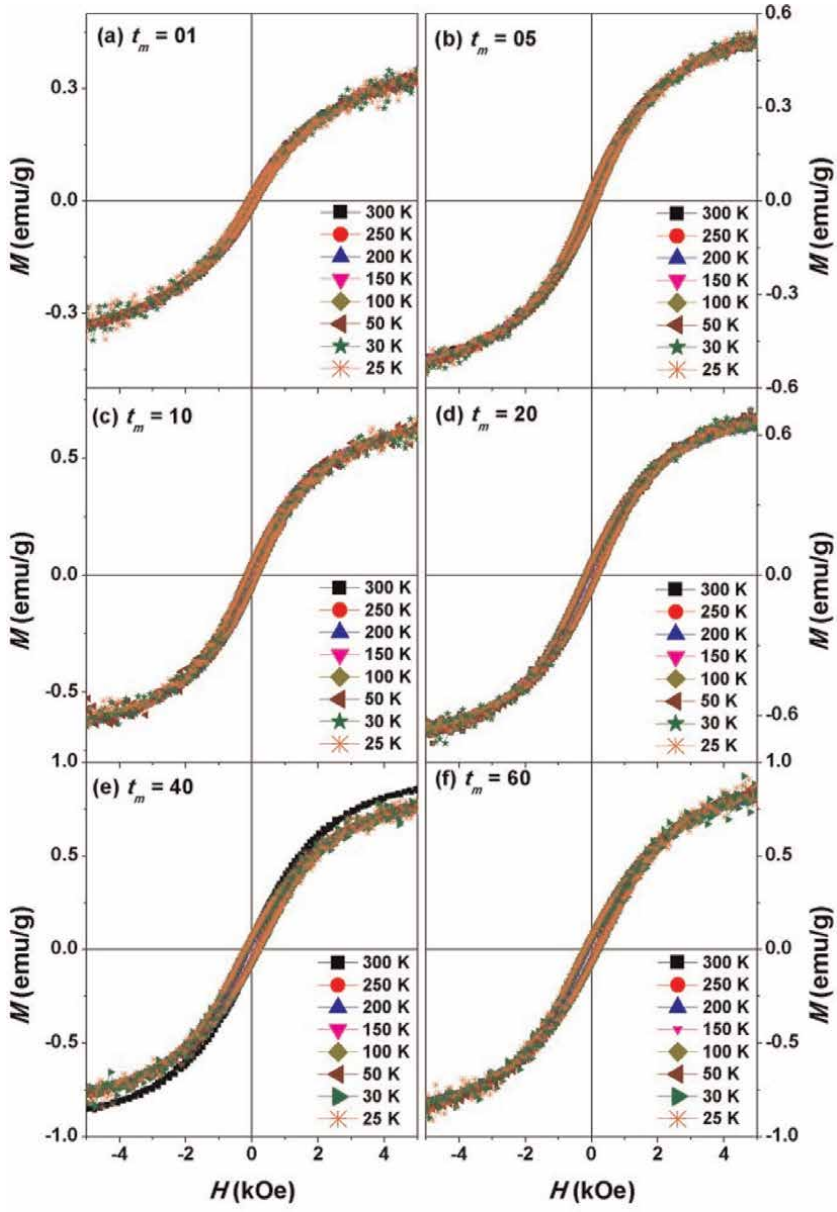

Figure 7.
(a-f) Low-temperature M-H loops of t_m = 01–60 hours ZnO milled samples [43].

milling time-dependent defects that are dependent on temperature and field. However, for ZnO milled at various t_m, no regular fluctuations in the exchange field H_E(T) with temperature were observed.

The influence of temperature-dependent magnetic characteristics of ZnO milled powders at different milling time t_m was investigated using low-temperature *M-T* measurements at various constant applied fields under zero-field cooling (*ZFC*) and field cooling (*FC*) conditions. The measurements were conducted at 2 K and 399 K temperature ranges. Before being measured, the sample was cooled down to 2 K

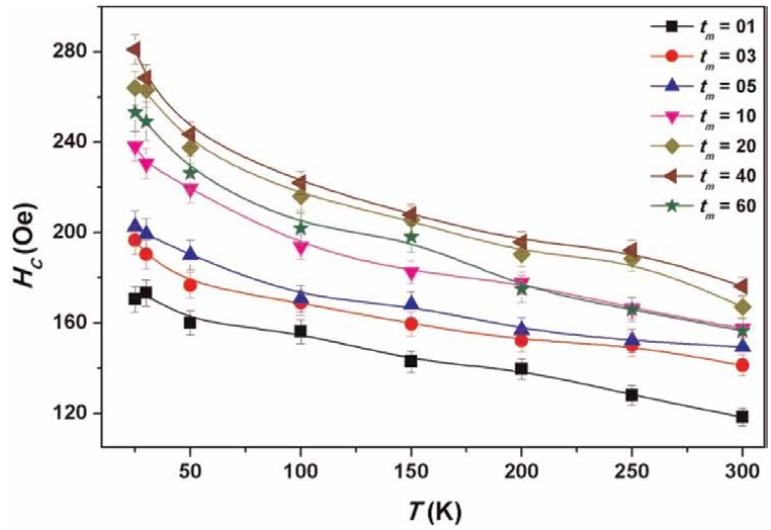

Figure 8.
Variations of coercivity with temperature for milled ZnO powders [43].

without the application of a magnetic field. Next, a probing constant DC magnetic field was employed to monitor the magnetization as a function of temperature (*ZFC* method) during the warming procedure up to 399 K. The sample was then subjected to a continual applied field cooling to 2 K (*FC* method) and measured magnetization up to 399 K. Normalized magnetizations [M(T)/M_{399K}] as a function of temperature for the ZnO powders milled at 01 and 40 hours are displayed in **Figure 9** under *ZFC* (M_{ZFC}) and *FC* (M_{FC}) conditions at various applied magnetic fields of

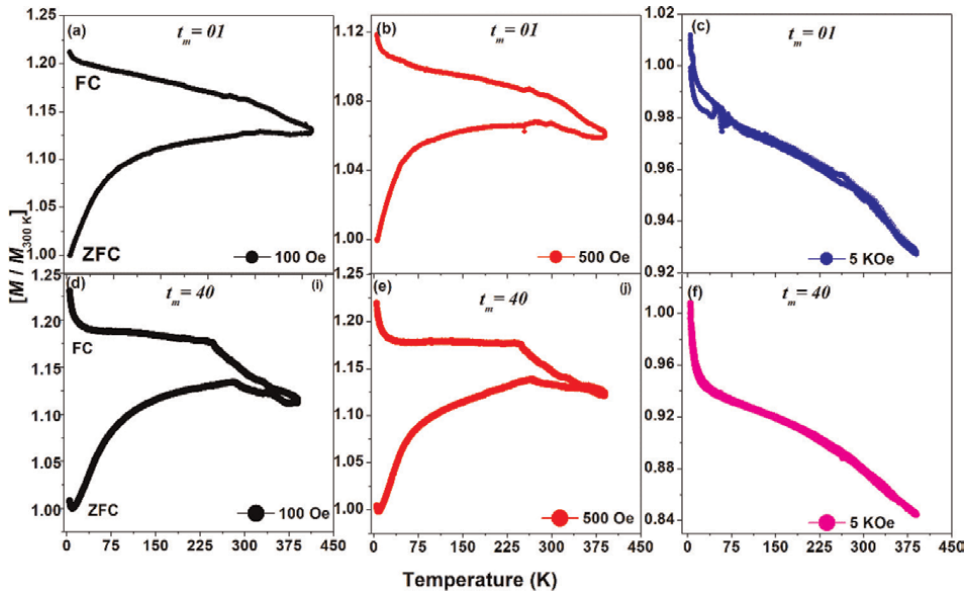

Figure 9.
ZFC and FC curve for (a-c) t_m = 01 hours and (d-f) for t_m = 40 hours milled ZnO at different field variations 100, 500, and 5 kOe with temperature.

100 Oe, 500 Oe, and 5 Koe, respectively. The figure clearly shows that there are considerable differences in the magnetization data measured under *ZFC* and *FC* conditions for each material tested under low applied magnetic fields of less than 500 Oe.

Consequently, for every sample, the bifurcation between M_{ZFC} and M_{FC} was noted at around 399 K. When the temperature drops below 300 K, M_{ZFC} declines significantly, but M_{FC} increases gradually until it reaches 20 K, at which point it suddenly increases. With the increasing t_m, there is a noticeable increase in the M_{FC} increase below 20 K. This could be because significant defects in fine ZnO nanocrystals with temperature and field-dependent magnetic characteristics cause a magnetic moment to be generated in milled ZnO powders. Moreover, as **Figure 9** shows, the presence of bifurcation between M_{ZFC} and M_{FC} suggests a wider distribution of magnetic moment, which results from the crystals' wide size variation. Interestingly, for samples measured below 5000 Oe, the bifurcation point vanishes. ZnO NPs, nanowires, nanoflowers, and thin films have all previously been documented to exhibit similar properties [22, 23, 36, 65]. Curiously, no sharp peak is observed in the M_{ZFC} curve at lower temperatures, unlike what has been shown in NiO where the disordered surface spins freeze. Furthermore, no regular variation in the bifurcation point with the applied magnetic field has been noticed by us. So, the ZFC and FC show the FM in nature in milled ZnO powders.

4. Conclusions

The study of the structural, vibrational, and magnetic characteristics at room and low temperature of ZnO nanoparticles that were prepared by mechanically alloying process to reduce their sizes systematically. As the milling time is increased, the average crystallite size decreases, and the paramagnetic properties of pure ZnO are replaced by induced ferromagnetic ordering. For 40 hours, milled ZnO particles produced a maximum moment of ~0.9 emu/g at 12 kOe achieved and a coercivity value of ~172 Oe. From the Raman spectra studies showed defect densities, like (V_O) and (V_{Zn}), cause FM in ZnO. The findings are examined about the decrease in crystallite size and the defect density resulting from the oxygen vacancy and zinc interstitial in the nanoparticles. Photonic and spintronic devices may be useful for these prepared milled ZnO materials.

Acknowledgements

The authors acknowledge the Raman Spectra measurement facility of the Department of Physics at Utkal University, Bhubaneswar, India. The authors also declare financial support from the OURIIP seed fund 2022/090-physics, Odisha State Higher Education Council, Bhubaneswar, Odisha, India.

DOI: http://dx.doi.org/10.5772/intechopen.1006296

Author details

Bhagaban Kisan[1,2*] and Rajat Kumar Das[2]

1 School of Physical Science, Jawaharlal Nehru University, New Delhi, India

2 Department of Physics, Utkal University, Odisha, India

*Address all correspondence to: bhagabankisan@mail.jnu.ac.in; bhagaban.physics@utkaluniversity.ac.in

IntechOpen

References

[1] Ohno H. Making nonmagnetic semiconductors ferromagnetic. Science. 1998;**281**:951-956

[2] Zhang Y, Nayak TR, Hong H, Cai W. Biomedical applications of zinc oxide nanomaterials. Current Molecular Medicine. 2013;**13**(05):1633-1645

[3] Özgür U, Ya AI, Liu C, Teke A, Reshchikov MA, Dogan S, et al. A comprehensive review of ZnO materials and devices. Journal of Applied Physics. 2005;**98**:041301

[4] Dietl T, Ohno H, Matsukura F, Cibert J, Ferrand D. Zener model description of ferromagnetism in zinc-blende magnetic semiconductors. Science. 2000;**287**(11): 1019-1022

[5] Dongting W, Xuehong Z, Yuzhen F, Jianhong S, Cong Z, Xianxi Z. Simultaneously composition and interface control for ZnO-based dye-sensitized solar cells with highly enhanced efficiency. Nano-Structures & Nano-Objects. 2017;**10**:1-8

[6] Sharma P, Gupta A, Rao KV, Owens FJ, Sharma R, Ahuja R, et al. Ferromagnetism above room temperature in bulk and transparent thin films of Mn-doped ZnO. Nature Materials. 2003;**2**:673-677

[7] Venkatesan M, Fitzgerald CB, Coey JMD. Unexpected magnetism in a dielectric oxide. Nature (London). 2004; **430**:630

[8] Hong NH, Sakai J, Poirot N, Brize V. Room-temperature ferromagnetism observed in undoped semiconducting and insulating oxide thin films. Physical Review B. 2006;**73**:132404-132408

[9] Ghosh S, Khan GG, Das B, Mandal K. Vacancy-induced intrinsic d ferromagnetism and photoluminescence in potassium doped ZnO nanowires. Journal of Applied Physics. 2011;**109**: 123927-123933

[10] Akbar S, Hasanain SK, Abbas M, Ozcan S, Ali B, Shah SI. Defect induced ferromagnetism in carbon-doped ZnO thin films. Solid State Communications. 2011;**151**:17-20

[11] Hong NH, Sakai J, Brize V. Observation of ferromagnetism at room temperature in ZnO thin films. Journal of Physics: Condensed Matter. 2007;**19**: 036219-036225

[12] Bartolome F, Blasco J, Garcia LM, Garcia J, Jimenez S, Lozano A. Is ball milling a worthy route to produce magnetic semiconductors? Journal of Magnetism and Magnetic Materials. 2007;**316**:e195-e198

[13] Sanyal D, Roy TK, Chakrabarti M, Dechoudhury S, Bhowmick D, Chakrabarti A. Defect studies in annealed ZnO by positron annihilation spectroscopy. Journal of Physics: Condensed Matter. 2008;**20**: 045217-045221

[14] Potzger K, Zhou SQ, Grenzer J, Helm M, Fassbender J. An easy mechanical way to create ferromagnetic defective ZnO. Applied Physics Letters. 2008;**92**:182504-182507

[15] Xing G, Wang D, Yi J, Yang L, Gao M, He M, et al. Correlated d ferromagnetism and photoluminescence in undoped ZnO nanowires. Applied Physics Letters. 2010;**96**:112511-112514

[16] Podila R, Queen W, Nath A, Arantes JT, Schoenhalz AL, Fazzio A, et al. Origin of FM ordering in pristine micro-

and nanostructured ZnO. Nano Letters. 2010;**10**:1383-1386

[17] Banerjee S, Mandal M, Gayathri N, Sardar M. Enhancement of ferromagnetism upon thermal annealing in pure ZnO. Applied Physics Letters. 2007;**91**:182501-182504

[18] Phan TL, Zhang YD, Yang DS, Nghia NX, Thanh TD. Defect-induced ferromagnetism in ZnO nanoparticles prepared by mechanical milling. Applied Physics Letters. 2013;**102**:072408-072413

[19] Ghose S, Sarkar A, Chattopadhyay S, Chakrabarti M, Das D, Rakshit T, et al. Surface defects induced ferromagnetism in mechanically milled nanocrystalline ZnO. Journal of Applied Physics. 2013; **114**:073516-073521

[20] Rainey K, Chess J, Eixenberger J, Tenne DA, Hanna CB, Punnoose A. Defect induced ferromagnetism in undoped ZnO nanoparticles. Journal of Applied Physics. 2014;**115**:17D727

[21] Zhan P, Wang WP, Liu C, Hu Y, Li ZC, Zhang ZJ, et al. Oxygen vacancy–induced ferromagnetism in un-doped ZnO thin films. Journal of Applied Physics. 2012;**111**:033501

[22] Tian Y, Bakaul SR, Wu T. Nanoscale. 2012;**4**:1529-1540

[23] Xu XY, Xu CX, Dai J, Hu JG, Li FJ, Zhang S. Size dependence of defect-induced room temperature ferromagnetism in undoped ZnO nanoparticles. Journal of Physical Chemistry C. 2012;**116**:8813-8818

[24] Mal S, Nori S, Jin C, Narayan J, Nellutla S, Smirnov AI, et al. Reversible room temperature ferromagnetism in undoped zinc oxide: Correlation between defects and physical properties. Journal of Applied Physics. 2010;**108**:073510

[25] Panigrahy B, Aslam M, Misra DS, Ghosh M, Bahadur D. Defect-related emissions and magnetization properties of ZnO nanorods. Advanced Functional Materials. 2010;**20**:1161

[26] Zhang X, Cheng YH, Li LY, Liu H, Zuo X, Wen GH, et al. Evidence for high- ferromagnetism in granular films mediated by native point defects. Physical Review B. 2009;**80**:174427

[27] Li LY, Cheng YH, Luo XG, Liu H, Wen GH, Zheng RK, et al. Room-temperature ferromagnetism and the scaling relation between magnetization and average granule size in nanocrystalline Zn/ZnO core–shell structures prepared by sputtering. Nanotechnology. 2010;**21**:145705

[28] Yi JB, Lim CC, Xing GZ, Fan HM, Van LH, Huang SL, et al. Ferromagnetism in dilute magnetic semiconductors through defect engineering: Li-doped ZnO. Physical Review Letters. 2010;**104**:137201

[29] Schoenhalz AL, Arantes JT, Fazzio A, Dalpian GM. Surface magnetization in non-doped ZnO nanostructures. Applied Physics Letters. 2009;**94**:162503

[30] Xu XY, Xu CX, Lin Y, Ting D, Fang SJ, Shi ZL, et al. Surface photoluminescence and magnetism in hydrothermally grown undoped ZnO nanorod arrays. Applied Physics Letters. 2012;**100**:172401

[31] Hong J, Choi J, Jang SS, Gu J, Chang YL, Wortman G, et al. Magnetism in dopant-free ZnO nanoplates. Nano Letters. 2012;**12**:576

[32] Xu QG, Wen Z, Zhang H, Qi X, Zhong W, Xu L, et al. AIP Advances. 2011;**1**:032127

[33] Peng CX, Liang Y, Wang K, Zhang Y, Zhao G, Wang Y. Possible origin of ferromagnetism in an undoped ZnO d^0 semiconductor. Journal of Physical Chemistry C. 2012;**116**:9709

[34] Botello-Mendez AR, LopezUrıas F, Terrones M, Terrones H. Magnetic behavior in zinc oxide zigzag nanoribbons. Nano Letters. 2008;**8**:1562

[35] Zhou S, Xu Q, Potzger K, Talut G, Grötzschel R, Fassbender J, et al. Journal of Applied Physics. 2008;**93**:3048076

[36] Xing GZ, Lu YH, Tian YF, Yi JB, Lim CC, Li YF, et al. Defect-induced magnetism in undoped wide band gap oxides: Zinc vacancies in ZnO as an example. AIP Advances. 2011;**1**:022152

[37] Ungar T, Tichy G. The effect of dislocation contrast on X-ray line profiles in untextured polycrystals. Physica Status Solidi A. 1999;**171**:425-434

[38] Othman AA, Osman MA, Abd-Elrahim AG. The effect of milling time on structural, optical and photoluminescence properties of ZnO nanocrystals. Optik. 2018;**156**:161-168

[39] Singh J, Sharma S, Soni S, Sharma S, Singh RC. Influence of different milling media on structural, morphological and optical properties of the ZnO nanoparticles synthesized by ball milling process. Materials Science in Semi-conductor Processing. 2019;**98**:29-38

[40] Anand K, Varghese S, Kurian T. Effect of ball size on milling efficiency of zinc oxide dispersions. Particulate Science and Technology. 2018;**36**: 308-311

[41] Kisan B, Perumal A. Room temperature ferromagnetism in finite sized ZnO nanoparticles. Physica B. 2014;**448**:115-119

[42] Zhang KHL, McLeod IM, Lahti M, Pussi K, Dhanak VR. The evolution of the electronic structure at the Bi/Ag (111) interface studied using photoemission spectroscopy. Journal of Physics: Condensed Matter. 2012;**24**: 435502

[43] Kisan B, Kumar J, Alagarsamy P. Experimental and first-principles study of defect-induced electronic and magnetic properties of ZnO nanocrystals. Journal of Physics and Chemistry of Solids. 2020;**146**:109580

[44] Patterson AL. The diffraction of X-rays by small crystalline particles. Physics Review. 1939;**56**:972-978

[45] Elilarassi R, Chadrasekaran G. Synthesis and characterization of ball milled Fe-doped ZnO diluted magnetic semiconductor. Optoelectronics Letters. 2012;**8**:0109

[46] Sreckovic T, Bernik S, Ceh M, Vojisavlevic K. Microstructural characterization of mechanicallyactivated ZnO powders. Journal of Microscopy. 2008;**232**:639

[47] Wang JB, Huang GJ, Zhong XL, Sun LZ, Zhou YC, Liu EH. Raman scattering and high-temperature ferromagnetism of Mn-doped ZnO nanoparticles. Applied Physics Letters. 2006;**88**:252502

[48] Singhal A, Achary SN, Manjanna J, Chatterjee S, Ayyub P, Tyagi AK. Chemical synthesis and structural and magnetic properties of dispersible cobalt-and nickel-doped ZnO nanocrystals. Journal of Physical Chemistry C. 2010;**114**:3422

[49] Calleja JM, Cardona M. Resonant raman scattering in ZnO. Physical Review B. 1977;**16**:3753

[50] Cuscó R, Alarcón-Lladó E, Ibáñez J, Artús L, Jiménez J, Wang BG, et al. Temperature dependence of Raman scattering in ZnO. Physical Review B. 2007;**75**:165202

[51] Wang X, Xu J, Yu X, Xue K, Yu J, Zhao X. Structural evidence of secondary phase segregation from the Raman vibrational modes in Zn1− xCoxO (< x< 0.6). Applied Physics Letters. 2007;**91**:031908

[52] Tapily K, Gu D, Baumgart H, Rigo M, Seo J. Raman spectroscopy of ZnO thin films by atomic layer deposition. ECS Transactions. 2010;**33**:117

[53] Mead DG, Willkinson GR. The temperature dependence of the raman effect in some wurtzite type crystals. Journal of Raman Spectroscopy. 1997;**6**:123

[54] Kuriakose S, Choudhary V, Satpati B, Mohapatra S. Facile synthesis of Ag–ZnO hybrid nanospindles for highly efficient photocatalytic degradation of methyl orange. Physical Chemistry Chemical Physics. 2014;**16**:17560

[55] Khan M, Wei C, Chen M, Tao J, Huang N, Qi Z, et al. CTAB-mediated synthesis and characterization of ZnO/Ag core–shell nanocomposites. Journal of Alloys and Compounds. 2014; **612**:306

[56] Bechambi O, Chalbi M, Najjar W, Sayadi S. Photocatalytic activity of ZnO doped with Ag on the degradation of endocrine disrupting under UV irradiation and the investigation of its antibacterial activity. Applied Surface Science. 2015;**347**:414

[57] Melo AHN, Macedo MA. Permanent data storage in ZnO thin films by filamentary resistive switching. PLoS One. 2016;**11**:0168515

[58] Alaria J, Bieber H, Colis S, Schmerber G, Dinia A. Absence of ferromagnetism in Al-doped Zn0. 9Co0. 10O diluted magnetic semiconductors. Applied Physics Letters. 2006;**88**:112503

[59] Vojisavljevic K, Scepanovic M, Sreckovic T, Grujic-Brojcin M, Brankovic Z, Brankovic G. Structural characterization of mechanically milled ZnO: influence of zirconia milling media. Journal of Physics: Condensed Matter. 2008;**20**:475202

[60] Phan TL, Yu SC, Vincent R, Bui HM, Thanh TD, Lam VD, et al. Influence of Mn doping on structural, optical, and magnetic properties of Zn1− xMnxO nanorods. Journal of Applied Physics. 2010;**108**:044910

[61] Parashar SKS, Murty BS, Repp S, Weber S, Erdem E. Investigation of intrinsic defects in core-shell structured ZnO nanocrystals. Journal of Applied Physics. 2012;**111**:113712

[62] Choi YI, Jung HJ, ShinWG, Sohn SY. Band gap-engineered ZnO and Ag/ZnO by ball-milling method and their photocatalytic and Fenton-like photocatalytic activities. Applied Surface Science. 2015;**356**:615

[63] Mishra SR, Losby J, Dubenko I, Roy S, Ali N, Marasinghe K. Magnetic properties of mechanically milled nanosized cupric oxide. Journal of Magnetism and Magnetic Materials. 2004;**279**:111

[64] Wang Y, Piao JY, Xing GX, Lu YH, Ao Z, Bao N, et al. Journal of Material Chemistry C. 2015;**3**:11953-11958

[65] Bie XF, Wang CZ, Ehrenberg H, Wei YJ, Chen G, Meng X, et al. Room-temperature ferromagnetism in pure ZnO nanoflowers. Solid State Sciences. 2010;**12**:1364

Chapter 7

Impact of Zinc Oxide Nanoparticles Application on Rice Yield and Quality

Norollah Kheyri

Abstract

Rice is the staple food of more than half of the world's population. Zinc (Zn) is a key micronutrient for plants, especially rice. Zinc deficiency can be a serious threat to global food security due to a significant reduction in rice yield. Currently, the application of zinc oxide nanoparticles (ZnO-NPs) through improving grain yield (GY) and increasing rice grain enrichment can be considered as an effective strategy to achieve the dual goal of ensuring food security and improving human health. This chapter describes the applications of ZnO-NPs in rice plants in terms of resistance to biotic and abiotic stresses, nutrient uptake and crop yield. The addition of ZnO-NPs improves growth, increases agronomical parameters, enhances GY, and reduces the allocation of heavy metals into edible parts like grains, thereby improving the yield and quality of rice grains. In general, the present chapter emphasizes the beneficial role of ZnO-NPs in improving the yield and quality of rice grains.

Keywords: grain enrichment, grain yield (GY), nanoparticles (NPs), nutrient uptake, rice, zinc (Zn)

1. Introduction

Using nanoparticles (NPs) to feed crops is a modern technology in the agricultural sector [1]. The diameter of NPs is less than 100 nm [2]. The small size of NPs facilitates the uptake of NPs by plants [3]. Fertilizers containing NPs increase the availability of nutrients, improve soil fertility and reduce environmental hazards when compared with chemical fertilizers [4]. The application of NPs can accelerate plant germination, improve resistance to biotic and abiotic stresses, increase the nutrient use efficiency, enhance plant growth, and reduce environmental impacts compared with traditional methods [5]. It has been reported that the application of ZnO-NPs has a significant role in improving agronomic parameters and increasing the yield and quality of rice grains [1, 6]. The application of ZnO-NPs increases the rice biomass by improving the photosynthesis rate [7]. The addition of ZnO-NPs to the rice plants increases the crop yield due to the gradual release of nutrients at the critical stages of plant growth [8]. It has been proven that the foliar application of ZnO-NPs plays a vital role in reducing the accumulation of heavy metals like cadmium (Cd) and

increasing the concentration of nutrients like Zn in rice grains [7]. Many studies indicated that the application of ZnO-NPs at different growth stages enhances GY and ameliorates Zn concentration in rice grains [9].

Therefore, in this chapter, we study the impacts of ZnO-NPs on the yield and quality of rice, with special emphasis on the role of ZnO-NPs in improving the nutrients uptake, reducing the heavy metals toxicity, and increasing the rice grains yield.

2. Impacts of ZnO-NPs on rice yield and quality

Many studies indicate the positive effects of ZnO-NPs application on the yield and quality of rice grains [1, 6–9]. Application of Zn has a significant impact on improving growth, increasing yield [10] and enhancing Zn content in rice grains [11, 12]. Foliar application of ZnO-NPs leads to improvement of rice grain yield through providing nutrients and improving the process of absorption and allocation of mineral nutrients to the grains [13]. The ZnO-NPs foliar application significantly enhanced nutrient uptake like nitrogen, silicon, and Zn in rice, and as a result, improved the quantitative and qualitative yield of rice grains [14]. Foliar application of ZnO-NPs on rice plants reduced the Cd-induced toxicity in rice plant by increasing the chlorophyll content, gas exchange parameters, Zn accumulation and alleviating the Cd concentration in the plant [7]. ZnO-NPs contribute to the resistance of rice plants against heavy metals such as Cd and Pb, thereby ameliorating GY and quality of rice under stress (**Table 1**) [15].

2.1 Impacts of ZnO-NPs on increasing yield components, grain yield, and nutrient uptake of rice

The impacts of ZnO-NPs on yield components, GY and nutrient uptake of rice are well recognized. Foliar spraying is an effective approach to increase Zn enrichment in crops. Foliar application of nano-ZnO at the doses of 1 and 2 ml L^{-1} increased the GY by 50.4 and 40.4%, respectively, when compared with the control treatment [6]. Sheikhnazari et al. [16] showed the positive impacts of ZnO-NPs foliar spray on rice plants. They reported that the addition of ZnO-NPs to rice plants enhanced the panicle length, number of fertile tiller $hill^{-1}$, 1000-grain weight, and GY by 4.6, 13.8,

Impact on rice	References
(i) Increased fertile tillers $hill^{-1}$, number of filled grains $panicle^{-1}$, and GY; (ii) improved Si and Zn uptake in grain; and (iii) ameliorated protein yield in grain	Kheyri et al. [1]
(i) Increased GY; and (ii) enhanced N, P, K, and Zn uptake in grain	Apoorva et al. [6]
(i) Reduced Cd accumulation in grains and shoots; and (ii) increased growth and yield	Ali et al. [7]
(i) Increased panicle length, number of fertile tillers $hill^{-1}$, number of filled grains $panicle^{-1}$, and GY; and (ii) improved concentration and uptake of Zn in grain	Kheyri et al. [9]
(i) Improved chlorophyll content; (ii) increased yield components and GY; and (iii) enhanced N, Si and Zn concentrations in grain	Kheyri et al. [14]
(i) Improved plant resistance to Cd and Pb toxicity; and (ii) increased GY	Venkatachalam et al. [15]

Abbreviations: Si: silicon; N: nitrogen; P: phosphorus; K: potassium; Zn: zinc; Cd: cadmium; Pb: lead; GY: grain yield.

Table 1.
Beneficial impacts of ZnO-NPs on rice yield and quality.

2.3, and 8.3%, respectively, when compared with non-Zn treated plants. Upadhyaya et al. [17] observed that foliar application of 25 and 50 mg L^{-1} nano-ZnO increased the rice growth by improving the activity of antioxidant enzymes such as catalase, peroxidase, and superoxide desmutase, as well as preventing the damage of reactive oxygen species (ROS). The addition of nano-ZnO to rice significantly increased the total tillers number $hill^{-1}$, the 1000-grain weight, the GY, and the Zn concentration in grain [18]. Baral et al. [19] concluded that the zinc oxide nanoparticles application along with 100% NPK resulted in a significant increase in plant height by 14.4%, Zn concentration in grain by 17.6%, Zn uptake in grain by 65.9%, and GY by 58.8%, compared with control treatment. Kheyri et al. [20] demonstrated that the foliar application of ZnO-NPs increased the chlorophyll content (3.5%), the Si uptake in grain (26.7%), the Zn uptake in grain (54.3%), and the protein yield in grain (21%). In a study, Gomaa et al. [21] investigated the effects of nano-ZnO and Fe fertilizer on growth and productivity of some rice cultivars. They reported that the nano-ZnO application increased the plant height (15 and 13.4%), the panicle length (15.4 and 13.9%), the number of panicles per m^2 (16.7 and 21.1%), and the number of filled grains per panicle (16.1 and 16.2%), respectively in 2017 and 2018 seasons, when compared with control treatment (water). Rameshraddy et al. [22] observed that the ZnO-NPs-treated plants showed higher plant height, higher chlorophyll content, higher biomass, higher tiller number, and greater GY, when compared with non-treated plants. Zhang et al. [23] investigated the yield and quality of rice plants under ZnO-NPs. Plants that received ZnO-NPs showed higher panicle number (4.8–13.1%), higher spikelets per panicle (4.81–10.69%), higher 1000-grain weight (3.82–6.62%), and higher filled grain rate (0.28–2.36%), when compared with plants that did not receive ZnO-NPs. Also, the rice plants had higher leaf area index (LAI) and greater SPAD values under ZnO-NPs. Additionally, the application of ZnO-NPs had a high potential to improve the rice quality. The highest amylose content, protein content and Zn content of edible polished rice was obtained by the ZnO-NPs application. In this study, the higher GY was achieved through increasing photosynthetic materials and higher dry matter accumulation. Foliar application of Zn at the flowering stage significantly increased the Zn content in rice, thereby enhancing the rice quality [24]. Saad Kheir et al. [25] investigated the effects of ZnO-NPs compared with Si-NPs on yield and yield components of rice. Compared with the nano-Si foliar application, the nano-ZnO foliar spray was more effective in increasing yield and yield components of rice (**Table 2**). The nano-ZnO-treated plants showed higher plant height (5%), higher panicle length (9.8%), higher chlorophyll content (2.1%), higher number of grains $panicle^{-1}$ (12.4%), higher 1000-grain weight (6.8%), higher straw yield (2.5%), and higher GY (11.8%), when compared with nano-Si-treated plants. Additionally, ZnO-NPs foliar application increased plant height, panicle length, chlorophyll content,

Nanoparticles	Plant height (cm)	Panicle length (cm)	Chlorophyll content (SPAD)	Number of grains $panicle^{-1}$	1000-grain weight (g)	Grain yield (t ha^{-1})	Straw yield (t ha^{-1})
Control	71.4	18.5	39.9	55.2	24.8	3.9	7.5
Nano-ZnO	81.4	22.5	42.4	70.2	27.7	5.1	8
Nano-Si	77.3	20.3	41.5	61.5	25.8	4.5	7.8

Table 2.
Comparison of ZnO-NPs foliar application with Si-NPs foliar spraying on yield components and yield of rice [25].

Nanoparticles	Plant height (cm)	Number of fertile tillers hill^{-1}	Number of filled grains panicle^{-1}	Chlorophyll content (SPAD)	Grain yield (kg ha^{-1})	Zn concentration in grain (mg kg^{-1})	N concentration in grain (%)
Control	135.2	13.13	81.53	35.03	3503	16.20	1.36
Nano-ZnO	140.1	16.50	90.93	36.30	4133	30.30	1.45
Nano-Si	138.9	15.90	85.80	35.70	4031	23.70	1.43

Table 3.
Comparison of nano-ZnO foliar application with nano-Si foliar spraying on morphophysiological traits of rice [14].

number of grains panicle^{-1}, 1000-grain weight, GY, and straw yield by 12.3, 17.8, 5.9, 21.4, 10.5, 23.5, and 6.2%, respectively, compared with the control treatment.

In another study, Kheyri et al. [14] compared the impacts of nano-ZnO and nano-Si on the morphophysiological traits of rice. These researchers found that foliar application of nano-ZnO on rice plants increased the plant height by 1 and 3.5%, number of fertile tillers hill^{-1} by 3.6 and 20.4%, number of filled grains panicle^{-1} by 5.6 and 10.3%, chlorophyll content by 1.6 and 3.5%, GY by 2.5 and 15.2%, Zn concentration in grain by 21.8 and 46.5%, and N concentration in grain by 1.4 and 6.2%, respectively, when compared with nano-Si and control treatment (**Table 3**).

Studies have shown that the application of Zn in the form of NPs has more positive effects than traditional Zn in terms of improving yield components, yield and nutrients content in rice. Kheyri et al. [1] documented that foliar application of ZnO-NPs significantly increased agronomic traits, grain yield and Zn concentration in rice tissue when compared with zinc sulfate (**Table 4**). They found that the ZnO-NPs foliar application resulted in a significant increase in number of fertile tillers hill^{-1} by 4.5 and 15.2%, number of filled grains panicle^{-1} by 2 and 6.5%, GY by 3.7 and 12.7%, straw yield by 2 and 9.6%, Zn concentration in grain by 9 and 33.2%, and Zn concentration in straw by 14.3 and 42.2%, respectively, compared with zinc sulfate application and control treatment.

The application of different doses of ZnO-NPs can have various impacts on agronomic and physiological characteristics of rice. In a study, effects of different application dosage of ZnO-NPs (0, 3.75, 7.5, 15, 30, and 60 kg hm^{-2}) during two cropping years (2019 and 2020) on rice yield and quality were investigated. In this section, the two-year average of the results of these researchers was examined. The addition of ZnO-NPs (30 kg hm^{-2}) to rice plants significantly increased the spikelets per panicle (116.88), the seed-setting rate (92.40%), the 1000-grain weight (26.81 g), the harvest yield (10.41 t hm^{-2}), the dry matter weight at maturity stage (18.64 t hm^{-2}), and the grain Zn accumulation (236.16 g hm^{-2}) compared with other doses of ZnO-NPs. However, the higher protein content (7.80%) and the greater grain Zn content (22.83 mg kg^{-1}) were obtained by the application of ZnO-NPs at the dose of 60 kg hm^{-2}. The higher amylose content (12.45%) was observed under the conditions of application of 15 kg hm^{-2} of ZnO-NPs (**Table 5**). In general, the results of these researchers showed that the ZnO-NPs application at the rate of 30 kg hm^{-2} had the greatest impact in improving the yield and quality of rice compared with other doses used [26].

Ghasemi et al. [27] investigated the effects of different ZnO-NPs rates at mid-tillering + panicle initiation stages on yield and yield components of rice. The rice

Zinc fertilizer	Fertile tillers hill^{-1}	Number of filled grains panicle^{-1}	Grain yield (kg ha^{-1})	Straw yield (kg ha^{-1})	Zn concentration in grain (mg kg^{-1})	Zn concentration in straw (mg kg^{-1})
Control	15.0	87.8	3887	5239	21.13	24.67
Zinc sulfate	16.9	92.0	4285	5676	28.78	36.62
Nano-ZnO	17.7	93.9	4451	5793	31.64	42.72

Table 4.
Comparison of ZnO-NPs foliar application with zinc sulfate application on agronomic traits, grain yield and zinc concentration in rice [1].

ZnO-NPs application dosage (kg hm^{-2})	Spikelets $panicle^{-1}$	Seed-setting rate (%)	1000-grain weight (g)	Harvest yield (t hm^{-2})	Dry matter weight (t hm^{-2})	Protein content (%)	Amylose content (%)	Grain Zn content (mg kg^{-1})	Grain Zn accumulation (g hm^{-2})
0	107.82	90.14	25.40	9.91	17.03	7.27	11.89	17.20	165.93
3.75	114.77	90.73	26.05	10.25	18.10	7.45	12.25	19.70	202.62
7.5	115.14	91.17	26.30	10.30	18.22	7.58	12.37	21.01	217.18
15	115.47	91.72	26.54	10.38	18.34	7.55	12.45	21.83	228.60
30	116.88	92.40	26.81	10.41	18.64	7.53	12.17	22.45	236.16
60	116.14	92.37	26.49	10.27	18.56	7.80	12.06	22.83	233.40

Table 5.
Effects of ZnO-NPs application dosage on rice yield and quality [26].

ZnO-NPs application rate (ppm)	Number of total tillers hill^{-1}	Number of total spikelets panicle^{-1}	1000-grain weight (g)	Grain yield (kg ha^{-1})	Straw yield (kg ha^{-1})
0	21.7	119.4	26.03	5600	6750
20	22.4	125.2	26.14	6332	7470
40	23.7	128.9	26.58	6483	7502

Table 6.
Effects of ZnO-NPs application rate on yield components and yield of rice [27].

plants treated with nano-ZnO at the rate of 40 ppm had higher number of total tillers hill^{-1} (5.5 and 8.4%), higher number of total spikelets panicle^{-1} (2.9 and 7.4%), higher 1000-grain weight (1.6 and 2.1%), higher GY (2.3 and 13.6%), and higher straw yield (0.5 and 10%), respectively, compared with nano-ZnO foliar application at the rate of 20 ppm and control treatment or non-use of ZnO-NPs (**Table 6**).

2.2 Impacts of ZnO-NPs on improving yield and quality of rice under biotic and abiotic stresses

Nanotechnology is a new and developing technology that can play a vital role in reducing abiotic stress [28]. The application of ZnO-NPs has a high potential to compensate for Zn deficiency and to deal with various stresses, which are used by different methods such as seed priming, foliar application on plants, and root application [29]. In rice plants, the ZnO-NPs alleviated the drought stress by maintaining the membrane stability and higher expression of Cu/Zn superoxide dismutase (SOD) [22]. Saad Kheir et al. [25] found that ZnO-NPs foliar application on rice plants under saline and alkaline soils enhanced plants' resistance to abiotic stresses and thus ameliorated rice growth and yield. Elamawi et al. [30] evaluated the impact of ZnO-NPs at the dosage of 0, 10, 20 and 30 ppm during two cropping years (2013 and 2014) on brown spot disease, morphological traits, yield attributes and GY of rice under saline soil. In this section, researchers' findings were presented as a two-year average. The higher plant height (80 cm), the higher panicle length (18.41 cm), the higher number of tillers m^2 (471.9), the higher number of panicles m^2 (429.7), the higher number of filled grains panicle^{-1} (106.4), the higher 1000-grain weight (21.7 g), the higher GY (4.83 t ha^{-1}), and the higher straw yield (6.12 t ha^{-1}) when observed that the rice plants treated with ZnO-NPs at the dosage of 30 ppm. However, the application of all dosage of ZnO-NPs improved the yield components and GY of rice compared with the control treatment. The lowest infection severity (133.3) was observed by the application of ZnO-NPs at the dosage of 20 ppm. They concluded that the ZnO-NPs foliar application at the rate of 20 ppm can simultaneously reduce brown spot disease severity, ameliorate rice growth, yield attributes, GY, thereby improves rice plants resistance and/or tolerance to salinity stress (**Table 7**).

The application of nano-ZnO is a novel strategy to improve the growth and yield of rice plants by increasing tolerance to biotic and abiotic stresses [31]. Singh et al. [32] studied the impact of ZnO-NPs on seed germination characteristics in rice plants under salinity stress. They revealed that application of ZnO-NPs at the rate of 50 mg L^{-1} alleviated the negative effect of salinity stress on rice genotypes during the germination stage. Application of ZnO-NPs at the rate of 50 mg L^{-1} modulated the impact of salinity stress on relative seed germination rate, root and shoot growth, chlorophyll and

ZnO-NPs application dosage (ppm)	Severity of infection (number of spots per 100 leaves)	Plant height (cm)	Panicle length (cm)	Number of tillers m^2	Number of panicles m^2	Number of filled grains $panicle^{-1}$	1000-grain weight (g)	Grain yield ($t\ ha^{-1}$)	Straw yield ($t\ ha^{-1}$)
0	236.8	75.75	17.90	421.2	364.1	90.6	20.8	3.68	4.97
10	146.1	79.05	18.18	444.4	384.6	99.6	21.4	4.17	5.56
20	133.3	79.75	18.28	464.3	419.8	103.9	21.6	4.69	6.01
30	157.4	80.00	18.41	471.9	429.7	106.4	21.7	4.83	6.12

Table 7.
Effects of ZnO-NPs application dosage on brown spot disease and rice yield [30].

Impact on rice	References
(i) Increased SOD activity; and (ii) alleviated the drought stress	Rameshraddy et al. [22]
(i) Increased plant height, panicle length, number of tillers m^2, number of panicles m^2, number of filled grains $panicle^{-1}$, 1000-grain weight, GY, and straw yield; and (ii) reduced brown spot disease severity	Elamawi et al. [30]
(i) Increased growth and yield; and (ii) Improved tolerance to biotic and abiotic stresses	Qiu et al. [31]
(i) Modulated the impact of salinity stress on relative seed germination rate, root and shoot growth, chlorophyll and carotenoid stability; (ii) reduced MDA content; and (iii) increased activity of antioxidant enzymes like SOD and APX	Singh et al. [32]
(i) Increased panicle length, number of tillers per plant, number of panicles per plant, number of spikelets per panicle, and paddy yield; (ii) reduced MDA content; (iii) enhanced activity of antioxidant enzymes like CAT, POD, and SOD; and (iv) reduced drought stress	Waqas Mazhar et al. [33]

Abbreviations: CAT: catalase; POD: peroxidase; SOD: superoxide dismutase; APX: ascorbate peroxidase; MDA: malondialdehyde; GY: grain yield.

Table 8.
Beneficial impacts of ZnO-NPs on yield and quality of rice under biotic and abiotic stresses.

carotenoid stability, and malondialdehyde content. Also, when ZnO-NPs are applied at the dosage of 50 mg L^{-1}, the activity of antioxidant enzymes like SOD and ascorbate peroxidase (APX) increased. The significant effect of ZnO-NPs in mitigating drought stress depended on the dosage of ZnO-NPs used. Waqas Mazhar et al. [33] investigated the effect of seed nano-priming with different dosage of ZnO-NPs (0, 5, 10, 15, 25, and 50 ppm) on agronomic characteristics of rice plants under drought stress. They demonstrated that the rice plants treated with ZnO-NPs at the dosage of 25 ppm had higher panicle length, higher number of tillers per plant, higher number of panicles per plant, higher number of spikelets per panicle, and higher paddy yield, when subjected to drought stress. Application of 25 ppm ZnO-NPs also reduced the leaf MDA content and increased the activities of antioxidant enzymes like CAT, POD, and SOD in rice plants under drought stress. However, the greatest reduction in the MDA value was observed when ZnO-NPs were applied at a dosage of 50 ppm. These researchers reported that seed priming with ZnO-NPs led to a 53% reduction in MDA content and a 13%, 38%, and 11% increase in CAT, POD and SOD, respectively, in rice plants under water stress (**Table 8**).

3. Conclusions

The findings of the studies show that the proper use of ZnO-NPs can be a promising option to improve the quality of rice by fortifying rice with Zn. Additionally, application of ZnO-NPs has a high potential to increase rice yield by improving yield components. The application of ZnO-NPs is helpful in biotic and abiotic stresses mitigation by increasing activity of antioxidant enzymes like CAT, POD, APX, and SOD and reducing MDA content. However, a complete understanding of how ZnO-NPs affect the physiological and molecular interactions affecting the quantitative and qualitative yield of rice, especially rice plants under stress, requires further detailed research. In general, ZnO-NPs application has a beneficial role in increasing the yield and quality of rice grains, thus the use of ZnO as nanoparticles can provide a modern insight in the agricultural industry.

Author details

Norollah Kheyri
Agronomy, Gorgan Branch, Islamic Azad University, Gorgan, Iran

*Address all correspondence to: norollah.kheyri@yahoo.com

IntechOpen

References

[1] Kheyri N, Ajam Norouzi H, Mobasser HR, et al. Effects of silicon and zinc nanoparticles on growth, yield, and biochemical characteristics of rice. Agronomy Journal. 2019;**111**:3084-3090. DOI: 10.2134/agronj2019.04.0304

[2] Shaw AK, Hossain Z. Impact of nano-CuO stress on rice (*Oryza sativa* L.) seedlings. Chemosphere. 2013;**93**:906-915. DOI: 10.1016/j.chemosphere.2013.05.044

[3] Mousavi SR, Rezaei M. Nanotechnology in agriculture and food production. Journal of Applied Environmental and Biological Sciences. 2011;**1**:414-419

[4] Sabir S, Arshad M, Ghaudhari SK. Zinc oxide nanoparticles for revolutionizing agriculture: Synthesis and applications. Scientific World Journal. 2014:1-8. DOI: 10.1155/2014/925494

[5] Alharby HF, Metwali EMR, Fuller MP, et al. Impact of application of zinc oxide nanoparticles on callus induction, plant regeneration, element content and antioxidant enzyme activity in tomato (*Solanum lycopersicum* mill.) under salt stress. Archives of Biological Sciences. 2016;**68**:723-735. DOI: 10.2298/ABS151105017A

[6] Apoorva MR, Chandrasekhar Rao P, Padmaja G. Effect of zinc with special reference to nano zinc carrier on yield, nutrient content and uptake by rice (*Oryza sativa* L.). International Journal of Current Microbiology and Applied Sciences. 2017;**6**:1057-1063. DOI: 10.20546/ijcmas.2017.602.131

[7] Ali S, Rizwan M, Noureen S, et al. Combined use of biochar and zinc oxide nanoparticle foliar spray improved the plant growth and decreased the cadmium accumulation in rice (*Oryza sativa* L.) plant. Environmental Science and Pollution Research. 2019;**26**:11288-11299. DOI: 10.1007/s11356-019-04554-y

[8] Yuva Raj M, Subramanian KS. Fabrication of zinc nano fertilizer on growth parameter of rice. Trends in Biosciences. 2014;**7**:2564-2565

[9] Kheyri N, Abbasalipour M. Effect of foliar application of ZnO nanoparticles on yield components, yield and Zn efficiency indices in rice under water stress. Environmental Stresses in Crop Sciences. 2021;**13**:1203-1218. DOI: 10.22077/escs.2020.2298.1591

[10] Dwivedi R, Srivastva PC. Effect of zink sulphate application and the cyclic incorporation of cereal straw on yields, the tissue concentration and uptake of Zn by crops and availability of Zn in soil under rice-wheat rotation. International Journal of Recycling of Organic Waste in Agriculture. 2014;**3**:1-12. DOI: 10.1007/s40093-014-0053-3

[11] Shivay YS, Prasad R, Kaur R, et al. Relative efficiency of zinc sulphate and chelated zinc on zinc biofortification of rice grains and zinc use-efficiency in basmati rice. Proceedings of the National Academy of Sciences, India Section B: Biological Sciences. 2016;**86**:973-984. DOI: 10.1007/s40011-015-0544-7

[12] Farooq M, Ullah A, Rehman A, et al. Application of zinc improves the productivity and biofortification of fine grain aromatic rice grown in dry seeded and puddle transplanted production systems. Field Crops Research. 2018;**216**:53-62. DOI: 10.1016/j.fcr.2017.11.004

[13] Kheyri N, Ajam-Norouzi H, Mobasser HR, et al. Comparison of NPs foliar application of silicon and zinc with soil application on agronomic and physiological traits of rice (*Oryza sativa* L.). Iranian Journal of Field Crops Research. 2019;**17**:503-515. DOI: 10.22067/gsc.v17i3.80028

[14] Kheyri N, Ajam-Norouzi H, Mobasser HR, et al. Effect of different resources and methods of silicon and zinc application on agronomic traits, nutrient uptake and grain yield of rice (*Oryza sativa* L.). Applied Ecology and Environmental Research. 2018;**16**:5781-5798. DOI: 10.15666/aeer/1605_57815798

[15] Venkatachalam P, Jayaraj M, Manikandan R, et al. Zinc oxide nanoparticles (ZnONPs) alleviate heavy metal-induced toxicity in Leucaena leucocephala seedlings: A physiochemical analysis. Plant Physiology and Biochemistry. 2017;**110**:59-69. DOI: 10.1016/j.plaphy.2016.08.022

[16] Sheikhnazari S, Niknezhad Y, Fallah H, et al. Effect of application of nitrogen doses along with biochar and zinc nanoparticles on quantitative and qualitative characteristics of rice (*Oryza sativa* L.). Iranian Journal of Field Crops Research. 2022;**20**:349-361. DOI: 10.22067/jcesc.2022.75649.1150

[17] Upadhyaya H, Shome S, Tewari S, et al. Effect of Zn nano-particles on growth responses of rice. Nano Science Technology Conference. 2014:508-512

[18] Sheykhzadeh M, Mobasser HR, Rahimi Petrodi E, et al. Silicon and zinc improves grain yield and nutrient status in rice when supplied during the different growth stages. Romanian Agricultural Research. 2022:39

[19] Baral K, Kumar D, Shivay YS. Effect of zinc oxide nanoparticles embedded NPK fertilizer on growth, yield and zinc concentration and uptake of aromatic rice (*Oryza sativa*). Indian Journal of Agricultural Sciences. 2020;**90**:1626-1630. DOI: 10.56093/ijas.v90i8.105980

[20] Kheyri N, Ajam-Norouzi H, Mobasser HR, et al. Evaluation of the effect of foliar and soil application of zinc and silicon nanoparticles on some physiological traits of rice (*Oryza sativa* L.). Journal of Plant Environmental Physiology. 2017;**12**:52-64

[21] Gomaa MA, Kandil EE, Abdelsalam NR, et al. Growth, productivity of some rice cultivars in relation to nano-zinc and iron fertilizer. Middle East Journal of Agriculture Research. 2018;**7**:1352-1358

[22] Rameshraddy GJ, Pavithra GJ, Rajashekar Reddy BH, et al. Zinc oxide nano particles increases Zn uptake, translocation in rice with positive effect on growth, yield and moisture stress tolerance. Indian Journal of Plant Physiology. 2017;**22**:287-294. DOI: 10.1007/s40502-017-0303-2

[23] Zhang H, Wang R, Chen Z, et al. The effect of zinc oxide nanoparticles for enhancing rice (*Oryza sativa* L.) yield and quality. Agriculture. 2021;**11**:1247. DOI: 10.3390/agriculture11121247

[24] Fang Y, Wang L, Xin ZH, et al. Effect of foliar application of zinc, selenium, and iron fertilizers on nutrients concentration and yield of rice grain in China. Journal of Agricultural and Food Chemistry. 2008;**56**:2079-2084. DOI: 10.1021/jf800150z

[25] Saad Kheir AM, Abouelsoud HM, Hafez EM, et al. Integrated effect of nano-Zn, nano-Si, and drainage using crop straw–filled ditches on saline sodic soil properties and rice productivity. Arabian Journal of

Geosciences. 2019;**12**:471. DOI: 10.1007/s12517-019-4653-0

[26] Mi K, Yuan X, Wang Q, et al. Zinc oxide nanoparticles enhanced rice yield, quality, and zinc content of edible grain fraction synergistically. Frontiers in Plant Science. 2023;**14**:1196201. DOI: 10.3389/fpls.2023.1196201

[27] Ghasemi M, Noormohammadi G, Madani H, et al. Effect of foliar application of zinc nano oxide on agronomic traits of two varieties of rice (*Oryza sativa* L.). Crop Research. 2017;**52**:195-201

[28] Zafar S, Hasnain Z, Aslam N, et al. Impact of Zn nanoparticles synthesized via green and chemical approach on okra (*Abelmoschus esculentus* L.) growth under salt stress. Sustainable. 2021;**13**:3694. DOI: 10.3390/SU13073694

[29] Rossi L, Fedenia LN, Sharifan H, et al. Effects of foliar application of zinc sulfate and zinc nanoparticles in coffee (*Coffea arabica* L.) plants. Plant Physiology and Biochemistry. 2019;**135**:160-166. DOI: 10.1016/J.PLAPHY.2018.12.005

[30] Elamawi RM, Bassiouni SM, Elkhoby WM, et al. Effect of zinc oxide nanoparticles on brown spot disease and rice productivity under saline soil. Journal of Plant Protection and Pathology Mansoura University. 2016;**7**:171-181

[31] Qiu J, Chen Y, Liu Z, et al. The application of zinc oxide nanoparticles: An effective strategy to protect rice from rice blast and abiotic stresses. Environmental Pollution. 2023;**331**:121925. DOI: 10.1016/j.envpol.2023.121925

[32] Singh A, Sengar RS, Rajput VD, et al. Impact of zinc oxide nanoparticles on seed germination characteristics in rice (*Oryza sativa* L.) under salinity stress. Journal of Ecological Engineering. 2023;**24**:142-156. DOI: 10.12911/22998993/169142

[33] Waqas Mazhar M, Ishtiaq M, Hussain I, et al. Seed nano-priming with zinc oxide nanoparticles in rice mitigates drought and enhances agronomic profile. PLoS One. 2022;**17**:e0264967. DOI: 10.1371/journal.pone.0264967

Chapter 8

Bioinspired Fibrous Architectures Based on ZnO Templated by Eggshell Membranes

Nicoleta Preda, Marcela Socol, Andreea Costas and Irina Zgura

Abstract

ZnO-based nanostructures emerge as promising materials due to their potential applications in fields including electronic devices, photodetectors, photocatalysts, biocides, etc. The bio-template-mediated synthesis is a straightforward approach for obtaining inorganic or hybrid organic/inorganic materials with tailored morphologies and functional properties. Eco-friendly waste, eggshell membrane (ESM) is an ideal bio-template for the development of 3D hierarchical porous architectures due to its specific 3D interlaced fiber protein network structure. Therefore, this chapter is focused on the ESM-mediated synthesis of 3D fibrous architectures based on ZnO, the ESM organic network being functionalized with inorganic nanostructures or replicated into an inorganic one as follows: i) coated with ZnO layer by RF magnetron sputtering, (ii) covered with ZnO by electroless deposition and (iii) replicated into ZnO web by biomorphic mineralization. The obtained ZnO shows wurtzite structure, band-gap value and emission bands typical for this semiconductor. The electrical properties of the ZnO fiber webs were measured using interdigitated metallic electrodes patterned substrates. The ESM conversion from a bio-waste into new value-added nanomaterials is very attractive from the sustainability and recycle waste perspective, the ZnO-based fibrous architectures featured by a large specific surface area having potential applications in water purification, photocatalysis or chemical sensors areas.

Keywords: ZnO, eggshell membranes, organic/inorganic fibers, inorganic fibers, fibrous architectures

1. Introduction

Over the last decades, zinc oxide (ZnO) has been extensively and intensively assessed attracting an enormous interest from both science and industry. Thus, ZnO micro/nanostructures emerge as a powerful class of advanced functional materials [1–20], which can find applications in various domains ranging from electronics, energy, and environmental protection to healthcare. Recently, a large number of comprehensive review papers provide synopses on the recent achievements attained in the preparation and properties of ZnO nanomaterials and their use in electronic devices [8], UV photodetectors [9], photovoltaic devices [10], gas sensors [11], nonlinear

optical materials [12], biosensors [13, 14], photocatalysis [15–17], antibacterial agents [18, 19], surface coating with special wetting properties [20], and so on. ZnO is an outstanding material due to its properties [21, 22] such as wide bandgap (~3.3 eV in bulk), high exciton binding energy (~60 meV), high thermal conductivity (50 W/mK), ultraviolet light absorption, high transmittance of visible light, strong luminescence (even at room temperature), mechanical stability at room temperature, good biocompatibility, biodegradability and low toxicity. Moreover, the ZnO characteristics, such as abundance, environmental friendly, and a vast family of 0D, 1D, 2D, and 3D morphologies, recommend the ZnO-based materials for mass production with low manufacturing costs, which can subsequently broaden their use in different industrial settings. Furthermore, ZnO micro/nanostructures can be relative easily synthesized in large quantities by different approaches [1–22] including physical techniques, conventional chemical methods, or green synthesis routes. Hence, in previous papers, we reported on the preparation of various ZnO micro/nanostructures (particle, rod, wire, core-shell, flower, or snowflake) by thermal oxidation in air [23–26], chemical precipitation [27–29], aqueous solution growth [26] and chemical bath deposition [30] for potential applications in field effect transistors [26], photovoltaic cells [27], chemical sensors [30], photocatalysts [24, 28], antibacterial agents [28], and surfaces with special wetting properties (superhydrophobic, no-loss liquid transportation, anticorrosion, or self-cleaning) [23, 25, 30]. Finally, ZnO is an ideal system for exploring the morphology-properties-applications relationship being well-known that the size, shape, and surface chemistry of the semiconducting structures can strongly influence their properties, these being further responsible for their applications.

Eggshell membrane (ESM) is an affordable, inexpensive, easy-handling, and renewable biomaterial, which, for a long time, was considered just a common industrial and domestic waste. Nevertheless, owing to its unique three-dimensional (3D) interlaced fibrous protein network structure, ESM presents very useful properties [31–33] such as flexibility, high porosity, high absorption capacity, large surface area, good permeability, good mechanical strength, good thermal stability, biocompatibility, and biodegradability. As a consequence, in the last decade, ESM has been in the spotlight gaining a huge popularity in its conversion from an abundant daily waste into a source for developing new value-added materials using bioinspired strategies. It must be mentioned that the ESM biopolymeric network is formed by fibers containing 80–85% proteins in their composition (10% collagens types I, V, and X and 70–75% other proteins and glycoproteins) [31]. Accordingly, the ESM surface contains numerous functional chemical groups (amine, amides, carboxylic) that play a major role in its functionalization or replication. Thus, in different forms (pristine, modified, or carbonized), the ESM has been used as (i) component in triboelectric nanogenerators [34], fuel cells [35], supercapacitors [36], lithium-ion battery [37]; (ii) sorbent of water contaminants, such as dye molecules [38] or heavy metals [39]); and (iii) immobilization platform for biosensors [40]. Biomaterial with an antibacterial and anti-inflammatory activity, the ESM porous structure can favor the diffusion of gas and water molecules assisting the attachment and proliferation of the cells. In this way, ESM can control the moisture content of a wound, provides an antibacterial barrier, and helps the covering of the wound preventing and reducing the bacterial growth. Therefore, ESM is an excellent biocompatible material for wound healing of skin injuries [41] and tissue engineering [42]. Furthermore, the ESM fiber-interwoven architecture makes this biowaste an ideal bio-template for designing 3D hierarchical porous architectures. Hence, the ESM network was successfully functionalized with conducting polymers [43–45] or semiconducting

nanostructures [46–48] and replicated into a semiconducting one [49–51], the new materials having potential applications in areas, including supercapacitors [44], fuel cells [45], actuators [43], antibacterial agents [46], photocatalysts [49], and water treatment [47, 50].

In this context, the aim of this chapter is to highlight the way in which functional hybrid ESM/ZnO webs and ZnO fiber webs can be developed by combining ESM as bio-template and ZnO preparation approaches such as radio frequency (RF) magnetron sputtering, electroless deposition, and biomorphic mineralization. In the following, we summarized the major attribute of each ZnO preparation methods involved in our work.

The radio frequency magnetron sputtering can be regarded as a "clean" environmental friendly preparation approach being a solution-free route (does not involve hazardous precursors and does not generate harmful by-products), which uses only solid sputtering targets in the deposition of the metal oxide layer [46, 52, 53]. Versatile, high-yield, and low-temperature vapor deposition technique, this preparation path can be employed to obtain nanostructured layers on a wide range of substrates, the deposited films being usually polycrystalline, uniform, with a good adhesion on the surface intended to be covered.

The electroless deposition can be considered an easily approach, which uses accessible raw precursors (metal salt and reducing agent), low process temperature, ambient pressure processing, and simple equipment (the chemical redox reactions take place in aqueous solutions) [47, 54, 55]. This synthesis method is based on the growth of the metal oxide structures only on a metal-catalyzed surface, the surface intended to be coated being firstly modified with a catalyst metal, such as palladium or gold. Hence, the electroless deposition allows the coating of organic nonconductive substrates with plain or 3D shapes by a uniform and adherent metal oxide structured layer.

The biomorphic mineralization is a straightforward approach for obtaining metal oxide materials with tailored architectures and properties by selecting an appropriate bio-template, this preparation path using low-cost reagents (metal salt precursors), inexpensive equipment and involving just a simple immersion of a bio-template into precursor solution and a subsequent calcination [49–51, 56–60]. In the case of this method, nature is an inexhaustible source of organic templates (leaves [56, 57], wood [58], butterfly wings [59], eggshell membranes [50, 51], etc.), each of them with an innate architecture that a priori can be perfectly replicated into an inorganic one containing metal oxide particles as building blocks.

The properties of the prepared samples (pristine ESM, ZnO-functionalized ESM, and ZnO replica of ESM) were evaluated from the structural, optical, and morphological point of view employing X-ray diffraction (XRD), reflectance, photoluminescence, field-emission scanning electron microscopy (FESEM), and atomic force microscopy (AFM). The elemental composition and vibrational properties of some samples were investigated by energy dispersive X-ray analysis (EDX) and Fourier-transform infrared spectroscopy (FTIR). The wetting properties of the samples were also tested. Furthermore, a possible pathway to integrate the bioinspired ZnO fiber webs in the electronic devices is evaluated by using interdigitated metallic electrodes as substrates during the ESM removal by calcination treatment. The main advantage of this approach is represented by the fact that the semiconducting fibers form bridges over the neighboring grid structures providing electrical paths between them. In this way, the electrical circuit is closed without any additional lithographical contacting steps.

The information from this chapter provides new insights concerning the development of the bioinspired 3D fibrous architectures based on ZnO templated by eggshell membrane. In the same time, from the waste valorization perspective, a biowaste is converted into new value-added ZnO-based nanomaterials [61]. Furthermore, owing to their high surface area, these bioinspired architectures with a well-defined morphology can emerge as key materials for applications in gas sensing, water treatment, photocatalysis, etc.

2. Eggshell membrane mediated synthesis of 3D fibrous architectures based on ZnO

The eggshell membranes were obtained from commercial fresh hen eggs bought from local supermarkets using the following steps: (i) the eggs were gently broken, (ii) the eggshells were rinsed with distilled water in order to eliminate the yolk and the albumen, (iii) the eggshell membranes were manually stripped from eggshells and washed many times with distilled water for several days in order to remove any residual albumen traces (**Figure 1a**), (iv) the wet eggshell membranes were drying for a few days in air (ambient conditions) by fixing them mechanically between two overlapping stainless-steel frames for avoiding their warp (**Figure 1b**), and (v) the dried eggshell membranes were taken off from the metal supports and used as bio-template in the functionalization or replication processes. The FESEM images of the ESM reveal the distinctive 3D hierarchical porous architecture (**Figure 1c**) formed by interpenetrating fibers with diameters in the micrometer range (**Figure 1d**).

The preparation of ZnO-based architectures using ESM as bio-template was carried in accordance to the procedures described in the references [46, 47, 49] as follows:

Radio frequency (RF) magnetron sputtering: The native ESM was coated with the ZnO layer using a ZnO sputtering target as source, and the process was carried in argon atmosphere using the following experimental parameters: 3 h — deposition time, 5.4×10^{-3} mbar — pressure in the chamber, and 100 W – power applied on the magnetron.

Electroless deposition: The native ESM was firstly coated with a catalytic gold layer by magnetron sputtering, and the metalized ESM was subsequently immersed at 70°C for 2 h into an aqueous deposition solution containing zinc nitrate (0.07 M $Zn(NO_3)_2\ 6H_2O$) and dimethylamineborane (0.01 M $(CH_3)_2NHBH_3$), the growth of ZnO structures taking place only on the activated surface via the redox reactions.

Biomorphic mineralization: The native ESM was immersed for 24 h at room temperature into an aqueous solution containing 0.3 M $Zn(NO_3)_2\ 6H_2O$, the impregnated

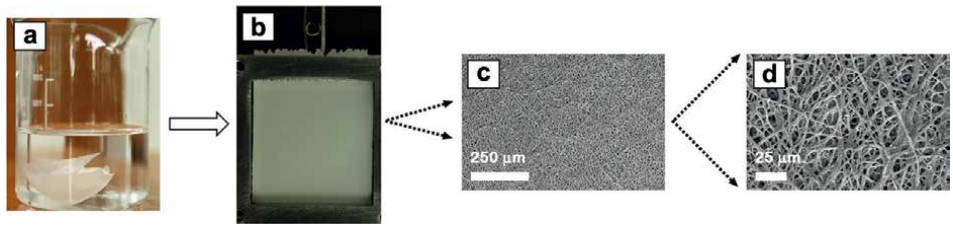

Figure 1.
Optical images of ESM during washing in water (a) and drying in air (b). FESEM images of ESM at two magnifications (c, d).

ESM being further placed on Si/SiO_2 substrates, dried in air for 12 h at ambient conditions and subsequently calcined at 550°C for 3 h.

The following will be given some particularities of the electroless deposition and biomorphic mineralization processes. Hence, according to references [55, 62], the chemical reactions involved in the ZnO electroless deposition are:

a. $Zn(NO_3)_2 \rightarrow Zn^{2+} + 2NO_3^-$

b. $2(CH_3)_2NHBH_3 + 4H_2O \rightarrow 2HBO_2 + 2(CH_3)_2NH_2^+ + 5H_2 + 2\,e^-$

c. $NO_3^- + H_2O + 2e^- \rightarrow NO_2^- + 2HO^-$

d. $Zn^{2+} + 2HO^- \rightarrow Zn(OH)_2$

e. $Zn(OH)_2 \rightarrow ZnO + H_2O$

Thus, in the presence of the Au catalyst, the dimethylamineborane is oxidized releasing electrons that further reduce nitrate ions to nitrite ions. In this way, the pH increases in the vicinity of the metalized surface, and the hydroxyl ions react with the zinc ions and lead to the formation of zinc hydroxide that subsequently is thermal dehydrated to ZnO. For this reason, the ZnO growth occurs mainly on the catalytic surface, the electroless deposition offering an excellent site-selectively deposition on complex structures such that of ESM, namely a 3D fibrous architecture.

As regards the replication of the ESM into ZnO, the functional chemical groups from the ESM surface [31] can assist the binding of zinc ions. The FESEM image (**Figure 2a**) and the corresponding EDX mapping (**Figure 2b**) of the ESM impregnated with zinc ions show the following chemical elements: (i) C, O, and N (ESM typical elements), (ii) Au (a thin layer of metal being deposited on the ESM prior to its morphological assessment), and (iii) Zn (zinc ions adsorbed on the ESM). The Zn distribution on the ESM surface confirms the ESM control through its functional groups on the uniform adsorption of the zinc ions during the immersion.

The vibrational fingerprints of these functional chemical groups presented in the ESM protein fibers can be identified in the FTIR spectrum (**Figure 3**), the assignment of the absorption bands being made based on the literature data [32]: (i) stretching vibrations of the O-H and N-H groups at 3310 cm^{-1}; (ii) asymmetric stretching

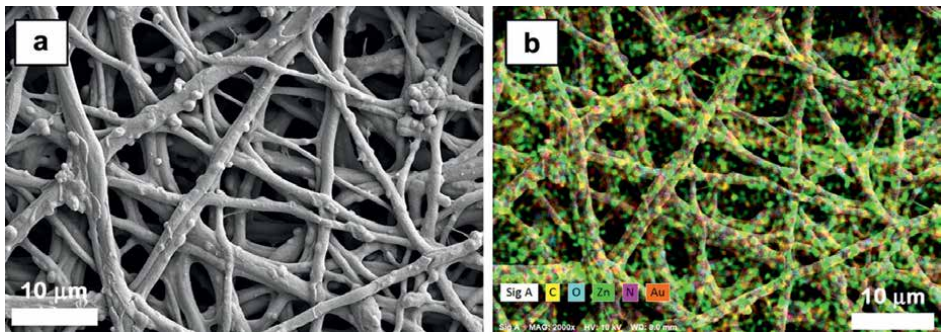

Figure 2.
FESEM (a) and EDX mapping (b) images of the ESM impregnated with zinc (used in the biomorphic mineralization).

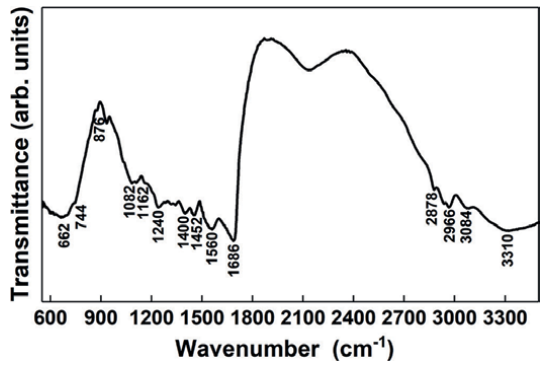

Figure 3.
FTIR spectrum of raw ESM.

vibrations of the C–H bond from =C–H and $=CH_2$ groups at 3084 cm^{-1}, 2966 cm^{-1} and 2878 cm^{-1}; (iii) amide I, amide II, and amide III groups from the ESM protein structure at 1686 cm^{-1}, 1560 cm^{-1} and 1240 cm^{-1} linked to vibrations of the C=O bond and the deformation vibrations of the C-N and N-H bonds; (iv) stretching vibrations of C=C at 1452 cm^{-1}; (v) asymmetric and symmetric stretching of the -COO from the ESM protein structure at 1400 cm^{-1}; (vi) vibration modes of C-O at 1082 cm^{-1}; and (vii) vibration modes of C-S at 662 cm^{-1}.

Concerning the ESM thermal behavior during the calcination step involved in the biomorphic mineralization, according to the literature [63], the thermal decomposition of ESM is a multistep process: the first stage of decomposition starts very early at ~60°C due to the thermal denaturation of collagen and finishes at ~120°C; the second stage of decomposition takes place in the range between 250 and 450°C as a consequence of the thermal degradation of collagen.

Optical and FESEM images at low magnification of the investigated samples are presented in **Figure 4** being labeled as follows: pristine ESM (P0), ZnO-functionalized ESM by RF magnetron sputtering (P1), and ZnO-functionalized ESM by electroless deposition (P2) and ZnO replica of ESM by biomorphic mineralization (P3). It can be noticed that the color of the samples varies from the white-ivory (P0) to beige (P1), brown (P2), and white-gray (P3). Also, it must be emphasized that the distinctive 3D framework of the ESM bio-template is well preserved during the functionalization process by RF magnetron sputtering and electroless deposition or is perfectly inherited during the replication process by biomorphic mineralization.

The structural information of the investigated samples was obtained by XRD analysis, while their optical properties were evaluated by diffuse reflectance and photoluminescence. Thus, XRD patterns, the reflectance spectra, the representation of the Kubelka–Munk function used for estimating the value of the band gap, and the photoluminescence spectra of the P0–P3 samples are presented in **Figures 5**–**8**, respectively.

In **Figure 5**, the XRD pattern of P0 sample discloses the amorphous character of ESM owed to its composition based on amine, amides, and carboxylic compounds. The XRD patterns of P1–P3 samples reveal the peaks at 2θ: 31.7°, 34.4°, 36.2°, 47.5°, 56.6°, and 62.8° assigned to (100), (002), (101), (102), (110), and (103) planes of the hexagonal wurtzite ZnO structure (ICDD 00-035-1451). Besides of these diffraction peaks, the XRD pattern of P2 sample exhibits peaks at 2θ: 38.2°, 44.4°, and 64.5° indexed to (111), (200), and (220) planes of the face-centered cubic Au structure

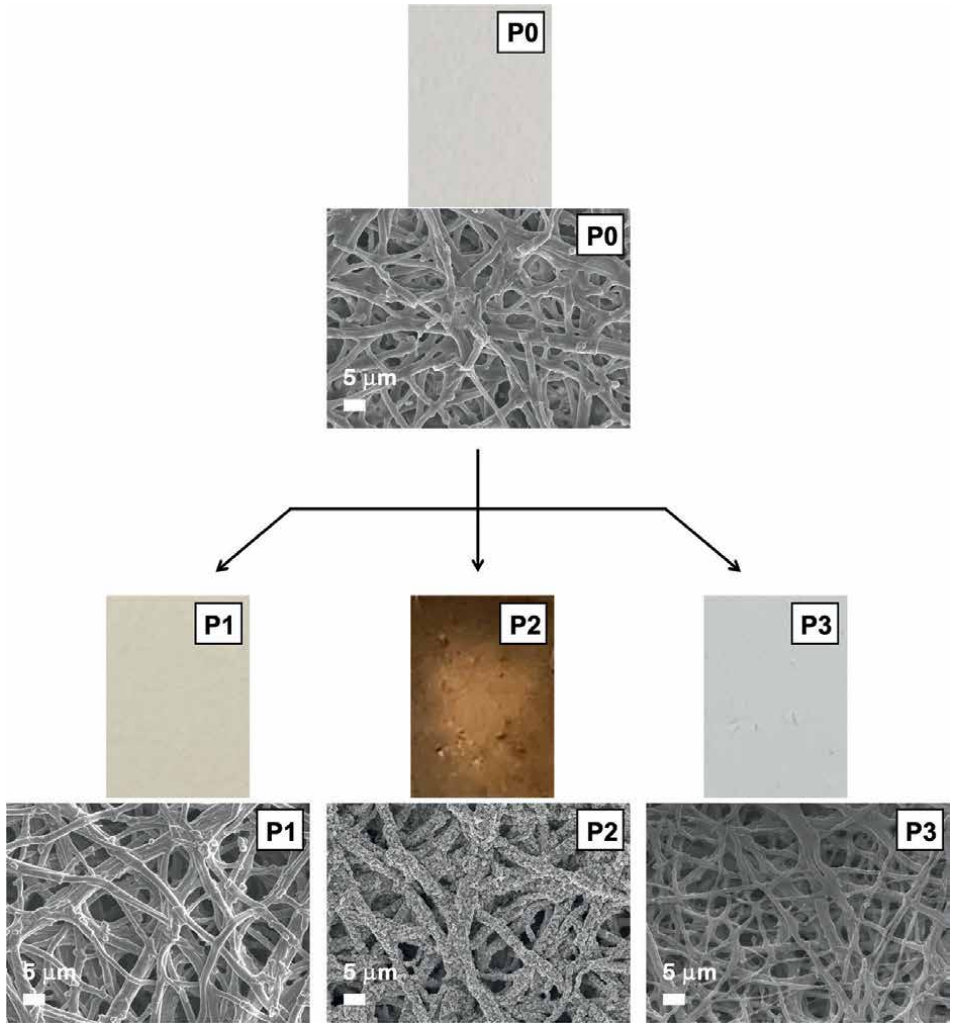

Figure 4.
Optical images and FESEM images of pristine ESM (P0), ZnO-functionalized ESM by RF magnetron sputtering (P1), ZnO-functionalized ESM by electroless deposition (P2), and ZnO replica of ESM by biomorphic mineralization (P3).

(ICDD 03-065-2870), the metal playing the catalytic role in the ZnO electroless deposition. Because the P2 sample was fixed with a Cu tape on the substrate, the XRD pattern of this sample discloses also the peaks at 2θ: 43.3° and 50.4° associated to (111) and (200) planes of the face-centered cubic Cu structure (ICDD 00-004-0836).

In **Figure 6**, the reflectance spectrum of P0 sample shows a decrease at ~330 nm, in agreement to that reported for ESM [64]. In the reflectance spectra of P1–P3 samples, a strong decrease can be noticed at about 380–420 nm associated to the band-to-band transition in ZnO [22, 65].

In **Figure 7**, based on the reflectance data and using the Kubelka–Munk function, the band-gap value of ZnO was evaluated at approximately 3.1 eV (P1), 3.3 eV (P2), and 3.24 eV (P3) by plotting $[F(R)^*E]^2$ vs. photon energy (E), where $F(R) = (1 – R)^2/2R$ and R was the measured diffuse reflectance.

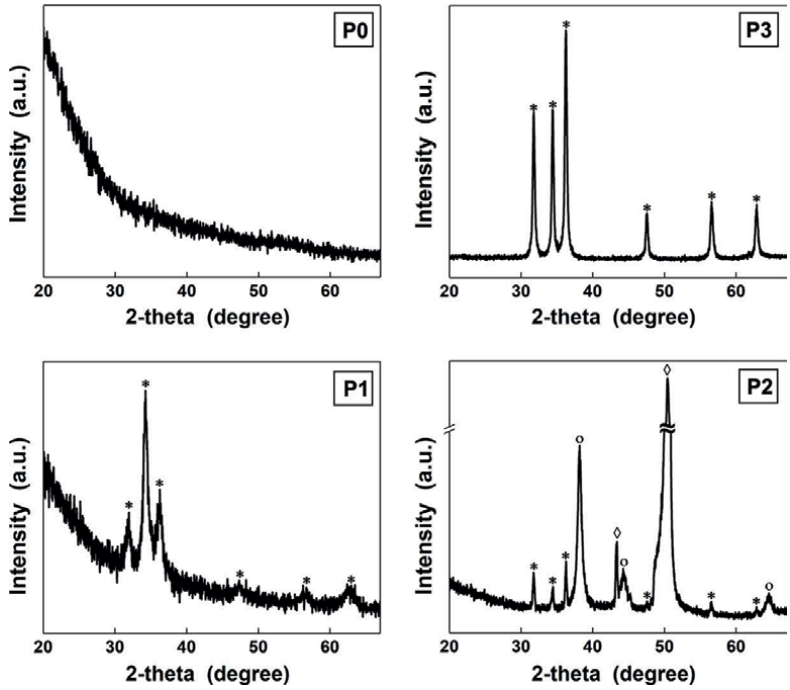

Figure 5.
XRD patterns of pristine ESM (P0), ZnO-functionalized ESM by RF magnetron sputtering (P1), ZnO-functionalized ESM by electroless deposition (P2), and ZnO replica of ESM by biomorphic mineralization (P3). The star, circle, and rhombus symbols are linked to the peaks attributed to ZnO, Au, and Cu, respectively.

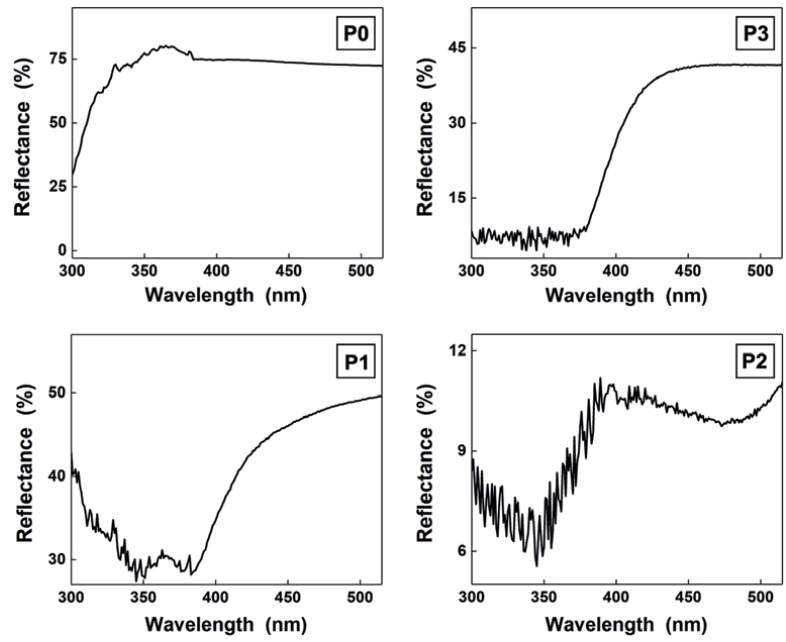

Figure 6.
Reflectance spectra of pristine ESM (P0), ZnO-functionalized ESM by RF magnetron sputtering (P1), ZnO-functionalized ESM by electroless deposition (P2), and ZnO replica of ESM by biomorphic mineralization (P3).

In **Figure 8**, the photoluminescence spectrum of P0 sample shows a broad emission band with two peaks at ~430 and ~470 nm, similar to those reported for ESM [66]. The photoluminescence spectra of P1 and P2 samples are dominated by the ESM emission, only a weak shoulder at ~550 nm (~2.25 eV) due to the ZnO emission being barely visible in the case of P2 sample. In the photoluminescence spectrum of P3 sample, it can be clearly noted the ZnO emission: (i) a weak band in the UV range centered at ~380 nm (~3.3 eV) linked to the band-band transition originating from the recombination of the free excitons and (ii) an intense and broadband in

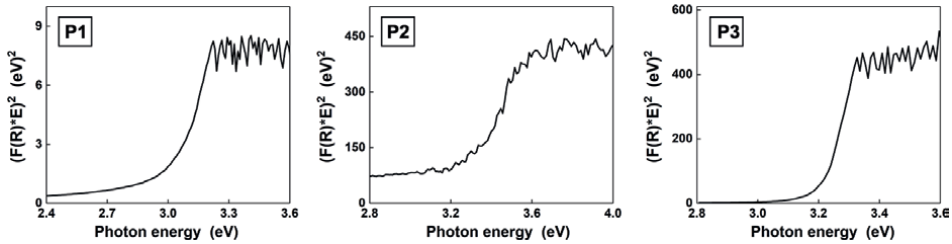

Figure 7.
Representation of Kubelka–Munk function employed to estimate the bad gap value of the ZnO-functionalized ESM by RF magnetron sputtering (P1), ZnO-functionalized ESM by electroless deposition (P2), and ZnO replica of ESM by biomorphic mineralization (P3).

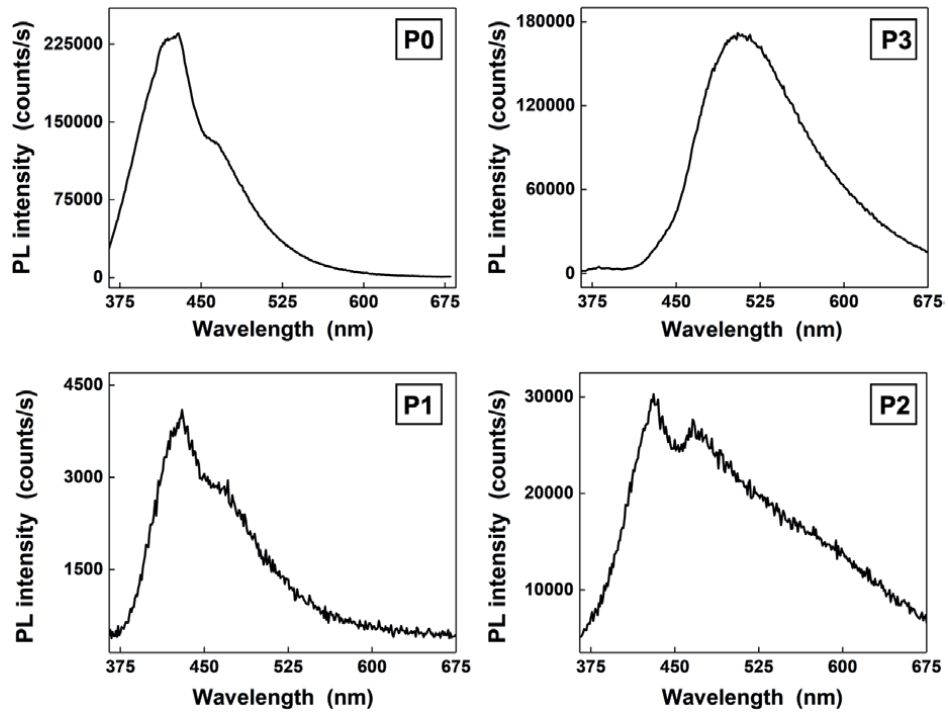

Figure 8.
Photoluminescence spectra of pristine ESM (P0), ZnO-functionalized ESM by RF magnetron sputtering (P1), ZnO-functionalized ESM by electroless deposition (P2), and ZnO replica of ESM by biomorphic mineralization (P3).

the visible domain centered at ~510 nm (~2.4 eV) related to various defects such as oxygen vacancy, zinc vacancy, interstitial oxygen, interstitial zinc, etc. [67].

The morphology of the investigated samples was evaluated by FESEM technique. The FESEM images acquired at different magnifications and in cross-sectional mode of the P0–P3 samples are given in **Figures 9–11**, respectively. In **Figure 9** (left side at lower magnification), the FESEM image of P0 sample reveals a 3D porous interwoven fibrous network structure consisting in a cross-linked smooth fiber with diameter sizes in the micrometer range and pores of several micrometers. The FESEM images of P1–P3 samples illustrate that this specific hierarchical porous configuration is

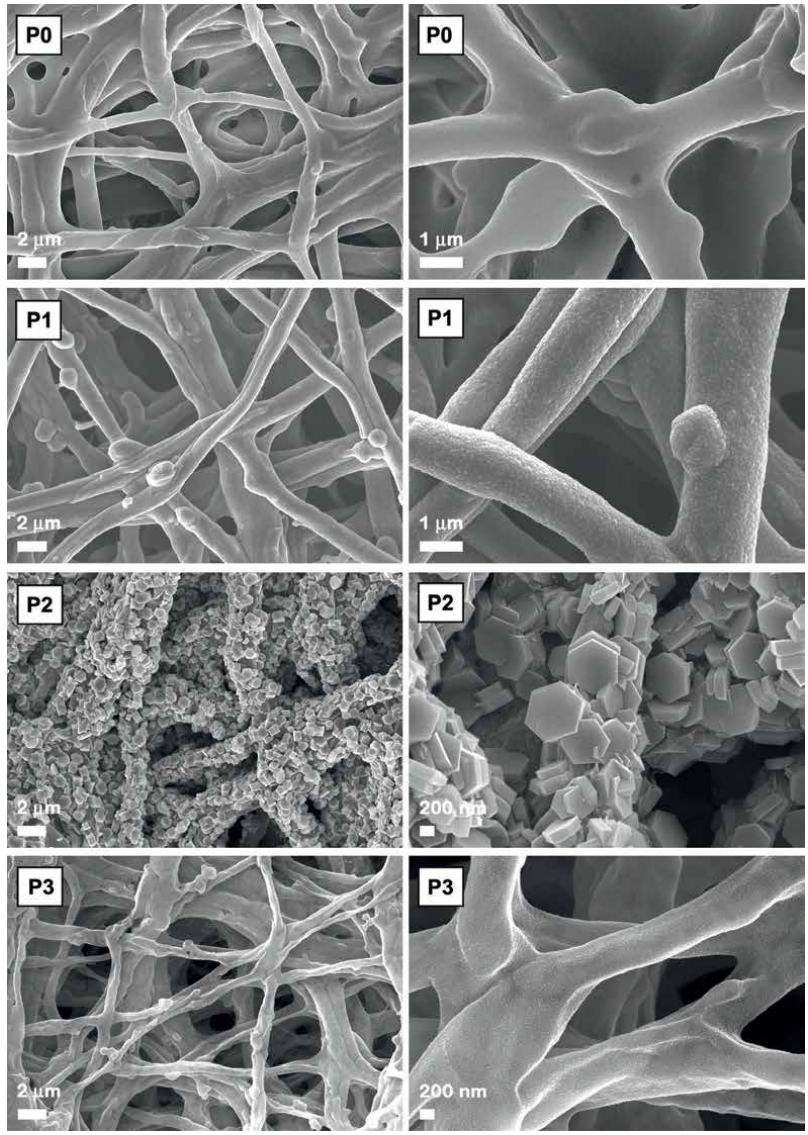

Figure 9.
FESEM images (at two magnifications) of pristine ESM (P0), ZnO-functionalized ESM by RF magnetron sputtering (P1), ZnO-functionalized ESM by electroless deposition (P2), and ZnO replica of ESM by biomorphic mineralization (P3).

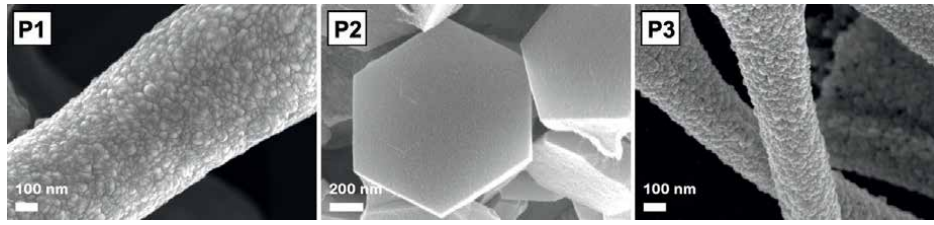

Figure 10.
FESEM images at higher magnification of ZnO-functionalized ESM by RF magnetron sputtering (P1), ZnO-functionalized ESM by electroless deposition (P2), and ZnO replica of ESM by biomorphic mineralization (P3).

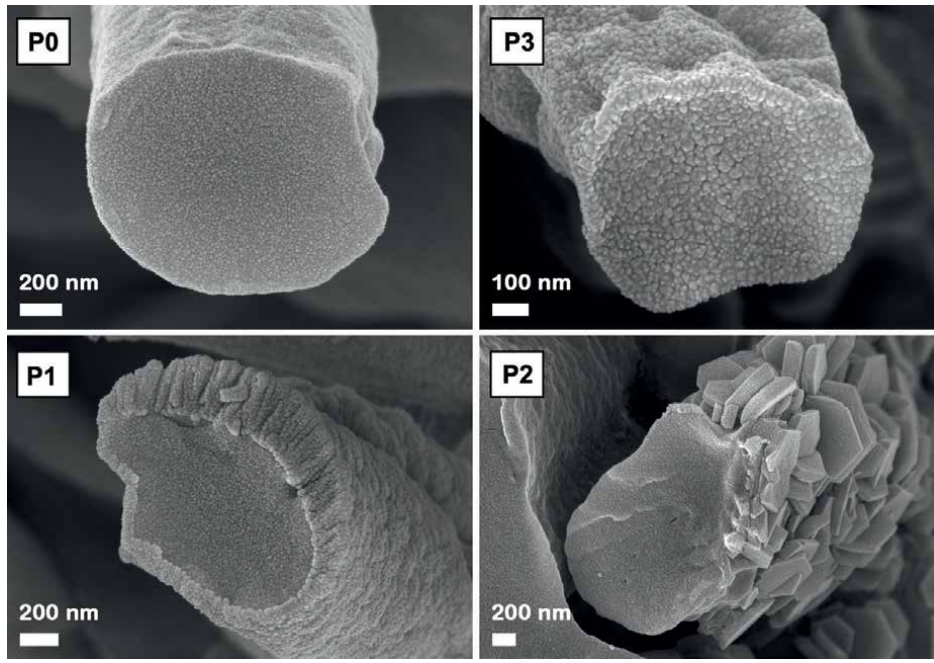

Figure 11.
Cross-sectional FESEM images of pristine ESM (P0), ZnO-functionalized ESM by RF magnetron sputtering (P1), ZnO-functionalized ESM by electroless deposition (P2), and ZnO replica of ESM by biomorphic mineralization (P3).

successfully preserved or replicated during the functionalization of replication, respectively. Hence, the experimental parameters involved in the RF magnetron sputtering, electroless deposition, or biomorphic mineralization processes are adequately chosen for avoiding the embedding of the ESM fibers into a metal oxide thick layer. In **Figure 9** (right side at medium magnification), the FESEM images of P1–P3 samples disclose the following details: (i) RF magnetron sputtering leads to the deposition of a continuous and uniform ZnO structured film on the surfaces of the ESM fibers, (ii) electroless deposition results in a completely and uniformly covered of the ESM fibers with densely packed twin well faceted hexagonal prisms, and (iii) biomorphic mineralization directs an accurate replication process in which the inorganic replica inherit perfectly the original 3D interconnected fiber skeleton of the organic template.

The FESEM images at higher magnification from **Figure 10** disclose the following details concerning the structure and the size of ZnO: (i) P1 sample — the

ZnO film consists in nanoparticles with a relatively homogeneous size at ~20 nm, (ii) P2 sample — the ZnO prisms have sizes varying from 400 nm to 1 μm, and (iii) P3 sample — the ZnO fibers are built from particles with a relatively homogeneous size distribution in the range of ~10–30 nm. In addition, the cross-sectional FESEM images from **Figure 11** emphasize interesting features such as (i) P1 and P2 samples — a hybrid structure based on ESM fiber organic core and ZnO inorganic shell, (ii) P1 sample — the thickness of the ZnO shell is of ~300 nm, (iii) P2 sample — a site-selectively growth of ZnO hexagonal prims only on the Au catalyst layer, and (iv) P3 sample — the assembly of ZnO nanoparticles as building blocks in the ZnO fibers. Hence, the mechanism involved in the ZnO growth by electroless deposition can be described as follows: (i) the nucleation process begins from the catalyst layer, (ii) the catalytic reaction leads to the formation of the ZnO nuclei, and (iii) when the activated surface of the fibers is entirely covered by the initial ZnO nuclei, these become the growth sites for the hexagonal prism structures. In the case of the biomorphic mineralization, the mechanism can take place as follows: (i) during the immersion in the zinc nitrate aqueous solution, the ESM governs the uniform adsorption of the zinc ions and (ii) during the calcination, the zinc-occupied positions become incipient centers of nucleation and initiate the growth of ZnO crystallites, the process being accompanied by the ESM burnout, and in this way, ESM directing the assembly of the ZnO crystallites in its particular architecture.

The topography of the investigated samples was analyzed by AFM technique. The AFM images of P0–P3 samples from **Figure 12** show that there is no distortion in the fibrous architecture after functionalization or replication processes.

Thus, in comparison to the P0 sample, P1–P3 samples show a lowering in the roughness due to (i) the uniform coverage of the surface of the fibers with the compact nanostructured ZnO layer by RF magnetron sputtering, (ii) the growth of ZnO hexagonal prisms by electroless deposition, and (iii) the assembly of the ZnO nanoparticles into the fiber resulting in an accurate inorganic replica of the organic bio-template by biomorphic mineralization.

The behavior of raw ESM or ZnO-functionalized ESM in the presence of water is a key parameter for potential applications in water purification, photocatalysis, antibacterial areas, etc. Thus, when a water droplet is placed on the surface of the pristine ESM, a hydrophobic behavior (water contact angle of ~122°) is noted immediately after the water droplet placement (**Figure 13a**), similar to the results previously reported for ESM [68]. In this case, the water droplet does not penetrate into the membrane due to the air entrapped in its 3D porous structure. But this hindrance disappears very quickly (~1min) and a penetration of the water droplet into membrane occurs (**Figure 13b**). The same behavior is observed for ZnO-functionalized ESM by electroless deposition but the penetration time of the water droplet increasing at ~3–4 min, the presence of the ZnO structures on the surface of the ESM fibers being responsible for the decrease of the space between them. Consequently, after the functionalization, the hybrid structure conserves the ESM characteristic regarding the water absorption.

In order to evaluate the potential integration of ZnO fiber webs in the electronic devices, sensors, etc., electrical measurements were carried on samples prepared as follows: the ESM impregnated with zinc ions were placed on Si/SiO_2 substrates patterned with interdigitated metallic electrodes, dried in air, and subsequently calcined. The fabrication of the interdigitated metallic electrodes combines conventional photolithography and RF magnetron sputtering deposition. Hence, a photoresist was spin-coated on the Si/SiO_2 wafers, the obtained layer was exposed to UV light through a mask, thermally treated, and after a developing procedure, the Ti (10 nm)/

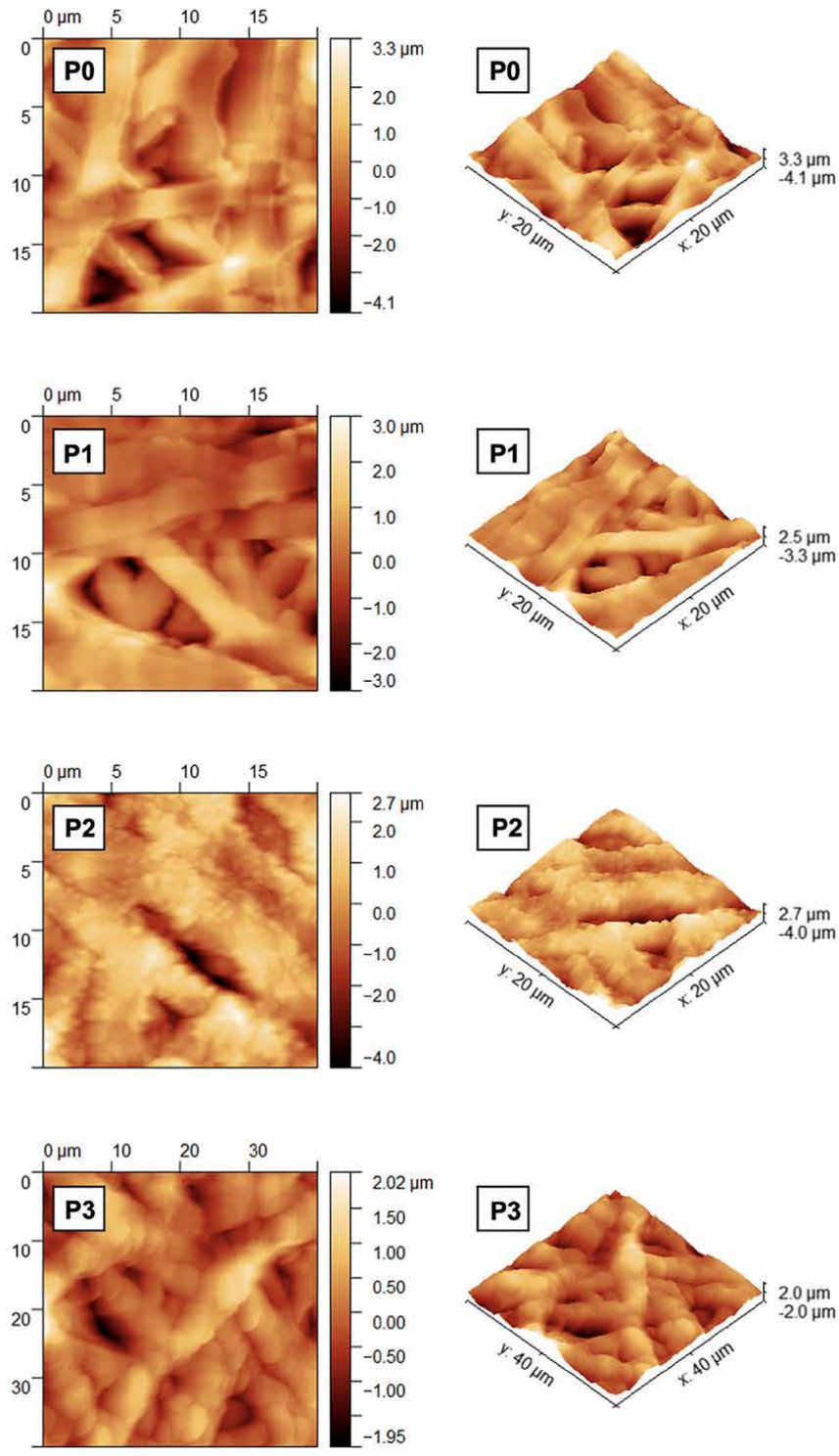

Figure 12.
AFM images of pristine ESM (P0), ZnO-functionalized ESM by RF magnetron sputtering (P1), ZnO-functionalized ESM by electroless deposition (P2) and ZnO replica of ESM by biomorphic mineralization (P3).

Figure 13.
The optical images of a water droplet immediately on its placement on the surface of the pristine ESM (a) and after its penetration into ESM (b).

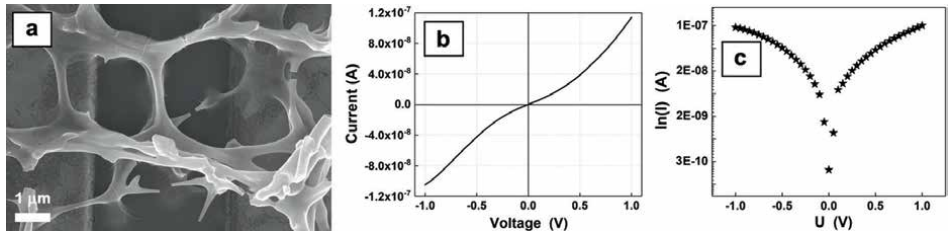

Figure 14.
FESEM image (a), I-V characteristic (b), and semilogarithmic representation of the I-V characteristic (c) of the 3D fibrous networks based on ZnO.

Pt (200 nm) thin layer was deposited. The Ti layer is required for the improvement of the adhesion of the Pt layer to the Si/SiO_2 substrates. Finally, after the photoresist removal in a solvent, the interdigitated Ti/Pt electrodes were obtained. As can be seen in the FESESM image of the ZnO fiber webs prepared on Si/SiO_2 patterned with interdigitated metallic electrodes, the semiconducting fibers formed bridges between the neighboring grid structures being electrically self-contacted (**Figure 14a**). Hence, the I–V characteristic of this sample recorded at room temperature in a two-point configuration when the bias was swept from –1 V to +1 V reveals a symmetrical nonlinear behavior (**Figure 14b**), indicating a Schottky contact between Pt and ZnO [69]. As consequence, the Pt/ZnO/Pt structure can be considered a system consisting of two back-to-back Schottky diodes, its ideality factor value being estimated at ~1.1 from the semilogarithmic representation of the I–V characteristic (**Figure 14c**). Because the ZnO fibers connect the interdigitated metallic electrodes, the transport of charges takes place by percolating through the semiconducting junctions until it reaches to the metallic electrodes [70].

Therefore, this approach that combines the biomorphic mineralization and substrates patterned with interdigitated metallic electrodes offers the opportunity to benefit in applications of both high surface-to-volume ratio and electrically self-contacted features.

3. Conclusions

Eggshell membrane, a naturally occurring biopolymer with a unique architecture consisting in 3D porous interwoven fibrous protein network, was used as biotemplate for developing ZnO-based nanomaterials using relatively simple and inexpensive preparation approaches such as radio frequency (RF) magnetron sputtering, electroless deposition, and biomorphic mineralization. The specific 3D fibrous web of the ESM was successfully preserved during its functionalization

with ZnO by RF magnetron sputtering and electroless deposition or perfectly inhered by its ZnO replica obtained by biomorphic mineralization. Thus, FESEM images disclose that the ESM fibers were coated with a continuous and uniform metal oxide layer formed by ZnO nanoparticles (RF magnetron sputtering), covered with ZnO hexagonal prisms (electroless deposition), or replicated into metal oxide fibers containing ZnO nanoparticles as building blocks (biomorphic mineralization). The experimental parameters involved in the functionalization processes were properly chosen for avoiding the embedding of the ESM fibers into a metal oxide thick layer, the hybrid organic core/inorganic shell structure being emphasized by the cross-sectional FESEM images. The XRD patterns and reflectance spectra confirm the presence of ZnO in the functionalized or replicated samples while the photoluminescence spectra clearly evidence ZnO only in the replicated one. The wettability investigation shows that after functionalization procedures, the hybrid structures maintain the ESM characteristic regarding the water absorption. By combining the biomorphic mineralization method and the substrates patterned with interdigitated metallic electrodes, the electrical properties of the self-contacted ZnO fiber webs were investigated, the transport of charges taking place through the formed junctions over the interdigitated metallic electrodes. Thus, electrical paths between the neighboring grid structures are provided without any additional contacting steps.

Consequently, such bio-template mediated synthesis pathway based on the conversion of an abundant biowaste, such as ESM, into a source for obtaining new value-added nanomaterials can be very attractive from the environmental sustainability and recycle waste perspective, the ZnO-based fibrous architectures having potential applications in different areas (photocatalysis, water purification, electronic devices, sensors, etc.).

Acknowledgements

This work was supported by a grant of the Ministry of Research, Innovation and Digitization, CNCS - UEFISCDI, project number PN-III-P4-PCE-2021-1131, within PNCDI III.

Conflict of interest

The authors declare no conflict of interest.

Author details

Nicoleta Preda*, Marcela Socol, Andreea Costas and Irina Zgura
National Institute of Materials Physics, Magurele, Romania

*Address all correspondence to: nicol@infim.ro

IntechOpen

References

[1] Rai RS, Girish JP, Bajpai V, Khan MI, Elboughdiri N, Shanableh A, et al. An eco-friendly approach on green synthesis, bio-engineering applications, and future outlook of ZnO nanomaterial: A critical review. Environmental Research. 2023;**221**:114807. DOI: 10.1016/j.envres.2022.114807

[2] Clarke B, Ghandi K. The interplay of growth mechanism and properties of ZnO nanostructures for different applications. Small. 2023;**19**:2302864. DOI: 10.1002/smll.202302864

[3] Raha S, Ahmaruzzaman M. ZnO nanostructured materials and their potential applications: Progress, challenges and perspectives. Nanoscale Advances. 2022;**4**:1868-1925. DOI: 10.1039/d1na00880c

[4] Noman MT, Amor N, Petru M. Synthesis and applications of ZnO nanostructures (ZONSs): A review. Critical Reviews in Solid State and Materials Sciences. 2022;**47**:99-141. DOI: 10.1080/10408436.2021.1886041

[5] Sheikh M, Pazirofteh M, Dehghani M, Asghari M, Rezakazemi M, Valderrama C, et al. Application of ZnO nanostructures in ceramic and polymeric membranes for water and wastewater technologies: A review. Chemical Engineering Journal. 2020;**391**:123475. DOI: 10.1016/j.cej.2019.123475

[6] Theerthagiri J, Salla S, Senthil RA, Nithyadharseni P, Madankumar A, Arunachalam P, et al. A review on ZnO nanostructured materials: Energy, environmental and biological applications. Nanotechnology. 2019;**30**:392001. DOI: 10.1088/1361-6528/ab268a

[7] Rong P, Ren S, Yu Q. Fabrications and applications of ZnO nanomaterials in flexible functional devices: A review. Critical Reviews in Analytical Chemistry. 2019;**49**:336-349. DOI: 10.1080/10408347.2018.1531691

[8] Natu K, Laad M, Ghule B, Shalu A. Transparent and flexible zinc oxide-based thin-film diodes and thin-film transistors: A review. Journal of Applied Physics. 2023;**134**:190701. DOI: 10.1063/5.0169308

[9] Hu JN, Chen J, Ma T, Li ZH, Hu J, Ma T, et al. Research advances in ZnO nanomaterials-based UV photodetectors: A review. Nanotechnology. 2023;**34**:232002. DOI: 10.1088/1361-6528/acbf59

[10] Otalora C, Botero MA, Ordonez G. ZnO compact layers used in third-generation photovoltaic devices: A review. Journal of Materials Science. 2021;**56**:15538-15571. DOI: 10.1007/s10853-021-06275-5

[11] Kang YL, Yu F, Zhang L, Wang WH, Chen L, Li YC. Review of ZnO-based nanomaterials in gas sensors. Solid State Ionics. 2021;**360**:115544. DOI: 10.1016/j.ssi.2020.115544

[12] Wang LY, Shi BY, Yao CB, Wang ZM, Wang X, Jiang CH, et al. Size and morphology modulation in ZnO nanostructures for nonlinear optical applications: A review. ACS Applied Nano Materials. 2023;**6**:9975-10014. DOI: 10.1021/acsanm.3c01509

[13] Krishna MS, Singh S, Batool M, Fahmy HM, Seku K, Shalan AE, et al. A review on 2D-ZnO nanostructure based biosensors: From materials to devices. Materials Advances. 2023;**4**:320-354. DOI: 10.1039/d2ma00878e

[14] Napi MLM, Noorden AFA, Tan MLP, Jamaluddin H, Abd Hamid F, Ahmad MK, et al. Review—Three dimensional zinc oxide nanostructures as an active site platform for biosensor: Recent trend in healthcare diagnosis. Journal of The Electrochemical Society. 2020;**167**:137501. DOI: 10.1149/1945-7111/abb4f4

[15] Mishra AK, Singh P, Zala D, Shaikh N, Vemuri SK, Suthar J, et al. Plasmonic solar energy harvesting by ZnO nanostructures and their composite interfaces: A review on fundamentals, recent advances, and applications. Energy Technology. 2023;**11**:2201393. DOI: 10.1002/ente.202201393

[16] Areeshi MY. A review on biological synthesis of ZnO nanostructures and its application in photocatalysis mediated dye degradation: An overview. Luminescence. 2022;**38**:1111-1122. DOI: 10.1002/bio.4432

[17] Samadi M, Zirak M, Naseri A, Kheirabadi M, Ebrahimi M, Moshfegh AZ. Design and tailoring of one-dimensional ZnO nanomaterials for photocatalytic degradation of organic dyes: A review. Research on Chemical Intermediates. 2019;**45**:2197-2254. DOI: 10.1007/s11164-018-03729-5

[18] Izzi M, Sportelli MC, Torsi L, Picca RA, Cioffi N. Synthesis and antimicrobial applications of ZnO nanostructures: A review. ACS Applied Nano Materials. 2023;**6**:10881-10902. DOI: 10.1021/acsanm.3c01432

[19] Cruz DM, Mostafavi E, Vernet-Crua A, Barabadi H, Shah V, Cholula-Diaz JL, et al. Green nanotechnology-based zinc oxide (ZnO) nanomaterials for biomedical applications: A review. Journal of Physics: Materials. 2020;**3**:034005. DOI: 10.1088/2515-7639/ab8186

[20] Mardosaite R, Jurkeviciute A, Rackauskas S. Superhydrophobic ZnO nanowires: Wettability mechanisms and functional applications. Crystal Growth & Design. 2021;**21**:4765-4779. DOI: 10.1021/acs.cgd.1c00449

[21] Xu S, Wang ZL. One-dimensional ZnO nanostructures: Solution growth and functional properties. Nano Research. 2011;**4**:1013-1098. DOI: 10.1007/s12274-011-0160-7

[22] Ahmad M, Zhu J. ZnO based advanced functional nanostructures: Synthesis, properties and applications. Journal of Materials Chemistry. 2011;**21**:599-614. DOI: 10.1039/c0jm01645d

[23] Costas A, Preda N, Zgura I, Kuncser A, Apostol N, Curutiu C, et al. Silver nanoparticles decorated ZnO–CuO core–shell nanowire arrays with low water adhesion and high antibacterial activity. Scientific Reports. 2023;**13**:10698. DOI: 10.1038/s41598-023-37953-w

[24] Florica C, Costas A, Preda N, Beregoi M, Kuncser A, Apostol N, et al. Core-shell nanowire arrays based on ZnO and CuxO for water stable photocatalysts. Scientific Reports. 2019;**9**:17268. DOI: 10.1038/s41598-019-53873-0

[25] Florica C, Preda N, Costas A, Zgura I, Enculescu I. ZnO nanowires grown directly on zinc foils by thermal oxidation in air: Wetting and water adhesion properties. Materials Letters. 2016;**170**:156-159. DOI: 10.1016/j.matlet.2016.02.035

[26] Florica C, Costas A, Kuncser A, Preda N, Enculescu I. High performance FETs based on ZnO nanowires synthesized by low cost methods. Nanotechnology. 2016;**27**:475303. DOI: 10.1088/0957-4484/27/47/475303

[27] Socol M, Preda N, Costas A, Breazu C, Stanculescu A, Rasoga O, et al. Hybrid organic-inorganic thin films based on zinc phthalocyanine and zinc oxide deposited by MAPLE. Applied Surface Science. 2020;**503**:144317. DOI: 10.1016/j.apsusc.2019.144317

[28] Zgura I, Preda N, Enculescu M, Diamandescu L, Negrila C, Bacalum M, et al. Cytotoxicity, antioxidant, antibacterial, and photocatalytic activities of ZnO–CdS powders. Materials. 2020;**13**:182. DOI: 10.3390/ma13010182

[29] Preda N, Enculescu M, Enculescu I. Polysaccharide-assisted crystallization of ZnO micro/nanostructures. Materials Letters. 2014;**115**:256-260. DOI: 10.1016/j.matlet.2013.10.081

[30] Florica C, Preda N, Enculescu M, Zgura I, Socol M, Enculescu I. Superhydrophobic ZnO networks with high water adhesion. Nanoscale Research Letters. 2014;**9**:385. DOI: 10.1186/1556-276X-9-385

[31] Torres FG, Troncoso OP, Piaggio F, Hijar A. Structure–property relationships of a biopolymer network: The eggshell membrane. Acta Biomaterialia. 2010;**6**:3687-3693. DOI: 10.1016/j.actbio.2010.03.014

[32] Balaz M. Eggshell membrane biomaterial as a platform for applications in materials science. Acta Biomaterialia. 2014;**10**:3827-3843. DOI: 10.1016/j.actbio.2014.03.020

[33] Park S, Choi KS, Lee D, Kim D, Lim KT, Lee KH, et al. Eggshell membrane: Review and impact on engineering. Biosystems Engineering. 2016;**151**:446-463. DOI: 10.1016/j.biosystemseng.2016.10.014

[34] Lin MF, Chang PY, Lee CH, Wu XX, Jeng RJ, Chen CP. Biowaste eggshell membranes for bio-triboelectric nanogenerators and smart sensors. ACS Omega. 2023;**8**:6699-6707. DOI: 10.1021/acsomega.2c07292

[35] Tanifuji N, Shimizu T, Yoshikawa H, Tanaka M, Nishio K, Ida K, et al. Assessment of eggshell membrane as a new type of proton-conductive membrane in fuel cells. ACS Omega. 2022;**7**:12637-12642. DOI: 10.1021/acsomega.1c06687

[36] dos Reis GS, Lima RMAP, Larsson SH, Subramaniyam CM, Dinh VM, Thyrel M, et al. Flexible supercapacitors of biomass-based activated carbon-polypyrrole on eggshell membranes. Journal of Environmental Chemical Engineering. 2021;**9**:106155. DOI: 10.1016/j.jece.2021.106155

[37] Nguyen VH, Lee DH, Baek SY, Kim YH. Recycling different eggshell membranes for lithium-ion battery. Materials Letters. 2018;**228**:504-508. DOI: 10.1016/j.matlet.2018.06.081

[38] Saratale RG, Sun QZ, Munagapati VS, Saratale GD, Park J, Kim DS. The use of eggshell membrane for the treatment of dye-containing wastewater: Batch, kinetics and reusability studies. Chemosphere. 2021;**281**:130777. DOI: 10.1016/j.chemosphere.2021.130777

[39] Peigneux A, Puentes-Pardo JD, Rodriguez-Navarro AB, Hincke MT, Jimenez-Lopez C. Development and characterization of magnetic eggshell membranes for lead removal from wastewater. Ecotoxicology and Environmental Safety. 2020;**192**:110307. DOI: 10.1016/j.ecoenv.2020.110307

[40] Ray PG, Roy S. Eggshell membrane: A natural substrate for immobilization and detection of DNA. Materials Science and Engineering: C. 2016;**59**:404-410. DOI: 10.1016/j.msec.2015.10.034

[41] Chen XF, Chen YQ, Fu BF, Li KJ, Huang DH, Zheng CH, et al. Eggshell membrane-mimicking multifunctional nanofiber for in-situ skin wound healing. International Journal of Biological Macromolecules. 2022;**210**:139-151. DOI: 10.1016/j.ijbiomac.2022.04.212

[42] Park S, Gwon Y, Kim W, Kim J. Rebirth of the eggshell membrane as a bioactive nanoscaffold for tissue engineering. ACS Biomaterials Science & Engineering. 2021;**7**:2219-2224. DOI: 10.1021/acsbiomaterials.1c00552

[43] Beregoi M, Preda N, Evanghelidis A, Costas A, Enculescu I. Versatile actuators based on polypyrrole-coated metalized eggshell membranes. ACS Sustainable Chemistry & Engineering. 2018;**6**:10173-10181. DOI: 10.1021/acssuschemeng.8b01489

[44] Alcaraz-Espinoza JJ, de Melo CP, de Oliveira HP. Fabrication of highly flexible hierarchical polypyrrole/carbon nanotube on eggshell membranes for supercapacitors. ACS Omega. 2017;**2**:2866-2877. DOI: 10.1021/acsomega.7b00329

[45] Tang QW, Wu JH, Tang ZY, Li Y, Lin JM, Huang ML. Flexible and macroporous network-structured catalysts composed of conducting polymers and Pt/Ag with high electrocatalytic activity for methanol oxidation. Journal of Materials Chemistry. 2011;**21**:13354-13364. DOI: 10.1039/c1jm11857a

[46] Preda N, Costas A, Beregoi M, Apostol N, Kuncser A, Curutiu C, et al. Functionalization of eggshell membranes with CuO–ZnO based p–n junctions for visible light induced antibacterial activity against *Escherichia coli*. Scientific Reports. 2020;**10**:20960. DOI: 10.1038/s41598-020-78005-x

[47] Preda N, Costas A, Beregoi M, Enculescu I. A straightforward route to obtain organic/inorganic hybrid network from bio-waste: Electroless deposition of ZnO nanostructures on eggshell membranes. Chemical Physics Letters. 2018;**706**:24-30. DOI: 10.1016/j.cplett.2018.05.073

[48] Lee SM, Grass G, Kim GM, Dresbach C, Zhang LB, Gosele U, et al. Low-temperature ZnO atomic layer deposition on biotemplates: Flexible photocatalytic ZnO structures from eggshell membranes. Physical Chemistry Chemical Physics. 2009;**11**:3608-3614. DOI: 10.1039/b820436e

[49] Preda N, Costas A, Enculescu M, Enculescu I. Biomorphic 3D fibrous networks based on ZnO, CuO and ZnO–CuO composite nanostructures prepared from eggshell membranes. Materials Chemistry and Physics. 2020;**240**:122205. DOI: 10.1016/j.matchemphys.2019.122205

[50] Mallampati R, Valiyaveettil S. Biomimetic metal oxides for the extraction of nanoparticles from water. Nanoscale. 2013;**5**:3395-3399. DOI: 10.1039/c3nr34221b

[51] Dong Q, Su HL, Song F, Zhang D, Wang N. Hierarchical metal oxides assembled by nanocrystallites via a simple bio-inspired route. Journal of the American Ceramic Society. 2007;**90**:376-380. DOI: 10.1111/j.1551-2916.2006.01392.x

[52] Puthiyottil H, Thankamani PR, Saji KJ. Exploring the effects of substrate and substrate temperature on the properties of radio frequency magnetron sputtered ZnO thin films. Materials Today Communications. 2023;**36**:106455. DOI: 10.1016/j.mtcomm.2023.106455

[53] Chuang KT, Abdullah H, Leu SJ, Cheng KB, Kuo DH, Chen HC, et al.

Metal oxide composite thin films made by magnetron sputtering for bactericidal application. Journal of Photochemistry and Photobiology, A: Chemistry. 2007;**337**:151-164. DOI: 10.1016/j.jphotochem.2017.01.012

[54] Nagaya S, Nishikiori H. Preparation of dye-adsorbing ZnO thin films by electroless deposition and their photoelectrochemical properties. ACS Applied Materials & Interfaces. 2013;**5**:8841-8844. DOI: 10.1021/am4026483

[55] Shinagawa T, Otomo S, Katayama JI, Izaki M. Electroless deposition of transparent conducting and oriented ZnO films from aqueous solutions. Electrochimica Acta. 2007;**53**:1170-1174. DOI: 10.1016/j.electacta.2007.03.056

[56] Shao TC, Li C, Lv MS, Zhang XF, Deng ZP, Xu YM, et al. Biomorphic ZnO nanotubes for n-pentanol sensing. ACS Applied Nano Materials. 2022;**5**:737-746. DOI: 10.1021/acsanm.1c03483

[57] Firooz AA, Darvishnejad MH. Biomorphic ZnO structures: Synthesis and optical properties. Inorganic and Nano-Metal Chemistry. 2017;**47**:412-415. DOI: 10.1080/15533174.2016.1186074

[58] Zhou M, Zang DL, Zhai XL, Gao ZX, Zhang WB, Wang CY. Preparation of biomorphic porous zinc oxide by wood template method. Ceramics International. 2016;**42**:10704-10710. DOI: 10.1016/j.ceramint.2016.03.188

[59] Xu Z, Yu K, Li B, Huang R, Wu P, Mao HB, et al. Optical properties of SiO_2 and ZnO nanostructured replicas of butterfly wing scales. Nano Research. 2011;**4**:737-745. DOI: 10.1007/s12274-011-0130-0

[60] Fan TX, Chow SK, Di Z. Biomorphic mineralization: From biology to materials. Progress in Materials Science. 2009:542-659. DOI: 10.1016/j.pmatsci.2009.02.001

[61] Lizundia E, Luzi F, Puglia D. Organic waste valorisation towards circular and sustainable biocomposites. Green Chemistry. 2022;**24**:5429-5459. DOI: 10.1039/d2gc01668k

[62] Fu ZG, Pan ZC, Sun DL, Zhan GH, Zhang HC, Zeng XF, et al. Multiple morphologies of ZnO films synthesized on flexible poly(ethylene terephthalate) by electroless deposition. Materials Letters. 2016;**184**:185-188. DOI: 10.1016/j.matlet.2016.08.046

[63] Torres FG, Troncoso OP, Montes MR. The effect of temperature on the mechanical properties of a protein-based biopolymer network: The eggshell membrane. Journal of Thermal Analysis and Calorimetry. 2013;**111**:1921-1925. DOI: 10.1007/s10973-012-2915-0

[64] Li YL, Zhou J, Fan YD, Ye Y, Tang B. Preparation of environment-friendly 3D eggshell membrane-supported anatase TiO_2 as a reusable photocatalyst for degradation of organic dyes. Chemical Physics Letters. 2017;**689**:142-147. DOI: 10.1016/j.cplett.2017.10.019

[65] Ozgur U, Alivov YI, Liu C, Teke A, Reshchikov MA, Dogan S, et al. A comprehensive review of ZnO materials and devices. Journal of Applied Physics. 2005;**98**:041301. DOI: 10.1063/1.1992666

[66] Shao CY, Yuan B, Wang HQ, Zhou QA, Li YL, Guan YF, et al. Eggshell membrane as a multimodal solid-state platform for generating fluorescent metal nanoclusters. Journal of Materials Chemistry. 2011;**21**:2863-2866. DOI: 10.1039/c0jm04071a

[67] Djurisic AB, Leung YH. Optical properties of ZnO nanostructures.

Small. 2006;**2**:944-961. DOI: 10.1002/smll.200600134

[68] Hsieh S, Chou HH, Hsieh CW, Wu DC, Kuo CH, Lin FH. Hydrogen peroxide treatment of eggshell membrane to control porosity. Food Chemistry. 2013;**141**:2117-2121. DOI: 10.1016/j.foodchem.2013.04.115

[69] Yan FP, Wang YH, Zhang JY, Lin Z, Zheng JS, Huang F. Schottky or ohmic metal–semiconductor contact: Influence on photocatalytic efficiency of Ag/ZnO and Pt/ZnO model systems. ChemSusChem. 2014;**7**:101-104. DOI: 10.1002/cssc.201300818

[70] Krausmann J, Sanctis S, Engstler J, Luysberg M, Bruns M, Schneider JJ. Charge transport in low-temperature processed thin-film transistors based on indium oxide/zinc oxide heterostructures. ACS Applied Materials & Interfaces. 2018;**10**:20661-20671. DOI: 10.1021/acsami.8b03322

Edited by Ana Rovisco and Ana Pimentel

This book explores the remarkable potential of zinc oxide (ZnO) nanostructures, one of the most versatile materials in nanotechnology, notable for their wide bandgap, high exciton binding energy, and adaptable surface chemistry. It provides a comprehensive overview of the latest advancements in ZnO research, focusing on their synthesis, properties, and diverse applications across key scientific and industrial fields. Readers will discover how ZnO nanostructures are revolutionizing environmental science with sustainable pollution control solutions, advancing biomedicine through innovative drug delivery systems and diagnostics, and enhancing agriculture by improving crop yield and quality. The book also delves into the precision engineering of ZnO for cutting-edge sensors and electronic devices while exploring bioinspired approaches to designing nanomaterials with tailored functionalities. With its multidisciplinary scope, this volume serves as an essential resource for researchers, academics, and professionals, offering valuable insights into the transformative role of ZnO nanoparticles in addressing today's scientific and technological challenges.

Jung Huang,
Nanotechnology and Nanomaterials Series Editor

ISSN 3029-0538
ISBN 978-0-85466-603-4
9 780854 666034

Published in London, UK

IntechOpen